Hydraulic fracture monitoring: Integrated analysis of borehole logs, seismic reflectivity, microseismicity, ISIP analysis and PKN modelling.

by

Tahmina Mirzayeva

A thesis submitted in partial fulfillment of the requirements for the degree of

Master of Science

Department of Physics
University of Alberta

Abstract

Hydraulic fracturing operations in Montney formation present challenges due to anomalous microseismic behavior and inconsistent cloud patterns. Fracture propagation is mostly uni-directional, moving predominantly towards the northeast. However, some stages exhibit behavior contrary to this trend. The overall cloud pattern is inconsistent, lacking a clear explanation for such phenomena. This study aims to use different types of datasets to explain the behavior of fracture propagation in the Montney formation. Therefore, this study aims to elucidate the dynamics of fracture propagation through four key objectives: assessing fracture treatment parameters, unraveling microseismic behavior mechanisms, exploring the link between microseismic events and geological features, and investigating stress shadow effects.

Employing the Perkins-Kern-Nordgren (PKN) model alongside novel parameters, including variation in fracture height and Plane strain modulus, we analyze fracture treatment parameters (Perkins & Kern, 1961). Using the PKN model, we calculate the fracture half-length and compare it with the microseismic cloud fracture length to understand the link between treatment parameters and actual fracture propagation. The PKN fracture length estimation is mostly affected by the fracture duration, showing a small correlation between the PKN and microseismic cloud lengths, suggesting that higher duration may affect the results. However, there are significant discrepancies between the results, with PKN overestimating the fracture length, which is normal due to the simplicity of the PKN approach. The observed anomalies suggest additional factors influencing propagation behavior beyond treatment parameters alone.

Later, we used Microseismic Analysis (MS) to understand the general pattern of cloud propagation and trajectories and explore possible causes of unidirectional propagation. Microseismic events revealed that most propagation occurs toward the northeast, although some stages show a tendency toward the southwest after some stages. To investigate unidirectional propagation, we applied a magnitude filter, considering that it might be due to the distance between treatment well and monitoring well. Results revealed that this is not the cause; the magnitude cut-off only affected the cloud thickness. We also interpreted r-t plots, revealing the existence of "Normal," "halted-growth," and "Reactivation" patterns. Later, we used r-t plots and applied a model-based approach to understand fracture length propagation over time by fitting the model equation. By doing so, we have defined the regimes of fracture treatment with time-dependency relationships. We found that regimes on the northeast side are mostly storage-dominated, while those on the southwest are mostly leak-off dominated.

Integration of borehole logs and seismic reflectivity data underscores the influence of geological features on fracture propagation. Natural fractures and pore pressure changes emerge as significant contributors to variation in fracture patterns, emphasizing their strategic importance. Using the Formation Micro-Imager (FMI) logs, we identified natural fractures and bedding planes around the wellbore. The "Reactivation" pattern observed was because of the existence of open fractures. We also analyzed that the well has landed in different horizons. On the other hand, reflectivity analysis using seismic attributes (dip, azimuth, minimum and maximum curvature) and pore pressure maps helped us understand that fractures tend to move in the up-dip direction. Moreover, there are zones identified as high-pressure zones forcing fractures to move predominantly in the northeast direction.

When a single planar fracture is created, it increases the stresses around it due to the fracture opening. Such changes in stress are called "stress shadow." The stress shadow affects fracture propagation, as it may cause changes in horizontal stresses, leading to differential fracture propagation. For instance, when horizontal stresses are flipped, fractures tend to move toward the next stage. Therefore, we applied the Stress Escalation Model (SEM) using Instantaneous Shut-In Pressure (ISIP) data by Roussel (2017). We found that stress reorientation is not the case; however, stress shadow might be the cause of the change in cloud patterns, as uni-directional propagation increases stress shadow on one side of the well, affecting subsequent stages to move in the opposite direction.

This comprehensive analysis emphasizes the interplay of treatment parameters, geology, and stress effects on hydraulic fracture propagation. These findings contribute to optimizing hydraulic fracturing strategies and enhancing reservoir management practices for more sustainable energy extraction from unconventional reservoirs.

Preface

This dissertation is submitted for the degree of Master of Science in Geophysics at the University of Alberta. The research described herein is original, and neither this nor any substantially similar dissertation was or is being submitted for any other degree or other qualification at any other university.

To my dad, whose strength made me feel invincible and whose unwavering support fueled my ambition to pursue a master's degree.

To my mom, whose unconditional love has been my rock, nurturing me with boundless care and encouragement.

Acknowledgements

I would like to extend my heartfelt gratitude to Professor Mirko van der Baan, my supervisor, whose unwavering guidance and support have been invaluable throughout my master's journey. Professor van der Baan provided me with the freedom to explore and was always available to clarify any challenges I encountered. Working under his mentorship has been an enriching experience, both academically and personally, and I consider myself fortunate to have had such an exceptional supervisor.

I am also deeply thankful to the Sponsors of Consortium for Distributed and Passive Sensing (C-DAPS) for their generous financial support, as well as to an anonymous company for granting permission to utilize their data. Their contributions have played a significant role in facilitating my academic pursuits.

Furthermore, I wish to express my appreciation to my peers and friends at the University of Alberta and the University of Calgary for their camaraderie and collaborative spirit.

Finally, I want to acknowledge the unwavering support of my family and loved one. Their unconditional love and encouragement have been the cornerstone of my journey, and I am profoundly grateful for their presence in my life. Thank you for always believing in me and standing by my side.

Table of Contents

1 Introduction **1**

1.1 Multistage Hydraulic Fracturing 1

1.2 Hydraulic Fracture Propagation and Properties 2

1.3 Research Motivation 4

1.4 Research Objectives 5

1.5 Thesis Outline 6

2 Overview of hydraulic fracturing in the Montney formation **10**

2.1 Introduction 10

2.2 Stratigraphy of Canadian Western Basin 11

2.3 Geological characterization of the Montney Formation 13

2.3.1 Regional stresses in study area 13

2.4 Summary of Prior Study Findings within Study Wells 17

2.4.1 Distributed Acoustic Sensing (DAS) 17

2.4.2 Microseismic Analysis (MS) 19

2.4.3 Microseismic cloud growth patterns and MS-DAS integration results 22

2.4.4 The Perkins-Kern-Nordgren (PKN) model 23

2.5 Available Data 25

3 Treatment Parameters **28**

3.1 Summary 28

3.2 Introduction 29

3.3 Methods and Procedure 29

3.4 Perkins-Kern-Nordgren (PKN) 29

3.5 Results and Discussion 33

3.5.1 PKN Model 33

3.6 Conclusions 34

4 Microseismicity Analysis **38**
4.1 Summary 38
4.2 Introduction/Theory 39
4.2.1 Moment magnitude 41
4.2.2 Radial distance versus time plots 41
4.2.3 Hydraulic fracture regimes 44
4.3 Methodology 47
4.3.1 Location bias with Distance vs magnitude plot 47
4.3.2 R-T plot Analysis 48
4.3.3 Defining the regimes 49
4.3.4 Microseismic cloud analysis 49
4.3.5 Comparison of Microseismic (MS) and Perkins-Kern-Nordgren (PKN) Fracture Half Lengths 50
4.3.6 Workflow 50
4.4 Results and Discussion 52
4.4.1 Location bias with Distance vs Magnitude plot 52
4.4.2 Reclassification of microseismic events 53
4.4.3 Microseismic cloud analysis 55
4.4.4 R-T plot 63
4.4.5 Regimes 65
4.5 MS Behaviour for each stage 70
4.6 MS vs PKN 73
4.7 Conclusions 76

5 Petrophysical Analysis **78**
5.1 Summary 78
5.2 Background 79
5.2.1 Definitions some geological phenomena 80
5.2.2 Tool working principles 80
5.2.3 Understanding Resistivity and FMI Tool Responses in Horizontal Wells with Bedding Variations 88
5.3 Methods and Procedure 94
5.3.1 Triple Combo logs 94
5.3.2 Image log interpretation 96
5.3.3 Integration of logs wireline logs. 97
5.4 Results and Discussion 97
5.4.1 Triple Combo 97

5.4.2 Formation Micro Imager (FMI) 99
5.4.3 Integration of different borehole data (Triple Combo vs FMI) . 110
5.4.4 Integration of Natural fractures with MS data 111
5.5 Conclusions 113

6 Seismic Reflectivity 115
6.1 Summary 115
6.2 Introduction 116
6.3 Data 117
6.4 Methodology 119
6.4.1 Data Preparation 120
6.4.2 Interpretation 124
6.5 Results and Discussion 130
6.5.1 Data Preparation: Integrating Well Data with Seismic Data and Horizon Picking 131
6.5.2 Seismic Interpretation: Generation of Seismic Attributes and Pore Pressure Map with Interpretation 139
6.5.3 Seismic Interpretation: Microseismic Events and Seismic Attributes 144
6.6 Conclusions 147

7 Stress Analysis 148
7.1 Summary 148
7.2 Introduction 149
7.3 Theory 150
7.3.1 Horizontal Stress Anisotropy 152
7.3.2 Instantaneous Shut-in Pressure (ISIP) 153
7.3.3 Stress Escalation Model (SEM) 155
7.4 Methodology 159
7.4.1 Data 159
7.4.2 ISIP value acquisition 161
7.4.3 SEM method methodology 161
7.4.4 Curve matching technique 164
7.5 Results and Discussion 164
7.5.1 Determining ISIP 164
7.5.2 ISIP Analysis 167
7.5.3 Validation of the results with MS derived fracture heights . . . 171

7.6 Conclusion 172

8 Integration Chapter **174**

8.1 Summary 174

8.2 Introduction 175

8.2.1 Observations 176

8.3 Variability of microseismic clouds across stages 186

8.4 Uni-directional propagation 188

8.5 Stress shadow affect 189

8.6 Defined Scenario for the Well 3 190

8.7 Conclusion 190

9 Conclusions and suggested directions for future research **192**

9.1 Conclusions 192

9.2 Suggested directions for future research 195

Bibliography **197**

List of Tables

2.1 Comparative Analysis of In-Situ Stress Calculations: Insights from Han and van der Baan (2024), Shen et al. (2018) and Enlighten Geoscience (2021) . . . 16

2.2 The available data is for four wells in the study area. The focus of the study is mainly on Well 3. . . . 26

3.1 Geomechanical and completion parameters for the PKN fracture propagation model. . . . 32

4.1 Approximations for the time-dependent behavior of hydraulic fracture length (L), and radius (R) across various fracture models for different fluid efficiency η and behavior index n (modified from Economides and Nolte (2000)). . . . 46

6.1 Comparative Analysis of In-Situ Stress Calculations: Insights from Han and van der Baan (2024), Shen et al. (2018) and Enlighten Geoscience (2021) . . . 131

6.2 1D velocities for 3 layers in 3 wells. . . . 138

7.1 Phenomenon responsible for stress plateau (Modified from Roussel (2017). . . . 154

7.2 In-Situ Stress Calculations: Insights from Han and van der Baan (2024). 160

7.3 Input Parameters Table for SEM Methodology . . . 160

7.4 Refined Step-by-Step Workflow for SEM Analysis adapted from Roussel (2017) . . . 163

7.5 Correlation equations for Stress Escalation type-curves. The variable y represents escalation, while x denotes the spacing-to-height ratio, $s_f/2h_f$. 164

7.6 Correlation equations for Stress interference type-curves. the variable y represents stress interference ratio, while x denotes the spacing-to-height ratio, $s_f/2h_f$. . . . 165

7.7 Table depicting stress plateau (σ_{plateau}) and escalation results based on the fit in Figure 7.13. 169
7.8 Table Displaying Results Following Workflow for Stress Load, Fracture Height, and P_{net} Pressure Calculations. 171
7.9 Comparison Table of Fracture Heights Derived from MS and ISIP Data. 172

8.1 Table Displaying Results Following Workflow for Stress Load, Stress Plateau , and P_{net} Pressure Calculations. 183

List of Figures

1.1 The impact of stress anisotropy on hydraulic fracture propagation. In low stress anisotropy, fracturing generates narrow or straight fractures, while in high stress anisotropy, fracturing creates intricate fracture shapes (reproduced from Fan et al. (2010) with permission from the Society of Petroleum Engineers (SPE)). 3

1.2 Effect of wellbore direction on hydraulic fracture propagation: when drilled in the minimum horizontal stress direction, the fracture propagates transverse, while when drilled perpendicular to the minimum horizontal stress direction, it propagates longitudinally (axially) (reproduced from Salah et al. (2016) with permission from Society of Petroleum Engineers (SPE)). 4

2.1 Schematic cross-section from central Alberta to British Columbia, depicting Montney stratigraphy in a west-east orientation. The diagram highlights intra and extraformational unconformities delineating the Lower, Middle, and Upper Montney members (designated as numbers 1–5). The basal Montney contact (1) is typically unconformable across most of the basin, though it may exhibit conformable characteristics in certain western subsurface and outcrop regions. The earliest intraformational unconformity (2) approximates the Dienerian-Smithian boundary (Induan-Olenekian boundary). A subsequent mid-Montney unconformity occurs around the Smithian-Spathian boundary (mid-Olenekian) (3). The upper Montney contact is unconformable with overlying Middle Triassic strata, either the Sunset Prairie Formation or the Doig phosphate zone (unconformities 4 and 5) (reprinted from Zonneveld and Moslow (2018b) with permission from Canadian Society of Petroleum Geologists (CSPG)). 12

2.2 Structural Variation of the Montney Formation Across British Columbia and Alberta. The structure map depicts a gradual deepening of the Montney Formation towards the southwest (reprinted with permission from Chalmers et al. (2022)). 14
2.3 Map illustrating the re-evaluated in-situ stress area. The grey shading represents the KSMMA region. The small blue rectangle denotes the precise well locations utilized for in-situ stress analysis within this designated area by Han and van der Baan (2024) (reprinted from Han and van der Baan (2024) with permission Elsevier). 15
2.4 Strain Front from DAS Data for a Single Stage: The timeline (x-axis) correlates with the measured depth (y-axis), displaying extension in red and compression in blue (reproduced from Ortega Perez (2022) with permission from University of Alberta Library). 17
2.5 Map depicting Fracture Connections across all stages alongside original well geometry. Each stage is represented by specific characteristics: Green indicates the presence of a heart-shaped tip, purple signifies the presence of an antenna, yellow represents multiple fractures, cyan indicates a distinct FBP (Fracture Breakdown Pressure) peak, and pink arrows denote stages that did not propagate perpendicular from the treated well (reproduced from Ortega Perez (2022) with permission from University of Alberta Library). 18
2.6 Planar view of well layout displaying microseismic clouds from all stages. The treated well is represented by the blue line, while the monitoring well is depicted in black. Different colors denote microseismic clouds from distinct stages (reproduced from Ortega Perez (2022) with permission from University of Alberta Library). 20
2.7 Findings from microseismic analysis conducted by (Ortega Perez, 2022). (a) Cloud length, (b) Cloud height (reproduced from Ortega Perez (2022) with permission from University of Alberta Library). 21
2.8 Stage 14: DAS-MS plot. Ongoing microseismic events from the prior stage are evident, indicated by immediate activity at the injection's start (orange circle). Mid-injection fault/fracture reactivation (green circle) is likely due to stress changes rather than fluid-related effects (reproduced from Ortega Perez (2022) with permission from University of Alberta Library). 22

2.9 Horizontal depiction of well placements, illustrating the Perkins-Kern-Nordge (PKN) fracture half-lengths at the conclusion of injection (depicted in steel blue) with the lengths of the microseismic clouds (shown in pink). Green arrows highlight stages characterized by SW propagation of microseismic events (MS). Orange circles denote stages where the fracture half-length at the DAS hit time exceeded expectations, while yellow circles indicate stages where it fell short (reproduced from Ortega Perez (2022) with permission from University of Alberta Library). 24
2.10 The wells are visually differentiated by color, with their numbering following the sequence of hydraulic fracture treatments. Specifically, the Monitoring well is identified as well 4 and is positioned at a distance of 150 meters from the study well, denoted as well 3. 27

3.1 Overview of Microseismic Clouds: Arrows depict propagation trends. Blue denotes northeast movement, red indicates SW. Predominantly, propagation is northeastward. Up to stage 17, most events move toward the northeast direction, but after stage 17, the event direction changes, exhibiting a cyclic pattern where stages with predominantly northeast movement are followed by stages moving in the opposite direction. 30
3.2 Treatment Parameters used as input parameters for PKN half-length calculation. (a) Injection rate, (b) Plane strain Module, (c) Injection Duration, (d) Fracture height calculated from MS clouds. Injection rate and plane strain modulus remained constant, while significant variations were observed across stages for fracture height and treatment duration. 36
3.3 Predicted PKN fracture half-length based on input parameters. Longer half-lengths are predicted for initial stages, while shorter fracture lengths are forecasted for later stages. The results suggest that PKN is most affected by the duration of each stage. 37

4.1 Example of an r-t plot. Distances of the MS events from the center of the injection interval versus their occurrence times. The microseismic events with different distinct patterns: (upper) a linear diffusion type approximation of the triggering ($t^{1/2}$); (bottom) a cubic root parabola ($t^{1/3}$), providing better fit to data (reprinted from Shapiro and Dinske (2009) with permission from American Geophysical Union). 43

4.2 Visual representation depicting various fluid-driven fracture propagation regimes, including viscosity-dominant, toughness-dominant, leak-off-dominant, and storage-dominant scenarios (reprinted from Shovkun and Espinoza (2019) with permission from Elsevier). 45
4.3 The magnitude-distance graph illustrates complete event mapping, encompassing both low and high magnitude occurrences (left), alongside normalized events (right) achieved by filtering out events below the threshold value (reproduced from Cipolla et al. (2011) with permission from Society of Petroleum Engineers (SPE)). 48
4.4 Magnitude-distance graph showing treatment stages for Well 3. Each color represents a different fracture treatment stage. The magnitude threshold is set at -3.2, based on the far event at stage 38 being recorded around 1200 meters away. 52
4.5 Planar views of microseismic cloud distributions: (a) Original data, (b) After applying magnitude cut-off resulting in decreased cloud thickness but no change in the cloud pattern, (c) After applying magnitude cut-off and event reclassification. 54
4.6 Event origin times and depth measurements for the first 9 stages with -3.2 magnitude filter:(a) Original events by pumping time (pre-classification); (b) Reclassified events. Green rectangle represents the events due to bad event locations. Reclassification successfully removed the tailing events and reassigned them to the corresponding stages. 56
4.7 R-t plot for the Stage 7. Magnitude cut-off -3.2 is applied. Left figure shows original events based on pumping time. The green rectangle shows early events with high radial distance values, while the right figure shows reclassified events. Red bracket represents newly assigned events. The events that were in the green bracket (left) are now eliminated and assigned to the previous stage after the reclassification. . . 57
4.8 Overview of Microseismic Clouds: Arrows depict propagation trends. Blue denotes northeast movement, red indicates SW. Predominantly, propagation is northeastward. Up to stage 17, most events move toward the northeast direction, but after stage 17, the event direction changes, exhibiting a cyclic pattern where stages with predominantly northeast movement are followed by stages moving in the opposite direction. 58

4.9 Planar view of the microseismic clouds for: (a) Stages 1-5; (b) Stages 6-10; (c) Stages 11-15; (d) Stages 15-20. The arrows represent the direction of propagation, green is NE while gray is SW. Stage 5 and 10 show arching (propagation of events) toward the subsequent stage. . . 59
4.10 Planar view of the microseismic clouds for: (a) Stages 21-25; (b) Stages 26-30; (c) Stages 31-35; (d) Stages 35-38. The arrows represent the direction of propagation, green is NE while gray is SW. Stage 30 and 35 show arching (propagation of events) toward the subsequent stage. 60
4.11 True Vertical Depth (TVD) vs. Measured Depth (MD) plot for (a) Stage 6; (b) Stage 13. Black dots represent the port depth of stages for 38 stages. The black line depicts the well trajectory, with Stage 1 starting from the toe of the well and Stage 38 located at the heel of the well. The events from both stage is moving toward the previous stage. 61
4.12 Graph that shows the measured height (after magnitude threshold and reclassification) for all microseismic clouds which represents the fracture height for every stage. The cloud height over the stages exhibits a cyclic pattern of increase and decrease. The average height is 162.8 meters. 62
4.13 Graph that shows the measured length for all microseismic clouds which represents the fracture length for every stage. The NE wing of the fracture represented by blue, while SW wing is represented by green. In the first 17 stages, NE fractures are long, while later stages show relatively shorter lengths. Conversely, SW fractures start short and become longer after stage 18. Overall, early stages predominantly show NE propagation, while later stages exhibit longer SW fractures compared to NE. 62
4.14 Stage 11: The black line depicts the wellbore, with the left side representing the SW and the right side representing the NE. On the NE side, a "normal" pattern is observed with a "reactivation" pattern (red ellipse), while the SW side exhibits two distinct patterns: "Normal" pattern and "Halted-growth". 64
4.15 Stage 6: The black line depicts the wellbore, with the left side representing the SW and the right side representing the NE. On the NE side, a linearly developed "Reactivation" pattern is observed, while the SW side exhibits "Halted-growth" patterns as there is no increase in the fracture radial length. 65

4.16 Illustration of r-t plots and plan view of stages: (a) 13, (b) 24. The black line represents the wellbore, with the left side indicating the SW and the right side indicating the NE. Stage 13 shows two different patterns for each NE and SW wing, while Stage 24 represents reactivation on one side and "Halted-Growth" on the other. 66
4.17 The black line represents the wellbore, with the left side indicating the SW and the right side indicating the northeast. The Y-axis depicts the radial distance from the injection point, while the X-axis denotes the time of event occurrence. (a) Radial-time plots with the 90th percentile applied, (b) Radial-time plots with equation fits. The color codes indicate the estimated Time Dependency Exponent (β_t) at different period of Hydraulic Fracure (HF) stage. 68
4.18 Evolution of the Time Dependency Exponent (β_t). The blue line depicts the time exponent for the northeast side, while the green line represents the time exponent for the southwest side of the well. Each color corresponds to different regimes: red for leak-off regimes (PKN with $\eta \to 0$ and Radial), and green for storage-dominated regime (PKN and KGD with $\eta \to 1$). The northeast side predominantly exhibits a storage-dominated regime, whereas the southwest side corresponds to both storage and leak-off dominated regimes. 69
4.19 Stage 11. (a) 90th percetile representing cloud shape, (b) Evolution of the Time Dependency Exponent (β_t). 71
4.20 Stage 6. (a) 90th percetile representing cloud shape, (b) Evolution of the Time Dependency Exponent (β_t). 72
4.21 Overview of microseismic (MS) observations across stages, depicting propagation patterns in radial-time (r-t) plots: "Normal" (red circle), "Reactivation" (purple circular ring), and "Halted-growth" (yellow rhombus). Black arrows indicate HF treatment propagation trend. The bracket highlights stages where we suspect the reactivation of the same pre-existing fractures. The order of the symbols away from the well indicates relative time in each stage. The NE side is mostly characterized by "Reactivation" and "Normal" patterns, while the SW side is mostly characterized by the "Normal" and 'Halted-growth" patterns. 74

4.22 Overview of hydraulic fracture (HF) treatment regimes: "Reactivation" (β_t shown as purple circular rings), PKN ($\eta \rightarrow 1$) represented by yellow squares or red circles, and Radial flow denoted by green squares or blue triangles. Black arrows indicate HF treatment propagation trend. The blue brackets indicate the stages during which the "Reactivation" of pre-existing fractures occurred for the same fracture. The NE side is mostly characterized by the PKN and KGD regimes, while the SW side is mostly characterized by the KGD and Radial regimes. 75
4.23 PKN fracture half-lengths at injection completion (black) and microseismic cloud lengths for NE (blue) and SW (red) shown side by side. Significant discrepancies between PKN and MS results are apparent, especially for the middle stages (17-26). The initial and later stages show correlation with NE half fracture length. 76

5.1 Strike and dip representation of inclined sedimentary planes/beds. The dip angle, denoting the angle between the horizontal plane and the inclined surface, is illustrated. The strike and dip azimuth are indicated by a two-sided arrow and a single-sided arrow, respectively (generated in accordance to Dang (2008)). 81
5.2 Illustration of simplified Density/Neutron porosity tools. (a) the Neutron Tool with a bow string; (b) the Density Tool with open pads. Both tools demonstrate the scenario where the tool was pushed toward the formation wall (modified from Ellis et al. (2003) and Smithson (2015)). 83
5.3 Simplified induction tool, illustrating asymmetric receiver pairs and a single transmitter coil based on Halliburton tools (generated in accordance to Halliburton (2005)). 83
5.4 Weatherford Compact Oil-Based Mud Sonde Section (Weatherford, 2015). 85

5.5 Illustration of sinusoidal features on borehole images, depicting surfaces that cross-cut the borehole wall. In the borehole view, the green line crosses the borehole at an angle, while the red line represents the case with a 0-degree angle. When the borehole figure is opened in a 2D plane, the green line represents the sinusoidal line (case with an angle), while the red line is a straight line (0-degree angle case). The dip angle is calculated as $\tan^{-1}(h/d)$, where h is the height and d is the diameter of the wellbore. The azimuth in the figure is represented as a tapole, where the tail direction indicates the dip azimuth with reference to North (using the lowest point in the sinusoidal pattern) (modified from Rider and Martin (2014)). 86
5.6 Illustration depicting phase (RP) and attenuation (RA) resistivity responses in a three-layer formation model (RT). Modeled logs showcase the tool response dependency on dip angles (0°, 70°, and 85°) across three tracks, as per the three-layer formation model (reproduced from Zhou (2008) with permission from Society of Petroleum Engineers (SPE)). 89
5.7 Comparison of intersections between a vertical and horizontal wellbore and a shallow-dipping plane. The top right diagram depicts the intersections, while the bottom left shows corresponding FMI images. The horizontal wellbore intersection generates a long, drawn-out, high-amplitude sinusoid, whereas the vertical wellbore intersection forms a tight, low-amplitude sinusoid. DD indicates the drilling direction (reproduced from Lofts et al. (1997) with permission from The Geological Society of London (Lyell Collections)). 91
5.8 "Saddle" and "bull's eye" patterns created by bedding planes in horizontal wells, highlighting the distinct features of these geological formations. The both patters happen due to changes in the azimuth of the sinusoid as the well intersects the bedding plane (reproduced from Ghosh (2022) with permission from Springer Nature). 92
5.9 Detection of fractures in horizontal wells using image logs: (a) a fracture intersecting a horizontal well at a high angle, nearly perpendicular, resulting in a straight line pattern , (b) the fracture intersects the wellbore at a lower angle, creating a sinusoidal shape (reproduced from Gong et al. (2021) with permission from Society of Petroleum Engineers (SPE)). 93

5.10 Borehole breakouts, depicted in Formation Micro Imager (FMI) logs, are clear, well-defined conductive features positioned at 180-degree intervals along the borehole's sides, filled with conductive mud (reproduced from Lofts et al. (1997) with permission from The Geological Society of London (Lyell Collections)). 95
5.11 Basic well logs: First track: Gamma ray (green), second track: Resistivity at depth investigations of 20, 40, 60, and True resistivity. The grey zone indicates a notable increase in gamma ray, possibly attributed to the presence of K-feldspar in the Montney formation or clay content. Conversely, yellow denotes areas with low gamma ray values. Dashed lines correspond to the bullhorns presented in resistivity. The change in resistivity with bullhorn patterns indicates possible bedding changes, especially in the intervals [3200;2600] and [3950, 4050]. The neutron and density porosity reflect the gamma ray results. 100
5.12 Quality control assessment of the Formation Micro Imager data for Well 3. FMI Figure illustrating logging artefacts:(a) tool telemetry and low pad pressure, (b) low quality data due to bad pad contacts. . 101
5.13 Formation Micro Imager observations in Well 3 at four different depths. The 1st figure displays resistive fractures in white, oriented at 90 degrees to the wellbore. The 2nd depicts partially visible discontinuous resistive fractures at a 90-degree angle. The 3rd illustrates disturbed conductive fractures, influenced by tool characteristics. The 4th represents intermittent conductive fractures visible only in the first three columns. 103
5.14 Rose diagrams depicting the orientation of Conductive fractures (Pink), Discontinuous Conductive fractures (Red), Resistive fractures (Dark Blue/purple), Discontinuous Resistive fractures (Cyan): (a) Strike (deg). The majority display a striking orientation between 20-40 degrees, (b) Dip (deg) of the same fractures, with most showing a 90-degree dip angle, indicating a perpendicular orientation to the wellbore. 104
5.15 Wellbore trajectory overlaid with natural fractures: Conductive fractures (green), Discontinuous Conductive fractures (Red), Resistive fractures (orange), Discontinuous Resistive fractures (blue). The majority of conductive fractures are located in the middle and toe sections of the well, whereas resistive fractures seem to predominate in the heel of the well. 105

5.16 Formation Micro-Imager log depicting Well 3: (a) Vertical well section with lithological variation, (b) and (c) same horizontal section of the well depicting the change in the bedding azimuth at different scale. . 106
5.17 Wellbore trajectory overlaid with bullhorn patterns (red). The bullhorn pattern coincides with directional changes of the wellbore. . . . 107
5.18 Rose diagrams illustrating bedding characteristics in a horizontal well section. (a) The true azimuth of the bedding being 210-230 deg., (b) Depicts true dip of bedding being below 10. 109
5.19 Visualization of the well trajectory presented in two tracks. The first track illustrates the trajectory with lines indicating Middle Montney members, dots representing provided well tops, and lines depicting calculated well top horizons for the horizontal well. Various depths where the Middle Montney members intersect the well are shown. In the second track, the well trajectory is displayed along with the projection of the intersected horizon. Middle Montney members are highlighted, with red indicating D3 and blue representing D2. Red dots along the wellbore indicate manually identified bullhorn patterns, while black dots denote hydraulic stages. 110
5.20 Integration of wellbore data and Formation Micro-Imager log. The first track illustrate triple combo results, while the bottom track depicts the well trajectory and bedding planes based on the intersection of D2 and D3, as shown in Figure 5.19. The well has moved out of the Horizon D3 (red bracket). 111
5.21 Planar view of the well: Black dots indicate treatment stages, with arrows showing propagation direction. Stages displaying a "Reactivation" pattern are marked with purple rings. Natural fractures are depicted as follows: Dis. Conductive (red), Dis. Resistive (blue), Resistive (yellow), Conductive (green). Most conductive fractures appear toward the toe of the well. Reactivation patterns overlap with conductive fractures. Some reactivation patterns do not overlap with any fractures because they occur due to the activation of existing fractures (indicated with brackets). 112

6.1 Overview of Microseismic Clouds: Arrows depict propagation trends. Blue denotes northeast movement, red indicates SW. Predominantly, propagation is northeastward. Up to stage 17, most events move toward the northeast direction, but after stage 17, the event direction changes, exhibiting a cyclic pattern where stages with predominantly northeast movement are followed by stages moving in the opposite direction. 117
6.2 Schematic cross-section from central Alberta to British Columbia, depicting Montney stratigraphy in a west-east orientation. The diagram highlights intra and extraformational unconformities delineating the Lower, Middle, and Upper Montney members (designated as numbers 1–5). The basal Montney contact (1) is typically unconformable across most of the basin, though it may exhibit conformable characteristics in certain western subsurface and outcrop regions. The earliest intraformational unconformity (2) approximates the Dienerian-Smithian boundary (= Induan-Olenekian boundary). A subsequent mid-Montney unconformity occurs around the Smithian-Spathian boundary (mid-Olenekian) (3). The upper Montney contact is unconformable with overlying Middle Triassic strata, either the Sunset Prairie Formation or the Doig phosphate zone (unconformities 4 and 5) (reprinted from Zonneveld and Moslow (2018b) with permission from Canadian Society of Petroleum Geologists (CSPG)). 118
6.3 Structural Variation of the Montney Formation Across British Columbia and Alberta. The structure map depicts a gradual deepening of the Montney Formation towards the southwest (reprinted with permission from Chalmers et al. (2022)). 119
6.4 Seismic interpretation workflow: Data preparation involves linking well information with seismic-to-well tie, time to depth conversion, QC, and horizon picking. Interpretation focuses on understanding seismic attributes such as Dip, Azimuth, Maximum and Minimum Curvature, and Pore Pressure Mapping. 120
6.5 Illustration depicting the methodology of well-tying, wherein velocity and density logs are utilized to generate reflections, enabling the production of synthetic seismic data (reprinted from Tylor-Jones and Azevedo (2023) with permission from Springer Nature BV). 121

6.6 Visualization of interval velocities computed from ground level (for onshore seismic) to the primary horizon Hrz A, followed by calculations for layer A between Hrz A and Hrz B, and layer B between Hrz B and Hrz C. Sonic data reveals vertical velocity variations within each layer (drawn in accordance to GMDK (2015)). 123
6.7 Diagram illustrating the terminology used for dip magnitude and azimuth. The vectors **n** and **a** represent unit vectors perpendicular to the plane and indicating the dip along the reflector, respectively. $\boldsymbol{\theta}\mathbf{x}$ and $\boldsymbol{\theta}\mathbf{y}$ denote the apparent dips along the inline and crossline, respectively. $\boldsymbol{\theta}$ denotes the dip magnitude, while $\boldsymbol{\theta}$ represents the dip azimuth (reproduced from Rijks and Jauffred (1991) with permission from Society of Exploration Geophysicists (SEG)). 126
6.8 Dip magnitude and Dip azimuth map depicted on a time map. Black arrows denote lineations where subtle changes in dip occur (reproduced from Rijks and Jauffred (1991) with permission from Society of Exploration Geophysicists (SEG)). 127
6.9 2D curvature profile along a line. Anticlinal features exhibit positive curvature, synclinal features show negative curvature, and planar features, whether horizontal or dipping, demonstrate zero curvature (reproduced from Chopra and Marfurt (2007) with permission from Society of Exploration Geophysicists (SEG)). 128
6.10 The synthetic seismogram data for three wells is provided. For each well, the first column represents density values, the second column represents sonic values, and the third column presents the synthetic results. The red line indicates the wavelet extracted from the inline and crossline data near the well, generated by the Seisware software. . 132
6.11 Synthetic seismograms for three wells (two horizontal and one vertical) plotted alongside the respective well logs. The good match between the wells and seismic has been made. 133
6.12 Seismic reflection overlaid with well tops to illustrate the alignment consistency among three wells. Middle Montney (MNTN) members were only provided for the vertical well. 134
6.13 Time map after horizon picking: (a) MNTN D4 ; (b) MNTN D3. The black brackets represents the zones with acquisition artefacts. 135
6.14 Time map after horizon picking: (a) MNTN D1; (b) Belloy. Black brackets represent zones with acquisition artifacts. Belloy, which exhibits minimal artifacts, portrays the geology of the Montney accurately. 136

6.15 Quality Control (QC) assessment of the horizon picking. The base map indicates the location of the inline and crossline data for Montney D4 and Montney D3, highlighting areas with artifacts. The red line denotes the corresponding inline and crossline locations on seismic section. Regions along the red line exhibit low-quality data, posing challenges for picking. Notably, discerning troughs is difficult due to their proximity to converging peaks. 137
6.16 Isochron map displaying inline locations. The map illustrates a consistent thickness between the Belloy and Montney D4 horizons. This phenomenon is depicted on a seismic section where, from north to south, the thickness between these horizons remains approximately constant; in the north, it measures 113 ms, while in the south, it is 110 ms. . . 138
6.17 Annotated maps of the Belloy horizon: (a) Time map; (b) Depth map. The black line denotes the well. The depth decreasing from Northeast to Southwest. The black bracket indicates the presence of a structural low. The red bracket represents the potential channel location. 139
6.18 Horizon-based attribute maps of the Belloy horizon. (a) Dip attribute; (b) Dip azimuth attribute map. The well trajectory is depicted by the black line. The study area has been divided into zones to simplify the interpretations. 141
6.19 The pore pressure map generated from the depth map of the Belloy horizon by multiplying the depth with the pore pressure gradient of 12.2 kPa from Han and van der Baan (2024). The pore pressure increases towards the southwest direction due to the dipping. Variations in pore pressure are observed around the well. 143
6.20 Horizon-based curvature maps for the Belloy formation: (a) Minimum curvature map and (b) Maximum curvature map. The study area has been divided into three zones: Zone 1, medium curvature; Zone 2, high curvature; and Zone 3, low curvature zones. The well is situated in a high curvature zone, exhibiting two striking curvature directions: parallel and perpendicular to the wellbore. The circles represents the artefacts. 145

6.21 The dip azimuth attribute map of the Belloy horizon (Figure 6.18b) zooms in on the well area. The black line marks the well trajectory, and dots show the depth of hydraulic fracture treatment ports. Black arrows indicate stages where microseismic events mainly moved southwestward. The circle highlights an artifact. Initial observations suggest microseismic events trend toward the northeast, up-dip direction. . . 146
6.22 The left figure shows pore pressure map focuses on the Belloy horizon (Figure 6.19), centered on the well. The black line depicts the well trajectory, while dots denote the depth of hydraulic fracture treatment ports. Black arrows highlight stages where microseismic events predominantly moved southwestward. The circle denotes data quality issues. Initial observations suggest microseismic events tend to move NE when pressure is high in the SW. Right figure shows planar view of microseismic clouds. The circled zone represents the elaveted pressure zone that forces events to move toward NE direction. 146

7.1 The wells are visually differentiated by color, with their numbering following the sequence of hydraulic fracture treatments. The landing height difference between Well 1 and Well 3 is 100 m. 150
7.2 Planar view of the microseismic clouds for: (a) Stages 1-5; (b) Stages 6-10; (c) Stages 11-15; (d) Stages 15-20. The arrows represent the direction of propagation, green is Northeast while gray is southwest . 151
7.3 Planar view of the microseismic clouds for: (a) Stages 21-25; (b) Stages 26-30; (c) Stages 31-35; (d) Stages 35-38. The arrows represent the direction of propagation, green is Northeast while gray is southwest . 152
7.4 Illustration of the physics of the SEM method: The left figure represents the plateau stage where stress load (σ_{load}) is smaller than the net pressure (P_{net}), leading to transversal fracture propagation. The right figure illustrates stress reorientation, where stress load (σ_{load}) exceeds the net pressure (P_{net}), resulting in longitudinally propagating fractures. 154
7.5 Comparison of analytical solutions for the stresses normal (y=z=0) to a semi-infinite and penny-shaped fracture. h_f represents the fracture halft length, x represents the fracture length, Φ represents the stress correction factor, $\Delta\sigma_{xx}$ represents the minimum horizontal stress, P_{net} represents the net pressure (reproduced from Roussel (2017) with permission from Society of Petroleum Engineers (SPE)). 156

7.6 Load-normalized magnitude of stress interference versus the number of fracture stages for different $s_f/2h_f$ ratios for a single perforation cluster (reproduced from Roussel (2017) with permission from Society of Petroleum Engineers (SPE)). 157
7.7 Type-curves of (a) the load-normalized stress plateau and (b) the escalation number for different numbers of perforation clusters (reproduced from Roussel (2017) with permission from Society of Petroleum Engineers (SPE)). 158
7.8 (a) Graphical representation of the Interference Ratio; (b) Type-curve of Interference ration or different numbers of perforation clusters (reproduced from Roussel (2017) with permission from Society of Petroleum Engineers (SPE)). 159
7.9 Analyzing wellhead pressure fluctuations during shut-in with ISIP determination through quadratic fit (red line), a method pioneered by Roussel et al. (2021) for enhanced evaluation (reproduced from Roussel et al. (2021) with permission from Society of Petroleum Engineers (SPE)). 162
7.10 Visualization of Bottomhole Pressure Zoomed at Shut-In Time: capturing bottomhole pressure fluctuations. An imaginary line is used to trace pressure drop points, and the corresponding crosspoint with bottomhole pressure at shut-in is considered as the ISIP value. Consistent methodology is applied across all stages in four wells. 166
7.11 Illustration of ISIP data for all stages in four wells. Beyond stage 20, wells 1, 2, and 3 exhibit a decrease in ISIP below the initial value, as depicted by the red and blue zones in the figure. Notably, well 3 (green line) displays an initial ISIP value higher than any other, attributed to hydraulic fracturing in well 1, which penetrates a different formation in the same area. Additionally, Well 3 demonstrates a notable decrease in ISIP values across the last three stages, indicating a significant alteration in formation properties. 166
7.12 Illustration of the first 20 stages for four wells. The ISIP at the first stage for each well has been correlated to other wells to ensure more accurate results. The higher ISIP at the first stage is resultant of hydraulic fracturing processes prior to well 3 in wells 1 and 2, leading to an increase in p_{net}. 167

7.13 Illustration of the escalation model (equation 7.6) fitting graph for calculating the stress plateau ($\sigma_{plateau}$) and escalation for four wells using 20 stages. Prior to fitting, ISIP at the first stage was subtracted from all ISIP values across the stages to account for stress interference (stress shadow), as the first stage is not subject to any stress interference. 168
7.14 An illustration showcasing our utilization of type-curves depicting (a) the escalation and (b) the stress interference ratio for well 4. The red dashed line signifies the matched values for Escalation, spacing-to-height ratio, $\frac{s_f}{2h_f}$, and interference ratio. 170

8.1 Overview of Microseismic Clouds: Arrows depict propagation trends. Blue denotes northeast movement, red indicates SW. Predominantly, propagation is northeastward. Up to stage 17, most events move toward the northeast direction, but after stage 17, the event direction changes, exhibiting a cyclic pattern where stages with predominantly northeast movement are followed by stages moving in the opposite direction. 176
8.2 Graph depicting the measured height (after magnitude threshold and reclassification) for all microseismic clouds, representing the fracture height for every stage. The cloud height over the stages exhibits a cyclic pattern of increase and decrease. The fracture height fluctuates across stages. The average height is 162.8 meters. 177
8.3 Graph illustrating the measured length of microseismic clouds, indicating fracture length for each stage. Blue denotes the northeast wing of the fracture, while green represents the southwest wing. The initial 17 stages exhibit longer fracture lengths in the northeast direction. However, in subsequent stages, the fracture lengths become similar between the southwest and northeast wings, both relatively shorter than those of the northeast wing in the first 17 stages. 177
8.4 PKN fracture half-lengths at injection completion (black) and microseismic cloud lengths for Northeast (blue) and Southwest (red) shown side by side.Significant discrepancies between PKN and MS results are apparent, especially for the middle stages (17-26). The initial and later stages show correlation with NE half fracture length 178

8.5 Overview of microseismic (MS) observations across stages, depicting propagation patterns in radial-time (r-t) plots: ”Normal” (red circle), ”Reactivation” (purple circular ring), and ”Halted-growth” (yellow rhombus). Black arrows indicate HF treatment propagation trend. The bracket highlights stages where we suspect the reactivation of the same pre-existing fractures. Most of the reactivation happens toward the toe of the well explaining the longer fracture length up to stage 17. 179
8.6 Overview of hydraulic fracture (HF) treatment regimes: ”Reactivation” (β_t shown as purple circular rings), PKN ($\eta \to 1$) represented by yellow squares or red circles, and Radial flow denoted by green squares or blue triangles. Black arrows indicate HF treatment propagation trend. The blue brackets indicate the stages during which the ”Reactivation” of pre-existing fractures occurred for the same fracture. The NE side is mostly characterized by the PKN and KGD regimes, while the SW side is mostly characterized by the KGD and Radial regimes. 180
8.7 Planar view of the well: Black dots indicate treatment stages, with arrows showing propagation direction. Stages displaying a ”Reactivation” pattern are marked with purple rings. Natural fractures are depicted as follows: Dis. Conductive (red), Dis. Resistive (blue), Resistive (yellow), Conductive (green). Most conductive fractures appear toward the toe of the well. Reactivation patterns overlap with conductive fractures. Some reactivation patterns do not overlap with any fractures because they occur due to the activation of prefiously reactivated fractures (indicated with brackets). 181
8.8 Integration of wellbore data and Formation Micro-Imager log. The red bracketed zones represent where the well has moved out of the horizon, as indicated by the FMI analysis and the observed resistivity changes in these zones. 183
8.9 Illustration of ISIP data for all stages in four wells. Beyond stage 20, wells 1, 2, and 3 exhibit a decrease in ISIP below the initial value, as depicted by the red and blue zones in the figure. These discrepancies may be associated with the elevated pore pressure zone toward the toe of the well or changes in landing height or lithology. 184

8.10 Planar views of microseismic cloud distributions: (a) Original data, (b) After applying magnitude cut-off. The main change after the magnitude threshold filter is the thickness of each stage's clouds. There is no effect on the unidirectional propagation of the clouds; it remains the same. 185
8.11 The horizon-based dip azimuth attribute map of the Belloy horizon, focusing on the area around the well. The black line depicts the well trajectory, while dots denote the depth of hydraulic fracture treatment ports. Black arrows highlight stages where microseismic events predominantly moved southwestward. The circle denotes data quality issues. Initial observations suggest microseismic events tend to move up-dip direction. 186
8.12 The left figure shows pore pressure map focuses on the Belloy horizon (Figure 6.19), centered on the well. The black line depicts the well trajectory, while dots denote the depth of hydraulic fracture treatment ports. Black arrows highlight stages where microseismic events predominantly moved southwestward. The circle denotes data quality issues. Initial observations suggest microseismic events tend to move northeastward when pressure is high in the southwest. Right figure shows planar view of microseismic clouds. the circled zone represents the elevated pressure zone that forces events to move toward NE direction. 187
8.13 Planar view illustrating pore pressure distribution and fracture behavior within the well. Higher pressure zones depicted in light red, contrasting with lower pressure areas in blue. The darker red denotes the high pore pressure zone. Landing height changes represented by varied colors such as blue and orange. Fractures inducing stress concentration depicted by a semicircle, influencing subsequent fracture propagation. The absence of such behavior until stage 17 attributed to high-pressure zones directing fractures northeastward, and the nullification of stress shadow effect beyond the horizon. "Reactivation" patterns marked by cloud shapes. 191

Abbreviations

CH Cased Hole.

DAS Distributed Acoustic Sensing.

DFIT Diagnostic Fracture Injection Test.

FMI Formation Micro-Imager.

GR Gamma Ray.

HF Hydraulic Fracture.

ISIP Instantaneous Shut-In Pressure.

KGD Kristianovich-Geertsma-de Klerk.

LTI Linear Time Invariant.

MD Measured Depth.

MNTN Montney.

MS Microseismic.

OH Open Hole.

PKN Perkins-Kern-Nordgren.

QC Quality Control.

RA Resistivity Attenuation.

RP Resistivity Phase.

S/N Signal-to-noise ratio.

SEM Stress Escalation Model.

TVD True Vertical Depth.

TWT Two-Way Traveltime.

WCSB Western Canada Sedimentary Basin.

Chapter 1

Introduction

1.1 Multistage Hydraulic Fracturing

Tight gas refers to natural gas reservoirs produced from rocks with extremely low permeability. Typically, these reservoirs are defined by having less than 0.1 millidarcy (mD) matrix permeability and less than 10 % porosity, necessitating hydraulic fracturing for extraction (Rajput & Thakur, 2016).

Hydraulic fracturing involves injecting fluid into the wellbore to create fractures in the rock, thereby increasing permeability and enabling the extraction of petroleum (Yu & Sepehrnoori, 2013). This fluid carries proppants into the fracture network, preventing the fractures from closing due to the high-pressure environment of the rock formation. Drilling numerous horizontal wells using single-stage fracturing is not cost-effective. Therefore, the industry has shifted towards employing multistage hydraulic fracturing as the prevailing operational norm.

Two common techniques employed in the Montney Formation to create numerous fractures along horizontal wells are the plug and perforate method and the open hole multistage system (Kimmitt, 2011; Vishkai & Gates, 2019). The fracturing process happens sequentially, one stage at a time, starting from the toe (bottom) side of the well and progressing towards the heel (top) side (Dontsov & Suarez-Rivera, 2020).

In cased hole (CH) hydraulic fracturing, the wellbore casing is perforated prior to fracturing, facilitating the release of fracturing fluid. These perforations, also known as perforation clusters, serve as openings through which the fluid is directed. Multistage hydraulic fracturing integrates specialized packers that expand to segregate areas for fracking. The identical procedure is replicated for each subsequent stage, following which the bridge plugs are drilled out. This methodology is referred to as plug and perforation (McDaniel, 2010; Vishkai & Gates, 2019).

Contrarily, open hole completion exposes the reservoir entirely without any casing in the targeted zone. Isolation between stages is achieved using open-hole (OH) packers, while sleeves featuring ports at specific intervals are employed (McDaniel, 2010). Activating these ports to open the sleeves and establish a flow path for fracturing fluid involves dropping a ball into a liner. Upon the ball's seating onto the sleeve assembly, the sleeve opens and activates—a method known as Sliding Sleeve. Typically, this technique entails one opening (cluster) per stage. However, it exposes a significantly larger area of the formation to fluids, allowing exploitation of pre-existing joints and weaknesses in the formation (Djabelkhir, 2020; McDaniel, 2010).

In the Montney Formation, the most cost-effective treatment approach identified is the use of slickwater treatment (King, 2010). This method involves employing a substantial volume of water with minimal sand content and small quantities of friction-reducing chemicals. Despite the potential challenge of rapid proppant settling due to the low sand concentration, the slickwater stands out as the optimal choice for brittle, heterogeneous rock formations characterized by higher silica content and lower clay content (Vishkai & Gates, 2019; Y. Wang & Miskimins, 2010).

1.2 Hydraulic Fracture Propagation and Properties

The direction and spread of hydraulic fractures result from various factors, primarily dictated by the existing stress conditions. These stresses are characterized by three main compressive forces: σ_v along the vertical direction, and σ_H and σ_h along two perpendicular horizontal directions representing maximum and minimum values respectively (Hossain et al., 2000). Depending on how these stresses compare (σ_v, σ_H and σ_h), three stress regimes are defined: normal faulting ($\sigma_v > \sigma_H > \sigma_h$), strike-slip faulting ($\sigma_H > \sigma_v > \sigma_h$), and reverse faulting ($\sigma_H > \sigma_h > \sigma_v$) (Hossain et al., 2000).

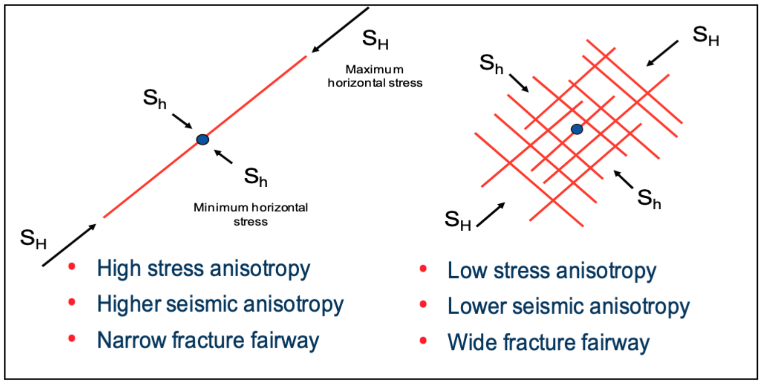

Figure 1.1: The impact of stress anisotropy on hydraulic fracture propagation. In low stress anisotropy, fracturing generates narrow or straight fractures, while in high stress anisotropy, fracturing creates intricate fracture shapes (reproduced from Fan et al. (2010) with permission from the Society of Petroleum Engineers (SPE)).

In instances where there's a significant contrast between the minimum and maximum horizontal stresses, the fracturing process generates a narrow or straight fracture pattern. Conversely, when stress contrast is minimal, the treatment leads to wider or more intricate fracture shapes, depicted in Figure 1.1 (Bahrami et al., 2016; Fan et al., 2010). Several other factors contribute to the creation of more intricate fracture patterns during hydraulic fracturing treatments. Elements like rock fabric, existing fractures within the formation, and layering play significant roles in shaping the complexity of fracture geometry (Fan et al., 2010).

When hydraulic fracturing a horizontal well, the resulting fracture orientation—whether transverse or longitudinal—is primarily influenced by the direction of the minimum principal stress. In the context of a horizontal well, two scenarios emerge: if drilled along the path of the minimum stress, transverse fractures form (perpendicular to the wellbore axis). Conversely, drilling the well perpendicular to the minimum stress leads to the creation of longitudinal (axial) fractures, running along or parallel to the

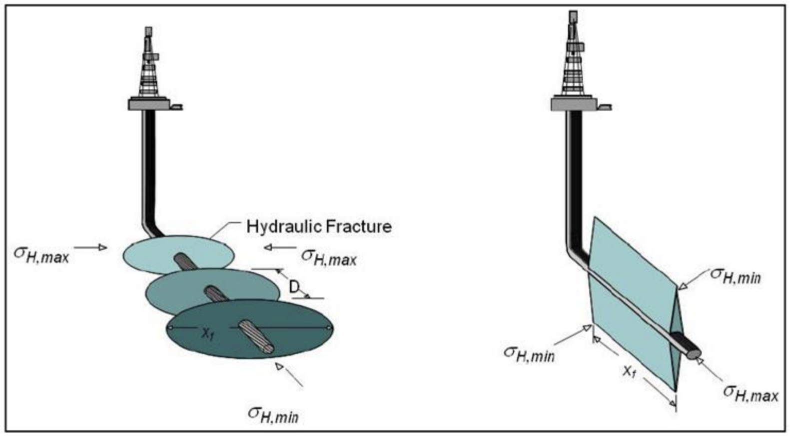

Figure 1.2: Effect of wellbore direction on hydraulic fracture propagation: when drilled in the minimum horizontal stress direction, the fracture propagates transverse, while when drilled perpendicular to the minimum horizontal stress direction, it propagates longitudinally (axially) (reproduced from Salah et al. (2016) with permission from Society of Petroleum Engineers (SPE)).

wellbore (Figure 1.2).

1.3 Research Motivation

Modeling hydraulic fractures in the Montney of northeast British Columbia, Canada encounters significant hurdles. Conventional planar hydraulic fracture models fail to incorporate a substantial portion of the pumped fluid (Bearinger, 2022). This limitation raises concerns about their efficacy in evaluating crucial aspects such as ideal well spacing, positioning within stratigraphic layers, potential induced seismic activity, and deformation of wellbores. Monitoring of fracturing activities reveals that the injected fluid permeates fault lines, folds, fractures, and bedding planes as supported (Bearinger, 2022).

The thesis focuses on investigating the expansion of hydraulic fractures across time and space. This will be achieved through the examination of various data sources including engineering records (pumping details), Formation MicroImager logs, seismic reflection data, and the microseismic activity during a specific hydraulic treatment. These findings will then be compared with a numerical model. Each data type contains distinct insights, and the combined analysis aims to provide a comprehensive understanding of the treatment process, ongoing phenomena in the study area, identification of potential issues in completion, their impact on fracture growth, and ultimately aiding in the development of more efficient unconventional reservoir completions.

1.4 Research Objectives

This thesis aims to enhance our comprehension of hydraulic fracture propagation by conducting a comprehensive analysis focused on the following objectives:

1. Investigating the Influence of Fracture Treatment Parameters: This study seeks to assess the impact of various fracture treatment parameters on hydraulic fracturing dynamics. Utilizing the Perkins-Kern-Nordgren (PKN) model, we aim to estimate fracture half length. However, our approach transcends the previous study by introducing two additional parameters previously considered constant.

2. Unraveling Mechanisms Governing Microseismic Behavior: Our research endeavors to elucidate the mechanisms governing the behavior of microseismic clouds observed during hydraulic fracturing operations. By analyzing microseismic clouds, r-t plots, and magnitude versus distance plots through visual interpretation, supplemented by a model-based approach to categorize fracturing regimes based on the time-dependency of microseismic event radial distances, we aim for a comprehensive understanding of microseismic behavior during hydraulic fracturing.

3. Investigating the link between Microseismic Events and Geological Features: The spatial distribution of microseismic events is intricately linked to the geological features of the region. Therefore, we aim to understand the geological features at both small and large scales by integrating seismic reflection data, basic well logs, and formation micro imager logs with microseismic event clouds. This integrated approach will aid in comprehending the influence of geological features on microseismic behavior.

4. Exploring the Impact of Stress Shadow Effects: This study aims to investigate the impact of stress shadow effects on the propagation of microseismic clouds during multi-stage fracturing operations. As each fracturing stage alters the minimum horizontal stress and stress anisotropy, there are significant implications for the behavior of microseismic events. By employing Instantaneous Shut-in Pressure Analysis (ISIP), we seek to comprehensively understand how stress perturbations influence the propagation patterns of microseismic clouds in subsequent fracturing stages.

1.5 Thesis Outline

The thesis is structured into 9 chapters as follows:

Chapter 1: This chapter serves as the starting point of the thesis, providing the background and scope of the research. It outlines the objectives of the study and previews the subsequent chapters.

Chapter 2: Firstly, we provide an overview of the geology in the study area, encompassing recent geomechanical studies. The chapter delves into the comprehensive body of work conducted in the area, with a particular emphasis on one of the study wells, which serves as the primary focus of this research.

Chapter 3: We use engineering data to explore the impact of treatment parameters on hydraulic fracture treatments. Microseismicity exhibits a notable pattern with variability across treatment stages, including predominant northeast propagation and fluctuating microseismic cloud lengths. Despite these observable phenomena, the underlying cause remains elusive. Our objective is to investigate the influence of treatment parameters using the Perkins-Kern-Nordgren (PKN) model, building upon its previous application by Ortega Perez and van der Baan (2024). We refine the approach by assigning distinct values to the Plane strain modulus (E') and fracture height (h) for each stage, aiming to mitigate geomechanical property influences on the model. Additionally, we incorporate stage duration derived from microseismic data propagation time. The findings suggest that changes in treatment parameters alone may not fully account for observed anomalies in propagation behavior. Further analysis is warranted to unravel the underlying mechanisms.

Chapter 4: Fracture propagation is a critical aspect of hydraulic fracturing operations, yet certain anomalies, like the directional behavior of microseismic clouds, remain poorly understood. We aim to elucidate the mechanisms driving such behavior through comprehensive microseismic propagation analysis. We investigate distance vs. magnitude plots to assess if directional propagation correlates with treatment and monitoring well distances. Cloud analysis and r-t plots further refine our understanding of propagation dynamics, incorporating equations to model radial distance growth over time. Integration of microseismic and Perkins-Kern-Nordgren (PKN) methods clarifies treatment parameter influences. Findings suggest that distance between wells alone doesn't explain directional cloud behavior, with dynamic changes in fracture characteristics observed. Various propagation regimes are identified, emphasizing the complexity of fracture dynamics. Discrepancies between microseismic and PKN results highlight the need for continued analysis. This study contributes to a deeper understanding of hydraulic fracturing mechanics, though further research is warranted for complete comprehension of fracture propagation phenomena.

Chapter 5: Petrophysical analysis shows the utilization of basic well logs and formation micro imager log (FMI) data. Hydraulic fracturing operations in unconventional reservoirs are profoundly influenced by small-scale geological features near the wellbore, such as natural fractures and bedding plane changes. Understanding these effects is crucial for optimizing fracturing strategies and enhancing reservoir performance. Here, we focus on analyzing the influence of these features within the Montney Formation. Our methodology includes examining basic well logs and FMI logs to detect variations in formation properties and identify natural fractures and bedding plane alterations. Our findings provide insights into how these features impact fracture propagation, confirming their presence and correlating them with observed variations in fracture propagation and microseismic data. This analysis underscores the significance of considering small-scale geological features in hydraulic fracturing operations for effective reservoir management.

Chapter 6: Seismic Reflection analysis shows an exploration of the correlation between geological features within the study area and microseismic data provides valuable insights into the influence of geology on microseismic patterns. Understanding geophysical data, particularly reflection seismic data, is crucial for successful oil and gas exploration. Integrating structural and lithological analyses helps us comprehend fracture propagation dynamics. Seismic attributes like Azimuth and Dip aid in structural geology understanding, while a pore pressure map derived from depth data assists in assessing pressure changes. Integration of seismic reflection interpretation with microseismic event analysis provides insights into fracture propagation. Despite data quality issues in the Montney formation, utilizing the Belloy formation helps represent the geology effectively. Interpretation reveals a southwestward dip in the area, with higher pore pressure correlating with this dip, potentially influencing fracture propagation.

Chapter 7: Stress Analysis shows the utilization of pumping datasets. Understanding horizontal stresses is crucial in multi-stage fracturing operations to comprehend how fractures propagate. With each stage, the minimum horizontal stress increases, altering stress distribution and affecting stress/strain near clusters. We utilize ISIP analysis to capture mechanical stress interference, observing how each fracturing stage adjusts stress perpendicular to the propagation axis and influences Instantaneous Shut-In Pressure (ISIP) values. By leveraging the Stress Escalation Model (SEM) by Roussel (2017), we can quantify stress anisotropy and fracture height, predicting potential fracture curvatures and spacing. Our method's application to field data aligns closely with observations, affirming its reliability. Through a detailed examination of four wells, particularly Well 3, we find no significant stress reorientation, validating our approach's effectiveness by comparing results from microseismic data and ISIP analysis. Additionally, calculated stress loads offer insights into potential changes in fracture propagation direction by serving as a proxy for alterations in minimum horizontal stresses.

Chapter 8: Integration of findings presents the synthesis of findings from surface seismic, microseismic, borehole, and engineering data culminate in a holistic understanding of hydraulic operational dynamics. The integration of different findings indicate that the microseismic data was mostly influenced by the geology.

Chapter 9: Conclusions consolidates various results and elucidates the expected characteristics observed across different findings. The findings suggest that the unidirectional propagation of fractures is primarily influenced by the structural geology of the Montney Formation, which dips toward the southwest direction, while microseismic events propagate updip. Variations in propagation direction indicate that geological phenomena such as the presence of natural fractures and changes in formation properties have had an effect. Despite the stress in the area not being sufficient to alter horizontal stresses significantly, stress shadows exerted when fractures propagate in one direction force fractures to propagate toward the opposite direction.

Chapter 2

Overview of hydraulic fracturing in the Montney formation

2.1 Introduction

The Western Canada Sedimentary Basin (WCSB) sprawls across about 450,000 square miles of Western Canada and can be characterized as a straightforward wedge of sedimentary rock tapering northeastward. Stretching from the western Rocky Mountains to the eastern Canadian Shield, this basin boasts a thickness of approximately 6 kilometers beneath the Rocky Mountains, gradually thinning to nothing along its eastern edges (Egbobawaye, 2013; Mossop & Shetsen, 1994; Porter et al., 1982). The Western Canada Sedimentary Basin (WCSB) took shape during the early Carboniferous and Permian periods, aligning with the region previously occupied by the Devonian Peace River Arch (Egbobawaye, 2013).

The Montney Formation is a prime candidate for horizontal drilling and hydraulic fracturing. The Montney Formation, dating back to the Triassic period, locates in northeast British Columbia and northwest Alberta. It stands out as one of the highly active plays in Western Canada and ranks among the most abundant sources of hydrocarbons across North America (Davey, 2012; Nelson & Rghei, 2008).The estimated gas potential for the Montney and Doig formations in Alberta and British Columbia is substantial, with 187 trillion cubic feet (TCF) for Montney and 139.7 TCF for Doig (Egbobawaye, 2013; Faraj et al., 2002). Despite significant interest in exploiting these unconventional reservoirs, there's still a lack of comprehensive understanding about their geology, geochemistry, mineralogy, petrophysics, and overall characterization. The intricate details and fundamental aspects of the Montney Formation are yet to be thoroughly defined or studied, as highlighted by Egbobawaye (2013).

2.2 Stratigraphy of Canadian Western Basin

The Lower Triassic Montney Formation represents a pivotal geological period characterized by several significant transitions. These include the shift from carbonate-dominated deposition in the Paleozoic era to clastic-dominated deposition in the Mesozoic era, alongside the evolution of invertebrate faunas from archaic Palaeozoic forms to modern forms. Additionally, the Montney Formation marks the transition from a passive margin setting to a foreland basin setting. These distinct characteristics make the Montney Formation stand out among Phanerozoic sedimentary successions in western Canada.

The figure displayed in Figure 2.1 provides an overview of the Montney Stratigraphy, spanning from western Alberta to the subcrop limit in British Columbia (Zonneveld & Moslow, 2018b). The Lower Triassic Montney Formation is bounded by unconformities at its base with the Paleozoic Belloy Formation and at its top with the Middle Triassic (Anisian) Doig-Phosphate or Sunset Prairie (Zonneveld & Moslow, 2018a, 2018b). Both surfaces are characterized by a Glossifungites trace fossil assemblage, signifying coplanar sequence boundary/flooding surfaces. A "Middle Montney" regionally correlatable sequence boundary aligns with the Smithian-Spathian boundary, associated with erosion and truncation of underlying strata. These boundaries likely result from regional tectonism coinciding with fluctuations in relative sea levels (Zonneveld & Moslow, 2018a, 2018b). Conodont-based biostratigraphy (Kendall, 2001; Orchard & Zonneveld, 2009; Zonneveld & Moslow, 2018b) facilitates the division of the Montney into three Lower Triassic sequences: Griesbachian-Dienerian (Sequence 1 or Lower Montney), Smithian (Sequence 2 or Middle Montney), and

Spathian (Sequence 3 or Upper Montney), with a fourth occurring in the Anisian Sunset Prairie Formation (Sequence 4). Sequences 3 and 4 are separated by a regional coplanar sequence boundary/flooding surface. Sequences 2 and 3 are delineated by a coplanar sequence boundary/flooding surface at the Smithian/Spathian boundary, while the boundary between Sequences 1 and 2 corresponds to the Dienerian/Smithian boundary at the base of the LaGlace Sandstone and Anten Coquina Members of the Middle Montney in west-central Alberta, interpreted as a sequence boundary (Davies et al., 1997; Zonneveld & Moslow, 2018b).

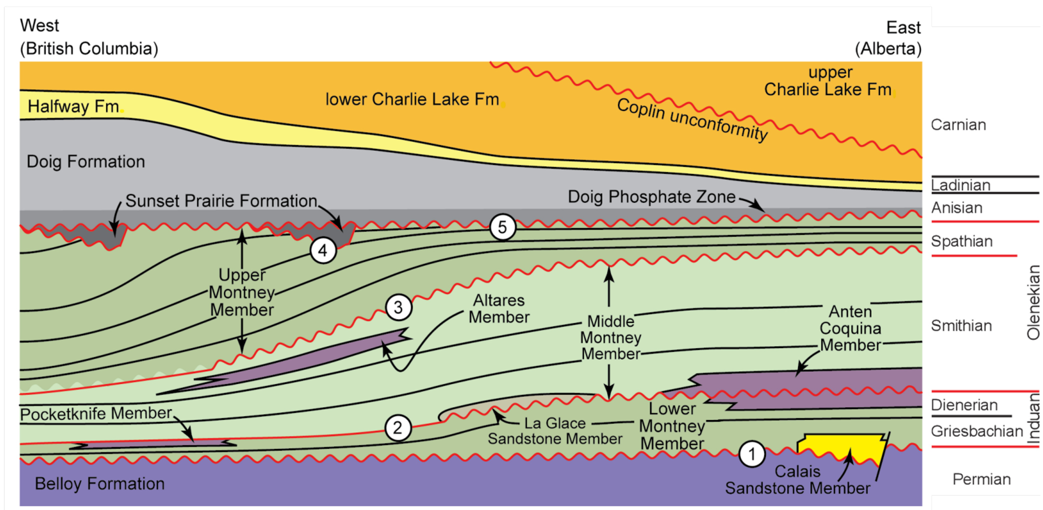

Figure 2.1: Schematic cross-section from central Alberta to British Columbia, depicting Montney stratigraphy in a west-east orientation. The diagram highlights intra and extraformational unconformities delineating the Lower, Middle, and Upper Montney members (designated as numbers 1–5). The basal Montney contact (1) is typically unconformable across most of the basin, though it may exhibit conformable characteristics in certain western subsurface and outcrop regions. The earliest intraformational unconformity (2) approximates the Dienerian-Smithian boundary (Induan-Olenekian boundary). A subsequent mid-Montney unconformity occurs around the Smithian-Spathian boundary (mid-Olenekian) (3). The upper Montney contact is unconformable with overlying Middle Triassic strata, either the Sunset Prairie Formation or the Doig phosphate zone (unconformities 4 and 5) (reprinted from Zonneveld and Moslow (2018b) with permission from Canadian Society of Petroleum Geologists (CSPG)).

The Middle Montney Member, which formed during the Smithian stage (Nelson & Rghei, 2008), comprises specific layers such as D1, D2, D3, and D4. The transition between D1 and D2 is characterized by the presence of silty shale beds (Prenoslo et al., 2018). Meanwhile, D3 and D4 are characterized by a variety of siltstone to sandstone ”event beds” enclosed within or interbedded with them (Popp, 2015).

2.3 Geological characterization of the Montney Formation

The Lower Triassic Montney Formation forms a west-dipping clastic wedge deposited on the northwestern margin of the supercontinent Pangea (Chevrot et al., 2020; Proverbs et al., 2018). To the northwest of the fold and thrust belt, the Montney Formation appears as a long belt extending up to 250 kilometers. It slopes downward to the southwest (Figure 2.2) (Chalmers et al., 2022). The upper and lower boundaries of the Montney Formation exhibit a near-parallel alignment, following the southwestward dip characteristic of the Phanerozoic within the basin. Presently, the subsea depths to the Montney Formation's upper boundary vary, ranging from 200 meters in the northeastern region near the border of British Columbia and Alberta to 3200 meters along the southwestern edge of the deformation front. Closer to Fort St. John, the top layer of the Montney Formation is shallower, forming a plateau with depths not exceeding 1500 meters (Chalmers et al., 2022).

2.3.1 Regional stresses in study area

Understanding and effectively managing seismicity induced by hydraulic fracturing treatments hinges on grasping key factors like in-situ stresses and pore pressure. In previous studies centered on the KSMMA area within British Columbia (BC), the Montney Formation's in-situ stresses were explored based on diverse datasets gauging pore pressure and closure pressure (Enlighten Geoscience, 2021). Earlier geomechanics analyses primarily leaned on the assumption of a strike-slip fault stress regime, where the maximum and minimum stress magnitudes correspond to the two horizontal principal stresses, while the vertical stress represents the intermediate one

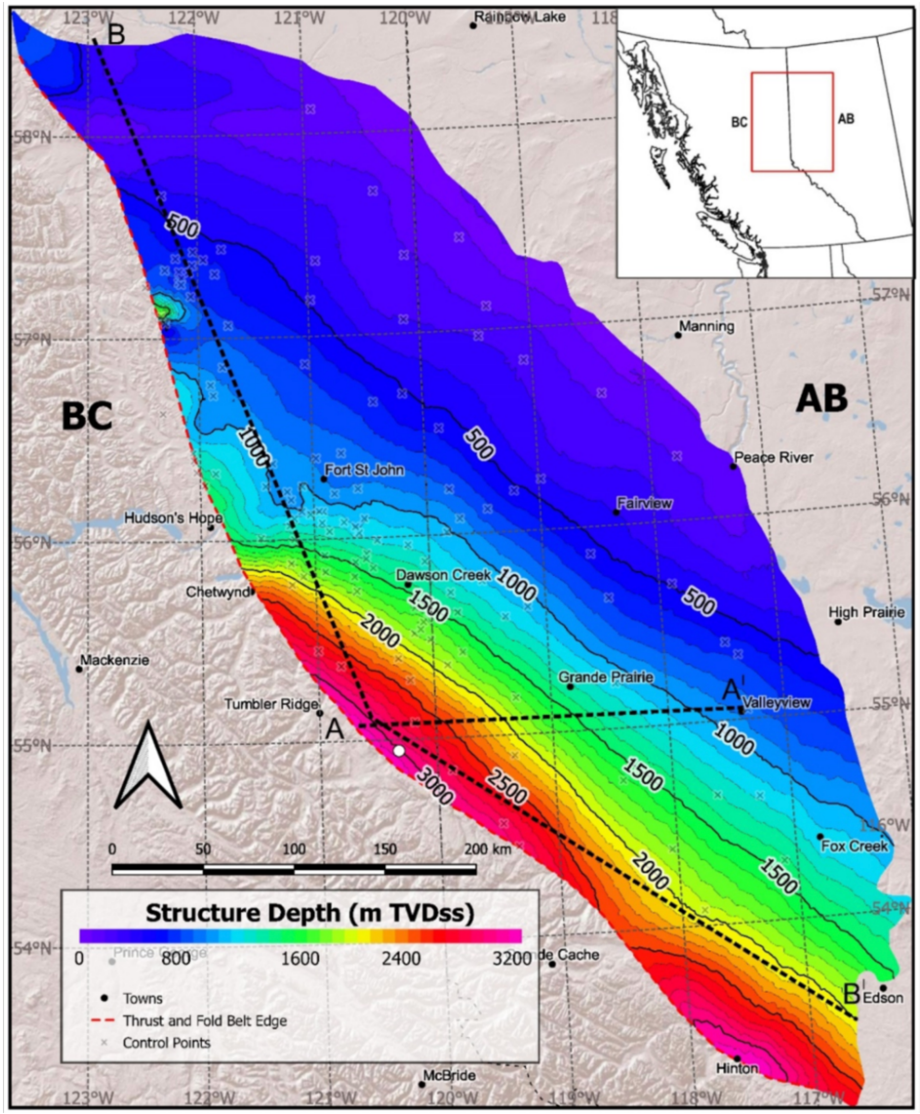

Figure 2.2: Structural Variation of the Montney Formation Across British Columbia and Alberta. The structure map depicts a gradual deepening of the Montney Formation towards the southwest (reprinted with permission from Chalmers et al. (2022)).

(Bell et al., 1990; Davey, 2012; Shen et al., 2018).

However, a recent study in the region has re-evaluated the in-situ stress regime by employing caliper readings. This reevaluation utilizes a methodology centered on poro-elastic horizontal strain modeling for estimating in-situ stresses. This method correlates rock mechanical properties with sonic (acoustic) logging data for the estimation process (Han & van der Baan, 2024). Figure 2.3 provides an overview of the study area where the assessment of in-situ stress took place, overlapping with the focus area of this study.

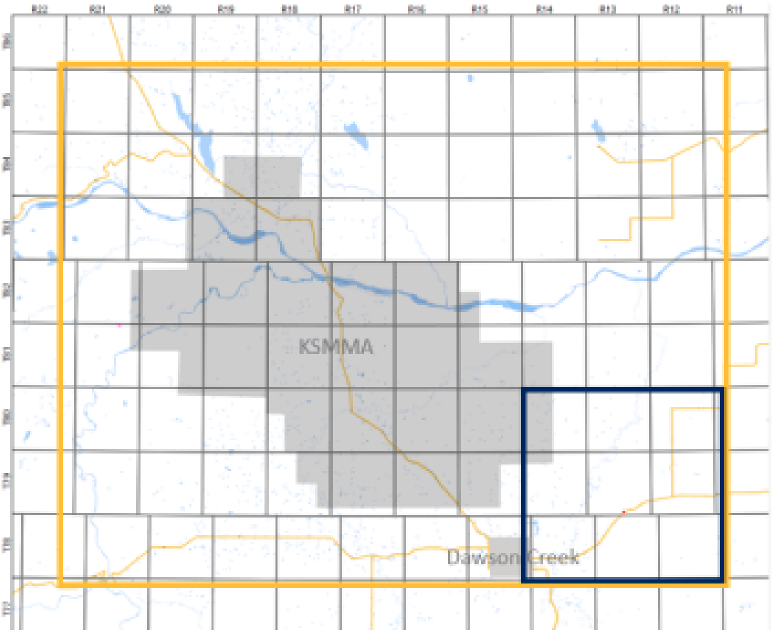

Figure 2.3: Map illustrating the re-evaluated in-situ stress area. The grey shading represents the KSMMA region. The small blue rectangle denotes the precise well locations utilized for in-situ stress analysis within this designated area by Han and van der Baan (2024) (reprinted from Han and van der Baan (2024) with permission Elsevier).

According to the recent research conducted by Han and van der Baan (2024), the eastern portion of the study area displays an in-situ stress pattern resembling a normal fault regime. In this area, the gradients of the minimum horizontal stress, maximum horizontal stress, and vertical stress are measured at 17.5 kPa/m, 21.5-23.6 kPa/m, and 25.2 kPa/m, respectively. However, the in-situ stress regime appears to shift towards a strike-slip fault stress regime in the western part of the study area. Here, the gradients for the minimum horizontal stress, maximum horizontal stress, and vertical stress are approximately 22.0 kPa/m, 28.6-32.0 kPa/m, and 25.6 kPa/m, respectively (Han & van der Baan, 2024). There is also another study by Shen et al. (2018), which also shows a strike-slip stress regime in the Fox Creek area. The gradients of the minimum horizontal stress, maximum horizontal stress, and vertical stress, on average, are measured at 17-21 kPa/m, 33 kPa/m, and 23-26 kPa/m,

Table 2.1: Comparative Analysis of In-Situ Stress Calculations: Insights from Han and van der Baan (2024), Shen et al. (2018) and Enlighten Geoscience (2021)

	Study by Han and van der Baan (2024)	Study by Enlighten Geoscience (2021) in KSMMA region	Study by Shen et al. (2018) in Fox Creek region
p_p(kPa/m)	$10.5 - 13.0$	$11.5 - 13.4$	16
σ_h(kPa/m)	$16.6 - 18.0$	$16.0 - 19.0$	17–21
σ_H(kPa/m)	$21.1 - 22.7$	$27.5 - 32.5$	33 ± 2
σ_v(kPa/m)	$24.5 - 25.5$	$25.1 - 25.3$	23–26
σ_H direction (deg)	$30 - 40$	$30 - 50$	$30 - 50$
In-situ stress regime	Normal fault	Strike-slip fault	Strike-slip fault

respectively.

The primary disparity lies in the magnitudes of the maximum horizontal stresses between the two studies, as shown in Table 2.1. This assumption of a strike-slip regime has been prevalent in numerous prior studies within the WCSB (Bell et al., 1990). This prevalence is largely attributed to the absence of concrete evidence regarding the in-situ stress regime, especially concerning the challenge in accurately or precisely measuring the magnitude of the maximum horizontal stress (Han & van der Baan, 2024; Schmitt et al., 2012).

In this thesis, our focus area falls within the anticipated zone of normal faulting regime. Consequently, we operate under the assumption that the stress regime within our study area aligns with this normal faulting regime.

2.4 Summary of Prior Study Findings within Study Wells

2.4.1 Distributed Acoustic Sensing (DAS)

The oil and gas industry has employed Distributed Acoustic Sensing (DAS) technology in well monitoring for over a decade, particularly focusing on its application in tracking hydraulic fracturing operations (Ortega Perez, 2022). DAS boasts high sensitivity to dynamic strain, allowing for clear identification of hydraulic treatment effects. These data play a pivotal role in monitoring and diagnosing potential completion issues during stimulation, aiding in the optimization of parameters and design for subsequent operations (Becker et al., 2020; Ortega Perez, 2022; Richter et al., 2019).

Jin and Roy (2017) and Ortega Perez (2022) showcased that low-frequency DAS data effectively capture subtle variations along the fiber induced by the opening, closing, and propagation of fractures during well stimulation. These insights allow for the constraint of hydraulic fracture geometry parameters such as length, density, width, propagation speed, and azimuth through the analysis of DAS strain front patterns (Becker et al., 2020; Jin & Roy, 2017; Ortega Perez, 2022; Ugueto et al., 2019).

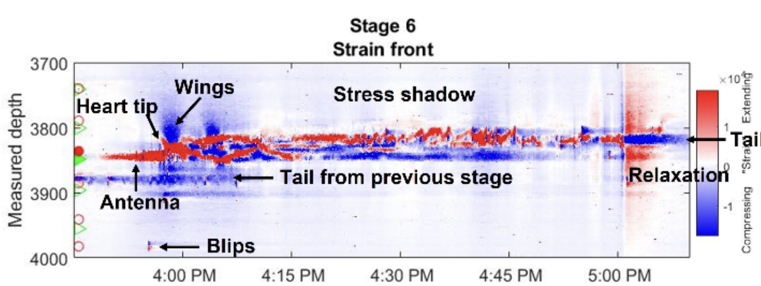

Figure 2.4: Strain Front from DAS Data for a Single Stage: The timeline (x-axis) correlates with the measured depth (y-axis), displaying extension in red and compression in blue (reproduced from Ortega Perez (2022) with permission from University of Alberta Library).

In the study by Ortega Perez (2022), DAS data from the same well utilized in our study was employed. Figure 2.4 showcases a practical instance of the low-frequency DAS response for a hydraulic fracture. The DAS data was obtained from a single treatment stage during well stimulation and recorded within the monitoring well. On the figure, the red dots on the left represent where the fractures intercepted the monitoring well (Frac hits). Filled triangles and dots denote the current stage, while unfilled ones represent other stages. Within the strain fronts, the color red signifies extension, while blue indicates compression.

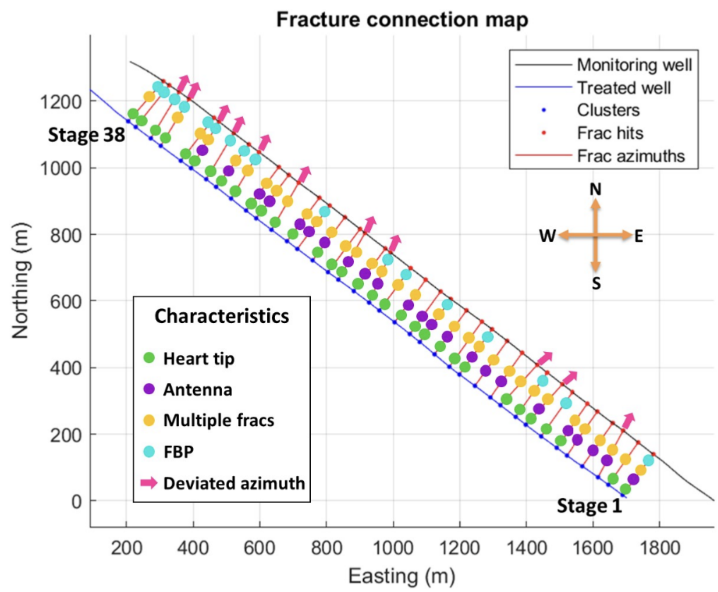

Figure 2.5: Map depicting Fracture Connections across all stages alongside original well geometry. Each stage is represented by specific characteristics: Green indicates the presence of a heart-shaped tip, purple signifies the presence of an antenna, yellow represents multiple fractures, cyan indicates a distinct FBP (Fracture Breakdown Pressure) peak, and pink arrows denote stages that did not propagate perpendicular from the treated well (reproduced from Ortega Perez (2022) with permission from University of Alberta Library).

In their study, Ortega Perez (2022) likened the fracture signal's appearance to that of a dragonfly. They described it as having a red heart-shaped tip, denoting the fracture hit, along with blue wings on the sides known as the stress shadow. When a newly created fracture intercepts the monitoring well, the dragonfly representation showcases a heart-shaped tip with wings on the sides. However, if the fracture was already opened, the dragonfly pattern would exhibit only an antenna, typically occurring at the initiation of the injection, and the stress shadow surrounding the fracture would lack the characteristic wing shape. An intriguing observation was made: if the dragonfly displays both an antenna and a heart-shaped tip, it indicates the stimulation of a pre-existing fracture alongside the creation of a new fracture during the injection process (Ortega Perez & van der Baan, 2024).

The results showcased in Figure 2.5 summarize the conclusive outcomes derived from the investigation led by Ortega Perez (2022). Certain stages, exemplified by Stage 11, exhibit antennas without heart-shaped tips, suggesting a lack of new fracture creation during injection. However, despite this observation, all these stages display evidence indicating the generation of multiple fractures. For instance, Stage 11 portrays two pairs of wings and two tails, strongly suggesting the occurrence of multiple fractures despite the absence of a clear indication of a newly created fracture.

2.4.2 Microseismic Analysis (MS)

In the preceding study by Ortega Perez (2022), microseismic cloud analysis was conducted across all stages, revealing a predominant hydraulic fracture propagation towards the North-East (NE) (Figure 2.6). However, intriguingly, certain stages displayed an unexpected South-West (SW) propagation, deviating from the anticipated bi-wing fracture pattern commonly observed. The work of Ortega Perez (2022) focused on calculating fracture length using microseismic cloud length, primarily measuring the length from the treated well towards the NE (Figure 2.7a), omitting consideration for the SW direction. This approach, detailed in their publication, provided insights into inferred cloud lengths perpendicular to the injection point at the treated well, with specific attention drawn to stages exhibiting predominant SW propagation through the use of marked purple arrows.

In our study, we intend to build upon methodology used by Ortega Perez (2022)

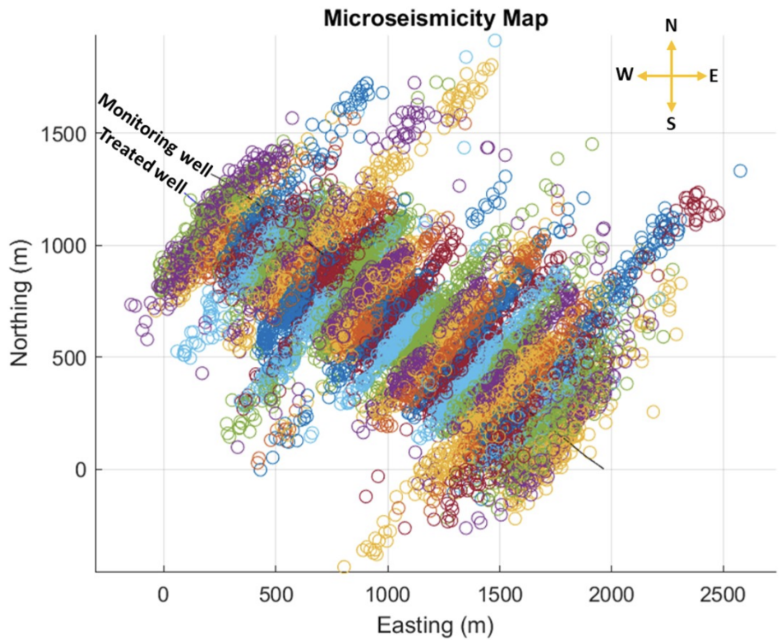

Figure 2.6: Planar view of well layout displaying microseismic clouds from all stages. The treated well is represented by the blue line, while the monitoring well is depicted in black. Different colors denote microseismic clouds from distinct stages (reproduced from Ortega Perez (2022) with permission from University of Alberta Library).

by incorporating a comprehensive assessment of fracture lengths for both the NE and SW wings. While replicating their calculations, our approach aims to expand the analysis beyond the NE direction, providing a more holistic evaluation of fracture propagation patterns. The detailed methodology for this extended analysis will be elucidated in Chapter 4.

Additionally,the investigation of Ortega Perez (2022) also delved into calculating fracture cloud height (Figure 2.7b), results of which were presented in their publication. As part of our validation process and for integration into our modeling endeavors discussed in Chapter 3, we recompute and validate these findings. By doing so, we seek to establish a solid foundation for our subsequent analyses, ensuring the accuracy and robustness of the data employed in our study.

Ortega Perez (2022) attributed the observed patterns in microseismic clouds to factors such as stress shadows, reactivation fractures, and treatment parameters. In this

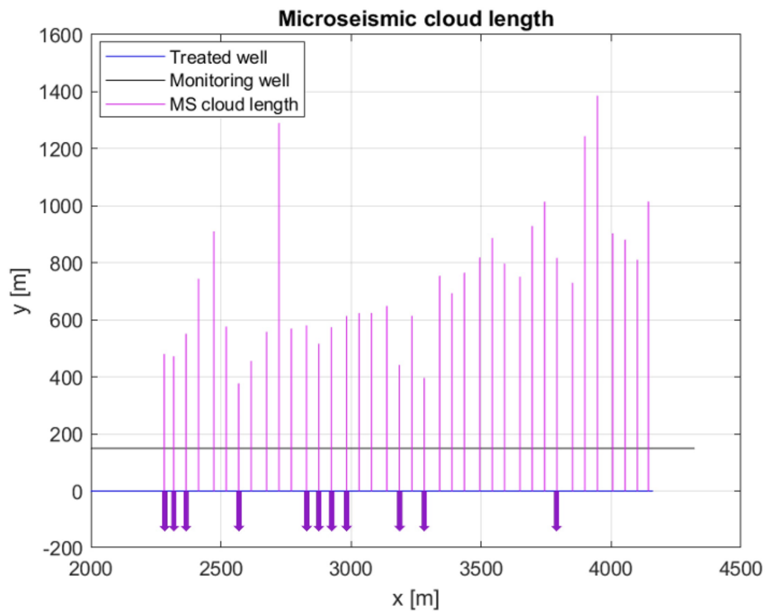

(a) Pink lines denote microseismic cloud lengths for all stages; purple arrows highlight SW propagation stages

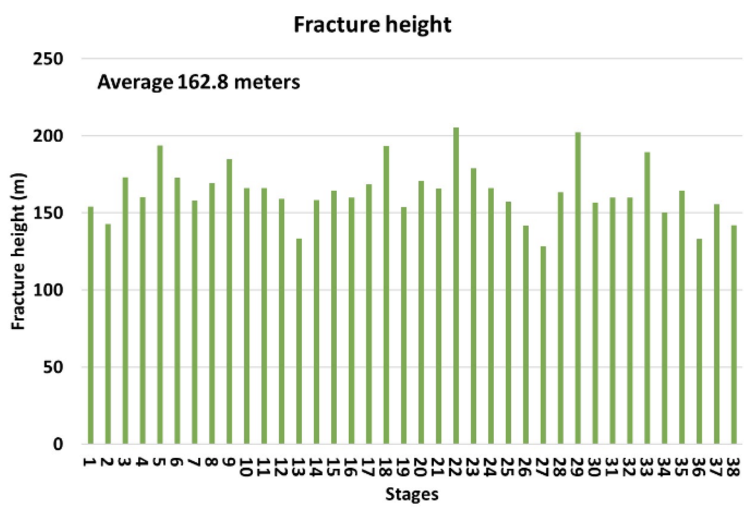

(b) Graph displays measured microseismic cloud heights

Figure 2.7: Findings from microseismic analysis conducted by (Ortega Perez, 2022). (a) Cloud length, (b) Cloud height (reproduced from Ortega Perez (2022) with permission from University of Alberta Library).

study, our objective is to validate and build upon the findings of Ortega Perez (2022). By incorporating new methodologies and additional data, we aim to enhance the investigation of microseismic patterns, seeking a deeper understanding and validation of the observed phenomena.

2.4.3 Microseismic cloud growth patterns and MS-DAS integration results

Furthering the study by Ortega Perez (2022), the integration of Microseismic (MS) data with Distributed Acoustic Sensing (DAS) data is showcased in Figure 2.8. As per her interpretation, early events observed are attributed to the preceding stage. An intriguing finding in the DAS-MS plot (Figure 2.8) reveals microseismic events occurring beneath the dragonfly pattern (green circle). This suggests potential fracture or fault reactivation, possibly due to residual fluid movement. These events, occurring mid-injection, are brief and localized, unlike Stage 6 where such events persisted until injection completion.

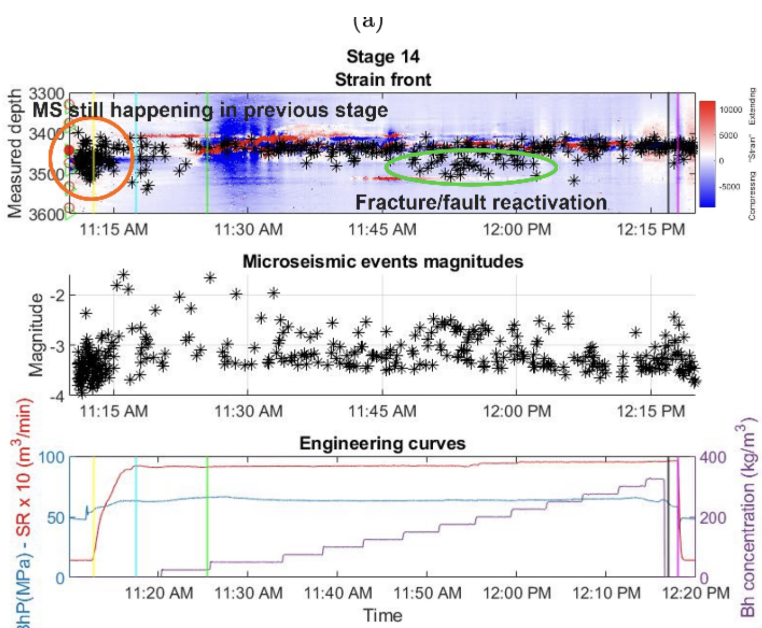

Figure 2.8: Stage 14: DAS-MS plot. Ongoing microseismic events from the prior stage are evident, indicated by immediate activity at the injection's start (orange circle). Mid-injection fault/fracture reactivation (green circle) is likely due to stress changes rather than fluid-related effects (reproduced from Ortega Perez (2022) with permission from University of Alberta Library).

Ortega Perez (2022) concluded that this pattern is a common response observed in DAS-MS plots during treatments. This analysis underscores the complementary nature of microseismicity and low-frequency DAS data. Integrating both methods allows for a more comprehensive interpretation. DAS effectively monitors cable location details, capturing nuances undetectable by microseismicity, such as multiple fracture creations. However, microseismicity remains crucial for monitoring occurrences away from the DAS cable's vicinity.

In line with this, our research will primarily concentrate on integrating MS data with different datasets, as detailed in Chapter 1. Our objective remains centered on comprehending hydraulic fracturing responses during multi-stage fracturing. We aim to apply new methods tailored to our study area to uncover additional insights.

2.4.4 The Perkins-Kern-Nordgren (PKN) model

Ortega Perez (2022) also calculated the Perkins-Kern-Nordge (PKN) model, which we will discuss in a later section. Essentially, it's a geomechanical model used to forecast fracture growth. This simplified model aids in understanding how hydraulic fracture generation was impacted. In figure 2.9, the PKN results for fracture half-lengths at the injection's conclusion were plotted with the lengths of the microseismic clouds. Downward green arrows highlight stages where microseismicity primarily propagated towards the SW. Circles at the bottom denote stages outside the range of good agreement for fracture half-length at the DAS hit time. Oranges signify longer-than-expected fractures, while yellow circles denote shorter ones. This visual comparison simplifies assessing length differences between the two methods, where similar lengths were anticipated. Large discrepancies might unveil treatment issues (Ortega Perez, 2022).

Ortega Perez (2022) pointed out that this simplified model does not capture all involved processes, thus an overestimation of fracture lengths isn't deemed abnormal. Around the middle of treatment, the company reported issues. These could explain the significant length differences. Ortega also highlighted that fractures tend to be

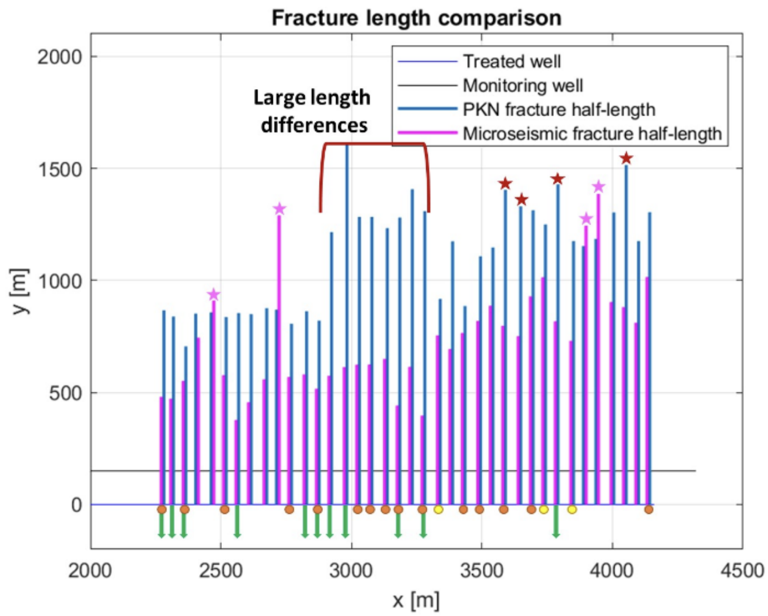

Figure 2.9: Horizontal depiction of well placements, illustrating the Perkins-Kern-Nordge (PKN) fracture half-lengths at the conclusion of injection (depicted in steel blue) with the lengths of the microseismic clouds (shown in pink). Green arrows highlight stages characterized by SW propagation of microseismic events (MS). Orange circles denote stages where the fracture half-length at the DAS hit time exceeded expectations, while yellow circles indicate stages where it fell short (reproduced from Ortega Perez (2022) with permission from University of Alberta Library).

longer in initial stages than later ones as shown in Figure 2.9. Early stages have less discrepancies, likely due to longer injection times initially, decreasing with subsequent stages. A discrepancy of over 500 meters in middle stages suggests an unexpected factor halting fracture growth, particularly in instances where microseismic clouds propagate towards the SW.

Longer-than-expected fractures might indicate slower-than-anticipated propagation, perhaps due to the cluster's failure to create a fracture, leading the fluid to travel along the well until finding a fracture to propagate. Shorter-than-expected fractures imply rapid propagation, possibly indicating an existing fracture. Most of the fractures longer than expected at DAS hit times are in the middle of treatment, where significant length differences between PKN and microseismic cloud lengths exist. This reinforces the notion that unexpected challenges occurred during these stages (Ortega Perez, 2022).

In our analysis, as detailed in Chapter 3, we'll adopt a similar methodology to calculate the treatment parameters and assess their influence on propagation. However, contrary to Ortega Perez (2022), we will introduce variations in two parameters (Plane strain modulus and fracture height) across stages instead of computing their averages. Our primary goal is to validate her findings and discern whether these parameters significantly impact fracture length.

2.5 Available Data

The anonymous company provided a dataset comprising four horizontal wells and one vertical well. These wells are indexed based on their hydraulic fracturing sequence, as visually depicted in Figure 2.10, illustrating their spatial arrangement. Notably, Well 3 serves as the focus, positioned centrally among all the wells. The monitoring well, represented in green, is located approximately 150 meters from Well 3. Each of these wells has been drilled into distinct Montney members, indicating diverse geological strata. Specifically, the study well has been drilled into the Montney D3 member.

Table 2.2 details the used datasets. Our primary goal is to understand the hydraulic fracture treatment in Well 3. Therefore, we have utilized all possible datasets for the well, including engineering data (pumping data, treatment information, Diagnostic Fracture Injection Test (DFIT)) to comprehend treatment parameters and stress changes, microseismic data to analyze event propagations, well logs (resistivity, gamma ray, neutron/density porosity, Formation Micro-Imager) to assess natural fractures around the wellbore and changes in formation properties, and seismic reflection to observe general trends in geology. The rationale behind prioritizing Well 3 stems from its possession of a micro-imager log and an ample number of stages, enabling comprehensive insights into the hydraulic fracturing process.

Table 2.2: The available data is for four wells in the study area. The focus of the study is mainly on Well 3.

Well	Engineering Data	Microseismic data	Seismic Reflection Data	Logs
Well 1	Pumping Data, Treatment Information, DFIT	39 stages		Not used
Well 2	Pumping Data, Treatment Information, DFIT	37 stages		Not used
Well 3	Pumping Data, Treatment Information, DFIT	38 Stages	Available	Resistivity, Neutron/Density porosity, Gamma ray, Micro-Imager
Well 4	Pumping Data, Treatment Information, DFIT	18 stages		Not used
Vertical well	DFIT	N/A		Not used

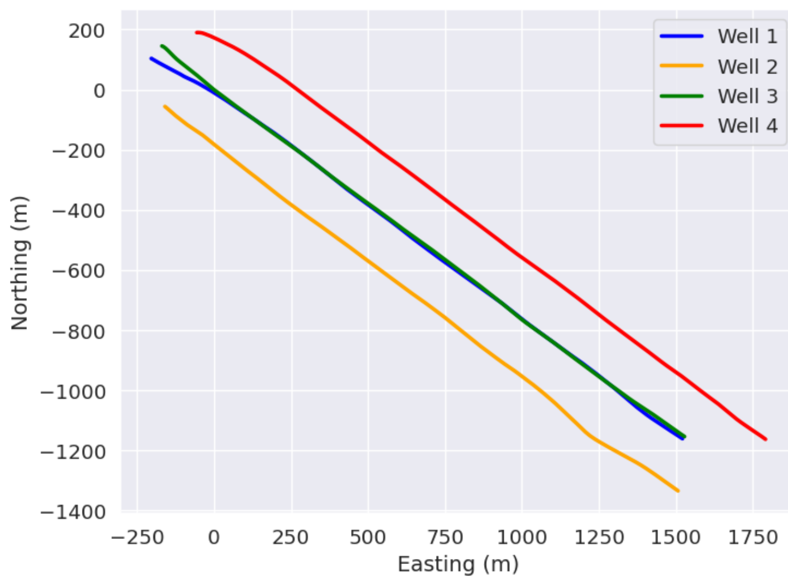

(a) Geometry of Wells: Lateral view

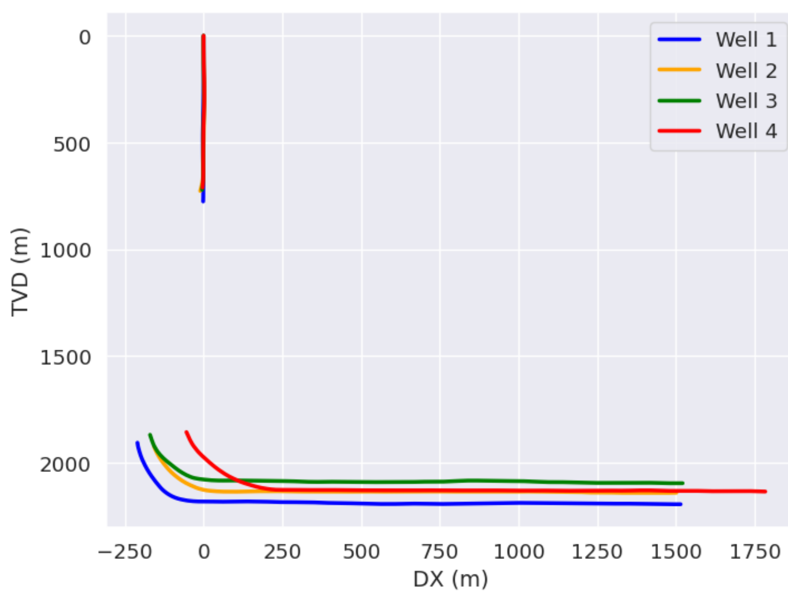

(b) Geometry of Wells: Upper view

Figure 2.10: The wells are visually differentiated by color, with their numbering following the sequence of hydraulic fracture treatments. Specifically, the Monitoring well is identified as well 4 and is positioned at a distance of 150 meters from the study well, denoted as well 3.

Chapter 3

Treatment Parameters

3.1 Summary

This chapter delves into a geomechanical analysis of pumping data aimed at exploring the impact of treatment parameters on hydraulic fracture treatments. The microseismicity presents an intriguing pattern, displaying considerable variability across treatment stages. Many events predominantly propagate in a northeast direction, while the length of the microseismic (MS) clouds fluctuates throughout the stages. Despite these observable phenomena, the underlying cause of this unusual behavior remains elusive. Consequently, our objective in this chapter is to investigate the influence of treatment parameters using the Perkins-Kern-Nordgren (PKN) model.

Previously employed by Ortega Perez and van der Baan (2024) to estimate fracture height using injection rates and treatment duration under constant Plane strain modulus, the PKN model serves as the foundation for our analysis. However, in our methodology, we adopt a nuanced approach by assigning distinct values to the Plane strain modulus (E') and fracture height (h) for each stage. This deliberate choice aims to mitigate the influence of geomechanical properties on the PKN model, which may otherwise confound the analysis. Additionally, we utilize stage duration derived from microcosmic data propagation time, as opposed to relying solely on injection time, which has proven inconsistent.

The findings of our study suggest that changes in treatment parameters do not solely account for the observed anomalies in propagation behavior.

3.2 Introduction

I analyze 38 stages within Horizontal Well 3 situated in a Montney reservoir in southwestern Alberta. In Figure 3.1, microseismic (MS) activity across all stages is illustrated and color-coded. It's evident that the MS clouds vary from stage to stage; some exhibit elongated fracture lengths while others appear shorter. Furthermore, directional arrows are provided below the figure, indicating the propagation direction of the stages. A blue arrow signifies fracture propagation in the northeast (NE) direction, whereas a red arrow indicates propagation in the southwest (SW) direction. Despite these observations, the underlying cause of this behavior remains unclear and warrants further investigation.

To shed light on why fracture lengths differ across stages, we turn to treatment parameters. By employing the Perkins-Kern-Nordgren (PKN) model, we aim to assess the impact of these parameters on fracture length propagation. The choice of this model stems from its foundational assumption that fracture length significantly exceeds fracture height. This assumption aligns with the typical orientation of the minimum in situ stress in reservoirs, which is predominantly horizontal. According to Nguyen et al. (2020), this model predicts the ease with which cracks propagate perpendicular to the minimum stress, leading to the formation of vertically-oriented hydraulic fractures.

3.3 Methods and Procedure

3.4 Perkins-Kern-Nordgren (PKN)

The Perkins-Kern-Nordgren (PKN) model plays a crucial role in our study of hydraulic fracturing's fracture length dynamics. The Perkins-Kern-Nordgren (PKN) model, developed by Perkins and Kern (1961), is a 2D hydraulic fracturing model.

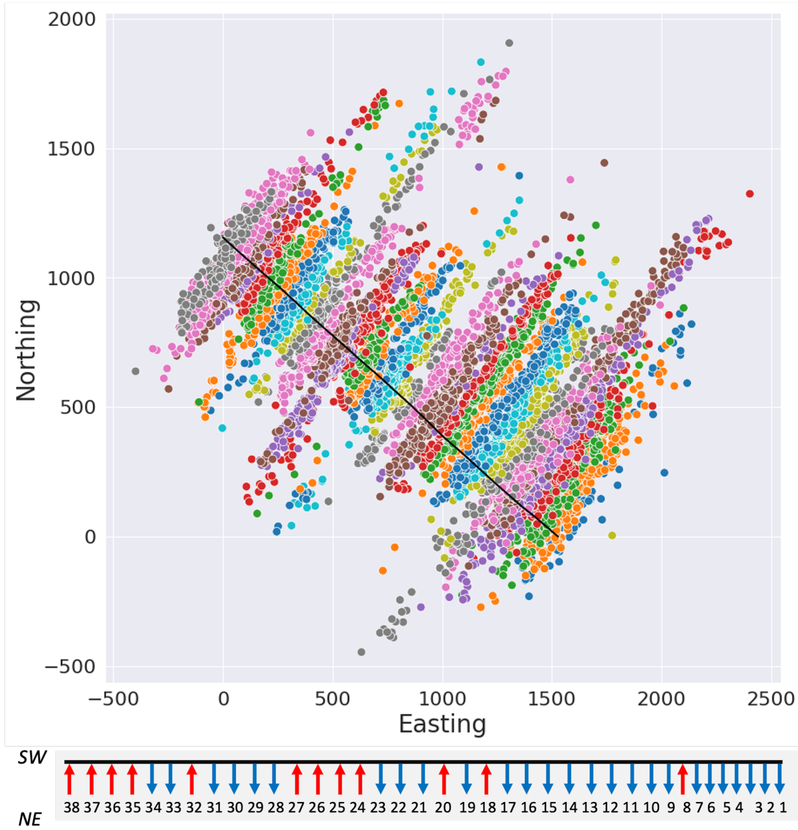

Figure 3.1: Overview of Microseismic Clouds: Arrows depict propagation trends. Blue denotes northeast movement, red indicates SW. Predominantly, propagation is northeastward. Up to stage 17, most events move toward the northeast direction, but after stage 17, the event direction changes, exhibiting a cyclic pattern where stages with predominantly northeast movement are followed by stages moving in the opposite direction.

Initially designed to calculate fracture length and width at a constant height, Nordgren (1972) later enhanced the model by incorporating fluid loss into its calculations. By simplifying fracture behavior and concentrating on key factors - Young's modulus, fracturing duration and injection rate - we use the PKN model to explore their impact on hydraulic fracture length. This analytical approach allows us to uncover how these parameters influence the hydraulic fracture pattern.

The PKN model is based on the premise of plane-strain conditions within the vertical plane. According to this model, the fracture exhibits an elliptical cross section, encompassing both horizontal and vertical dimensions, while propagating horizontally. It maintains a constant fracture height, which is distinct from and smaller than the fracture length. Furthermore, the width of the fracture varies, reaching its maximum value at the midpoint of the fracture's height.

$$L_h = 0.524 \left(\frac{q^3 E\prime}{\mu h^4} \right)^{1/5} t^{4/5}, \tag{3.1}$$

where L_h is fracture half-length (m), q is injection rate $(\mathrm{m}^3/\mathrm{s})$, E' is Plane strain modulus (Pa), μ is fluid viscosity $(\mathrm{Pa} * \ \mathrm{s})$, h is fracture height (m) and t is injection time (s) (Belyadi et al., 2019). The PKN (Perkins-Kern-Nordgren) model has been formulated by considering treatment parameters and reservoir rock properties as its foundation.

The PKN model was calculated with equation 3.1 to predict the evolution of the fracture half-length over time, incorporating treatment parameters and reservoir rock properties. To mitigate the influence of geomechanical properties on the PKN model, a deliberate decision was made to assign distinct values for the Plane strain modulus (E') and fracture height (h) for each stage (will be discussed in chapter 4). We also used stage duration from the microcosmic data propagation time due to inconsistent data for injection time. This differs from the approach taken by Ortega Perez (2022). The values for these parameters and rock reservoir properties are outlined in Table 3.1.

The fracture calculations for each stage were performed using a straightforward approach, and the results are detailed in Chapter 4.

The Plane strain modulus quantifies how well a material resists deformation under stress in two dimensions, with the third dimension allowed to expand freely. The Plane strain modulus, E' is computed for all stages using the following equation:

$$E' = \frac{E}{1 - \vartheta^2}, \tag{3.2}$$

where E represents Young's modulus, and ν denotes the Poisson ratio. Young's

Table 3.1: Geomechanical and completion parameters for the PKN fracture propagation model.

Parameters	**Value**	**Source**
Plane strain Module, E′ (Pa)	Varies	Sonic Logs
Injection rate, q (m^3/s)	Varies	Average injection rate
Injection time, t (s)	Varies	MS propagation time
Fracture height, h (m)	Varies	MS data
Fluid viscosity, μ $(Pa * s)$	Constant value of 0.001	Slick water properties

modulus and Poisson's ratio can be calculated using the following equations:

$$E = \rho_b \times V_s^2 \times \left(\frac{3V_p^2 - 4V_s^2}{V_p^2 - V_s^2} \right), \tag{3.3}$$

$$\nu = \frac{V_p^2 - 2V_s^2}{2 \times \left(V_p^2 - V_s^2\right)}, \tag{3.4}$$

Here, ρ_b represents bulk density, and V_p and V_s are the velocities of compressive and shear sonic waves, respectively. It's important to note that these values have been extracted from borehole logs which is described in details in chapter 5.

The stage duration was derived from the microcosmic data propagation time due to inconsistent data for injection time.

Injection rate (q) have been provided by the company and changes depending on the stage. The fluid viscosity is a fixed value and was chosen as the fluid viscosity of water as there was no record on the slick-water used.

Equation 3.2 was used to calculate the strain module per stage, considering a constant fluid viscosity of 0.001 $Pa * s$.

After obtaining the values of the PKN half-length, we will compare them with the MS-derived fracture length to investigate potential correlations between the two methods. Any observed correlation would suggest that treatment parameters have influenced the fracture length, thereby linking temporal changes in fracture length to the treatment parameters employed.

3.5 Results and Discussion

3.5.1 PKN Model

In this section, we delve into the presentation and discussion of the PKN analysis results. We initiate the discussion by introducing the input parameters, recognizing their paramount influence on the outcomes of the PKN model. Our central objective is to elucidate how treatment parameters shape the overarching results of MS data.

Next, we will then move on to represents the results of PKN model. This method previously applied by Ortega Perez (2022) with a constant fracture height and Plane strain modulus. Our aim is to assess the extent to which these parameters influence the results. If their impact is minimal, the conclusions drawn by Ortega Perez (2022) will be validated through the application of the PKN model.

Input parameters: Figures 3.2a 3.2b, 3.2c, and 3.2d provide an overview of key input parameters in well 3. These parameters include treatment duration, average injection rate, fracture height, and the calculated average Plane strain modulus between stages. The Plane strain modulus is determined using sonic logs to find Young's modulus and Poisson ratio, which are then employed in Equation 3.2. The average injection rate ranges from 6 to 9 m^3/min, the Plane strain modulus spans from 38×10^9Pa to 55×10^9Pa, and the treatment duration varies between 30 and 200 minutes. There are variations in treatment parameters, with certain stages exhibiting longer duration (e.g., stages 7, 17, 23, 24), relatively low injection rates, and strong Plane strain modulus (e.g., stages 19, 20, 26, 27, 37). Among these parameters, stage duration fluctuates the most. Longer treatments can generate larger fractures which is expected to effect the calculation of PKN the most. The fracture height varies between stages, a phenomenon further discussed in the subsequent chapter 4.

PKN Model: The fracture half-lengths at the end of the injection for every stage were estimated by programming the PKN model using equation 3.1. Figure 3.3 shows the PKN fracture half-length at the end of the injection for all stages. This figure displays the variations in lengths among the stages; they range from 310 to 2500 meters. One can observe that the PKN results we calculated differ from the calculations of Ortega Perez (2022), as depicted in Figure 2.9. These differences are mainly due to variations in input parameters such as stage duration, Plane strain modulus, and fracture height.

The duration of the stages significantly influences PKN results, as evidenced by the close resemblance between the PKN result and treatment duration distribution. The fractures are noticeably longer in the early stages than in the later ones. It is because of the longer fracture treatment in the early stages as shown in figure 3.2c. Surprisingly, the Plane strain modulus and average rate inputs have a minimal impact on the outcomes. The impact is mostly visible for later stages where the fracture treatment was constant (e.g., 38, 36, 24, 25).

Abnormally high PKN half-fracture length predictions are noticeable, particularly in stages 17, 24, 25, and 36. These stages encountered reported completion complications during injection. Furthermore, Ortega Perez (2022) noted that the company later confirmed complications in the middle stages as well. Consequently, it is anticipated that these stages may not accurately reflect the fracture half-length.

3.6 Conclusions

This chapter utilized the PKN model as a tool to investigate the influence of treatment parameters on cloud propagation. Specifically, the model was employed to calculate the fracture half-length at the conclusion of MS cloud propagation. The PKN model yielded predicted fracture half-lengths ranging from 310 to 2500 meters. The unusually long PKN fractures observed in certain stages were interpreted as a consequence of complications during treatment.

Notably, fractures in the early stages appeared longer compared to those in the later stages. This disparity is likely attributable to the initial stages having lengthier injection times, which gradually decreased in subsequent stages. Conversely, the later stages, associated with shorter fractures, were characterized by shorter treatment periods.

In the forthcoming chapter, we intend to utilize the PKN model to conduct a comparative analysis with the MS cloud analysis (fracture length). Our aim is to ascertain the correlation between the datasets and explore whether the microseismic data was influenced by treatment parameters, particularly treatment durations.

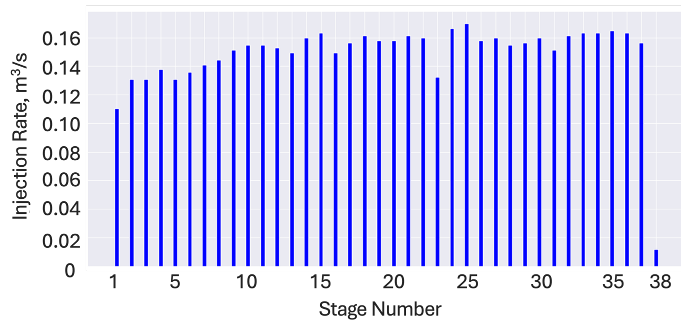

(a) Injection Rate, m^3/s,

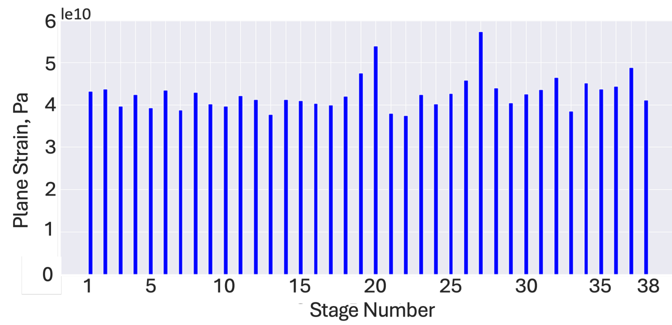

(b) Plane strain Module, Pa,

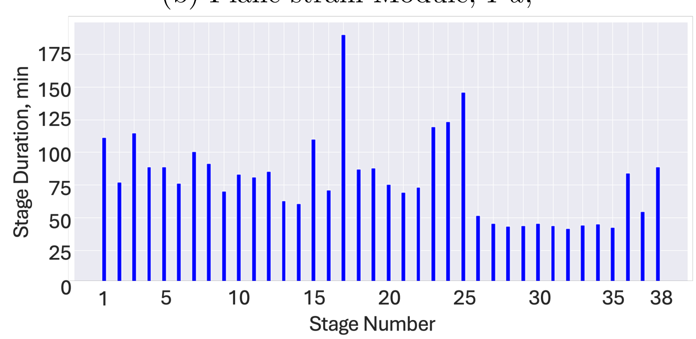

(c) Injection Duration, min,

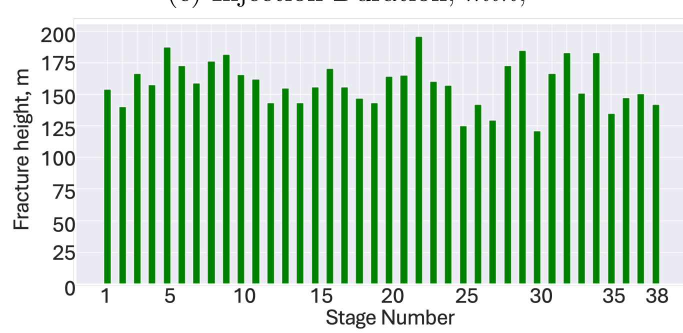

(d) Fracture height, m. Fracture height calculated from MS clouds in chapter 4

Figure 3.2: Treatment Parameters used as input parameters for PKN half-length calculation. (a) Injection rate, (b) Plane strain Module, (c) Injection Duration, (d) Fracture height calculated from MS clouds. Injection rate and plane strain modulus remained constant, while significant variations were observed across stages for fracture height and treatment duration.

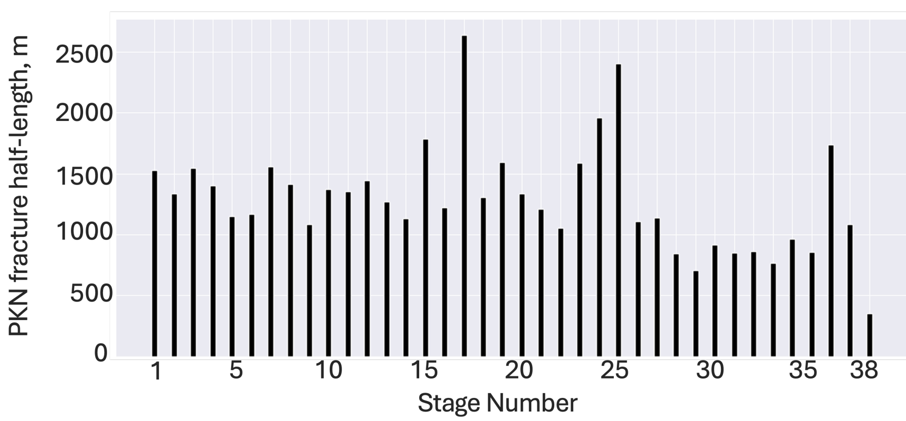

Figure 3.3: Predicted PKN fracture half-length based on input parameters. Longer half-lengths are predicted for initial stages, while shorter fracture lengths are forecasted for later stages. The results suggest that PKN is most affected by the duration of each stage.

Chapter 4

Microseismicity Analysis

4.1 Summary

Fracture propagation is a critical aspect of hydraulic fracturing operations, yet certain anomalies, such as the directional behavior of microseismic clouds, remain poorly understood. This chapter aims to elucidate the underlying mechanisms driving such behavior by conducting a comprehensive analysis of microseismic propagation. We begin by employing distance vs. magnitude plots to investigate whether the directional propagation observed could be attributed to variations in the distance between treatment and monitoring wells. Subsequently, we conduct cloud analysis, visually interpreting microseismic clouds and calculating key parameters such as cloud length and height. Through the utilization of r-t plots, we analyze the temporal evolution of radial fracture distances, further refining our understanding of propagation dynamics. Additionally, we employ equations proposed by Nustes Andrade and van der Baan (2021) to model the time-dependent growth of radial distances, providing insights into hydraulic fracture treatment regimes. Integration of results derived from microseismic (MS) and Perkins-Kern-Nordgren (PKN) methods offers further clarity regarding the influence of treatment parameters on fracture propagation.

Our findings indicate that the distance between treatment and monitoring wells does not solely account for the directional behavior observed in microseismic clouds. Cloud analysis reveals dynamic changes in fracture height and length across stages,

with a predominant northeastward movement of events. Analysis of r-t plots identifies distinct propagation regimes, including "normal," "reactivation," and underscoring the complexity of fracture dynamics. Furthermore, our physics-based approach highlights variations in hydraulic fracture treatment regimes across stages. For example, the north-east wing of the fractures exhibits mainly Perkins-Kern-Nordgren (PKN) and Kristianovich-Geertsma-de Klerk (KGD), while the south-west (SW) wing exhibits mostly KGD and leak-off dominated regimes. PKN results reveal discrepancies between MS and PKN results, with PKN overestimating the fracture half-length compared to MS results.

This study contributes to a deeper understanding of fracture mechanics in hydraulic fracturing operations. However, further analysis is necessarily to understand the fracture propagation.

4.2 Introduction/Theory

Microseismic monitoring, a seismic technique leveraging fracturing or water-injection-induced microseismic phenomena, plays a pivotal role in reservoir fracturing or water injection operations. This method monitors fracture activities and flow mobilities in oil or gas-producing pays during hydraulic fracturing stimulation (Van Der Baan et al., 2013; Zou, 2013). The process induces alterations in pore pressure and stress within the geological formation, resulting in the generation of minute seismic events, known as microseismic events.

During this process, a set of geophones is strategically placed in a shut-in offset monitoring well at a considerable distance from the injection well, enabling the detection of microseisms. The efficiency of this detection is influenced by the hardness and uniformity of the rock, where sound travels farther and more microseisms can be captured through down-hole telemetry (Rodvelt, 2020).

Real-time data are plotted to analyze height growth, length, and field width of the events, offering insights into the ongoing fracturing operations. This immediate feedback allows for on-the-fly adjustments to the fracturing schedule, influencing fracture growth. After preconditioning the data, the crucial step of locating microseismic events follows. This process holds significant importance as it aids in determining the distribution and geometry of fractures induced by the fracturing treatment (Rodvelt, 2020; H. Wang et al., 2016; Zou, 2013).

The event locations are categorized into two main methods: traveltime-based and waveform-based. The former relies on the first arrivals of the P and/or S waves, necessitating phase identification and picking. The latter method locates the source by integrating travel time, amplitude, and phase information from seismic waveforms to reconstruct and focus the source energy into an image profile (Li et al., 2020; Ortega Perez, 2022).

The final analysis post-treatment generates a fracture map, illustrating the length, width, and height growth of the fracture. This comprehensive information aids design engineers in optimizing future fracturing treatments, while also assisting reservoir engineers in strategically placing wells for effective production drainage. The detailed fracture map provides valuable insights into the effectiveness of the fracturing operations, enabling informed decision-making for enhanced reservoir management and optimization (Rodvelt, 2020).

The dimensions and propagation characteristics of hydraulic fractures, such as length, width, height, and azimuth, can be assessed either visually or through geometric and statistical methods (Maxwell, 2014). A simple approach involves measuring the microseismic clouds' height, width, and length by fitting a rectangular box to the cloud. The length is determined by the longest horizontal side, the depth by the vertical side, and the width by the shortest horizontal side (Maxwell, 2014).

It is crucial to recognize that pressures and stresses extend beyond the newly formed hydraulic fractures, impacting the surrounding formation in all directions. This is why the microseismic cloud does not solely correspond to the fractures; instead, it serves as a volumetric representation of the rock affected by the treatment (Van Der Baan et al., 2013). Despite this broader influence, employing microseismic monitoring remains possibly the most reliable method for estimating fracture geometry.

In the broader context, the success of fracturing operations greatly influences the enhancement of unconventional petroleum production, improved recovery ratios, and efficient utilization of reserves (Zou, 2013).

4.2.1 Moment magnitude

Magnitude, in the context of seismic events, is a numerical measure that quantifies the size or energy released during these events. It serves as a scale to categorize the strength of seismic occurrences. While various magnitude scales exist, most lack a direct link to a physical model. However, the moment magnitude scale stands out for its tangible basis in estimation. It measures event size by quantifying released energy, directly connected to rock movement and surface fracture extent (Hanks & Kanamori, 1979).

The effective range for observing microseismic events within a formation hinges primarily on the strength of these occurrences (Warpinski, 2009). As moment amplitude decreases, it becomes more difficult to detect the event due to attenuation of the signal. Further from the sensor array, only larger magnitude events can be detected. The most simple way to evaluate detection bias is to plot moment magnitude vs. distance from the monitor well (Yousefzadeh et al., 2018). With increasing distance from the sensor array, lower magnitude events become undetectable.

4.2.2 Radial distance versus time plots

The evolution of the microseismic cloud's spatial extent over time reveals crucial insights into the fundamental mechanisms driving these events (Shapiro et al., 2006). The $r - t$ plots depict the distance of microseismic events, r from the injection point throughout each stage over time, t. This gives us a picture of how the microseismic cloud grows. Shapiro et al. (1997) explained this growth using a simple equation that considers the diffusion of the events through the medium.

$$r = \sqrt{4\pi D t}, \tag{4.1}$$

Equation 4.1 links the distance, r, with the time, t, since injection began. When the diffusivity, D of the medium is unknown, equation 4.1 can be a valuable tool for inferring its value from the spatial and temporal patterns of fluid-induced microseismicity observed in an $r-t$ plot. This method was adopted from Shapiro et al. (1997), who, assuming a constant growth rate of the microseismic cloud proportional to the square root of time, proposed the model function equation $\hat{L}_t$ as shown in equation 4.2:

$$\hat{L}_t = \hat{\alpha}_t \sqrt{t}, \tag{4.2}$$

Here, $\hat{L}_t$ represents the distance at time t. $\hat{\alpha}_t$ is a scalar related to the apparent diffusivity of the medium, $\hat{D}_t$, as described in Equation 4.3, which directly stems from Equation 4.2:

$$\hat{D}_t = \frac{\hat{\alpha}_t^2}{4\pi}. \tag{4.3}$$

Shapiro et al. (1997) suggested fitting equation 4.2 to the microseismic cloud data to determine $\hat{\alpha}_t$, minimizing the sum of squared errors between $\hat{L}_t$ and the observed size of the microseismic cloud at different propagation times.

By employing equation 4.3, the apparent diffusivity, D, can be determined. Furthermore, Shapiro et al. (1997) suggested utilizing this correlation to explore the time-dependent growth of fracture length concerning both time and diffusivity. We include this equation in our methodology section as we have adopted this method for analyzing our data to identify the regimes of hydraulic fracture treatment. The concept of investigating the time dependency of fractures originates from the work of Shapiro and Dinske (2009).

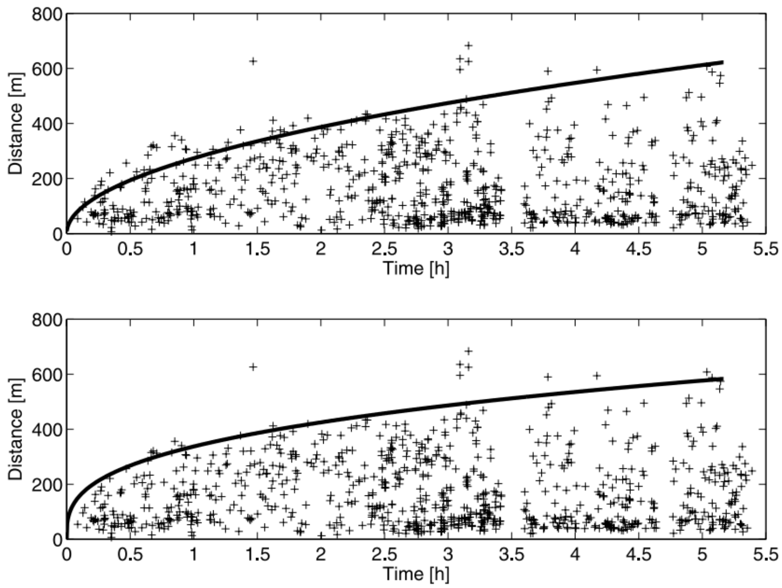

Figure 4.1: Example of an r-t plot. Distances of the MS events from the center of the injection interval versus their occurrence times. The microseismic events with different distinct patterns: (upper) a linear diffusion type approximation of the triggering ($t^{1/2}$); (bottom) a cubic root parabola ($t^{1/3}$), providing better fit to data (reprinted from Shapiro and Dinske (2009) with permission from American Geophysical Union).

Figure 4.1 illustrates the distribution of microseismic events over time, triggered by a hydraulic fracturing treatment in the Barnett shale gas reservoir (Shapiro & Dinske, 2009). The upper graph indicates that in the early stages, the triggering front closely aligns with a nearly linear function of time. This behavior is a direct consequence of the dominance of fracture volume during the initial phase of injection. However, over the long term, fluid-loss diffusion processes start to prevail over fracture growth, leading to the fracture length becoming proportional to the square root of time ($\sqrt{t}$).

The preceding analysis assumes either pore-pressure diffusion or elastic stress changes as the primary contributors to fracture growth, disregarding their interplay. Nonetheless, several studies have examined the impact of poroelastic coupling on injection-induced seismicity (Rozhko, 2010; Segall & Lu, 2015). In scenarios involving nonlinear diffusional processes, like the coupling between pore pressure and stress, the triggering front of microseismic events on an "$r - t$" plot better aligns with a $\sqrt[3]{t}$ curve (Shapiro et al., 2006).

4.2.3 Hydraulic fracture regimes

Fluid-driven fractures propagate when the pressure exerted by the fluid within fractures surpasses the confining stress, viscosity losses, and the energy required to create new fracture surfaces (Geertsma & De Klerk, 1969). In non-porous solids, the movement of fluid-driven fractures is a combined process involving fluid transport and mechanical behavior. The expansion of fractures is primarily governed by losses due to fluid viscosity and the energy expended in forming new solid surfaces, as characterized by fracture toughness (Detournay, 2004; Shovkun & Espinoza, 2019). Models for fluid-driven fractures consider different shapes:

1. Radial (or penny-shaped) fractures display elliptical vertical cross-sections, with their tips positioned on circles (Figure 4.2).

2. PKN fractures also exhibit elliptical vertical cross-sections, maintaining a constant height constrained by the bounding layers.

3. KGD fractures maintain a constant height but feature rectangular vertical cross-sections (Figure 4.2).

Besides their geometrical features, fluid-driven fractures can be categorized based on the relationship between the work required to fracture the rock and the frictional losses within the fracture (Detournay, 2004). Viscosity-dominated fracture propagation occurs when frictional losses outweigh rock-splitting work, typically seen in lengthy fractures with medium to high viscosity fluids. Conversely, toughness-dominated fracture propagation requires higher energy to fracture the rock in tension compared to moving the fluids. This type of propagation is favored in relatively short fractures containing low-viscosity fluids within high-toughness rocks (Shovkun & Espinoza, 2019).

Fluid-driven fractures within porous media experience fluid leak-off, where fluid flows from fractures into the fractured porous medium. This phenomenon causes

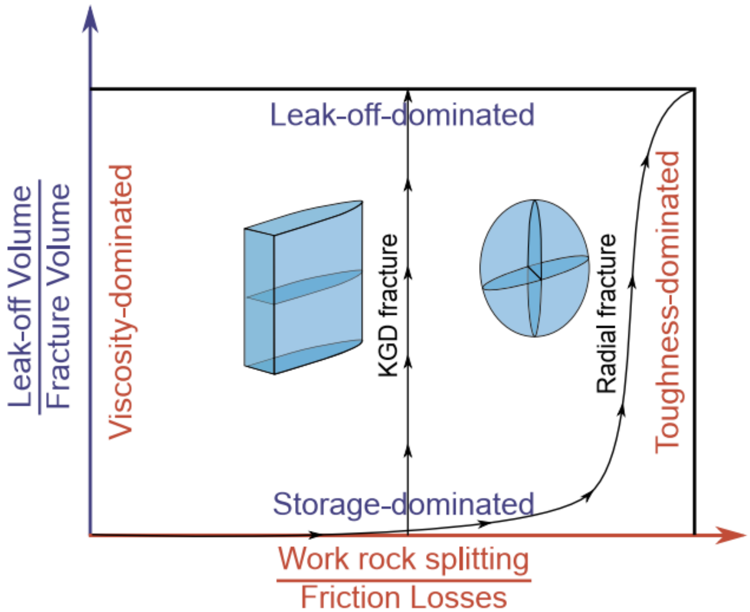

Figure 4.2: Visual representation depicting various fluid-driven fracture propagation regimes, including viscosity-dominant, toughness-dominant, leak-off-dominant, and storage-dominant scenarios (reprinted from Shovkun and Espinoza (2019) with permission from Elsevier).

additional viscous losses and fluid retention within the rock's pore spaces. Early attempts to describe this involved applying the Carter equation to PKN and KGD solutions (Howard & Fast, 1957), resulting in the development of PKN and KGD models (Valko et al., 1993). Storage-dominated fractures retain most injected fluid within the fracture, commonly found in low-permeability rocks (Bunger et al., 2005), whereas leak-off-dominated fractures suggest that most injected fluid enters the rock's pore spaces, favored in high-permeability reservoirs. However, these models, although widely used, focus only on fluid leak-off near the fracture, disregarding the poromechanical effects of porous media deformation around the fracture and the reduced effective stress near the fracture face (Shovkun & Espinoza, 2019).

The latter can be examined by considering the fluid efficiency parameter, η, which quantifies the relationship between the volume of the fracture generated and the total injected volume (Economides & Nolte, 2000). In general, in scenarios where leak-off dominates (fluid efficiency, $\eta \to 0$), the spatial and temporal characteristics of

Table 4.1: Approximations for the time-dependent behavior of hydraulic fracture length (L), and radius (R) across various fracture models for different fluid efficiency η and behavior index n (modified from Economides and Nolte (2000)).

Fluid efficiency	PKN	KGD	Radial
$\eta \approx 1$	$L \propto t^{\frac{2n+2}{2n+3}}$	$L \propto t^{\frac{n+1}{n+2}}$	$R \propto t^{\frac{2n+2}{3n+6}}$
$\eta \approx 0$	$L \propto t^{1/2}$	$L \propto t^{1/2}$	$R \propto t^{1/4}$

microseismicity exhibit a linear diffusion process, reflecting pore-pressure relaxation at the injection source (Shapiro et al., 1997). On the other hand, microseismic events in a storage-dominated regime (fluid efficiency, $\eta \to 1$) are driven by fracture propagation with minimal fluid loss.

The dissipation of energy at the crack-tip region plays a significant role in shaping the time-dependent behavior of hydraulic fracture length (Barthwal & van der Baan, 2019). This is quantified through a fluid rheology parameter known as the behavior index (n). Typically, most fracturing fluids exhibit an n around 0.5, while a Newtonian fluid approaches an n of 1 (Adachi & Detournay, 2002). Table 4.1 provides estimations for the time dependency of hydraulic fracture length, considering PKN, KGD, and radial models. The time exponents vary from 1/4 for the leak-off-dominated radial model to 4/5 for the storage-dominated PKN model involving a high-viscosity Newtonian fluid (e.g., n approaching 1) (Economides & Nolte, 2000; Nustes Andrade & van der Baan, 2021). The parameter n is assumed to be 0.5 as the fluid efficiency, η, approaches 1.

In Table 4.1, a time exponent (β_t) below 1/2 signifies a regime where leak-off dominates, while an exponent exceeding 1/2 suggests a fracturing regime predominantly characterized by storage. These differing growth rates stem from the hydraulic fracture propagation's potential to outpace pore-pressure diffusion notably in low-permeability rocks (Barthwal & van der Baan, 2019; Nustes Andrade & van der Baan, 2021). Therefore, a time exponent of 1/3 in Figure 4.1 denotes a leak-off-dominated regime attributable to pore pressure diffusion.

Later, Nustes Andrade and van der Baan (2021) introduced Equation 4.4, derived from the interrelation between Equation 4.1 and 4.2, leveraging the evolution of fracture length over time accounting for apparent diffusivity through the application of the Levenberg-Marquardt method (Nustes Andrade & van der Baan, 2021; Wright, 2006).

$$\hat{L}(t) = \widehat{a_t} t^{\widehat{\beta_t}}, \tag{4.4}$$

where β_t represents the time, t dependency of the fracture length growth, whereas $\widehat{a_t}$ represents the model parameter which is a multiplication factor.

4.3 Methodology

4.3.1 Location bias with Distance vs magnitude plot

A magnitude-distance graph allows us to determine whether the entire fracture geometry was mapped by observing the lowest detectable magnitude at the farthest point from the sensor array (Cipolla et al., 2011). Stronger seismic events exhibit detectability over greater distances compared to weaker ones. Figure 4.3 illustrates a magnitude-distance graph, showcasing two scenarios: one where all events are plotted (left), and another where events are normalized to account for biased data (right). Removing events falling below this threshold magnitude (as depicted in Figure 4.3, right graph) serves to normalize any distance-related bias. We employed this method for our data analysis.

In our study, adopting this method allows us to assess whether the unidirectional propagation of events results from detection bias or accurately reflects geological processes. This is accomplished by implementing a magnitude threshold on the magnitude vs. distance plot. Subsequently, we analyze the planar view of the microseismic cloud map, enabling a direct contrast between the modified cloud representation post-

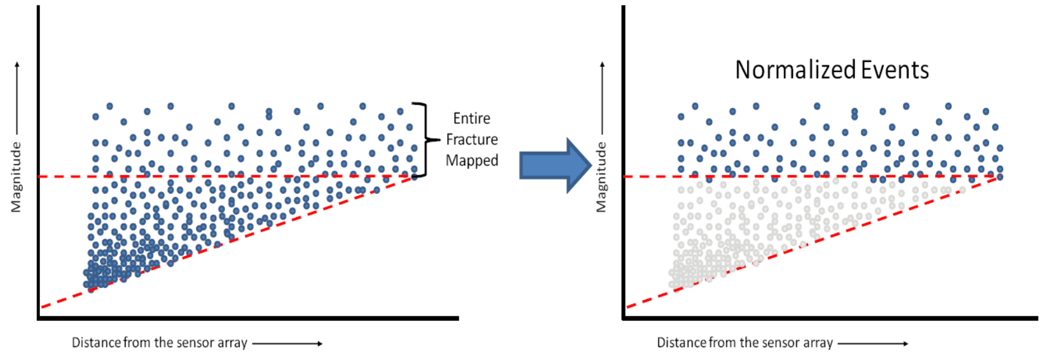

Figure 4.3: The magnitude-distance graph illustrates complete event mapping, encompassing both low and high magnitude occurrences (left), alongside normalized events (right) achieved by filtering out events below the threshold value (reproduced from Cipolla et al. (2011) with permission from Society of Petroleum Engineers (SPE)).

threshold application and the original cloud distribution. Alterations observed in the distance plot following threshold application serve as crucial indicators of any biases linked to distance-related detection constraints.

Nonetheless, the filtered events with magnitude cut-off will remain integral for subsequent sections of further processing. This step is essential to normalize the event data, preventing any potential bias in event density caused by detectability.

4.3.2 R-T plot Analysis

Sometimes, events happen at various distances from an injection point in a short timeframe. This suggests that some events are triggered by immediate stress transfer, while others occur due to the gradual transfer of pore pressure changes from the injection point to a reactivated fault over time (Shapiro & Dinske, 2009; Shapiro et al., 1997).

Based on Ortega Perez (2022) there are four development patterns in the r-t plots. The "normal" pattern shows microseismic events developing with a parabolic trend, driven by the diffusion of pore pressure. The "reactivation" pattern occurs when a pre-existing fracture is reactivated, leading to microseismicity developing in a linear fashion in distance-time plots. In the "halted growth" pattern, microseismic events cease to increase in distance and cluster within a specific range, indicating the fracture's growth has stopped. Lastly, in the "stress transfer" pattern, microseismic events happen instantly at different distances, indicating stress transfer as the cause of microseismicity.

4.3.3 Defining the regimes

We employed a physics-based method to investigate hydraulic fracture treatment, building on Nustes Andrade and van der Baan (2021). By fitting model equations (equation 4.4), we assessed whether fracture propagation was influenced by storage or leak-off dominance, providing insights into pore pressure diffusion dynamics.

We segmented the dataset into 10-minute intervals and calculated the 90th percentile of microseismic event distances to define the microseismic cloud's shape and extent, minimizing the impact of distant events and location uncertainties. Using curve fitting with equation 4.4 using the Levenberg-Marquardt approach, we established the relationship between hydraulic fracture length and time, deriving the time exponent (β_t) for each interval.

Analyzing the evolution of fracture propagation and the dominance of storage or leak-off mechanisms based on the table 4.1 enabled us to interpret observed patterns. Specifically, we evaluated changes in the time exponent (β_t) over time, where a β_t below $1/2$ indicates leak-off dominance and exceeding $1/2$ suggests storage dominance. Notably, in cases of "reactivation" patterns, β_t may exceed 1.

4.3.4 Microseismic cloud analysis

The Cloud Analysis workflow has been adapted from the methodology presented by Ortega Perez (2022), as detailed in Chapter 2. All the results outlined in this chapter closely mirror the findings of Ortega Perez (2022), with the sole addition of considering both wings of the fractures in length calculations.

1. The microseismic cloud reveals details about the dimensions and propagation

of hydraulic fractures, primarily estimated through visual inspection. Mapping the microseismic events along the treated and monitoring wells visually represents the volumetric extent of fracture shearing, opening, and closing. This visualization offers insight into the directional trend of cloud propagation.

2. The height of the fracture can be determined by subtracting the depth of the shallowest event from the depth of the deepest event.

3. The length of the fracture will be calculated subtracting the farthest event from the well projection.

4.3.5 Comparison of Microseismic (MS) and Perkins-Kern-Nordgren (PKN) Fracture Half Lengths

This section aims to compare the fracture half lengths derived from microseismic (MS) data with those obtained from the Perkins-Kern-Nordgren (PKN) method. The objective is to investigate any correlation between these two sets of results, which will help in understanding the potential impact of treatment parameters on fracture length changes over different stages. Additionally, we will compare the fracture regimes derived from the physics-based approach to provide further insights into the fracture behavior.

4.3.6 Workflow

1. We utilize the distance vs. magnitude relation to ascertain uncertainties associated with the distance between the treatment and observation wells. Applying a threshold based on plot interpretation, we proceed to the next step of fracture reclassification, facilitated by this process.

2. The microseismic clouds were initially categorized into clusters by the company based on the time window of treatment stages. While this method is convenient, it overlooks the spatiotemporal distribution that may coincide with the non-linear growth patterns of the microseismic clouds throughout the treatment stages. To

address this limitation, we classify the microseismic events by minimizing a sum of squares combination of Euclidean distance from the center of the interval (r) and the time difference since the start of each stage (t). This approach, as described by Nustes Andrade and van der Baan (2021), introduces a spatiotemporal constraint r_c, defined as:

$$r_c = \sqrt{\left(\frac{r}{\mu_r}\right)^2 + WF\left(\frac{t}{\mu_t}\right)^2}, \tag{4.5}$$

where μ_r represents the average microseismic cloud size across all stages, and μ_t denotes the average duration of stages from the beginning of pumping, as described by Nustes Andrade and van der Baan (2021). We applied a weighting factor (WF) of 0.01 to ensure equal consideration of both time and distance in the classification process. This normalization guarantees that the dimensions and magnitudes of both time and distance are comparable. This process reclassifies events by grouping them based on the value of r_c.

3. After applying magnitude threshold and reclassification, we calculate the cloud length and height using the simple approach discussed in the methodology.

4. We calculated the 90th percentile values within specific time grids of the r-t plot. Through interpolation techniques, we ensured seamless alignment of percentile trends over the microseismic cloud. This process effectively eliminates minute-scale fluctuations in the microseismic data, offering a smoother depiction of length changes over the defined time intervals.

5. We utilize the Levenberg-Marquardt method proposed by Nustes Andrade and van der Baan (2021) to determine the optimal parameters, β_t for time dependency, and a_t for model parameters in Equation 4.4 across various time intervals in the pumping schedule. The optimization process involves a constant time increment for different intervals. A good model fit in each interval is crucial as it reveals the time-dependent behavior of the microseismic cloud, as discussed in the theory section,

which in turn helps identify the fracture regime.

6. After defining the fracture regimes and calculating the fracture height, the next step involves comparing the results obtained from the PKN method, as discussed in the previous chapter, with those derived from the microseismic (MS) method. This comparison aims to ascertain whether treatment parameters have had any discernible impact on the data.

4.4 Results and Discussion

4.4.1 Location bias with Distance vs Magnitude plot

The primary aim in investigating the distance bias in event detection is to determine whether the spacing between the observation well and the monitoring well has introduced a bias leading to the predominant detection of microseismic events on the east side of the well.

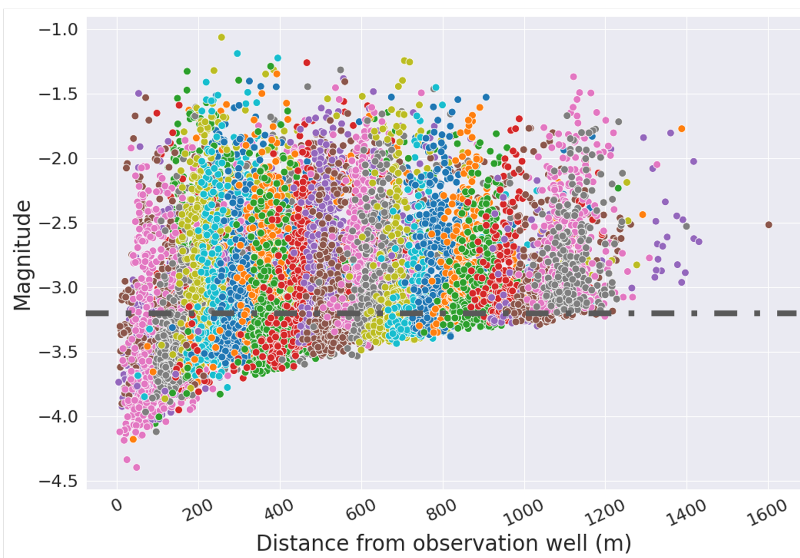

Figure 4.4: Magnitude-distance graph showing treatment stages for Well 3. Each color represents a different fracture treatment stage. The magnitude threshold is set at -3.2, based on the far event at stage 38 being recorded around 1200 meters away.

In Figure 4.4, we present a graphical representation illustrating the relationship between event magnitudes and their proximity to the center of the receiver array for the various stages of Well 3. These microseismic events are color-coded according to their respective stages, encompassing a total of 38 stages. Notably, we observe that the minimum recorded magnitude at a distance of approximately 1200 meters from the receiver array registers at around -3.2. This observation suggests that events with a magnitude lower than -3.2 should be excluded from a comparative interpretation, given their limited significance in the analysis.

Therefore, we apply a magnitude threshold of -3.2 to our data, as illustrated in Figure 4.5b. It is evident that there is a significant reduction in the number of events after the filtering process; however, there is no discernible alteration in the pattern of event cloud propagation. The reduction in event count predominantly occurs around the fractures, indicating that the filtering process did not eliminate events on one side of the well. This observation suggests that the distance between the treatment well and the observation well does not impact the unidirectional microseismic event propagation.

On the another hand, filtered events with a magnitude higher than -3.2 will continue to be utilized in subsequent sections for further processing, as it is significant step to normalize the events.

4.4.2 Reclassification of microseismic events

The primary objective of this updated classification approach is to categorize events based on both the timing of injection and the spatial distance from the source. To achieve more precise classification, we employed equation 4.5 with a weighting factor of 0.01. This decision was motivated by our intention to avoid solely relying on distance for reclassification. By incorporating both event propagation time and distance, a weighting factor of 0.01 consistently produced favorable outcomes, ensuring effective classification while considering both factors.

The plan view of microseismic events post re-classification is depicted in Figure 4.5c. A visual inspection reveals that while some events have shifted their classifica-

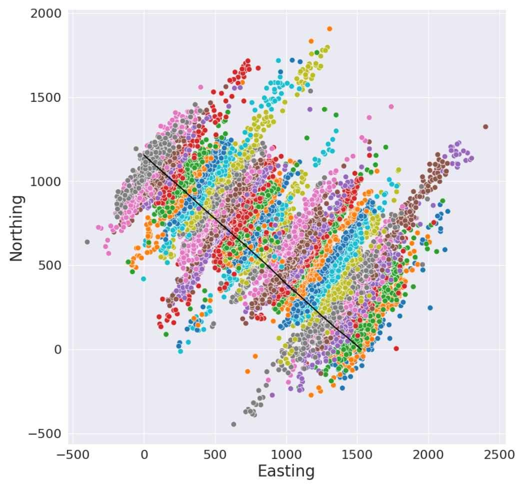

(a) Original microseismic cloud distribution observed from a planar view after completion of 38 stages.

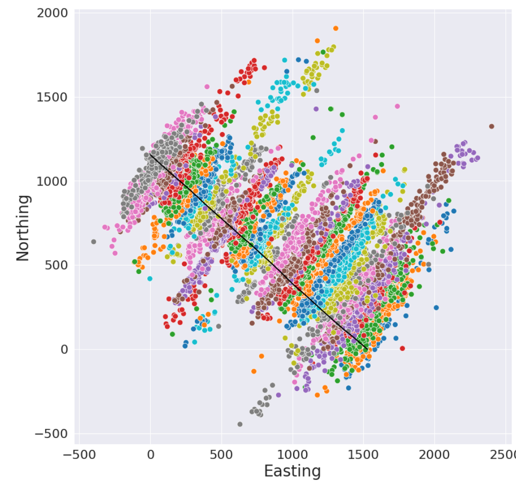

(b) Planar view of microseismic event pattern with -3.2 magnitude filter. Distance between wells minimally affects unidirectional cloud propagation.

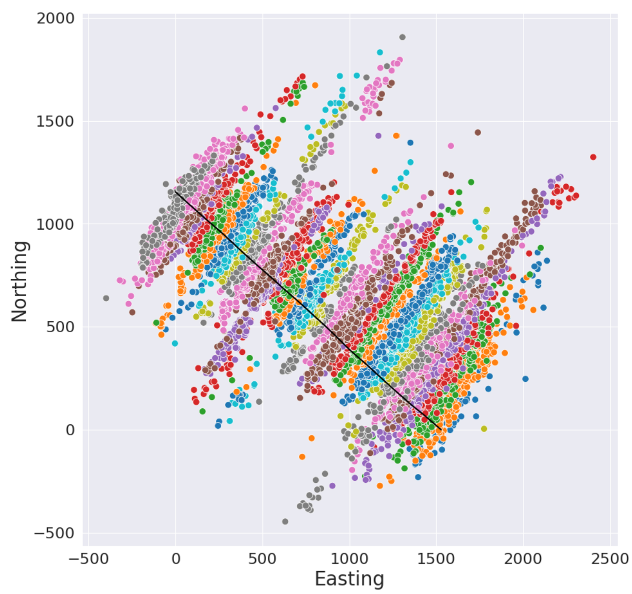

(c) Planar view of microseismic events after reclassification with -3.2 magnitude cutoff, considering radial distance and time. Noticeable change compared to Figure 4.5a.

Figure 4.5: Planar views of microseismic cloud distributions: (a) Original data, (b) After applying magnitude cut-off resulting in decreased cloud thickness but no change in the cloud pattern, (c) After applying magnitude cut-off and event reclassification.

tion group, the overall difference is not significant.

Quality Control (QC)

Figure 4.6 shows the measured depth versus distance plot a) before and b) after the reclassification. The green rectangle on the lower chart highlights events eliminated before classification due to bad event locations. Markers (x) in black signify the stage start time and injection point.

It's worth noting that Figure 4.6 is specifically designed to enhance clarity and facilitate visual understanding by concentrating exclusively on data from the initial 9 stages. Significantly improved classification is evident for events in stages 6, 7, and 8. Earlier events have been correctly reclassified to their respective stages, resolving the issue where events from stage 6 were included in stage 7 due to ongoing fracture propagation. This phenomenon has been rectified through the classification process. This effect is particularly pronounced in the r-t plots (Figure 4.7).

R-t plots is presented in Figure 4.7. The y axis represents the radial distance of events from the injection point, while x axis represents the time of the event propagation. Notably, for the presented stage, early events are detected, which correspond to high radial distance values (highlighted within the green bracket). In contrast, after reclassification, early events have been assigned to the previous stage. Moreover, new events have been reassigned from the next stage (highlighted within the red bracket).

4.4.3 Microseismic cloud analysis

Cloud Trajectories

In Figure 4.8, the illustration displays microseismic activity across all stages. The red and blue arrows represent the direction of fracture movement. One can observe a predominant propagation towards the NE. However, as stages progress, a shift in fracture propagation towards the southwest (SW) becomes apparent. Ortega Perez (2022) attributes this change to the stress shadow effect, which induces resistance in the northeast direction, consequently redirecting fluid flow towards the SW. Notably, until Stage 17, the stress shadow phenomenon is not clearly evident, with a

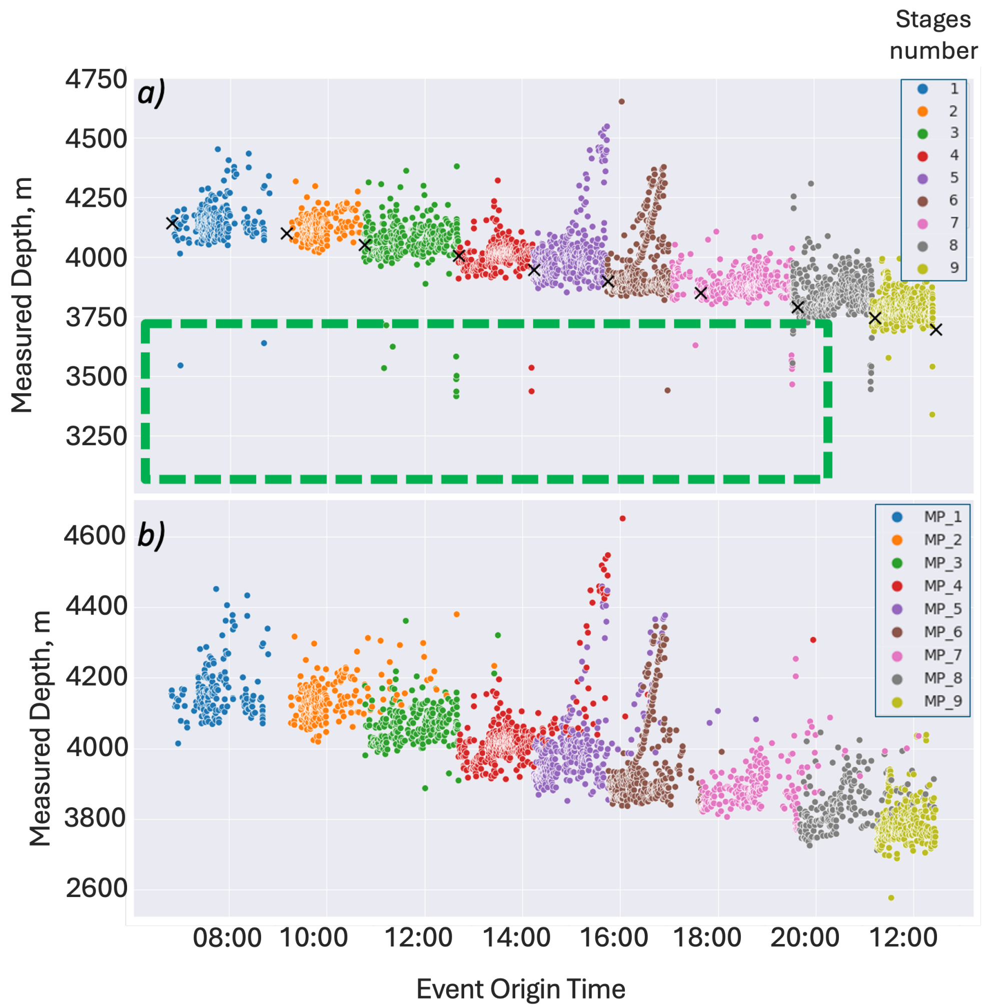

Figure 4.6: Event origin times and depth measurements for the first 9 stages with -3.2 magnitude filter:(a) Original events by pumping time (pre-classification); (b) Reclassified events. Green rectangle represents the events due to bad event locations. Reclassification successfully removed the tailing events and reassigned them to the corresponding stages.

single dominant directional movement. Thus, further analysis becomes crucial for a comprehensive understanding of the observed dynamics.

Figures 4.9, and 4.10 provide a comprehensive view of microseismic activity organized into groups of five stages each. Within these plots, the green arrows directed towards the right signify stages dominated by a predominant NE propagation of the microseismic cloud. Conversely, the grey arrows facing left denote stages where the microseismic cloud predominantly propagated towards the SW. These observations

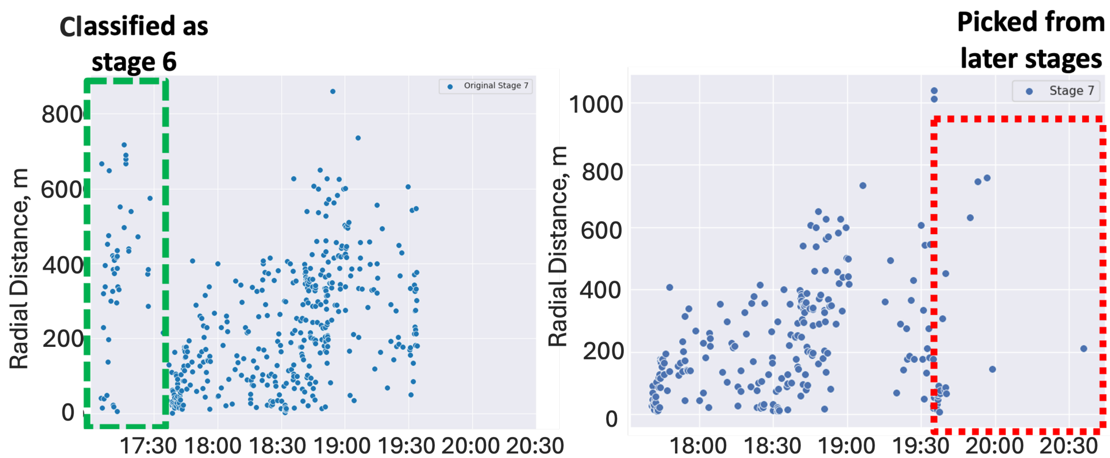

Figure 4.7: R-t plot for the Stage 7. Magnitude cut-off -3.2 is applied. Left figure shows original events based on pumping time. The green rectangle shows early events with high radial distance values, while the right figure shows reclassified events. Red bracket represents newly assigned events. The events that were in the green bracket (left) are now eliminated and assigned to the previous stage after the reclassification.

and results closely align with those found in Ortega Perez (2022).

Furthermore, we note that in certain stages, such as stages 5, 10, 35, and 30, the planar view depicted in Figures 4.9 and 4.10 illustrates arching towards the subsequent stage. This behavior may result from the stress shadow exerted by preceding stages that causing stress reorientation. This phenomenon will be elaborated upon in Chapter 7.

Another intriguing phenomenon is apparent from Figure 4.11, where we present the lateral view of the well for two stages: Stage 6 and Stage 13. The black dots represent the stage port depth. It is observable that microseismic events in these stages are shifting towards the previous stages. This phenomenon is observed across multiple stages, particularly in Stage 5, 6, 7, and 11, 12, 13, and 14, all demonstrating movement towards their respective preceding stages.

Cloud Height

The method for calculating fracture height has been adopted from Ortega Perez (2022). Figure 4.12 illustrates the variation in fracture height across different stages.

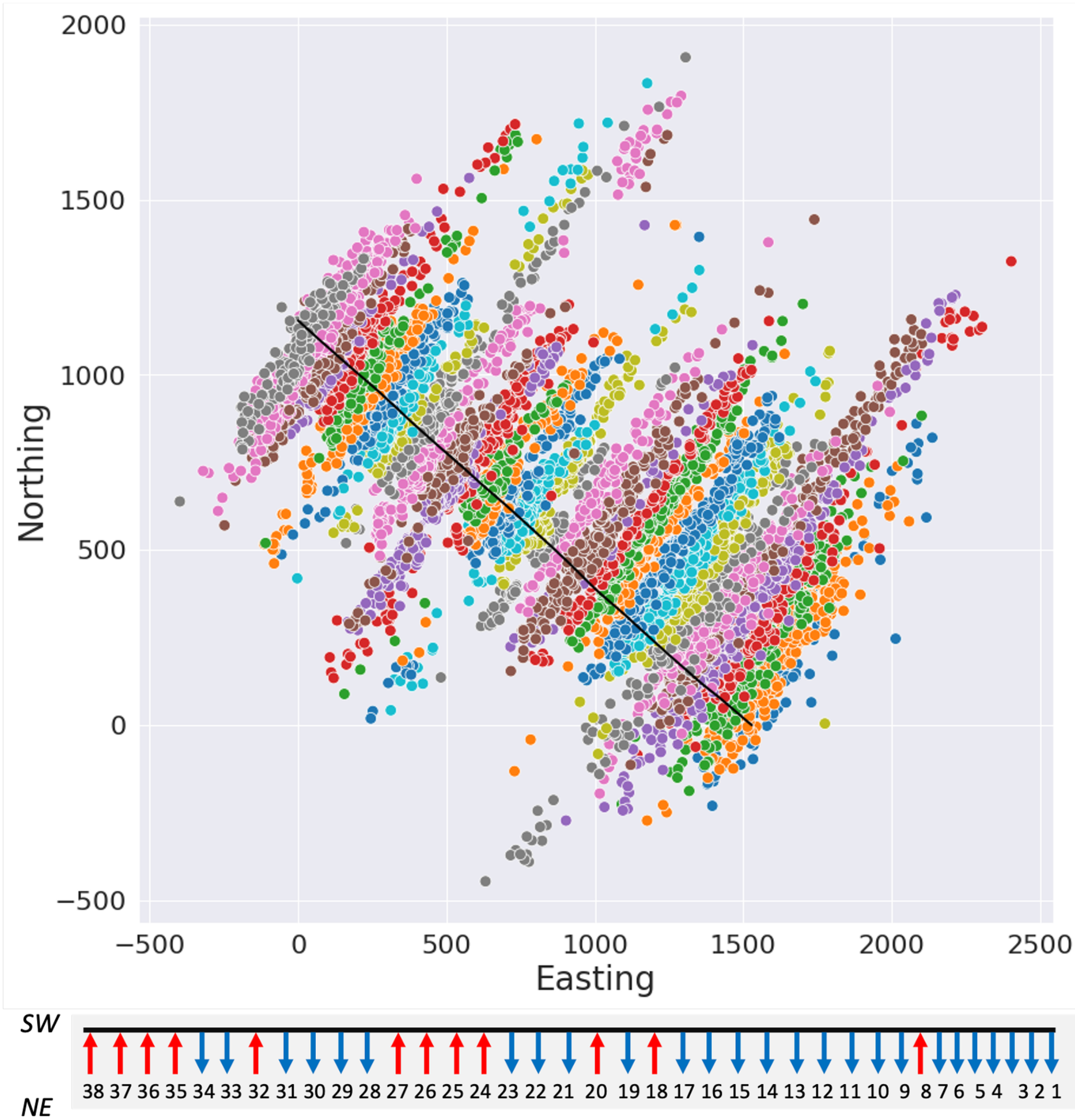

Figure 4.8: Overview of Microseismic Clouds: Arrows depict propagation trends. Blue denotes northeast movement, red indicates SW. Predominantly, propagation is northeastward. Up to stage 17, most events move toward the northeast direction, but after stage 17, the event direction changes, exhibiting a cyclic pattern where stages with predominantly northeast movement are followed by stages moving in the opposite direction.

This calculation serves as an input parameter for Chapter 3 and also functions as a validation method for stress analysis in Chapter 7. The observed heights predominantly fall within the range of 150 to 160 meters, showcasing variations from as low

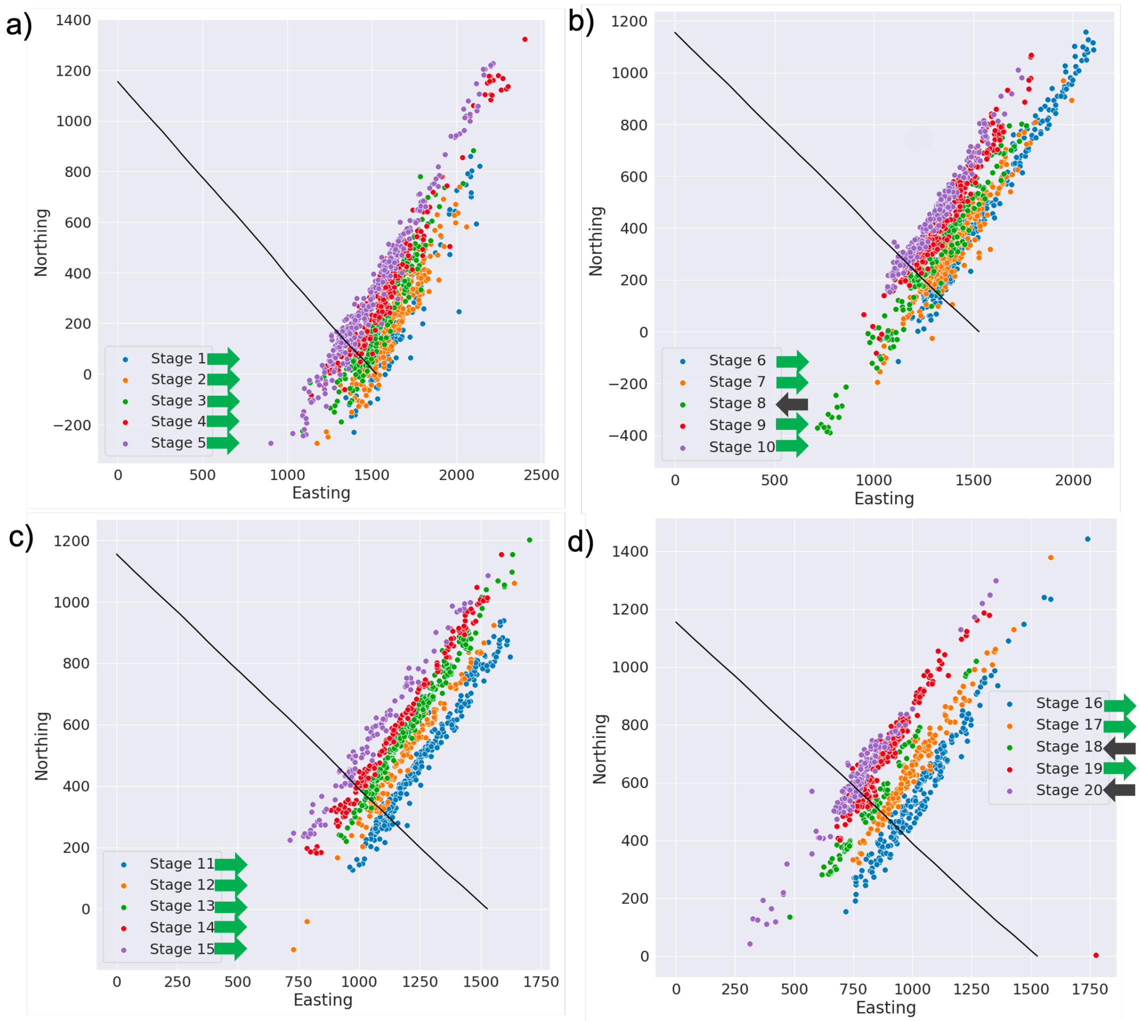

Figure 4.9: Planar view of the microseismic clouds for: (a) Stages 1-5; (b) Stages 6-10; (c) Stages 11-15; (d) Stages 15-20. The arrows represent the direction of propagation, green is NE while gray is SW. Stage 5 and 10 show arching (propagation of events) toward the subsequent stage.

as 128 meters to as high as 205 meters, culminating in an average height of 162.8 meters.

The fluctuation in fracture heights shows a repeating pattern across stages, possibly linked to the stress shadow effect. This elevated stress impedes the subsequent stage from propagating further. Another factor affecting heights could be the well's landing formation or changes in lithology and mineralogy. Changes in the well's position within the bedding boundaries may lead to different stress distributions, influencing

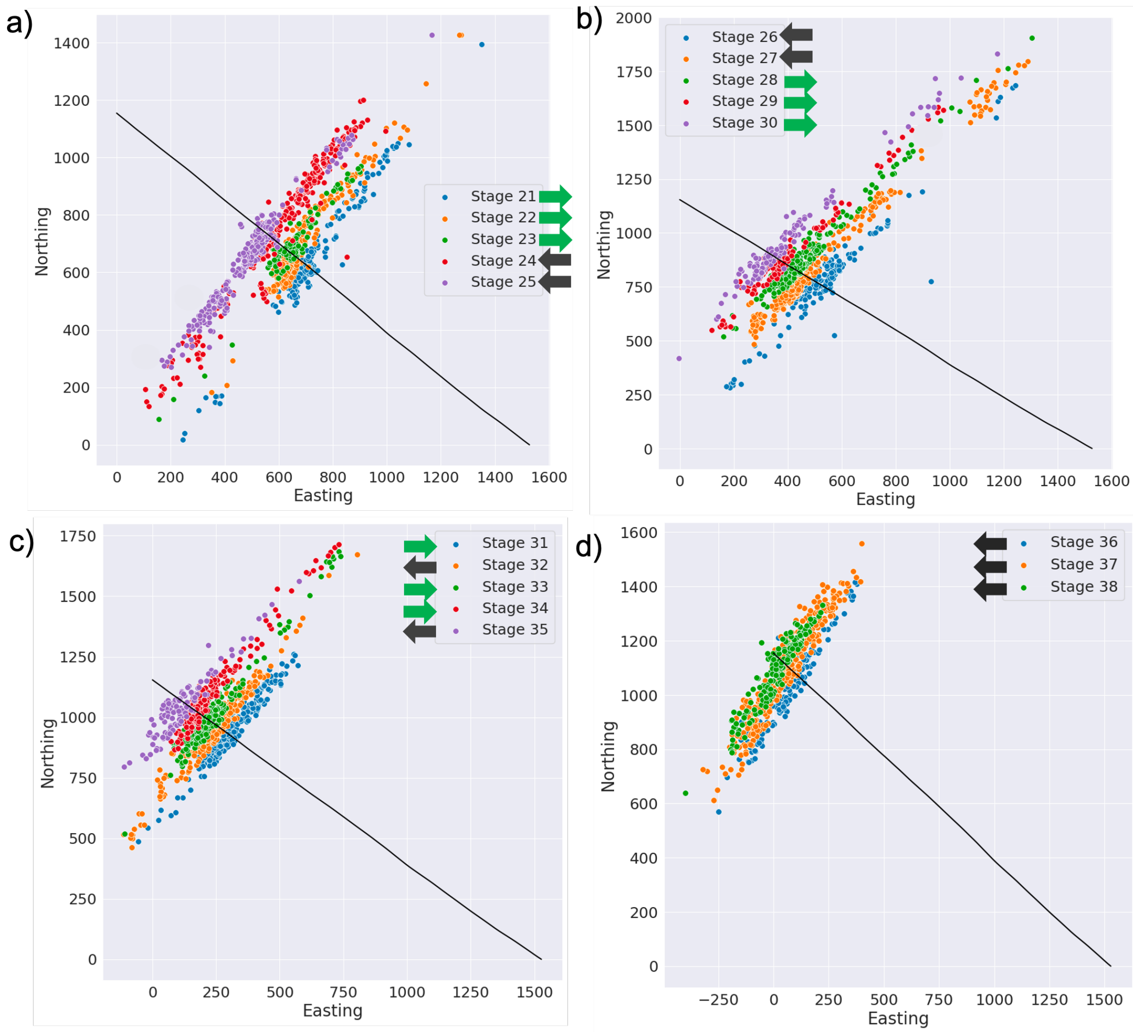

Figure 4.10: Planar view of the microseismic clouds for: (a) Stages 21-25; (b) Stages 26-30; (c) Stages 31-35; (d) Stages 35-38. The arrows represent the direction of propagation, green is NE while gray is SW. Stage 30 and 35 show arching (propagation of events) toward the subsequent stage.

how fractures propagate. These aspects will be explored further in Chapter 5.

Cloud Length

The schematic in Figure 4.13 illustrates wells using blue and red lines to depict fracture lengths corresponding to the microseismic cloud's dimensions. These results closely resemble the findings presented by Ortega Perez (2022), supplemented by additional calculations of the SW wing of the fracture cloud length.

There's a noticeable difference in lengths between the NE and SW wings of frac-

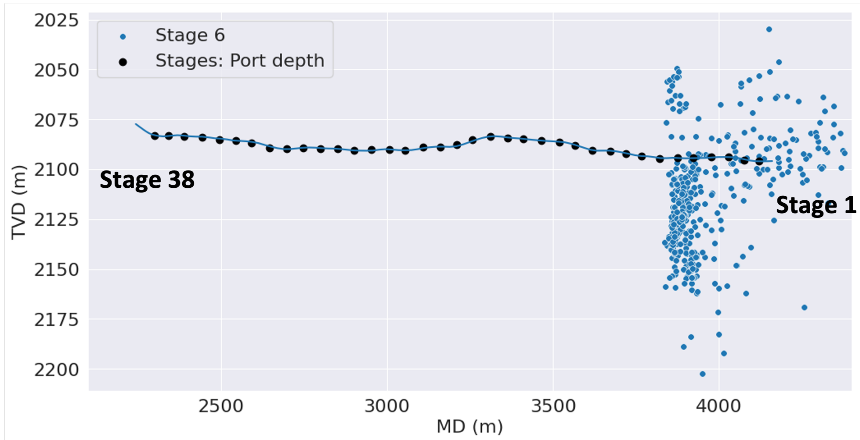

(a) Stage 6,

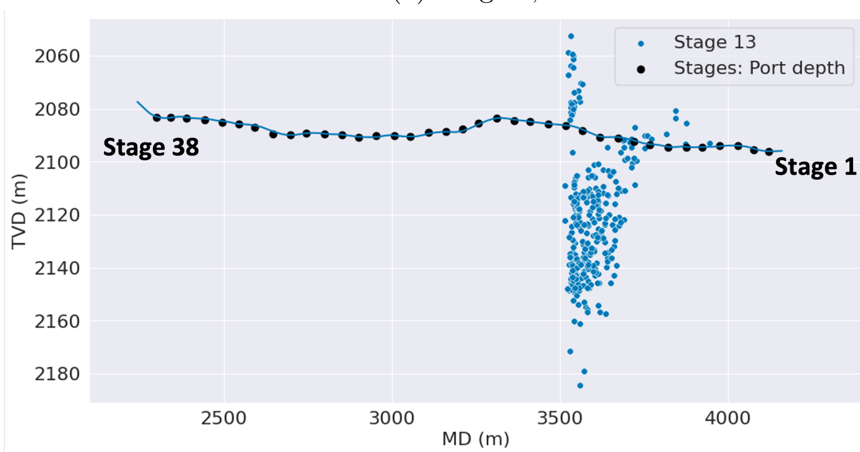

(b) Stage 13,

Figure 4.11: True Vertical Depth (TVD) vs. Measured Depth (MD) plot for (a) Stage 6; (b) Stage 13. Black dots represent the port depth of stages for 38 stages. The black line depicts the well trajectory, with Stage 1 starting from the toe of the well and Stage 38 located at the heel of the well. The events from both stage is moving toward the previous stage.

tures. According to Ortega Perez (2022), after extensive propagation in the northeast direction, multiple fractures develop longer southwest wings due to the stress shadow effect. Fractures adapt to less stressed and less saturated conditions in the SW direction. Chapter 7 will delve deeper into exploring and analyzing these specifics.

A noticeable trend emerges in the fracture lengths: the earlier stages, especially up to Stage 17, exhibit longer northeast fractures. As we progress to later stages, the length of northeast fractures decreases. Conversely, SW fractures have notably

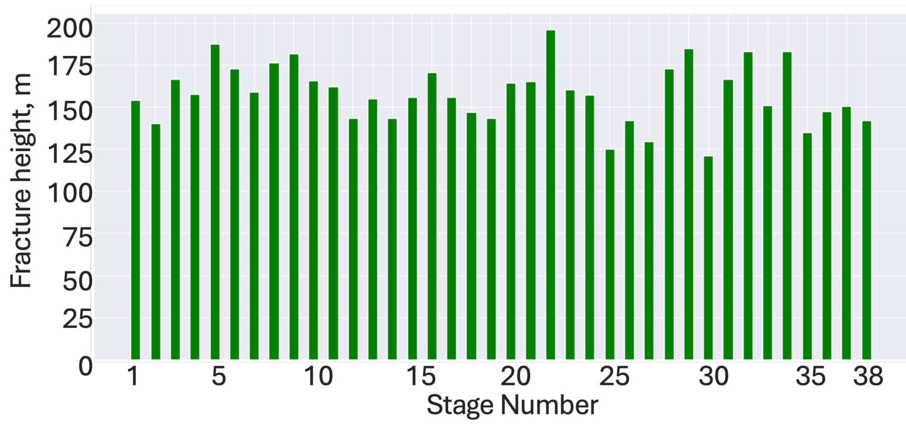

Figure 4.12: Graph that shows the measured height (after magnitude threshold and reclassification) for all microseismic clouds which represents the fracture height for every stage. The cloud height over the stages exhibits a cyclic pattern of increase and decrease. The average height is 162.8 meters.

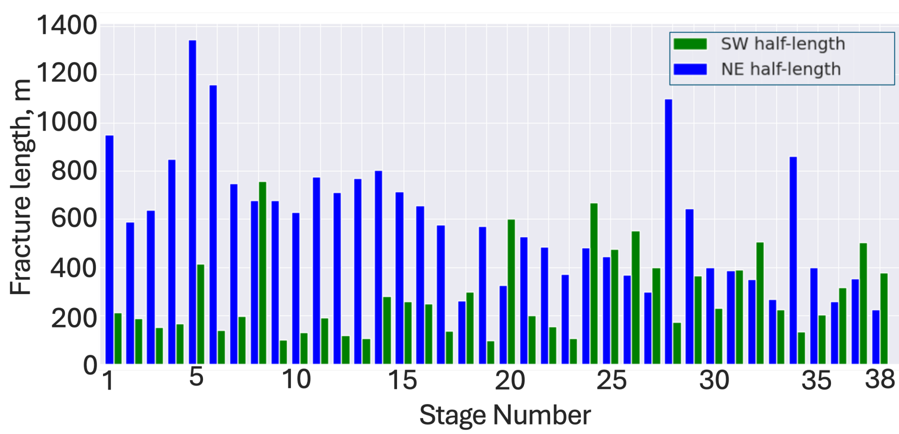

Figure 4.13: Graph that shows the measured length for all microseismic clouds which represents the fracture length for every stage. The NE wing of the fracture represented by blue, while SW wing is represented by green. In the first 17 stages, NE fractures are long, while later stages show relatively shorter lengths. Conversely, SW fractures start short and become longer after stage 18. Overall, early stages predominantly show NE propagation, while later stages exhibit longer SW fractures compared to NE.

smaller lengths in the initial stages compared to northeast fractures, but their lengths become similar in the later stages. Variations in fracture parameters, geological features, or the specific well landing position could play a significant role in shaping the propagation characteristics of these fractures. A thorough discussion of these details is reserved for Chapter 5.

4.4.4 R-T plot

In this section, we present various MS stages to illustrate the general pattern of microseismic cloud propagation throughout the stages. To comprehend the spread of fractures on both sides of the well, we have categorized the microseismic events into northeast and SW events, as depicted in Figures 4.14, 4.15, and 4.16.

Figure 4.14 illustrates the r-t plot of Stage 11. This stage serves as an example where microseismic events develop in a ”normal” pattern on the northeast side of the well, with events moving away monotonically from the treated well, following a parabolic trend. While the r-t plots of most stages exhibit this ”normal” pattern, they also demonstrate more ”reactivation” and ”halted-growth” patterns than observed in this particular example. In Stage 11, there is a predominance of northeast-propagating microseismicity (right). SW events (left) mostly occur at the beginning of the injection with a ”normal” pattern and close to the treated well (within 200 meters). From the middle of the stage, the SW side exhibits halted growth. This indicates that the fracture ceased propagating on the SW side fairly early during injection.

Figure 4.15 depicts the r-t plot of Stage 6, revealing a distinct ”reactivation” pattern on its northeast side. This observation aligns with our previous cloud analysis, which indicated a movement towards the preceding stage (Figure 4.11). Given that Stages 5 and 7 also exhibit reactivation patterns, it suggests the possibility of fluid infiltration into pre-existing fractures or faults, subsequently reactivating them multiple times. This inference is in line with the conclusions drawn by Ortega Perez (2022). Moreover, a similar behavior is observed for Stages 11, 12, 13, and 14, where the r-t plots and event progression indicate repeated reactivation of the same fracture. Conversely, on the SW side, the fracture displays a ”halted-growth” pattern, as illustrated in Figure 4.16a. Despite event generation, there is no noticeable increase

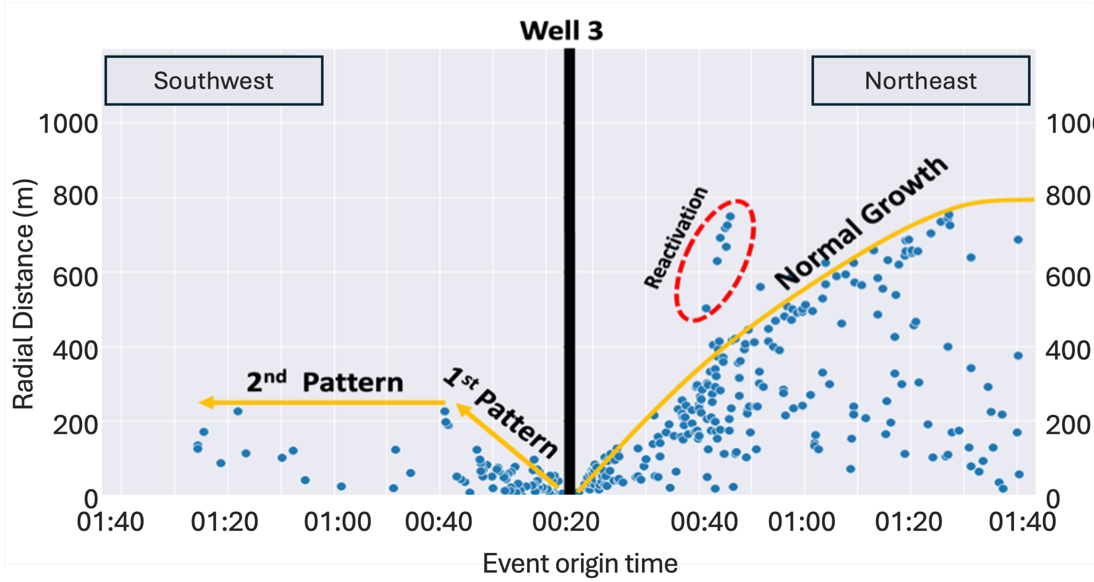

Figure 4.14: Stage 11: The black line depicts the wellbore, with the left side representing the SW and the right side representing the NE. On the NE side, a "normal" pattern is observed with a "reactivation" pattern (red ellipse), while the SW side exhibits two distinct patterns: "Normal" pattern and "Halted-growth".

in fracture length over the pumping period.

Figure 4.16 illustrates stages 13 and 24. In stage 13, the SW wing of the fracture demonstrates "Halted-growth," as evidenced by no increase in its length (Figure 4.16a). Notably, in stage 13, the r-t plot exhibits sequential fracture growth in the northeast direction, indicated by an orange arrow. This pattern aligns with the recognized characteristic of "reactivation." However, without the "Reactivation" pattern, two distinct diffusion patterns emerge, a phenomenon consistent across both stages 13 and 24. The first pattern, represented by arrows on both sides, signifies the "Normal" linear growth pattern. Subsequently, the advancement of the fracture tip halts, with events ceasing to move away from the injection point, resembling the "Halted-growth" pattern observed in both stages 13 and 24 (Figure 4.16a). In stage 24, the growth on the SW side of the well outpaces that on the northeast side.

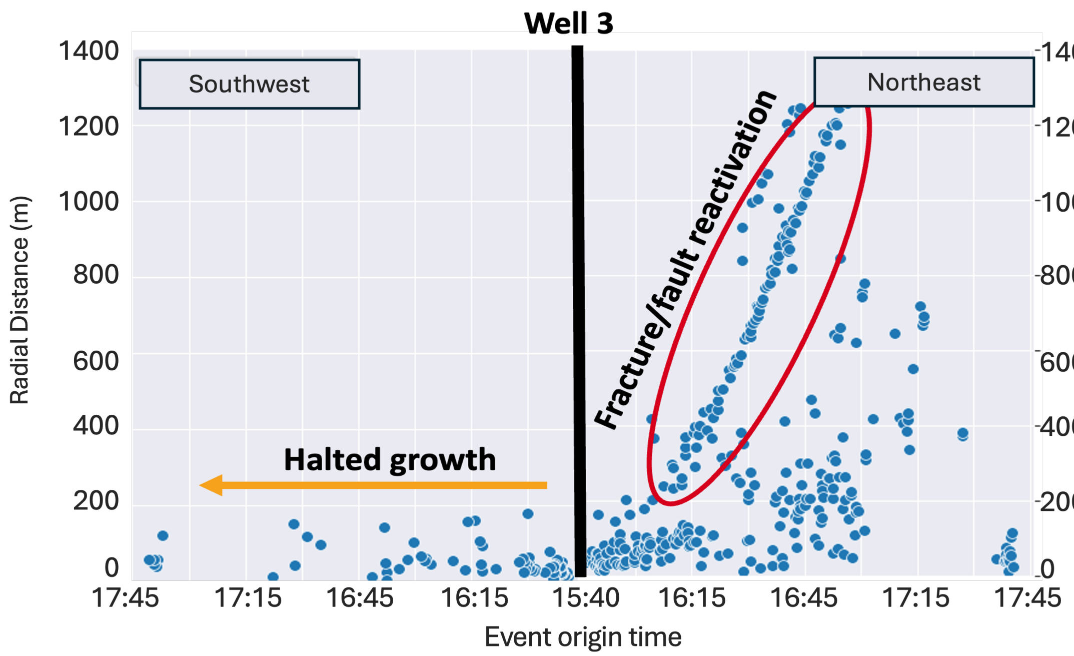

Figure 4.15: Stage 6: The black line depicts the wellbore, with the left side representing the SW and the right side representing the NE. On the NE side, a linearly developed "Reactivation" pattern is observed, while the SW side exhibits "Halted-growth" patterns as there is no increase in the fracture radial length.

4.4.5 Regimes

We employed a physics-based methodology to elucidate the fracturing regime at various stages of hydraulic fracture treatment. This approach, as introduced by Nustes Andrade and van der Baan (2021), involved fitting the model equation 4.5 to different stages to analyze cloud growth as a function of time. By doing so, we aim to understand whether the fracture regime is primarily influenced by storage or leak-off mechanisms by gaining insights into pore pressure diffusion dynamics. To ensure the accuracy of our analysis, we excluded post-pumping events (reclassified from previous stages) from our dataset.

Initially, we partitioned the dataset into time intervals, each spanning an 10-minute window. Within these segments, we computed the 90th percentile of the radial distance of microseismic events within an expanding time window (Figure 4.17a). Setting the percentile value at this level ensures the inclusion of the majority of microseismic-

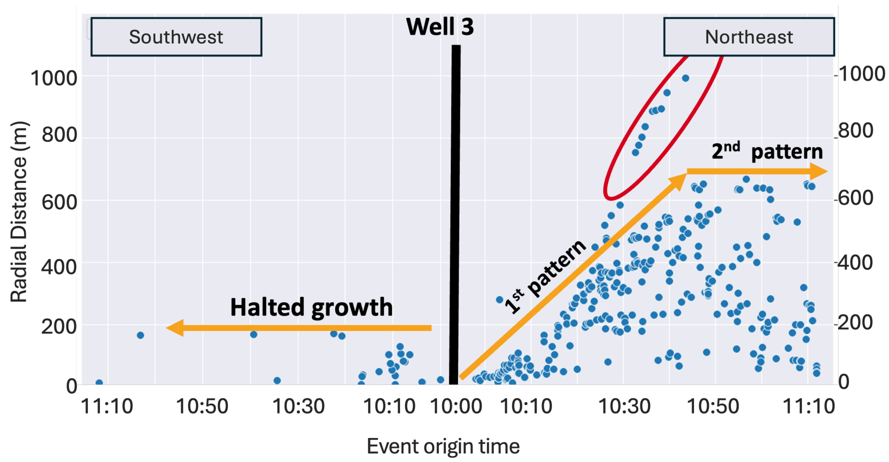

(a) Stage 13: On the northeast side, three distinct patterns are evident: "Normal propagation" (1st pattern), "Halted-growth" (2nd pattern), and "Reactivation" (highlighted by the red ellipse), with a "normal" pattern observed in the radial-time (r-t) plots. Conversely, the SW side demonstrates "Halted-growth" patter only.

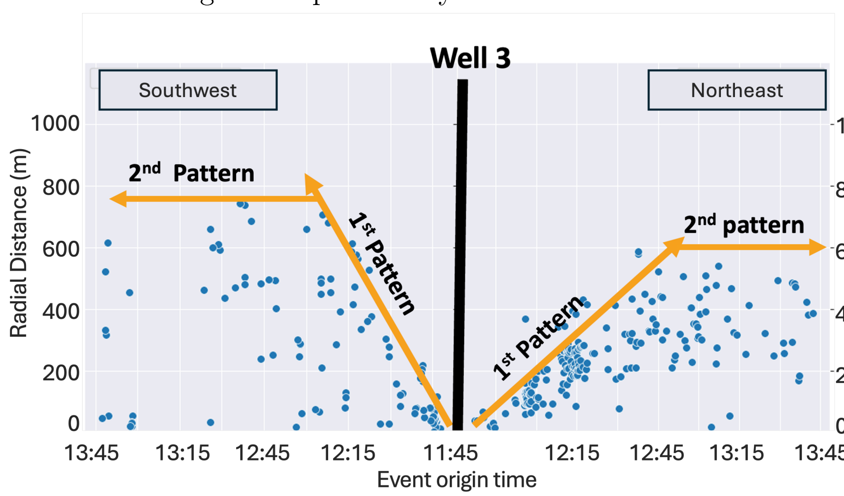

(b) Stage 24: Both side exhibits two distinct distinct patterns: "Normal propagation" (1st pattern), "Halted-growth" (2nd pattern).

Figure 4.16: Illustration of r-t plots and plan view of stages: (a) 13, (b) 24. The black line represents the wellbore, with the left side indicating the SW and the right side indicating the NE. Stage 13 shows two different patterns for each NE and SW wing, while Stage 24 represents reactivation on one side and "Halted-Growth" on the other.

ity over time, while mitigating the influence of distant events that could potentially inflate microseismic cloud sizes. Additionally, this approach minimizes the impact of uncertainties in event locations on growth rate estimates. Moreover, it helps to eliminate the effect of fracture reactivation for some stages (Figure 4.17a). Notably, our earlier analysis revealed distinct spatial distributions of events across different stages, with variations in percentile values yielding negligible changes.

In our effort to characterize the hydraulic fracturing regimes, we aimed to establish the relationship between hydraulic fracture length and the time exponent (β_t). To do this, we utilized equation 4.4 and applied it at various time intervals, increasing by 10 minutes from the onset of event propagation. The results of this fitting process are depicted in Figure 4.17b for stage 13, where each fitted curve is represented by a solid line, with distinct colors indicating different time intervals. Additionally, dashed lines delineate the predicted fracture length at the conclusion of the hydraulic fracturing process. Importantly, the behavior of fracture propagation evolves over time. No single fit consistently captures the entirety of the propagation process, underscoring the inherently dynamic nature of hydraulic fracture growth.

We applied this to all 38 stages. Lets closely examine how this method worked exploring the different type of observations we discussed in section 4.4.4. In general we found out that most of the stages has different pattern of growth, therefore it is normal that most of stages has different hydraulic fracturing regimes.

Figure 4.18 provides a visual representation of the evolution of fracture length during stage 13, where reactivation was ignored using the 90th percentile method (Figure 4.17a). It's evident that both sides exhibit distinct patterns: the northeast side displays a normal pattern with halted growth for last 20 mins, while the SW side experiences halted growth mostly. The results of fitting in Figure 4.18 depict the time exponent (β_t) for both the northeast (blue) and SW (green) sides of the fracture. Initially, the southwest wing of the fracture conforms to the KGD model ($\eta \rightarrow 1$), indicating a storage-dominated regime during the initiation of the fracture. Subsequently, a steep decrease in the time exponent (β_t) is observed, signifying a transition into a leak-off dominated regime. Conversely, the northeast side exhibits a "Normal" fracture pattern, indicating a storage-dominated regime (with PKN and

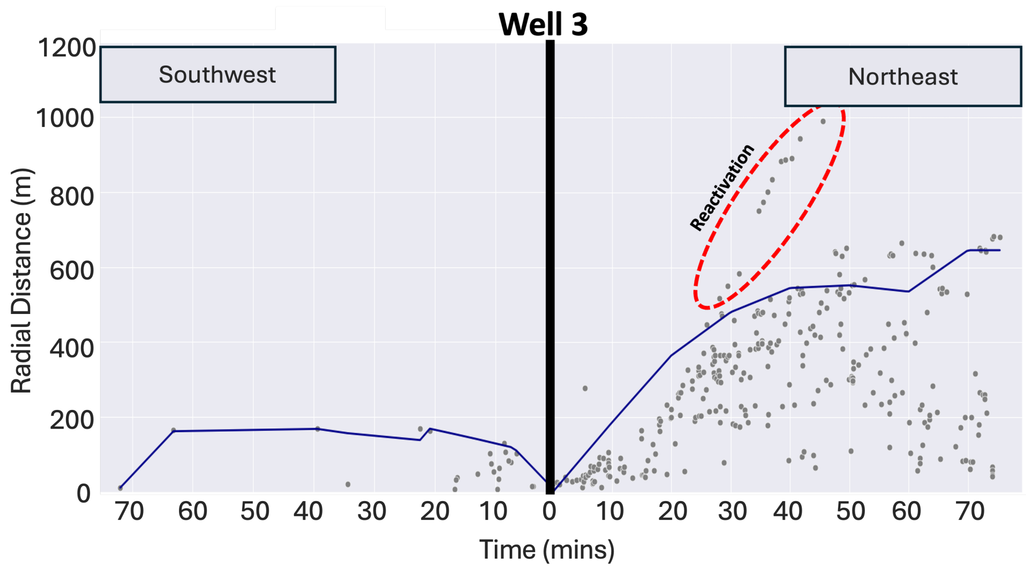

(a) Stage 13 radial-time (r-t) plots showing the 90th percentile calculated every 10 minutes to depict the shape of the microseismic cloud. The red ellipse represents the "reactivation" pattern, which is not captured by the 90th percentile method.

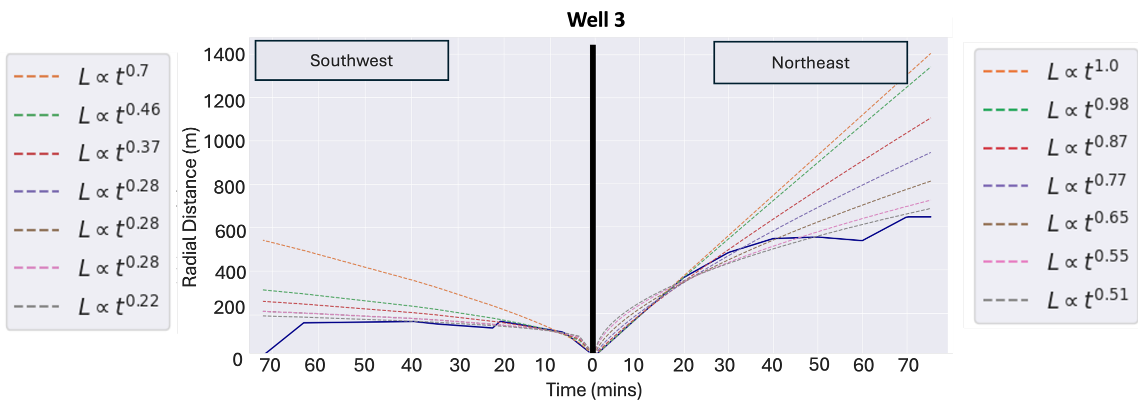

(b) Curve fitting applied over the 90th percentile data representing the microseismic cloud shape. Each color corresponds to a 10-minute interval of the data. Legends represents the time exponent values for each time grid.

Figure 4.17: The black line represents the wellbore, with the left side indicating the SW and the right side indicating the northeast. The Y-axis depicts the radial distance from the injection point, while the X-axis denotes the time of event occurrence. (a) Radial-time plots with the 90th percentile applied, (b) Radial-time plots with equation fits. The color codes indicate the estimated Time Dependency Exponent (β_t) at different period of Hydraulic Fracure (HF) stage.

KGD ($\eta \rightarrow 1$)). Towards the end of the stage, due to pore pressure diffusion, the dominant regime transitions to leak-off. Stage 13 illustrates the progression of stages in both scenarios of halted growth and normal patterns, taking into account cases where the "reactivation" pattern is excluded through the application of percentile filtering.

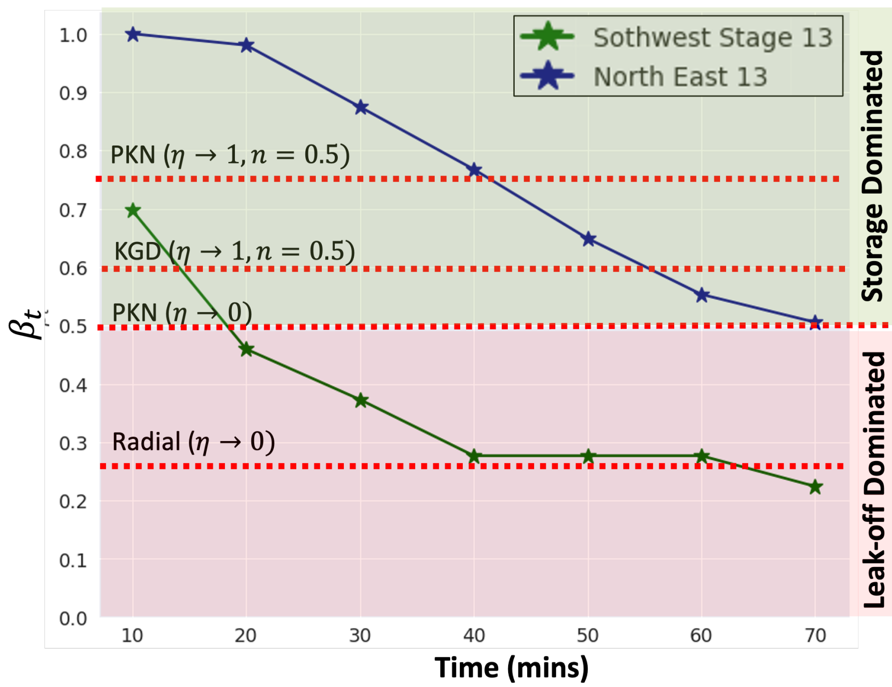

Figure 4.18: Evolution of the Time Dependency Exponent (β_t). The blue line depicts the time exponent for the northeast side, while the green line represents the time exponent for the southwest side of the well. Each color corresponds to different regimes: red for leak-off regimes (PKN with $\eta \rightarrow 0$ and Radial), and green for storage-dominated regime (PKN and KGD with $\eta \rightarrow 1$). The northeast side predominantly exhibits a storage-dominated regime, whereas the southwest side corresponds to both storage and leak-off dominated regimes.

Figure 4.19 illustrates a stage where the north side exhibits a "Normal" pattern exclusively, while the southwest side displays "Halted-growth." Notably, the 90th percentile value successfully represents the cloud shape in this scenario. The results of fitting are presented in Figure 4.19b. On the southern part of the well, we observe characteristics of PKN and KGD ($\eta \rightarrow 1$), despite minimal growth in cloud size. However, there is a noticeable transition to a leak-off dominated regime during the later period of cloud propagation. Conversely, the northern side of the well also exhibits features consistent with PKN and KGD ($\eta \rightarrow 1$). This outcome closely resembles the stage where two patterns were evident. This similarity arises because, in later stages, fracture propagation is not as pronounced as during the initiation, primarily due to pore pressure diffusion. However, the magnitude of this effect is smaller than for stages where "Halted-growth" occurs during the last period of the stage.

In cases where the reactivation pattern persists despite the percentile filtering, as depicted in Figure 4.20, characterizing the regime using Table 4.1 becomes challenging. The 90th percentile method, as shown in Figure 4.20a, proves ineffective in removing this pattern. Consequently, the time dependency exponent, β_t, exceeds 1 due to the rapid growth of the radial length of the fractures. Hence, when β surpasses 1, it signifies fracture reactivation. Conversely, southwest cloud, the predominant regime is leak-off, as evidenced by the time dependency exponent β_t falling below 0.5.

4.5 MS Behaviour for each stage

Figure 4.21 and 4.22 illustrates the stages of MS, displaying various propagation patterns in r-t plots (Figure 4.21) and fracture treatment regimes (Figure 4.22). The arrows signify the trend in HF treatment propagation. In Figure 4.21, fracture patterns are depicted in r-t plots: "Normal" (red circle), "Reactivation" (purple circular ring), and "Halted-growth" (yellow rhombus). Figure 4.22 employs the same shapes to represent different meanings: "Reactivation" (β_t as purple circular ring), PKN ($\eta \rightarrow 1$) as yellow square or red circle, and Radial flow as green square or blue triangle. If a stage displays more than one dominant pattern, corresponding shapes are used starting from HF treatment in chronological order.

The analysis of r-t plots reveals distinct patterns for each stage on both northeast and southwest sides of the well (Figure 4.21). On the northeast side, "Reactivation" and "Normal" patterns dominate, indicating fluid passage through pre-existing fractures. The blue bracket represents the stages where the "Reactivation" of pre-existing

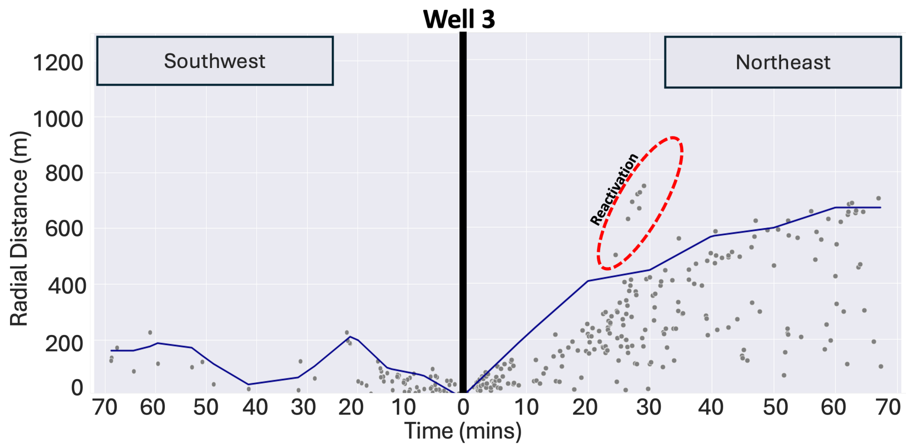

(a) Stage 11: r-t plots showing the 90th percentile calculated every 10 minutes to depict the shape of the microseismic cloud. The red ellipse represents the "reactivation" pattern, which is not captured by the 90th percentile method.

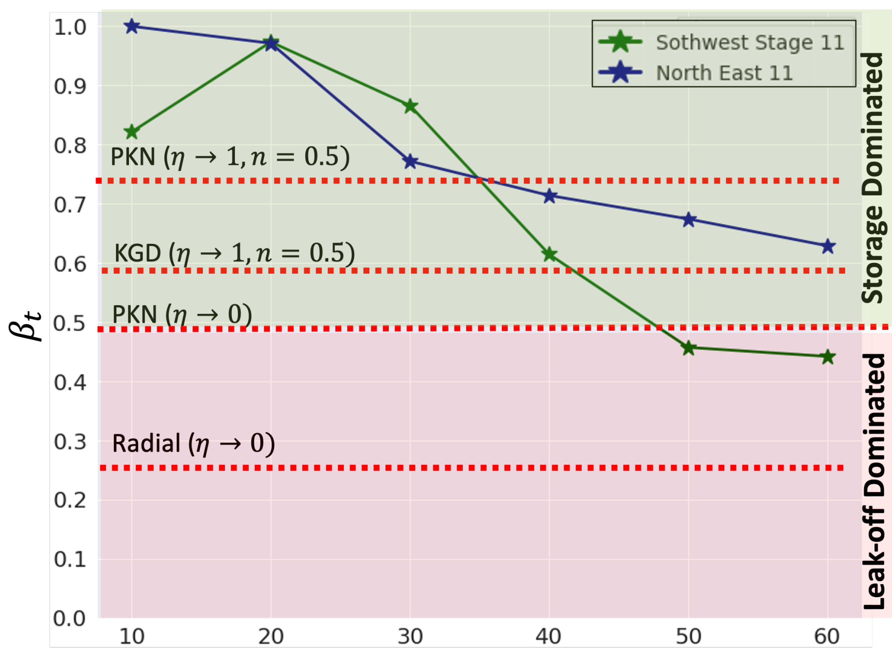

(b) Evolution of Time Dependency Exponent (β_t) in Stage 11. Blue line: northeast side, green line: southwest side. Red indicates leak-off regimes (PKN with $\eta \to 0$ and Radial), green for storage-dominated regime (PKN and KGD with $\eta \to 1$). Northeast: mostly storage-dominated; southwest: both storage and leak-off dominated regimes.

Figure 4.19: Stage 11. (a) 90th percetile representing cloud shape, (b) Evolution of the Time Dependency Exponent (β_t).

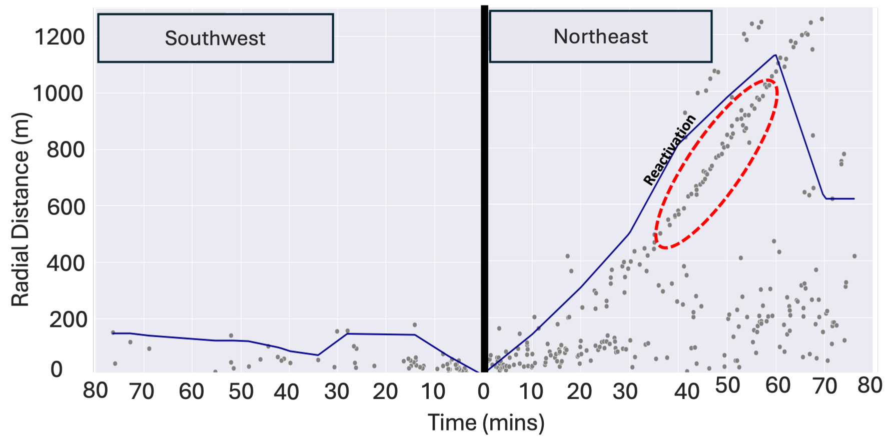

(a) Radial-time (r-t) plots showing the 90th percentile calculated every 10 minutes to depict the shape of the microseismic cloud including "re-activation" pattern.

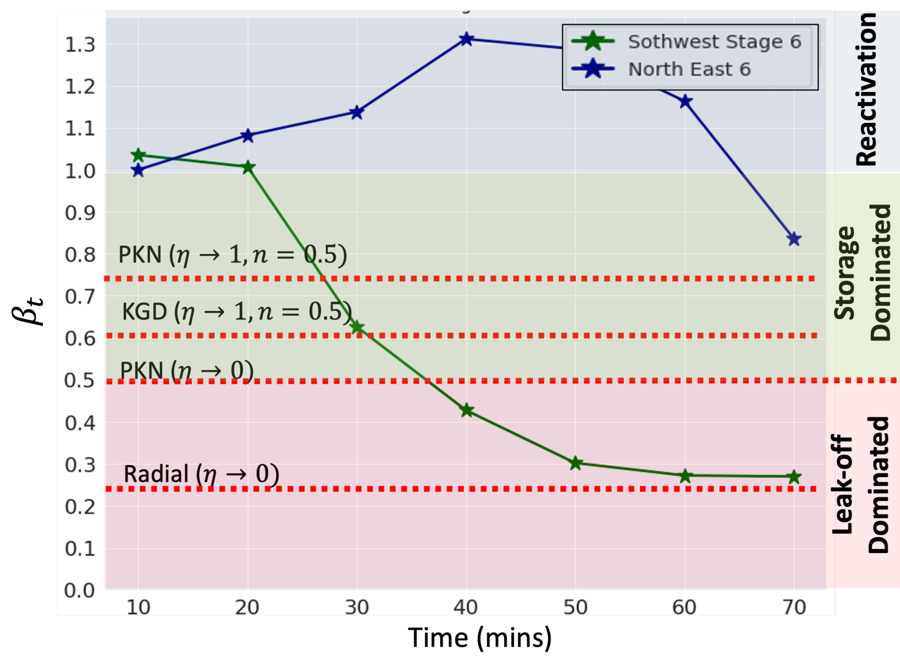

(b) Evolution of Time Dependency Exponent (β_t) in Stage 6. Blue line: northeast side, green line: southwest side. Red indicates leak-off regimes (PKN with $\eta \to 0$ and Radial), green for storage-dominated regime (PKN and KGD with $\eta \to 1$), and blue for "Reactivation" ($\beta_t > 1$). Northeast: $\beta_t > 1$ due to "reactivation" pattern in r-t plot. southwest: both storage and leak-off dominated regimes.

Figure 4.20: Stage 6. (a) 90th percetile representing cloud shape, (b) Evolution of the Time Dependency Exponent (β_t).

fractures happened for the same fracture. Instances of multiple patterns in a stage often denote halted growth towards the stage's end. Overall, "Reactivation" prevails, sometimes alongside "halted-growth", consistent with findings by Ortega Perez (2022). Discrepancies arise, particularly for the southwest side, attributed to differences in workflow, such as magnitude thresholding and event reclassification. On the southwest side, "Halted-growth" and "Normal" patterns are dominant. Instances of "Reactivation" are observed in select stages, correlating with southwest propagation.

Figure 4.22 delineates regimes for all stages based on physics, revealing varied hydraulic treatment regimes between the sides of the well. Both sides display storage-dominated and leak-off-dominated regimes, with occurrences of solely storage-dominated regimes being rare. Some stages, notably 1, 3, 9, 11, and 28, exhibit time-dependency exponent, β_t, greater than 1, indicating rapid length evolution due to the fracture reactivation. The northeast side predominantly displays PKN regime, transitioning to PKN ($\eta \rightarrow 0$) later, reflecting longer lengths. Conversely, the southwest side typically starts with KGD regime, followed by leak-of-dominated, PKN ($\eta \rightarrow 1$), and Radial regimes. In cases where propagation occurs in the southwest direction, we were unable to identify consistent patterns or regimes.

4.6 MS vs PKN

To evaluate treatment effectiveness, we meticulously compared the lengths of microseismic events' northeast (NE) and southwest (SW) wings with the anticipated half-length according to the Perkins-Kern-Nordgren (PKN) model (Figure 4.23). Our analysis uncovered significant disparities in fracture lengths, notably pronounced in the SW wing, which demonstrated a considerable shortfall compared to the PKN model. Similarly, the NE wing exhibited substantial differences, indicating an overall overestimation of fracture lengths by the simplistic PKN model. These findings echo the insights of Ortega Perez (2022), who anticipated such discrepancies owing to the PKN model excluding some critical parameters like leak-off. Additionally, our

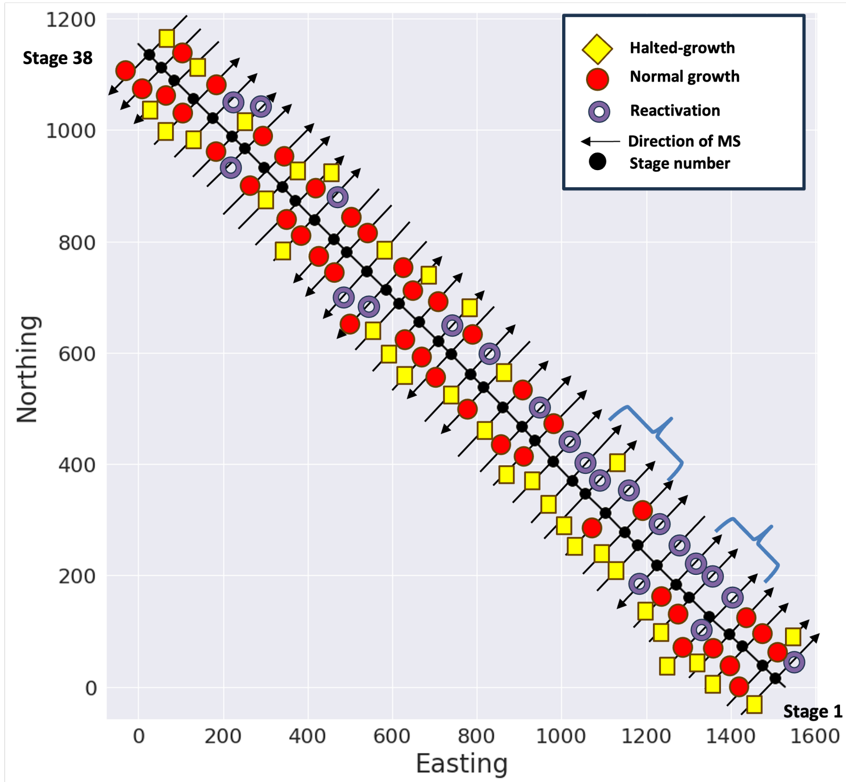

Figure 4.21: Overview of microseismic (MS) observations across stages, depicting propagation patterns in radial-time (r-t) plots: "Normal" (red circle), "Reactivation" (purple circular ring), and "Halted-growth" (yellow rhombus). Black arrows indicate HF treatment propagation trend. The bracket highlights stages where we suspect the reactivation of the same pre-existing fractures. The order of the symbols away from the well indicates relative time in each stage. The NE side is mostly characterized by "Reactivation" and "Normal" patterns, while the SW side is mostly characterized by the "Normal" and 'Halted-growth" patterns.

physics-based approach revealed that most stages encompassed more than one regime.

In contrast, both initial and later stages displayed relatively smaller discrepancies, particularly evident in the NE wing. Despite these differences, the NE side consistently showcased similarities, with both NE wing results and the PKN model indicating longer fracture half-lengths during initial stages (from 1 to 15). Conversely, during later stages (from 26 to 38), both the PKN model and NE microseismic events suggested relatively smaller fracture lengths. Notably, during intermediate stages (specifically, from stage 15 to 25), disparities between observed and modeled lengths intensified. This escalation can be attributed to complications in completions during

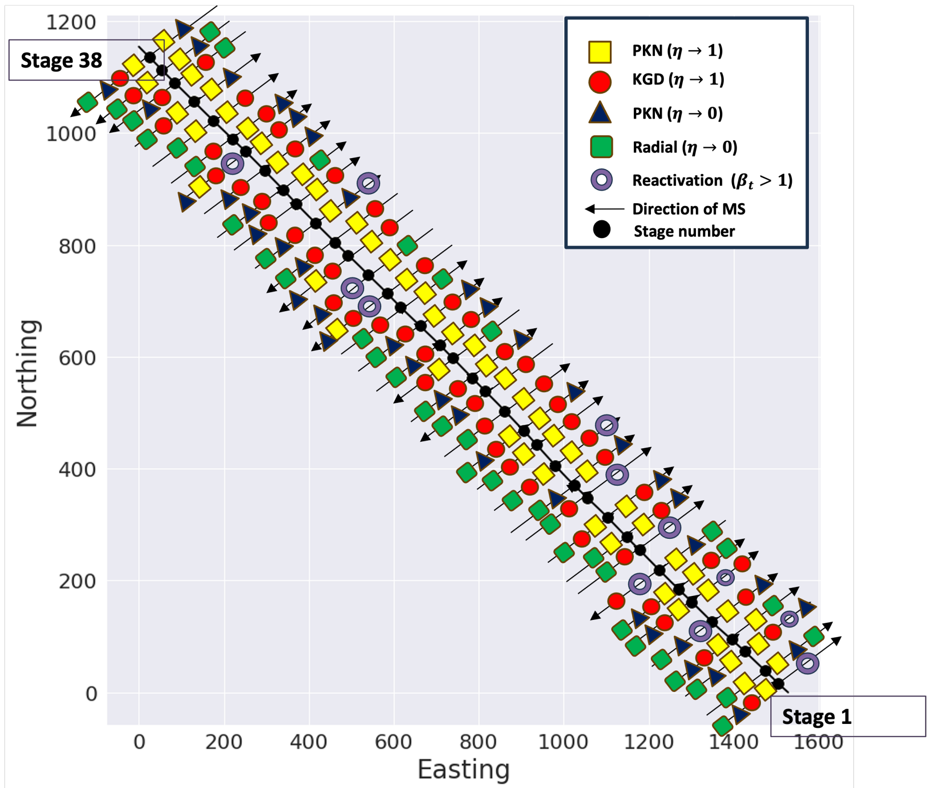

Figure 4.22: Overview of hydraulic fracture (HF) treatment regimes: "Reactivation" (β_t shown as purple circular rings), PKN ($\eta \to 1$) represented by yellow squares or red circles, and Radial flow denoted by green squares or blue triangles. Black arrows indicate HF treatment propagation trend. The blue brackets indicate the stages during which the "Reactivation" of pre-existing fractures occurred for the same fracture. The NE side is mostly characterized by the PKN and KGD regimes, while the SW side is mostly characterized by the KGD and Radial regimes.

these stages and prolonged treatment periods, as underscored by Ortega Perez (2022).

Conversely, the southwest side exhibited a distinct lack of similarities. Here, while the NE side displayed an increase in fracture length, the southwest side showcased a decrease, and vice versa. This disparity underscores the intricate and variable nature of fracture propagation across different sections of the well. We will investigate potential causes for the asymmetric growth predominantly towards the NE in chapter 6, using reflection seismic data.

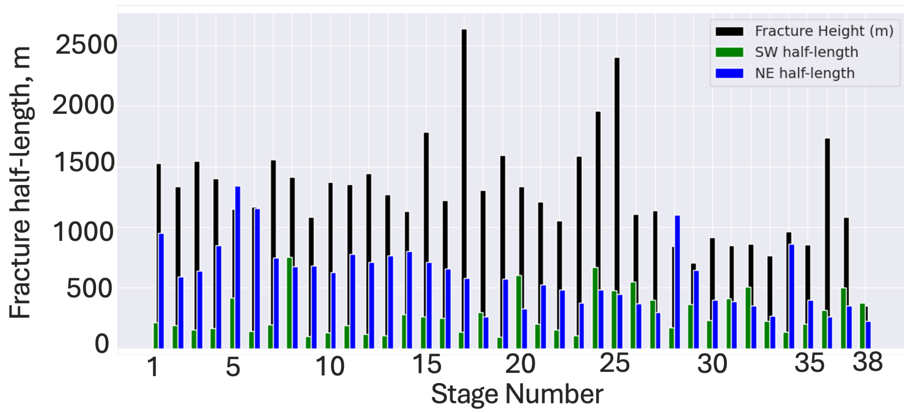

Figure 4.23: PKN fracture half-lengths at injection completion (black) and microseismic cloud lengths for NE (blue) and SW (red) shown side by side. Significant discrepancies between PKN and MS results are apparent, especially for the middle stages (17-26). The initial and later stages show correlation with NE half fracture length.

4.7 Conclusions

In this chapter, an analysis of the microseismicity generated during the hydraulic fracturing treatment was conducted to estimate the dimensions and propagation of hydraulic fractures during injection. The initial segment of this chapter closely mirrors the findings of Ortega Perez (2022). While the interpretation aligns closely with the previous study, our primary objective is to comprehend the unidirectional propagation and change in the fracture length from stage to stage.

Firstly, we initially applied a magnitude threshold to assess the impact of the distance between treatment and monitoring wells. However, solely considering this distance does not entirely explain the directional behavior observed in microseismic clouds. To address this, we employed both magnitude thresholding and a reclassification method to mitigate the influence of microseismic events' tails. Some disparities arose in cloud analysis compared to the findings of Ortega Perez (2022) due to differing methodologies, such as our utilization of magnitude thresholds and reclassification methods adapted from Nustes Andrade and van der Baan (2021). Nonetheless, the over trend in cloud propagation remains consistent. Our analysis unveiled dynamic changes in fracture height and length across stages, primarily showcasing a north-eastward movement of events.

Examining r-t plots revealed distinct propagation regimes, notably "normal" and "reactivation," underscoring the intricate nature of fracture dynamics. The north-east side predominantly exhibited "Reactivation" and "Normal" patterns, while the southwest side typically displayed "Normal" and "Halted-Growth" patterns. In rare cases, "Reactivation" occurred in the southwest, suggesting longer fracture lengths in this direction due to pre-existing fractures influencing the results.

Furthermore, a physics-based approach elucidated varying treatment regimes across stages. The northeast side primarily exhibited PKN and KGD regimes, whereas the southwest side showcased predominantly KGD and Leak-off dominated regimes (PKN ($\eta \rightarrow 0$) and Radial regime). This complexity suggests that no single mechanism can fully explain fracture propagation.

Comparing PKN half-length results from a previous chapter with microseismic data provided insights into the effects of fracture treatment. While the northeast region exhibited a similar pattern to PKN, the southwest region showed no correlation. This discrepancy implies that treatment parameters, particularly duration, influenced propagation, albeit not as the sole determinant.

While this study offers valuable insights, further analysis is imperative to comprehensively grasp fracture propagation intricacies.

Chapter 5

Petrophysical Analysis

5.1 Summary

Hydraulic fracturing operations in unconventional reservoirs are significantly influenced by small-scale geological features surrounding the wellbore, such as natural fractures and bedding plane changes. Understanding the intricate effects of these features on fracture propagation is essential for optimizing hydraulic fracturing strategies and enhancing reservoir performance.

In this chapter, we focus on analyzing the influence of small-scale geological features and bedding changes on hydraulic fracture propagation within the Montney Formation. Our methodology involves examining basic well logs, including gamma ray, resistivity, and neutron/density porosities, to detect variations in formation properties along the lateral section of the well. Additionally, Formation Microimager (FMI) logs are utilized to identify natural fractures and bedding plane alterations near the wellbore.

Our findings reveal valuable insights into the impact of these small-scale features on hydraulic fracture propagation. We identify discernible shifts in formation properties, indicating potential changes in horizons, and confirm the presence of natural fractures and bedding plane alterations surrounding the wellbore through FMI logs analysis.

By employing straightforward techniques, we determine that the well is drilled between two middle Montney members, providing explanations for observed variations in fracture propagation. Furthermore, our analysis establishes a correlation between identified natural fractures and microseismic data, highlighting their influence on fracture propagation, particularly the impact of conductive fractures on microseismic events.

5.2 Background

Canada's primary petroleum-producing region is the Western Canada Sedimentary Basin (WCSB). Historically, prior to 2010, the WCSB witnessed a prevalence of vertical well drilling activities over horizontal ones. The emphasis was on targeting mature, conventional oil and gas fields within the basin using vertical wells. However, a shift occurred around 2006 when the drilling of vertical wells declined, giving way to an increasing preference for horizontal wells. This transition was driven by the need to access oil and natural gas in tighter rock formations (CER, 2023).

As of 2010, horizontal well drilling has become the dominant activity, constituting the majority of drilling operations in the WCSB (CER, 2023). The primary objective behind drilling horizontal wells is to optimize the contact between the wellbore and the intended reservoir rock, aiming to extract the maximum volume of resources. Despite this shift, there exists a lag in our understanding of horizontal well log interpretation compared to the rapid pace of drilling these wells. This part of the study specifically addresses the challenges associated with well log interpretation, with a focus on horizontal and highly deviated wells.

In the case of vertical wells, the logging tools are deployed at a right angle to the bedding planes. They gather data about the type of rock, the fluids in the rock, and any other fluids that might be present. These same factors impact the log readings when dealing with deviated and horizontal wells. However, in instances where a horizontal well is drilled within a thin layer or closely adjacent to a surrounding bed, the log responses may be significantly influenced by the neighboring beds, as noted by Ghosh (2022) and Singer (1992). Hence, comprehending the impact of bedding planes on the logs is crucial.

One primary function of image logs is to gain insights into subsurface bedding features in the absence of available cores. Another significant application, especially within unconventional shales and tight formations, is the visualization of natural fractures. The challenge arises when attempting to image horizontal and highly deviated logs using wireline tools, primarily due to issues related to tool eccentricity and the complexity of tool movement.

5.2.1 Definitions some geological phenomena

In this chapter, frequent reference will be made to the geological phenomena illustrated in Figure 5.1. To enhance comprehension, we will provide explanations for some key geological concepts based on the definitions from Dang (2008).

Dip Angle: The angle between the horizontal plane and a bedding plane. A horizontal bed has a dip of 0°, while a vertical bed has a dip of 90°.

Dip Azimuth: The angle between geographic north and the direction of the greatest slope on a bedding plane. Dip azimuth is measured clockwise from North.

Strike: The line formed by the intersection of a horizontal plane and an inclined surface.

Bedding: Three-dimensional surface that is either planar, nearly planar, wavy, or curved. This surface is observable and serves to distinguish each consecutive bed, whether of the same or different lithology, from the beds that precede or follow it.

5.2.2 Tool working principles

Formation evaluation through well logging techniques is pivotal in assessing subsurface geological formations and properties. In this section, we delve into the utilization and significance of two fundamental logging methods: the Formation Micro Imager (FMI) logs and the Triple Combo Logs encompassing gamma ray, resistivity, and density/neutron porosity measurements.

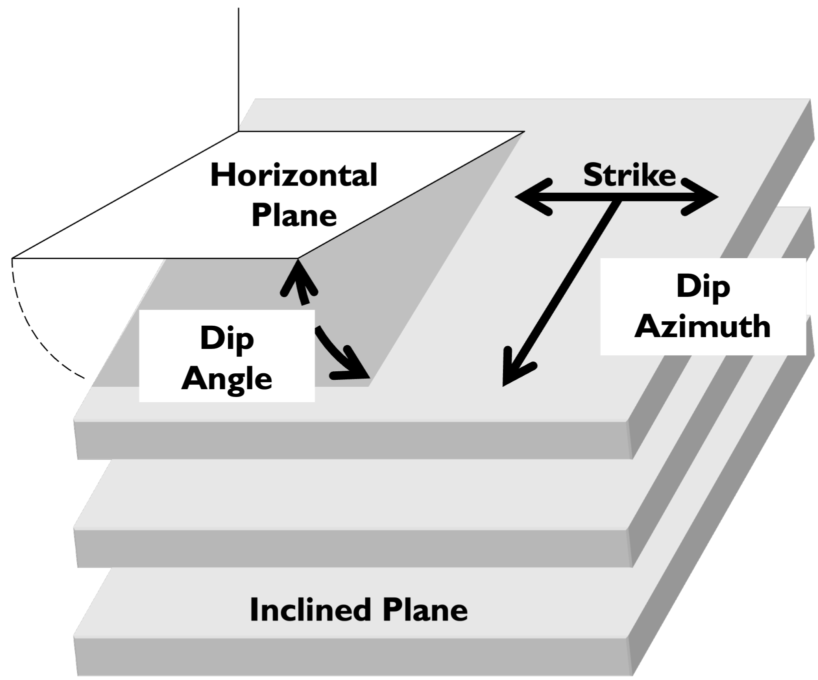

Figure 5.1: Strike and dip representation of inclined sedimentary planes/beds. The dip angle, denoting the angle between the horizontal plane and the inclined surface, is illustrated. The strike and dip azimuth are indicated by a two-sided arrow and a single-sided arrow, respectively (generated in accordance to Dang (2008)).

Triple Combo logs

In industry Triple Combo logs refer to the wireline logging where all gamma ray, resistivity, and Porosity (Neutron and Density) logs are deployed.

Gamma ray (GR) logs: The gamma-ray log operates as a passive tool, detecting natural radioactive emissions in American Petroleum Institute (API) units from rocks to discern their lithology. While all rocks emit some radiation, shales exhibit a higher propensity for this phenomenon. Consequently, the gamma-ray log aids in distinguishing between shale and non-shale zones. The primary sources of natural radioactivity include radioactive isotopes like potassium-40 (K40), uranium, and thorium. The level of radioactivity is also influenced by factors such as the rock's age and deposition type. The age of the rock plays a crucial role, with older rocks emitting less radiation. Generally, clay minerals contain a higher concentration of radioactive elements.

In the Montney Formation, the gamma ray response is typically high, suggesting a clay-rich formation. However, recent studies conducted in horizontal wells using drill cuttings have revealed that the gamma ray response in the Montney Formation is predominantly influenced by the presence of K-feldspar and mica, rather than organic matter and clay (Becerra et al., 2021; Krause et al., 2011). Therefore, when interpreting high gamma rays, we also consider the possibility of K-feldspar presence rather than clay-rich formation. Since we don't have any drill-cutting analysis available, we don't completely disregard the possibility of clay-rich formation.

Porosity Tools: Neutron Porosity and Density Porosity Tools

As depicted in Ellis et al. (2003), a typical compensated neutron porosity tool comprises a neutron source (Americium-Beryllium (Am-Be)) and two detectors positioned a few tens of centimeters along the tool's axis (Figure 5.2a). This tool serves to measure porosity due to its heightened sensitivity to hydrogen (H). This sensitivity arises from two key factors: hydrogen efficiently moderates or reduces the energy of source neutrons, and only moderated or low-energy neutrons are effectively detected. Given that hydrogen in the formation is often present in the form of hydrocarbons or water, predominantly occupying pore spaces, a clear correlation with formation porosity can be established (Ellis et al., 2003; Gilchrist, 2008).

Density porosity tools function by emitting medium-energy gamma rays into the wall of a borehole (refer to Figure 5.2b). These gamma rays undergo interactions with electrons within the formation, leading to energy loss and scattering through successive collisions. The frequency of these collisions corresponds to the electron density, which represents the number of electrons per unit volume. In typical minerals and fluids found in oil and gas wells, this electron density is directly proportional to the bulk density, denoted as ρ_{bul}. The tool measures the bulk density, which is influenced by both the fluid (porosity) and the rock (matrix). Subsequently, this measured bulk density is employed to compute density porosity (Ellis, 2003; Smithson, 2015).

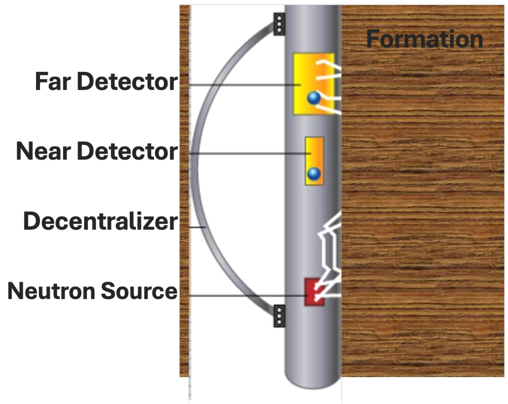

(a) Simplified Neutron Tool (DSNT) featuring a decentralized tool to obtain a better contact with formation (modified from Ellis et al. (2003)).

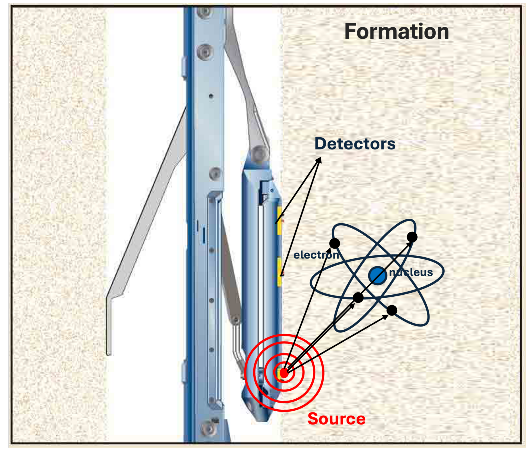

(b) Simplified Density Tool (SDLT) illustration with open pads pushing the tools towards the formation wall (modified from Smithson (2015).

Figure 5.2: Illustration of simplified Density/Neutron porosity tools. (a) the Neutron Tool with a bow string; (b) the Density Tool with open pads. Both tools demonstrate the scenario where the tool was pushed toward the formation wall (modified from Ellis et al. (2003) and Smithson (2015)).

Induction Tools

Induction tools accurately measure True Formation Resistivity (Rt) by reading formation properties at multiple distances, providing insights into changes in resistivity within the formation. This information proves valuable in investigating mud filtration and identifying fluid-bearing formations (Halliburton, 2005). These tools employ a

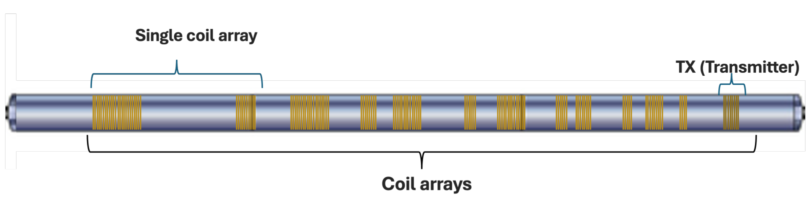

Figure 5.3: Simplified induction tool, illustrating asymmetric receiver pairs and a single transmitter coil based on Halliburton tools (generated in accordance to Halliburton (2005)).

single transmitter (TX) operating at different frequencies to generate magnetic fields, with coils wrapped around a fiberglass structure (light green) (Figure 5.3). Voltages are measured using six receiver coil arrays, yielding six elemental conductivity measurements. These measurements represent depths of investigation determined by the respective coil's transmitter-to-receiver spacing (Halliburton, 2005).

The application of alternating current to the wire coil (TX) creates a magnetic field in the surrounding environment, inducing current flow inversely proportional to formation resistivity. This current, in turn, generates a second magnetic field in the formation, intersecting an array of receiver coils and inducing voltage in each coil (Halliburton, 2005).

Image logs

Borehole image logs consist of electronic representations capturing the resistivity changes within the borehole wall. These images depict variations in resistivity among rocks and fluids, as well as the disparities in resistivity levels across different layers or structural elements intersecting the borehole. The contrast in resistivity is visually depicted through a color spectrum, where darker shades signify lower resistivity readings and brighter hues denote higher resistivity values. Formation resistivity, influenced by factors such as shale content, lithology, and fluid presence within pores and fractures, plays a pivotal role in determining these variations (Grace & Newberry, 1998).

The borehole image logs utilized in this study were obtained using the Compact oil-base microimager tool from Weatherford (Figure 5.4). This open hole logging tool provides microresistivity measurements and is employed in wells drilled with oil-based muds. The FMI tool comprises eight pads with a total of 72 measurement electrodes, ensuring optimal coverage. The upper calipers centralize the tool, while the lower calipers act independently (Weatherford, 2015).

Formation microresistivity imaging (FMI) techniques follow the basic principles of conventional borehole resistivity methods (Safinya et al., 1991). However, FMI tools have a distinctive approach: they employ multiple millimeter-scale button electrodes arranged on electrically conductive pads, which expand laterally to make contact with the borehole wall. During logging, which proceeds upward, a voltage is applied between the button electrodes and a return electrode positioned in the upper section of the probe. The recorded current magnitude is directly linked to the formation conductivity (or its inverse, resistivity) along the well trajectory (Safinya et al., 1991).

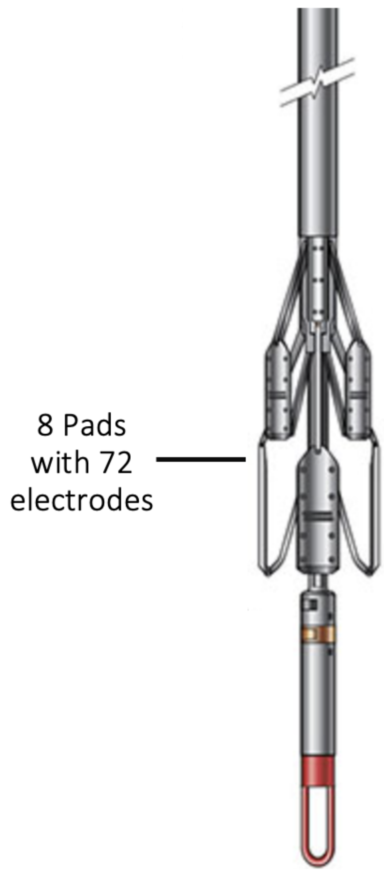

Figure 5.4: Weatherford Compact Oil-Based Mud Sonde Section (Weatherford, 2015).

In 2D borehole images, sinusoidal patterns, resembling waves, depict flat surfaces intersecting a cylindrical borehole (Figure 5.5). This visual representation aids in conceptualizing a 3D borehole within a 2D format. The sinusoid's low apex denotes the azimuth direction, while dip tadpoles in plots, as illustrated in Figure 5.5, portray the dips. These dips are computed using the formula $\tan^{-1}(h/d)$, where h and d represents the amplitude of the sinuosity and diameter of the well, respectively (Wilson, 2021).

In vertical wellbores, the sine wave's height is influenced by the feature's dip magnitude. Steeper planes result in higher amplitude sinusoids, generating lower angles for shallow angle bedding and nearly straight lines for horizontal bedding.

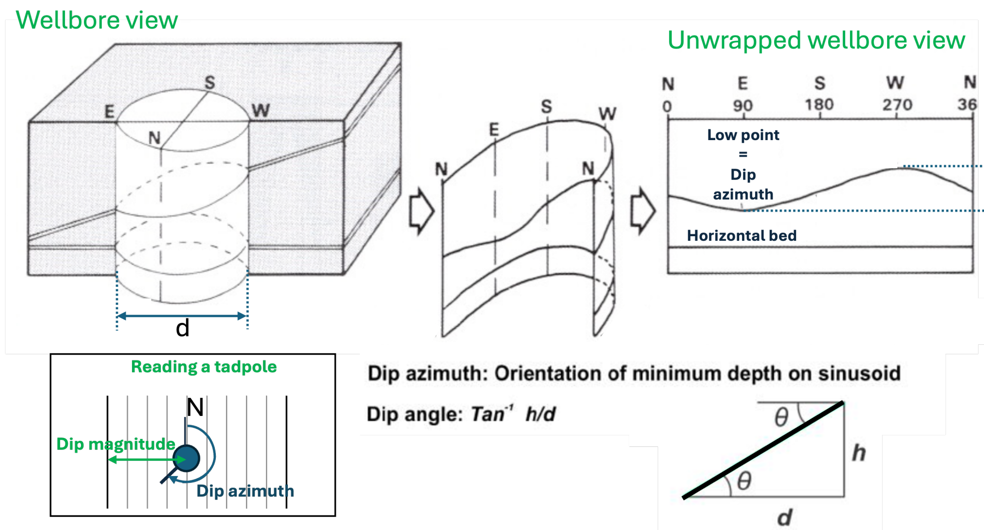

Figure 5.5: Illustration of sinusoidal features on borehole images, depicting surfaces that cross-cut the borehole wall. In the borehole view, the green line crosses the borehole at an angle, while the red line represents the case with a 0-degree angle. When the borehole figure is opened in a 2D plane, the green line represents the sinusoidal line (case with an angle), while the red line is a straight line (0-degree angle case). The dip angle is calculated as $\tan^{-1}(h/d)$, where h is the height and d is the diameter of the wellbore. The azimuth in the figure is represented as a tapole, where the tail direction indicates the dip azimuth with reference to North (using the lowest point in the sinusoidal pattern) (modified from Rider and Martin (2014)).

Image logs: Natural Fractures

Identifying open fractures on image logs is generally straightforward, as drilling fluid or mud tends to infiltrate the fracture openings, creating a thin, highly conductive sheet visibly different from the surrounding rock matrix. This creates modified current lines that differ from those in a homogeneous rock matrix. Open fractures, also known as conductive fractures, can be observed on an FMI image as features with dark color (indicating high conductivity), and intersections with bedding planes. These fractures can be categorized into three types: open natural fractures, drilling-induced fractures, and borehole breakouts (Luthi & Souhaite, 1990; Slim, 2007).

On the log, it's important to distinguish between true dips and apparent dips. Apparent dips are what we get when we calculate dips directly from images, showing the dip relative to the borehole trajectory (Grace & Newberry, 1998). The formula for apparent dip relates the height of the sine wave to the diameter of the borehole, represented as $\tan^{-1}(h/d)$, where h is the height and d is the borehole diameter. Inclinometry data, which includes information about borehole deviation, azimuth, and the orientation of the dipmeter sonde relative to north, helps convert apparent dips into true dips, using the Earth's geographic coordinates at the well site. In an ideally vertical borehole, the apparent dip aligns with the true dip (Grace & Newberry, 1998).

Conductive Natural Fractures: These fractures result from stress regime and tectonic activities, not the drilling process. They typically have a vertical orientation with a dip angle over 75 degrees, appearing planar (Slim, 2007).

Drilling-induced Fractures: The drilling process modifies the stress regime, causing drilling-induced fractures that appear vertical and 180 degrees apart in FMI logs. They are classified as "Drilling-induced Tensile fractures" or "Drilling-induced Shear fractures" (Slim, 2007).

Borehole Breakouts: Identified by caliper logs and FMI logs, borehole breakouts are flat surfaces expanding in the direction of minimum horizontal compression. They occur when the borehole caves in due to localized compressive shear failure (Slim, 2007).

Healed or Resistive Fractures: Unlike open fractures, healed fractures are filled with mineral cement, affecting resistivity measurements on image logs.The resistivity variation across these fractures manifests as a light-colored sinusoidal pattern (Slim, 2007).

Usually, it's easier to see closed (cemented) natural fractures with resistivity image logs because the difference in resistivity between the fracture cement and the rock around it is big. Acoustic logs might not show these fractures well because they don't pick up on the small differences in how well materials conduct sound. But, when it comes to open fractures or breakouts, acoustic logs work better because they can clearly show the difference between the rock around the fracture and the fluid inside it (Ghosh, 2022; Gong et al., 2021).

In our study, we will present the results from the resistivity microimager tool (resistivity tool), as provided by the data-contributing company. Consequently, the identification of cemented fractures is more prominent and easily discernible while the open fractures are challenging to identify due to less resistivity contrast.

5.2.3 Understanding Resistivity and FMI Tool Responses in Horizontal Wells with Bedding Variations

Resistivity logs

In their work, Zhou (2008) introduced a technique to interpret tool responses at various dip angles. They observed distinct "horns" patterns in resistivity logs when dealing with horizontal or highly deviated wells intersecting bed boundaries. The size of these features depends on the angle of intersection. By analyzing the tool response based on apparent dip, they uncovered geometric relationships.

Figure 5.6 illustrates an idealized tool response concerning induction log resistivity attenuation and phase, following a research by Zhou (2008). Attenuation describes the reduction in the amplitude of electromagnetic waves between two receivers, whereas phase shift occurs due to alterations in the peak positions of the waves between receivers (Ghosh, 2022). The model includes a 10 Ω-m layer within a 1 Ω-m host medium, with the true resistivity delineated by the squared red curve labeled as RT.

When the apparent dip is at 0° (perpendicular), neither the magenta curve representing resistivity attenuation (RA) nor the blue curve representing resistivity phase shift (RP) exhibit any discernible horns, as illustrated in Figure 5.6. The red curve represents the true resistivity. However, at an apparent dip of 70°, both the RP (blue curve) and RA (red curve) show prominent horns. As the apparent dip increases to

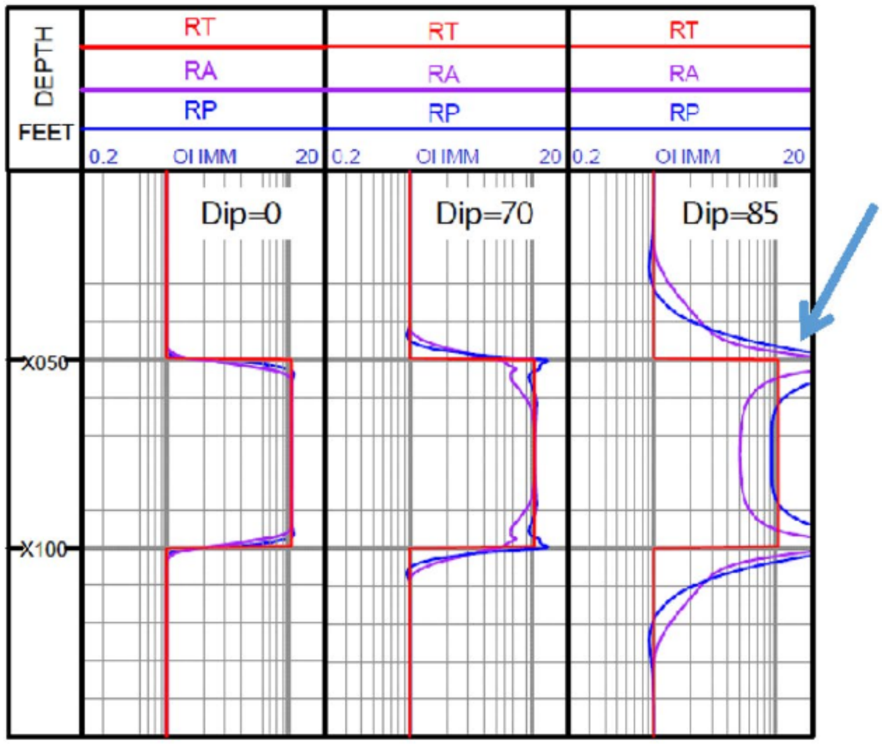

Figure 5.6: Illustration depicting phase (RP) and attenuation (RA) resistivity responses in a three-layer formation model (RT). Modeled logs showcase the tool response dependency on dip angles (0°, 70°, and 85°) across three tracks, as per the three-layer formation model (reproduced from Zhou (2008) with permission from Society of Petroleum Engineers (SPE)).

85° (nearly parallel), the horns in both RA and RP curves become so pronounced that they exceed the scale, indicating their enlargement with higher apparent dips (blue arrow) (Zhou, 2008).

These observations are crucial as the presence of bullhorn patterns indicates changes in bedding. However, in our case, we will utilize these patterns to identify bedding changes rather than calculate or demonstrate the degree of change.

Image logs

This section focuses on the interpretation of natural fractures, bedding planes as well as different features in horizontal wells, emphasizing the need to analyze these features separately.

Bedding Interpretation:

Distinguishing between bedding planes and natural fractures can be challenging because of their similar visual characteristics. However, by observing the continuous, parallel features of bedding planes that represent sedimentary layering, and noting their consistent dip angles and orientations across intervals, one can reliably differentiate them from natural fractures in geological formations.

In vertical wellbores, the amplitude of the sine wave is determined by the dip magnitude of the feature. A steeper plane results in a higher amplitude sinusoid, while shallow-angle bedding produces lower amplitude sinusoids. In the case of horizontal bedding, the sine wave appears almost straight. As the dip angle increases, the sinusoid elongates, and the amplitude of the sine wave increases. Features with truly vertical dips will produce two vertical lines 180° apart (Lofts et al., 1997). To better understand the dipping phenomenon, we can refer to the figure from Lofts et al. (1997) (Figure 5.7), which illustrates that within horizontal wellbores, shallow-dipping features appear as long, drawn-out sinusoids, while vertical features manifest as tight, low-amplitude sinusoids.

According to Ghosh (2022) and Gong et al. (2021), the 'saddle' and "bull-eye" patterns observed in well logs correspond to bedding features. Despite attempts to drill horizontal wells precisely along specific geological horizons, natural variations such as bedding or faults can cause the well to momentarily deviate, resulting in these distinctive visual patterns. This phenomenon is depicted in Figure 5.8, illustrating a pronounced bulls-eye effect caused by changes in the azimuth of the sinusoid as the well intersects the bedding plane.

Natural Fracture Interpretation:

Most natural fractures observed in subsurface environments are typically vertical or inclined at high angles, a phenomenon supported by studies such as those by Ghosh et al. (2018) and Gong et al. (2021). These fractures often bear a striking resemblance to those intersecting vertical wells, as depicted in the illustrative Figure

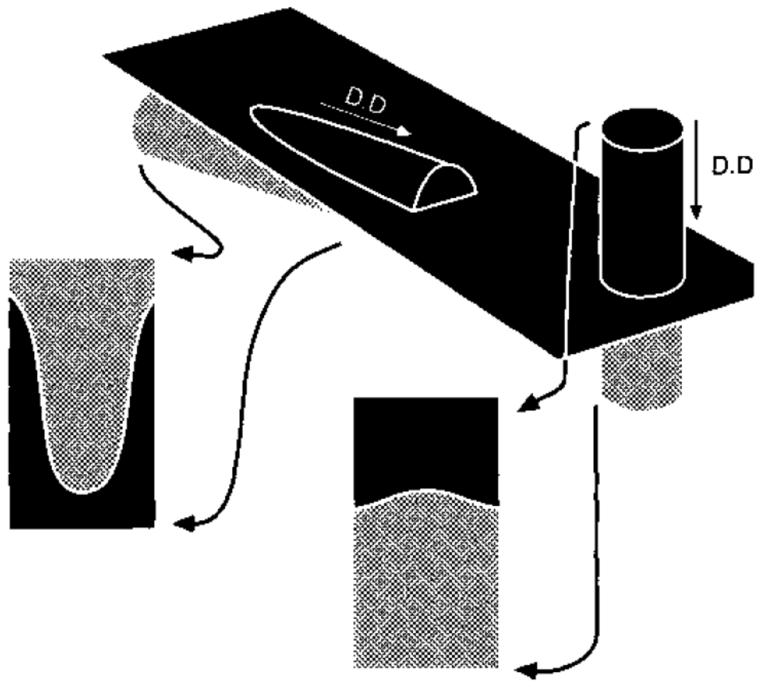

Figure 5.7: Comparison of intersections between a vertical and horizontal wellbore and a shallow-dipping plane. The top right diagram depicts the intersections, while the bottom left shows corresponding FMI images. The horizontal wellbore intersection generates a long, drawn-out, high-amplitude sinusoid, whereas the vertical wellbore intersection forms a tight, low-amplitude sinusoid. DD indicates the drilling direction (reproduced from Lofts et al. (1997) with permission from The Geological Society of London (Lyell Collections)).

5.5. However, to provide a real-world example of how natural fractures appear in the horizontal sections of wells, we turn our attention to Figure 5.9, which showcases resistive fractures in a horizontal well. The left track displays the uninterpreted image data, while the right track showcases the interpreted fractures highlighted with a line (Gong et al., 2021).

Figure 5.9 presents a visual representation of resistive fractures observed in horizontal wells. In cases where fractures intersect fracture planes perpendicularly, the sinusoidal amplitude may register as very low, resulting in fractures appearing as straight lines. Conversely, when fractures intersect beds at low angles, their appear-

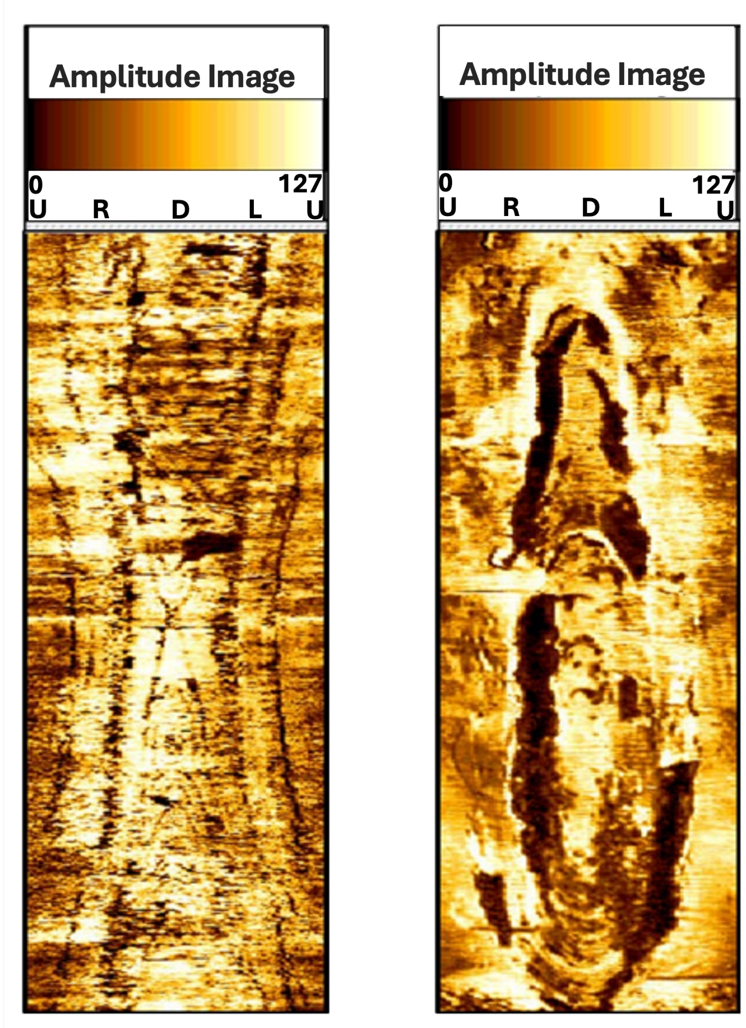

Figure 5.8: "Saddle" and "bull's eye" patterns created by bedding planes in horizontal wells, highlighting the distinct features of these geological formations. The both patters happen due to changes in the azimuth of the sinusoid as the well intersects the bedding plane (reproduced from Ghosh (2022) with permission from Springer Nature).

ance is sinusoidal. This scenario is illustrated in Figure 5.9b, which depicts an open fracture crossing a horizontal well at a low angle (Gong et al., 2021).

Borehole breakouts:

Borehole breakouts are frequently observed in horizontal wells, as illustrated in Figure 5.10 showcasing examples from unconventional plays. Borehole breakouts in horizontal wells differs from that in vertical wells, where they occur due to the dominant in situ horizontal stress direction. In horizontal wells, the dominant stress

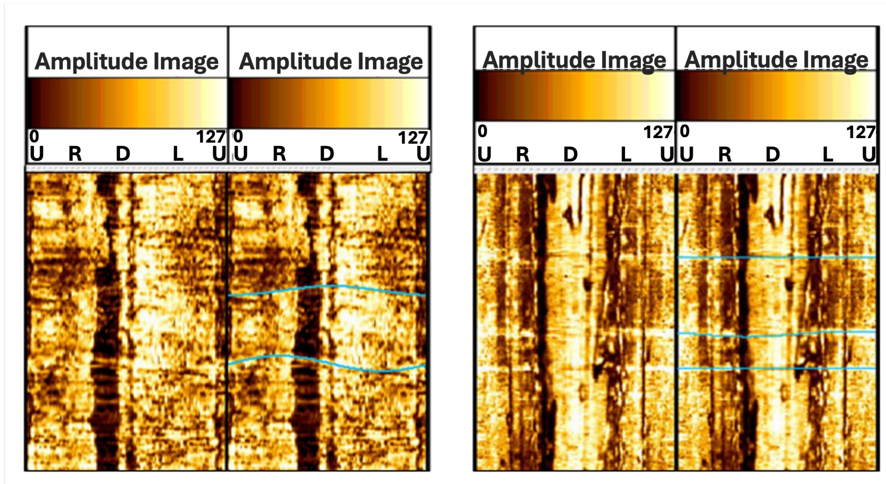

(a) Identifying Closed Fractures in Horizontal Wells: Fractures nearly perpendicular to the wellbore are characterized by a low sinusoidal amplitude. A turquoise line in the interpreted figure delineates the shape and presence of natural fractures.

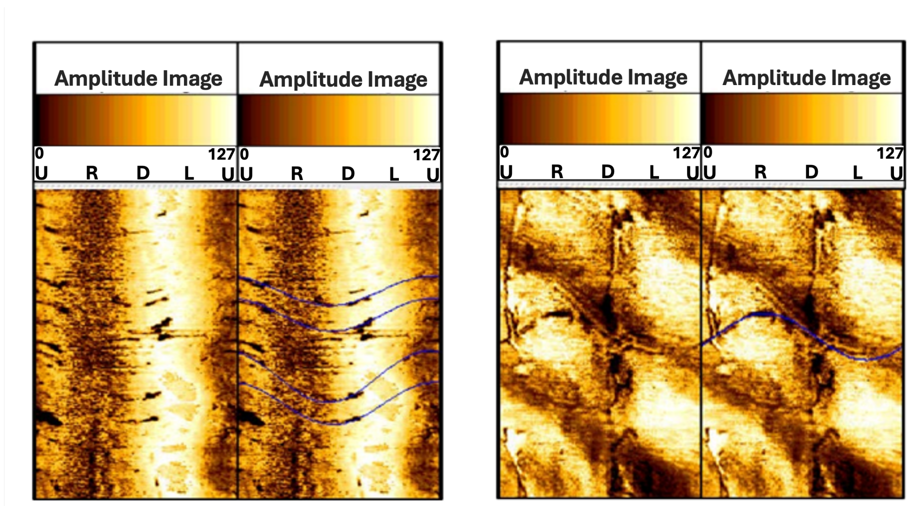

(b) Identifying Open Fractures in Horizontal Wells: Fractures intersecting the wellbore at low angles exhibit a sinusoidal pattern. A black line in the interpreted figure delineates the shape and presence of natural fractures.

Figure 5.9: Detection of fractures in horizontal wells using image logs: (a) a fracture intersecting a horizontal well at a high angle, nearly perpendicular, resulting in a straight line pattern , (b) the fracture intersects the wellbore at a lower angle, creating a sinusoidal shape (reproduced from Gong et al. (2021) with permission from Society of Petroleum Engineers (SPE)).

is vertical (gravity squeezing down on the borehole), resulting in a change in breakout orientation observed at the sides rather than the top and bottom of the borehole. This phenomenon is illustrated in Figure 5.10, where two dark stripes along the image signify conductive mud filling the space created by breakouts at the sides of the borehole.

Logging artifacts:

Various artifacts can occur during logging operations, one being associated with low pad pressure. When the artifact is related to low pad pressure, the logging pass will show blurred sections, indicating a loss of contact between the tool's pad and the borehole (Lofts & Bourke, 1999).

On the other hand, poor contact due to gas between the pad and the formation is another instance. Gas trapped between the tool's buttons and the formation leads to insufficient contact, causing the affected buttons to measure the gas instead of the formation. The high resistivity of the gas results in a distinct bright appearance in the image, as indicated by arrows (Lofts & Bourke, 1999).

5.3 Methods and Procedure

Our petrophysical analysis is centered around FMI logs and Triple Combo logs, aiming to comprehend both fractures in the area and bedding changes. Formation tops have been provided for all wells, with additional details for the vertical well, including formation tops for Middle Montney members D2, D3, D4 and Montney C.

To ensure clarity in our analysis, we have organized the methodology into three distinct sections: Triple Combo analysis, Image log interpretation, and the integration of both well logs.

5.3.1 Triple Combo logs

The Triple Combo logs serve as a valuable method for identifying physical changes in the area, aiding our understanding of lithology and bed changes. Our analysis begins with the examination of the Gamma Ray (GR) log to discern variations in well radioactivity, providing insights into lithological changes. Subsequently, we focus on resistivity logs, as mentioned in the introduction, where the appearance of 'horns'

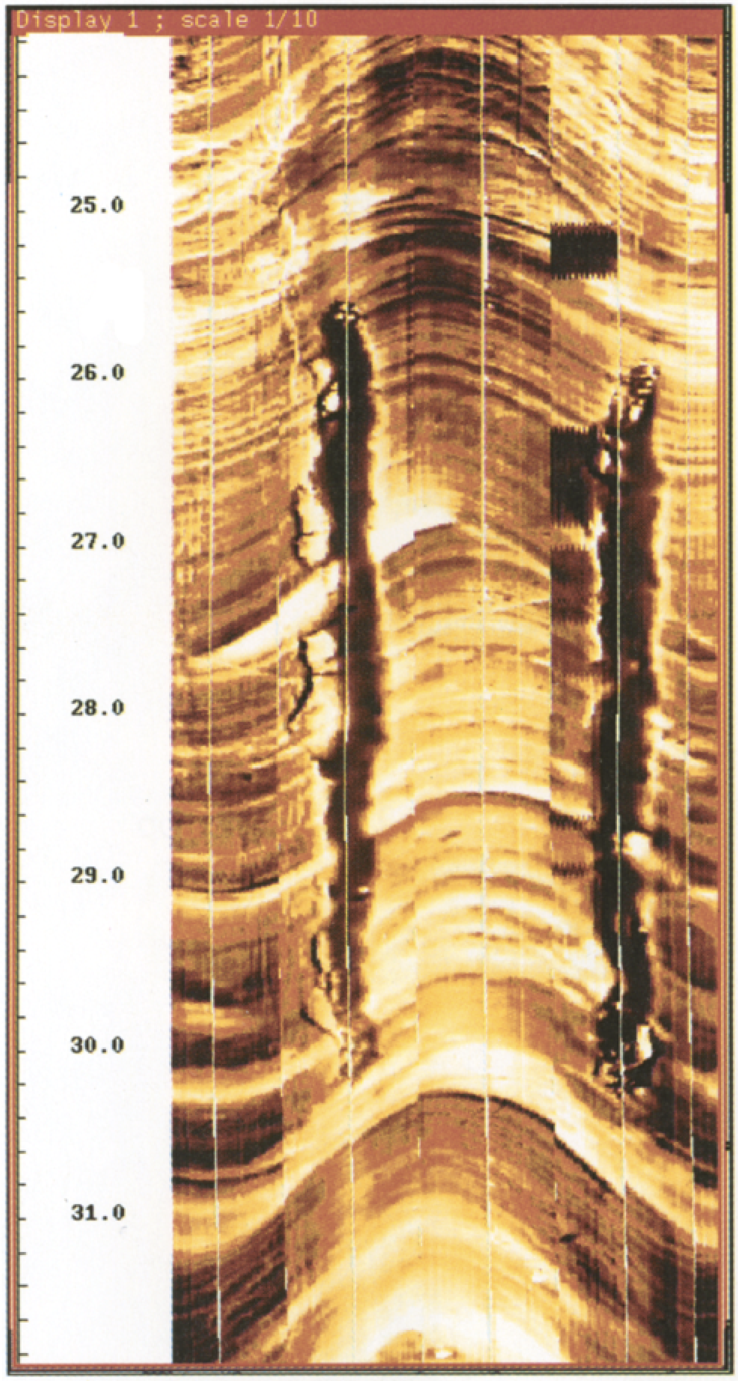

Figure 5.10: Borehole breakouts, depicted in Formation Micro Imager (FMI) logs, are clear, well-defined conductive features positioned at 180-degree intervals along the borehole's sides, filled with conductive mud (reproduced from Lofts et al. (1997) with permission from The Geological Society of London (Lyell Collections)).

indicates alterations in bedding planes. Finally, we use Density and Neutron logs to detect any changes indicative of variations in bedding or the presence of fractures.

5.3.2 Image log interpretation

The unnamed operator company initially detected fractures using proprietary methods applied to the Formation Micro Imager (FMI) logs. Our primary objective is to manually validate the provided data by scrutinizing the features in the image logs. Therefore, our first step is to analyse the provided log for the any artifacts that may cause any issues for interpretations.

In our analysis, fractures are classified into four types: Resistive fractures, Discontinuous resistive fractures, Conductive fractures, and Discontinuous conductive fractures. Resistive and Discontinuous resistive fractures are depicted as white lines, while conductive and discontinuous conductive fractures are represented as dark lines due to drilling mud infiltration into the open fractures. The differentiation between continuous and discontinuous fractures is based on the observation that some fractures do not appear to encircle the wellbore entirely. This discrepancy may stem from tool specifications, where open fractures might not be accurately recorded by resistivity-based imaging tools, as discussed in Section 5.2.2.

In this section, we will make use of the company-provided data to determine the true dipping angle of the bedding planes. This information will aid in understanding the variations in bedding throughout the well. Our approach entails utilizing the provided data for the top of the Montney formation in both horizontal and vertical wells. By extracting the true bedding angle, we will then calculate the projection of the top of the Montney onto the horizontal well using the slope formula. To ensure accuracy, we have cross-verified the provided depth values using Schlumberger's techlog software, albeit for a limited dataset.

Subsequently, we will utilize true dip around the vertical well to calculate the average true dip and identify changes in bedding. The approach involves utilizing the top depth of the Middle Montney Member from the vertical well and calculating the well tops of the Middle Montney Member for the horizontal well. This is necessary because only the top of the Montney has been provided for the horizontal well. After determining the well tops of the Middle Montney Member, we will use them for the horizontal well and compare them with the provided Montney well top to determine if the well has deviated from the drilled horizon.

5.3.3 Integration of logs wireline logs.

This phase focuses on establishing a correlation between the two methodologies by plotting their results together. Our objective is to discern the relationship between different datasets derived from the Triple Combo and FMI logs. Through this integrated analysis, we seek to unveil patterns, similarities, and variations, providing a comprehensive understanding of the subsurface characteristics. We anticipate that discrepancies may arise either from the robustness of the FMI method or the potential influence of natural fractures on the accuracy of the Triple Combo readings.

5.4 Results and Discussion

5.4.1 Triple Combo

Figure 5.11 showcases well logs obtained from a horizontal well, offering a comprehensive depiction of various parameters. Along the x-axis, the Measured Depth (MD) is uniformly represented across all tracks. The first track presents Gamma Ray (GR) readings, while the second track delineates resistivity measurements at distinct depths of investigation—RTAT (true resistivity), R60, R40, and R20. Additionally, neutron porosity and density porosity are depicted for further analysis. The fourth track provides a graphical representation of the horizontal section of the well, with the y-axis denoting the True Vertical Depth (TVD) of the well. Notably, dots are utilized to indicate the port depth of treatment stages.

Fluctuations in Gamma Ray (GR) readings along the length of the well are evident

(Figure 5.11). These variations are delineated by colored zones. Notably, within the depth intervals of [2300, 2610], [2780, 2970], [3000, 3100], [3610, 3750], and [3980, 4100], the GR readings are notably elevated, indicating the presence of clay. However, a recent study by Becerra et al. (2021) and Krause et al. (2011) has suggested that the gamma ray response in the Montney Formation is attributed to the abundant presence of K-feldspar. In the absence of drill cuttings analysis from the study well, we hypothesize that the fluctuations in gamma ray readings may be attributable to both clay and K-feldspar. This phenomenon is visually depicted with grey zones signifying areas of high gamma ray intensity and yellow representing zones with lower gamma ray readings. Consequently, it can be inferred that these variations denote changes in geological formation properties. In Chapter 8, we will attempt to incorporate different analysis results to better understand the phenomena.

In the second track, you'll notice clear "horns" in the resistivity response, marked with dashed lines for clarity (Figure 5.11). These horns appear due to changes in bedding, influencing resistivity readings at different depths of investigation (R90, R60, R40, and R20). These bulhorns were indicated by the dashed lines. In some cases, these dashed lines overlap with changes in gamma ray readings. On the other hand, in the middle part of the well, there's a more resistive area ([3200, 3600]), likely caused by shifts in bedding horizon where we observe separation in R20, R40, R60, and RTAT (true resistivity). However, this is not consistent with the gamma ray results. Possibly, the bedding has changed, but the formation may have similar properties. This demonstrates how various geological factors interact and impact well logs. Additionally, the dashed lines indicating changes in gamma ray readings also coincide with changes in resistivity, reflecting alterations in bedding that affect the log readings.

In the third track, we observe neutron and density porosity (Figure 5.11). Density is depicted in red, while blue represents neutron porosity. It's noticeable that where neutron porosity is high, density values are relatively low. These variations are due to changes in mineral content, indicating shifts in lithology. As expected, the colored zones used to represent changes in gamma ray also correspond to changes in neutron and density porosity.

In the fourth track, you can observe the trajectory of the well along with the treatment stages marked by black circles (Figure 5.11). It's evident that the well path is not consistently straight but fluctuates instead. These fluctuations are common in horizontal wells and can occur due to challenges encountered during drilling. Additionally, the landing height of the well changes over depth, contributing to the variation in trajectory. The dashed lines, drawn based on gamma ray readings and overlaid with resistivity and density/porosity readings presented here, further highlight how changes in the well trajectory impact the well log readings. As a result, it's expected that the hydraulic fracture treatment may have been affected differently across various stages. We'll explore this aspect further in the integration section.

5.4.2 Formation Micro Imager (FMI)

In this section, we primarily focus on the results obtained from the Formation Micro Imager (FMI). For clarity, we divide this part into three sections: 1) Quality Control (QC) of the data, 2) Fracture identification, and 3) Bedding identification.

QC of the Data

As mentioned earlier, the wireline logs were provided by the company and have been interpreted. Our role has been to validate the results. We begin with the QC of the data.

Figure 5.12 illustrates general phenomena of artifacts observed in the provided FMI logs. The figure includes static and dynamic images in the 3rd and 5th tracks, numbered based on the pad number. Here, 0 degrees represents north, labeled as 8.

Figure 5.12a highlights an artifact indicated by arrows. The 4th column in both dynamic and static images appears blurred and continuous throughout the logging.

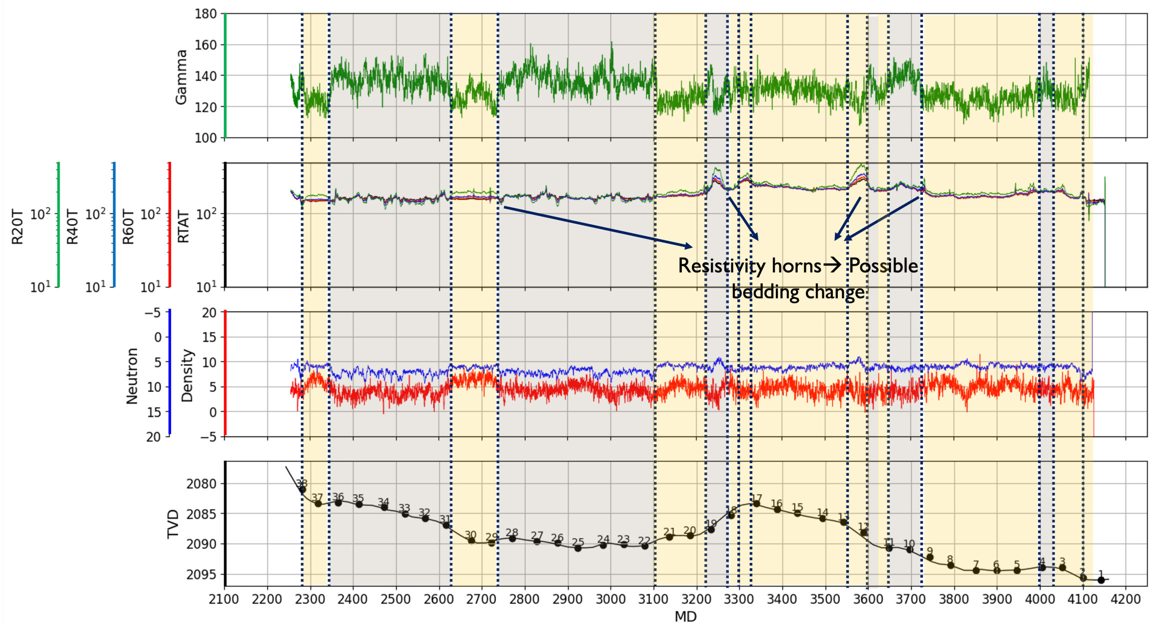

Figure 5.11: Basic well logs: First track: Gamma ray (green), second track: Resistivity at depth investigations of 20, 40, 60, and True resistivity. The grey zone indicates a notable increase in gamma ray, possibly attributed to the presence of K-feldspar in the Montney formation or clay content. Conversely, yellow denotes areas with low gamma ray values. Dashed lines correspond to the bullhorns presented in resistivity. The change in resistivity with bullhorn patterns indicates possible bedding changes, especially in the intervals [3200;2600] and [3950, 4050]. The neutron and density porosity reflect the gamma ray results.

We associate this with low pad pressure. Additionally, columns representing stretch (telemetry issues) can be observed, consistent with auxiliary curves.

Figure 5.12b presents another artifact. The 4th column is blurry due to low pad pressure. Moreover, the 5th column in both dynamic and static images shows a white patch, potentially associated with either bad pad contact or the presence of gas between the pads. Given the use of oil-based mud in this section, we interpret it as bad pad contact.

These artifacts appear in limited instances, leading us to conclude that no major issues have been found that would prevent further interpretations.

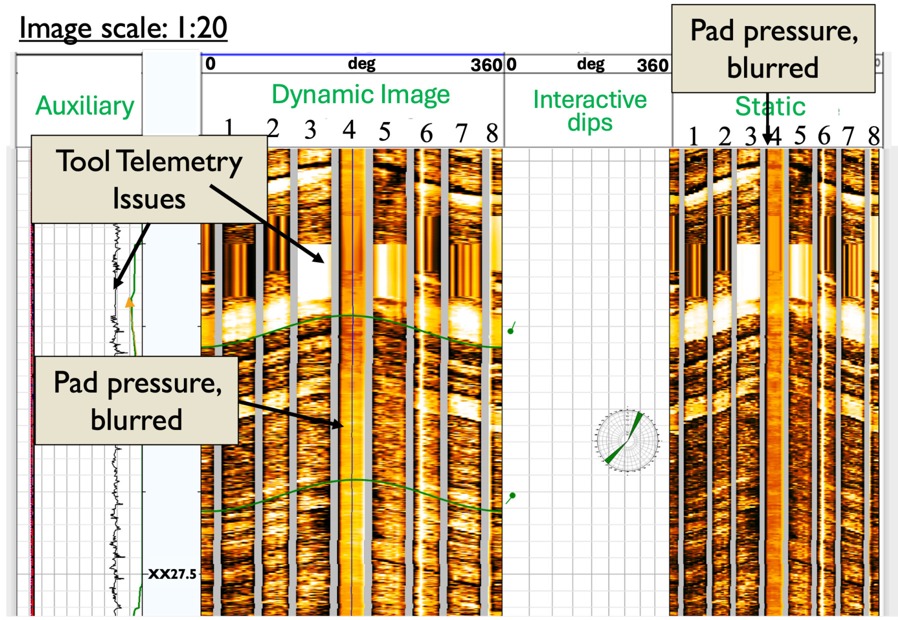

(a) Formation Micro Imager artifacts in column 4 indicative of low pad pressure. Across all 8 columns, square-stretched patterns emerge due to telemetry issues.

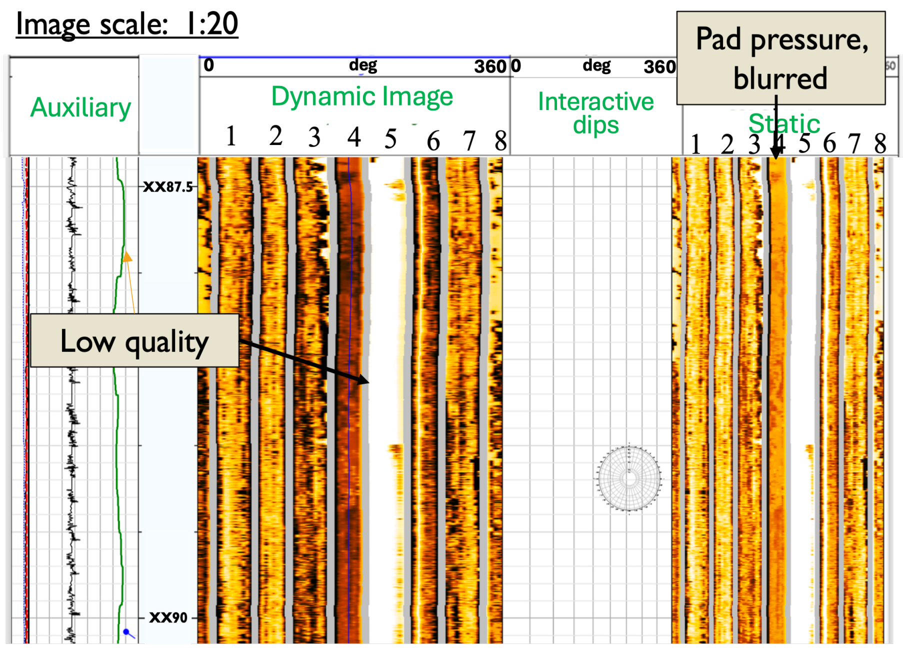

(b) Formation Micro Imager artifacts revealing white patches indicative of poor contact with the formation.

Figure 5.12: Quality control assessment of the Formation Micro Imager data for Well 3. FMI Figure illustrating logging artefacts:(a) tool telemetry and low pad pressure, (b) low quality data due to bad pad contacts.

Fracture Identification

Figure 5.13 illustrates fractures detected in the FMI log within the horizontal section of the well, classified as Continuous Resistive, Discontinuous Resistive, Continuous Conductive, and Discontinuous Conductive. In the upper two figures, white straight lines represent resistive fractures. Continuous resistive fractures are observed at a depth of 41XX, while discontinuous fractures with a dip of 90 degrees are evident at 27XX (given the horizontal orientation of the well). Determining the azimuth of these fractures is challenging due to their perpendicular alignment to the wellbore. Conductive fractures are less distinct compared to resistive fractures due to the characteristics of the tool, as previously discussed. At a depth of 37XX, a conductive line is visible, predominantly affecting columns 1, 2, 3, and 8, classifying it as a discontinuous conductive fracture.

For this particular well, no new fractures have been identified. The fractures predominantly appear as straight lines with a dip ranging between 80 to 90 degrees. We manually verified the dip for all fractures, finding consistency with the company's data. However, determining the azimuth manually from the log was challenging, as the fractures appeared as straight lines with a 90-degree true dip without forming any apex. Therefore, we relied on the provided data for azimuth calculation, as the dipping was accurately calculated.

Figures 5.14 and 5.15 display all identified fractures, comprising 23 Continuous Resistive, 12 Discontinuous Resistive, 18 Discontinuous Conductive, and 3 Continuous Conductive fractures. Figures 5.14a represent the strike of the fractures, where the radius of the rose diagram indicates the count of fractures. The predominant strike of the fractures lies between 20 to 40 degrees, suggesting that the fracture azimuth mainly ranges from 110 to 130 degrees, considering the dip is consistently 90 degrees. Figures 5.14b represent the dip of the fractures, with the radius of the rose diagram again indicating the count of fractures. Most fractures are located at 80 to 90 degrees,

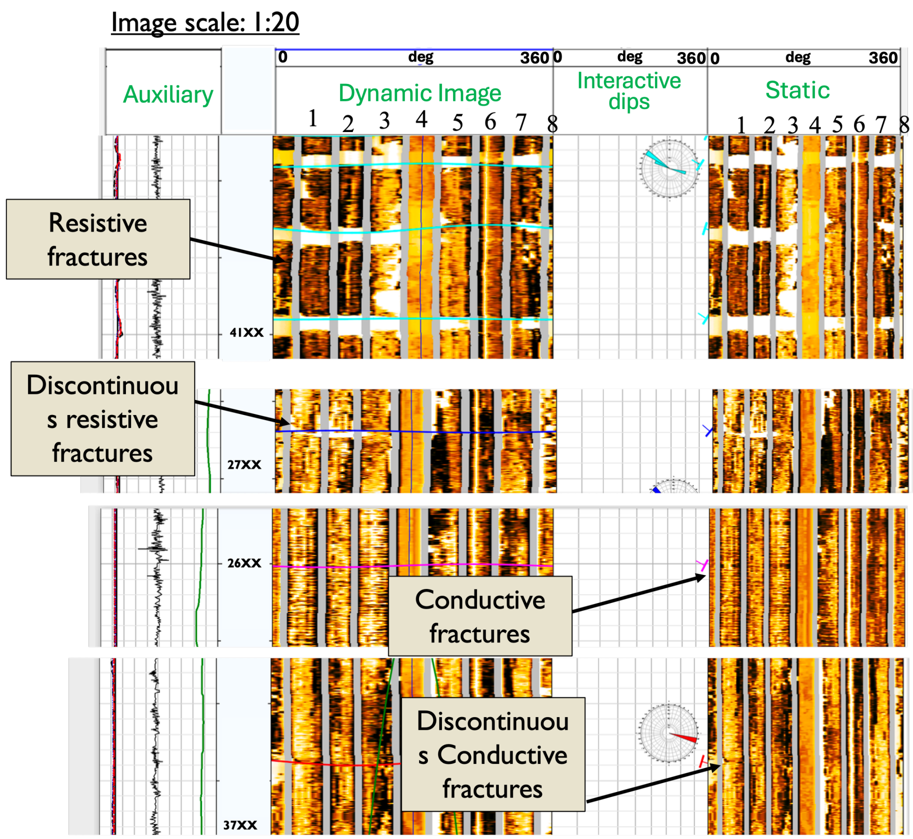

Figure 5.13: Formation Micro Imager observations in Well 3 at four different depths. The 1st figure displays resistive fractures in white, oriented at 90 degrees to the wellbore. The 2nd depicts partially visible discontinuous resistive fractures at a 90-degree angle. The 3rd illustrates disturbed conductive fractures, influenced by tool characteristics. The 4th represents intermittent conductive fractures visible only in the first three columns.

indicative of vertical fractures intersecting the wellbore. In Figure 5.15, it is evident that the majority of conductive fractures are located in the middle and toe sections of the well, whereas resistive fractures seem to predominate in the heel of the well.

Bedding Plane Identification

In this section, we explore the identification of bedding planes utilizing the Formation Micro Imager (FMI) logs. Figure 5.16 provides a comprehensive overview of the bedding information across the entire area. Initially, we utilize the FMI figures to identify the beddings. When interpreting these figures, it's essential to note that

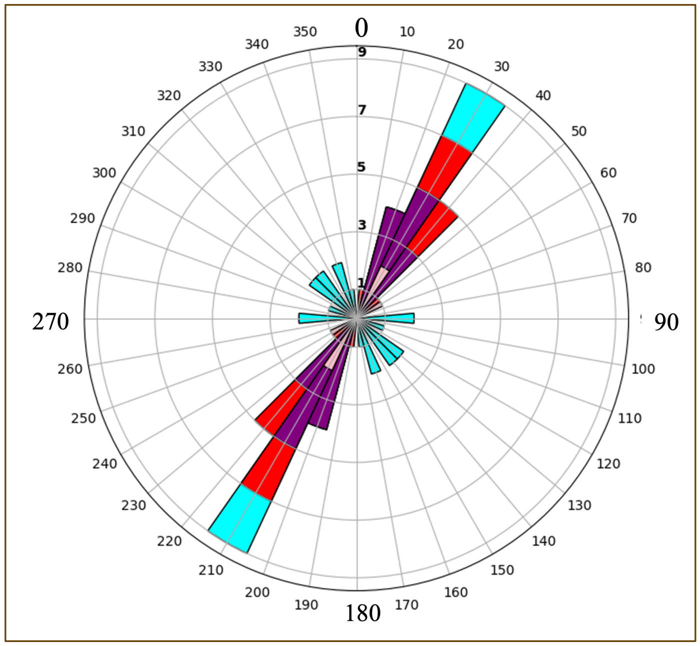

(a) Strike (deg) direction.

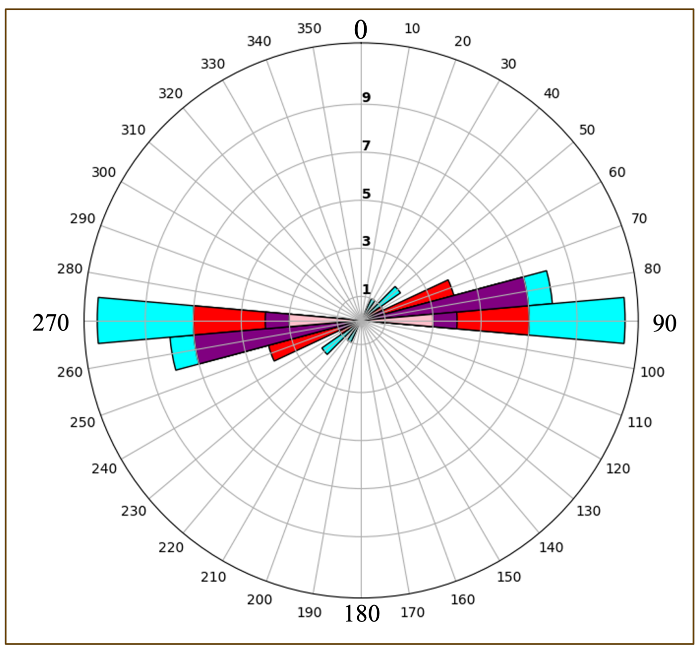

(b) True dip (deg) of the fractures.

Figure 5.14: Rose diagrams depicting the orientation of Conductive fractures (Pink), Discontinuous Conductive fractures (Red), Resistive fractures (Dark Blue/purple), Discontinuous Resistive fractures (Cyan): (a) Strike (deg). The majority display a striking orientation between 20-40 degrees, (b) Dip (deg) of the same fractures, with most showing a 90-degree dip angle, indicating a perpendicular orientation to the wellbore.

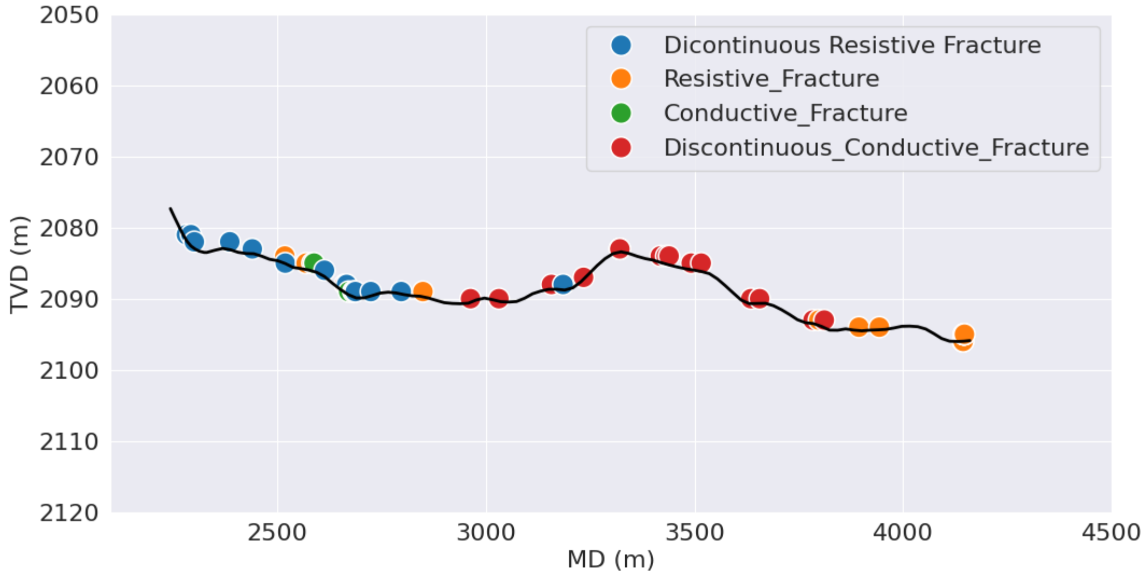

Figure 5.15: Wellbore trajectory overlaid with natural fractures: Conductive fractures (green), Discontinuous Conductive fractures (Red), Resistive fractures (orange), Discontinuous Resistive fractures (blue). The majority of conductive fractures are located in the middle and toe sections of the well, whereas resistive fractures seem to predominate in the heel of the well.

the apex of the sinusoids indicates the apparent dip azimuth, while the arctangent of the ratio of the height to the diameter represents the apparent dip angle. To determine the true dip and dip azimuth, integration of well trajectories is necessary. For simplicity, we examined only select dips relative to the well location using Techlog software. Our findings revealed consistent results. Consequently, we plotted the true dip of the beddings provided by the company.

Figure 5.16a illustrates the vertical section of the well, displaying changes in resistivity that signify lithological variations. Some beds exhibit whiter tones, indicating higher resistivity, whereas darker areas suggest relatively conductive formations. The sinusoids exhibit low amplitude, implying a small apparent dipping angle of approximately 5 degrees. It's noteworthy that the apparent dip and true dip are the same for the vertical section of the well.

Figure 5.16b illustrates the horizontal section of the well at a 1:20 scale, showcasing an upward arc (with the nadir at 90 degrees, or in column 4) on the left figure and

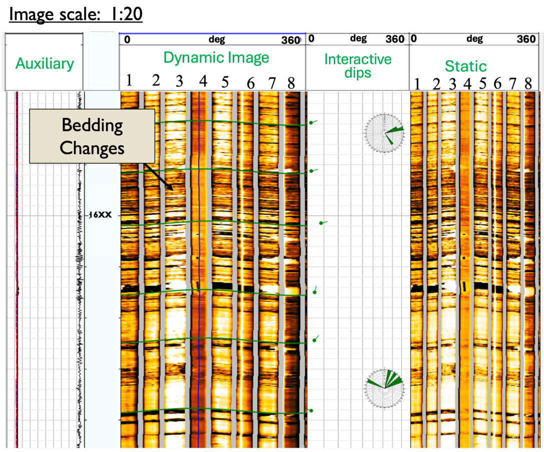

(a) Vertical section of the well with ithological variations indicated by changes in resistivity (color) at a 1:20 scale.

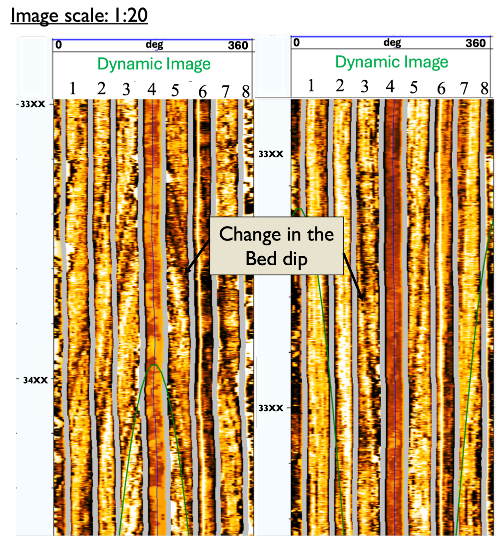

(b) Azimuth changes in the horizontal well section (1:20 scale). Left figure displays 180-degree azimuth (nadir of sinusoidal), while the right figure illustrates 0 degrees.

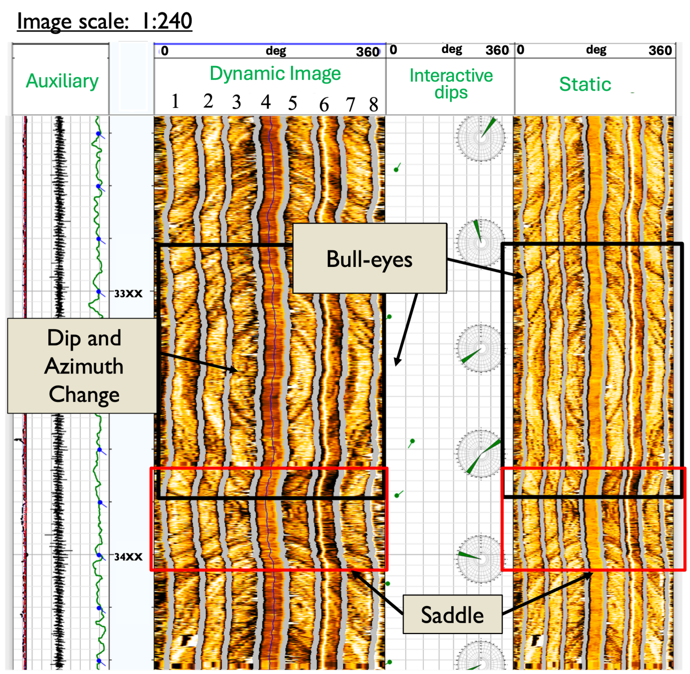

(c) Figure 5.16b in scale of 1:240 revealing distinctive patterns like bullseyes and saddle shapes.

Figure 5.16: Formation Micro-Imager log depicting Well 3: (a) Vertical well section with lithological variation, (b) and (c) same horizontal section of the well depicting the change in the bedding azimuth at different scale.

a downward arc (with the nadir at 0 degrees, or in column 1) on the right figure. Meanwhile, Figure 5.16c depicts the same well section at a scale of 1:240, revealing a distinct bull's-eye (black square) and saddle (red square) pattern. The bedding transitions from a northerly apparent azimuth at the top to a southerly apparent azimuth below, indicating that the well has deviated from its horizontal trajectory. These bull's-eye patterns are plotted in Figure 5.17 with light blue markers along the well trajectory. Importantly, these bull's-eye patterns coincide with changes in the well trajectory direction. Hence, it can be inferred that these patterns are primarily influenced by the trajectory of the well.

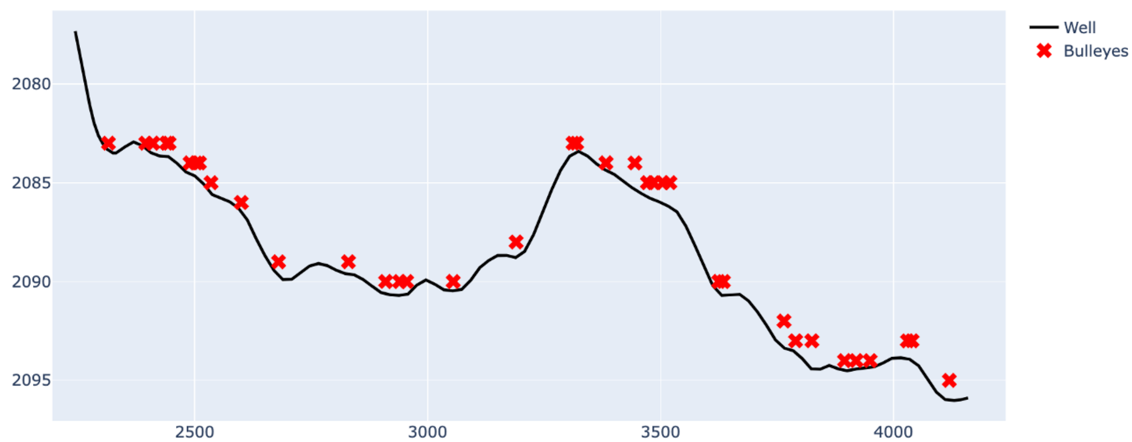

Figure 5.17: Wellbore trajectory overlaid with bullhorn patterns (red). The bullhorn pattern coincides with directional changes of the wellbore.

Figure 5.18 presents the results from the horizontal part of the well. In Figure 5.18a, the strike direction of the beddings is depicted. The radius of the rose diagram represents the count of bedding planes grouped by the strike of the bedding. The predominant azimuth direction ranges from 210 to 230 degrees. In Figure 5.18b, the true dip of the bedding is illustrated. The radius represents the degree of dipping. It is notable that the dipping degrees are predominantly below 10 degrees, with some dipping angles almost invisible. Specifically, in the zoomed part of the figure, it is evident that the degree is below 10 degrees in the horizontal section of the well. To quantify, we calculated the average dipping for the horizontal part of the well, which is approximately 2 degrees.

As detailed in the methodology section, our approach involves using the average dipping angle from Formation Micro-Imager (FMI) data to estimate bedding and well crosspoints. Given that we only have the depth information for the top of Montney horizons in horizontal wells, we employed the average dipping angle to calculate the horizon from the top of the Montney across the well. Figure 5.19 illustrates the results, with black dots indicating the location of the top of Montney for both vertical (represented by the black line in the middle) and horizontal wells.

Observing a dipping angle of 2 degrees, derived from Formation Microimager (FMI) logs, we have achieved satisfactory results, closely aligning with the provided data with minor differences. Subsequently, we utilized the Montney D2, D3, D4, and C top depths from the vertical well, represented by colored dots, to project the horizons onto the horizontal well. In Figure 5.19, D2 is depicted in red, C in purple, D3 in blue, D4 in green, and the Montney in gray. Upon inspection, it is evident that the red line representing D2 intersects the wellbore multiple times, indicating that the well traverses between two horizons. The identified zones are illustrated in the figure below, showcasing different horizons with colors, where red represents D2 and blue represents D3. The black dots denote the hydraulic stages, while red signifies the bullhorn patterns. This analysis suggests that the well has traversed between two middle Montney members, D2 and D3. The well has shifted out of the D3 horizon three times, as indicated by the color-coded zones (blue for D2 and red for D3). The bull's-eye pattern, on the other hand, emerges due to each middle Montney member being composed of multiple bedding planes.

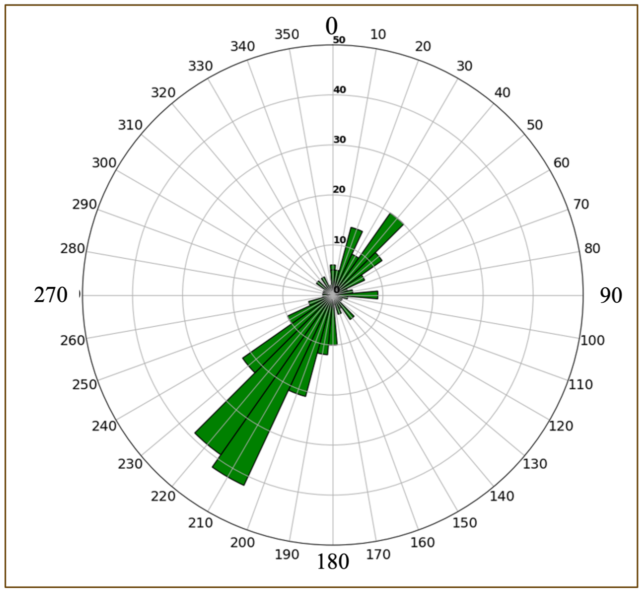

(a) True azimuth in a horizontal well section. The radius of the circle is the frequency of azimuth occurrences. The true azimuth of the bedding is ranging between 210-230 deg.

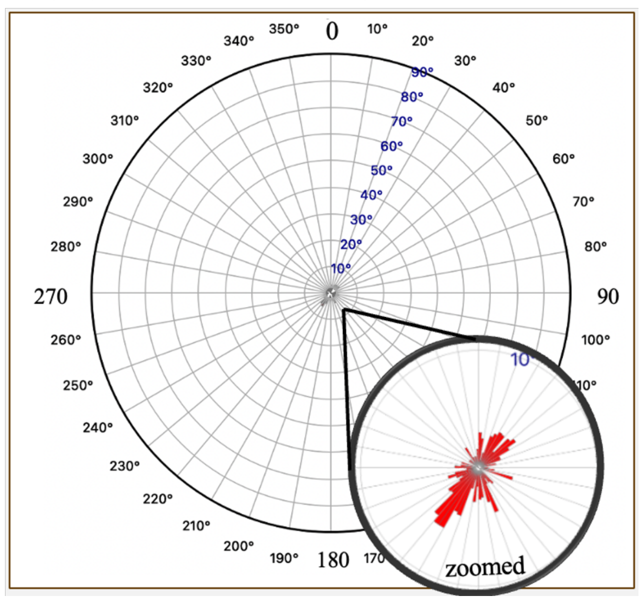

(b) True dip of bedding in a horizontal well. The circle radius indicates true dip angle. Zoomed section reveals dip angle below 10 degrees.

Figure 5.18: Rose diagrams illustrating bedding characteristics in a horizontal well section. (a) The true azimuth of the bedding being 210-230 deg., (b) Depicts true dip of bedding being below 10.

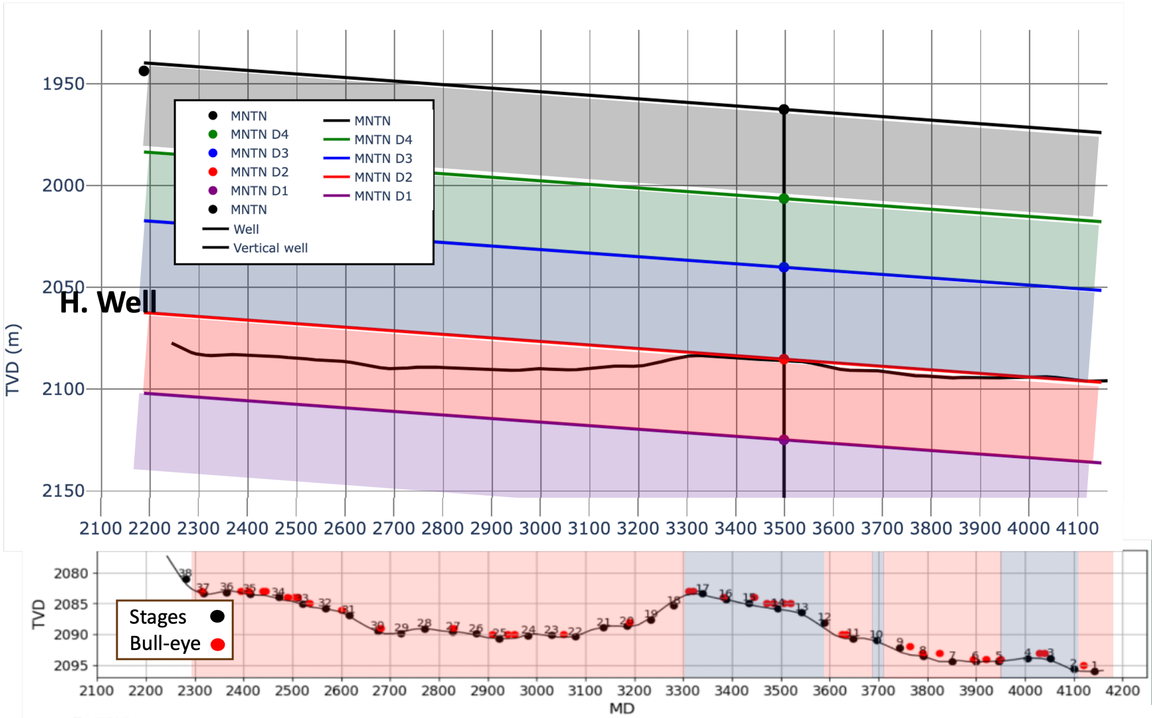

Figure 5.19: Visualization of the well trajectory presented in two tracks. The first track illustrates the trajectory with lines indicating Middle Montney members, dots representing provided well tops, and lines depicting calculated well top horizons for the horizontal well. Various depths where the Middle Montney members intersect the well are shown. In the second track, the well trajectory is displayed along with the projection of the intersected horizon. Middle Montney members are highlighted, with red indicating D3 and blue representing D2. Red dots along the wellbore indicate manually identified bullhorn patterns, while black dots denote hydraulic stages.

5.4.3 Integration of different borehole data (Triple Combo vs FMI)

The results obtained from the triple combo logs, as depicted in Figure 5.11, reveal significant changes in bedding based on resistivity measurements, along with variations in formation properties such as neutron/density porosity and gamma ray readings. Moreover, by leveraging the average true dip of the beddings, we have successfully identified the crossing points of middle Montney members with well trajectories, as illustrated in Figure 5.19. For ease of comparison, we have juxtaposed the outcomes of both Formation Microimager (FMI) and borehole logs in Figure 5.20. In Figure 5.20, the top tracks present the observed bedding changes derived from the FMI data, with red dots denoting the bullseye pattern. Meanwhile, the bottom track showcases the results obtained from basic well logs in Figure 5.19, with yellow indicating low gamma ray zones and grey indicating high gamma ray zones. Notably, the black dots in each figure correspond to the locations of hydraulic fracture treatments.

The agreement between both methods is notable in the midsection of the well toward the toe of the well; the dashed lines overlap with the bedding interpretation based on resistivity readings (dashed red rectangles). The primary discrepancies arise toward the heel of the well. The FMI log suggests that the well may have remained in the same horizon (D2) at the heel, while the resistivity readings indicated a possible change in the horizon. These disparities may be attributed to our assumption of a uniform layer, neglecting multiple internal bedding planes in the horizon. Alternatively, the presence of fractures in these sections of the well could have influenced the readings of resistivity, gamma-ray, and density porosity in both logging methods.

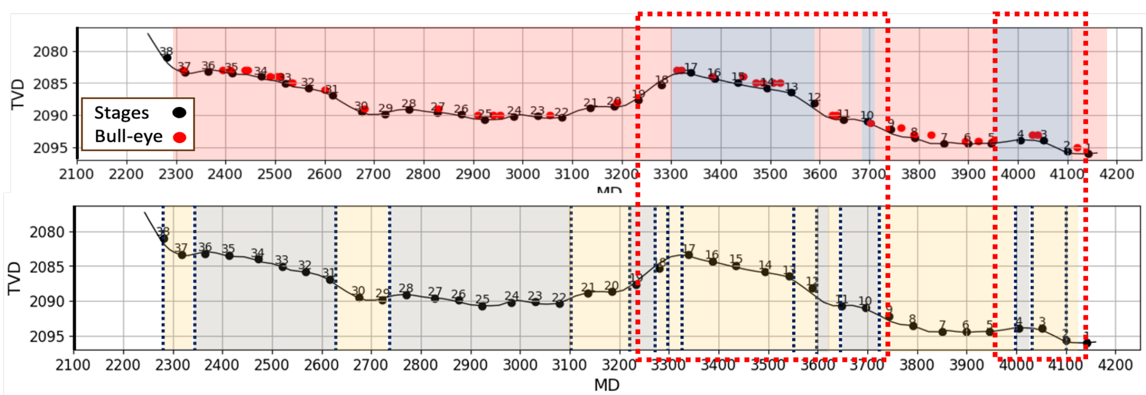

Figure 5.20: Integration of wellbore data and Formation Micro-Imager log. The first track illustrate triple combo results, while the bottom track depicts the well trajectory and bedding planes based on the intersection of D2 and D3, as shown in Figure 5.19. The well has moved out of the Horizon D3 (red bracket).

5.4.4 Integration of Natural fractures with MS data

In this section, we aimed to explore the correlation between observed instances of the "Reactivation" pattern and the presence of natural fractures identified from FMI logs. Figure 5.21 depicts a plan view of the well, illustrating various types of fractures identified from FMI logs: Discontinuous Resistive fractures in blue, Resistive Fractures in orange, Conductive fractures in green, and Discontinuous Conductive fractures in red. The black dots represent hydraulic stages ranging from stage 1 to 38. The blue bracket indicates stages where the same fractures were activated.

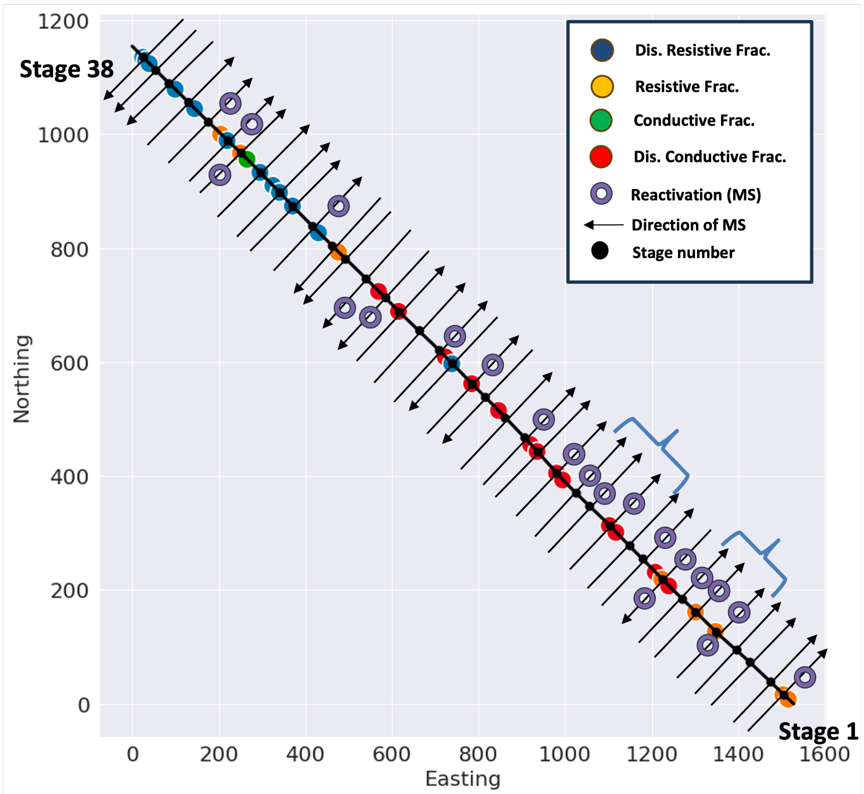

Figure 5.21: Planar view of the well: Black dots indicate treatment stages, with arrows showing propagation direction. Stages displaying a "Reactivation" pattern are marked with purple rings. Natural fractures are depicted as follows: Dis. Conductive (red), Dis. Resistive (blue), Resistive (yellow), Conductive (green). Most conductive fractures appear toward the toe of the well. Reactivation patterns overlap with conductive fractures. Some reactivation patterns do not overlap with any fractures because they occur due to the activation of existing fractures (indicated with brackets).

Observations reveal that reactivation predominantly occurs towards the toe of the well, where Discontinuous Conductive fractures are prevalent. Conversely, towards the heel of the well, Discontinuous Resistive fractures are more common. Notably, stages exhibiting "reactivation" patterns are largely confined to specific regions. For instance, stages 11-13, where reactivation of the same fracture was noted, only have one stage overlapping with the natural fractures.

This analysis suggests that "Reactivation" predominantly occurs in conjunction with Conductive, Discontinuous Conductive, and Resistive fractures. Discontinuous Resistive fractures, however, seem to have minimal impact on hydraulic fracture propagation.

5.5 Conclusions

The comprehensive analysis of borehole data from both the Triple Combo and Formation Micro Imager (FMI) logs has provided valuable insights into the geological characteristics of the studied area.

The Gamma Ray (GR) readings obtained from the Triple Combo logs, as depicted in Figure 5.11, reveal fluctuations indicative of changes in geological formations. Based on the field analysis in the Montney Formation by [Reference], the variation in gamma ray is attributed to the presence of K-feldspar. Since drill cutting analysis from the field was unavailable, it is inferred that these fluctuations in GR may correspond to changes in mineralogy, such as the presence of K-feldspar or clay. Additionally, the neutron and density porosity, and resistivity tracks show correlations with GR values. Notably, the distinct "horns" in the resistivity log signify alterations in bedding planes, especially in the mid-section of the well.

The Formation Micro Imager (FMI) logs, illustrated in Figure 5.12, underwent meticulous quality control to identify and mitigate artifacts, ensuring the reliability of further interpretations. Fracture identification efforts successfully categorized various fracture types. The correlation of fractures facilitated the identification of the "Reactivation" pattern, attributed to pre-existing fractures around the wellbore. Moreover, occurrences of 'reactivation' in stages where the natural fracture location does not overlap with the stage, and where we observe the microseismic cloud moving toward the previous stage, suggest the opening of the same fracture multiple times.

The integration of Triple Combo and FMI data in Figure 5.20 unveils that the well penetrated not only the D3 horizon but also the D2 horizon. Discrepancies observed at the heel of the well may stem from assumptions of a uniform layer or potential influences of fractures on readings. Minor inconsistencies noted at the toe, particularly concerning starting depths of D2, could be attributed to the robustness of the applied methodology.

Chapter 6

Seismic Reflectivity

6.1 Summary

Understanding geophysical data, particularly reflection seismic data, is essential for the success of oil and gas exploration endeavors. However, the effect of geology on unidirectional propagation of hydraulic fractures (depicted in Figure 6.1) is yet to be understood. Our objective is to comprehensively understand the geology in the area, which will serve as a means to understand fracture propagation dynamics by integrating structural and lithological analyses.

Initially, we generate seismic attributes such as Azimuth, Dip, Maximum, and Minimum curvature once we successfully perform seismic-to-well-tie and horizon picking. These seismic attributes aid in understanding structural geology. Recognizing the significance of lithology, particularly in assessing factors like pore pressure changes and fracture intensity, we adopt a simple approach: multiplying the depth map (after time-depth conversion) by the pore pressure gradient. This analysis helps us to understand the pore-pressure changes in the area. To incorporate the results and understand the propagation, we integrate seismic reflection interpretation with microseismic event analysis results, such as cloud propagation dynamics.

We successfully implemented seismic-to-well tie for three wells and picked the horizons. The horizon picking results indicate data quality issues in the Montney formation. Therefore, we used the Belloy formation, which depicts the geology of the

Montney well. Additionally, we performed time-depth conversion and generated a pore pressure map in the area.

The interpretation results show that the study area dips toward the southwest (SW) direction, and pore pressure maps indicate that one side of the well corresponds to higher pore pressure, which is related to the dipping of the area towards the southwest region. As the initial pore pressure increase corresponds to higher breakdown pressure of the rocks, the unidirectional propagation of the microseismics could be a result of it. However, we have not found any correlation between maximum and minimum curvature attributes.

6.2 Introduction

The Western Canada Sedimentary Basin (WCSB) sprawls across about 450,000 square miles of Western Canada and can be characterized as a straightforward wedge of sedimentary rock tapering northeastward. The stratigraphy of the Canadian Western Basin is depicted in Figure 6.2 and detailedly explained in Chapter 2. The Canadian Western Basin is characterized by ascending order, including the Belloy, the Montney Formation, the Doig plus Halfway formations, and the Charlie Lake Formation.

Depths to the top of the formation vary from 200 meters in the northeast (NE) near the BC-Alberta border to 3200 meters in the southwest (SW) near the deformation front, with slight shallowing in the north as depicted in Figure 6.3 (Chalmers et al., 2022). In general, the Montney Formation's subcrop area deepens towards the southwest. Such behavior is crucial as the deeper sections might correspond to higher pore pressure, as pore pressure increases with depth.

The Montney Formation has been divided into three parts: Upper, Middle, and Lower Montney (Kuppe et al., 2012). The Middle Montney Member, formed during the Smithian stage (Nelson & Rghei, 2008), comprises specific layers like D1, D2, D3, and D4 from bottom to top (Prenoslo et al., 2018). The well of interest is drilled into Montney D3 formation.

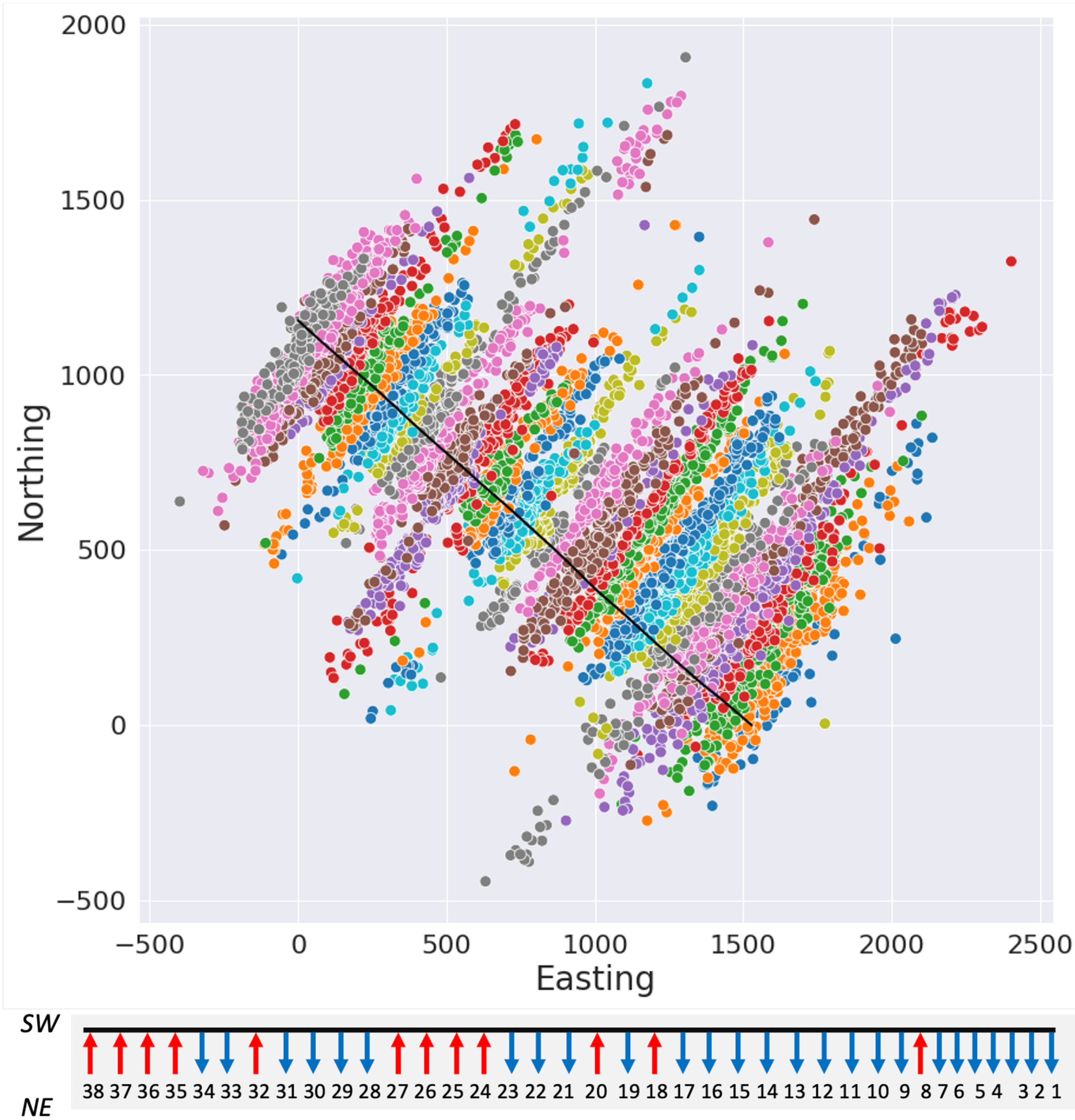

Figure 6.1: Overview of Microseismic Clouds: Arrows depict propagation trends. Blue denotes northeast movement, red indicates SW. Predominantly, propagation is northeastward. Up to stage 17, most events move toward the northeast direction, but after stage 17, the event direction changes, exhibiting a cyclic pattern where stages with predominantly northeast movement are followed by stages moving in the opposite direction.

6.3 Data

The dataset provided encompasses an area spanning 11,400 meters and 5,300 meters, processed by an anonymous company. According to the header information, the data

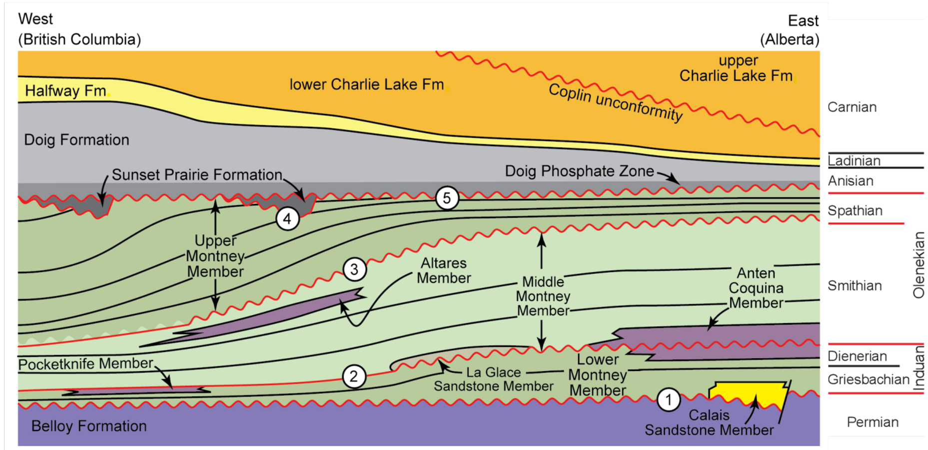

Figure 6.2: Schematic cross-section from central Alberta to British Columbia, depicting Montney stratigraphy in a west-east orientation. The diagram highlights intra and extraformational unconformities delineating the Lower, Middle, and Upper Montney members (designated as numbers 1–5). The basal Montney contact (1) is typically unconformable across most of the basin, though it may exhibit conformable characteristics in certain western subsurface and outcrop regions. The earliest intraformational unconformity (2) approximates the Dienerian-Smithian boundary (= Induan-Olenekian boundary). A subsequent mid-Montney unconformity occurs around the Smithian-Spathian boundary (mid-Olenekian) (3). The upper Montney contact is unconformable with overlying Middle Triassic strata, either the Sunset Prairie Formation or the Doig phosphate zone (unconformities 4 and 5) (reprinted from Zonneveld and Moslow (2018b) with permission from Canadian Society of Petroleum Geologists (CSPG)).

is irregularly sampled and the dynamite was a source for the seismic energy. The following processing steps have been undertaken:

1. Harmonic noise removal; 2. Geophone correction; 3. Refraction statics (Datum = 900M, Vw = 762M/S, Vr = 3300M/S); 4. Amplitude recovery; 5. Pre-Decon noise attenuation; 6. Velocity analysis; 7. Static and phase matching; 8. NMO (Normal Moveout); 9. Post-Decon denoise; 10. Noise attenuation; 11. NMO removal; 12. VTI (Transversely Isotropy with vertical axis of symmetry) Kirchhoff PSTM (Pre-Stack Time Migration) (Maximum Angle 45°); 13. FK Dip filter; 14. Radon demultiplication; 15. Mute; 16. Stack; 17. Global decon; 18. Signal enhancement; 19. Relative amplitude equalization.

Since the data processing has been handled by the company, our attention will

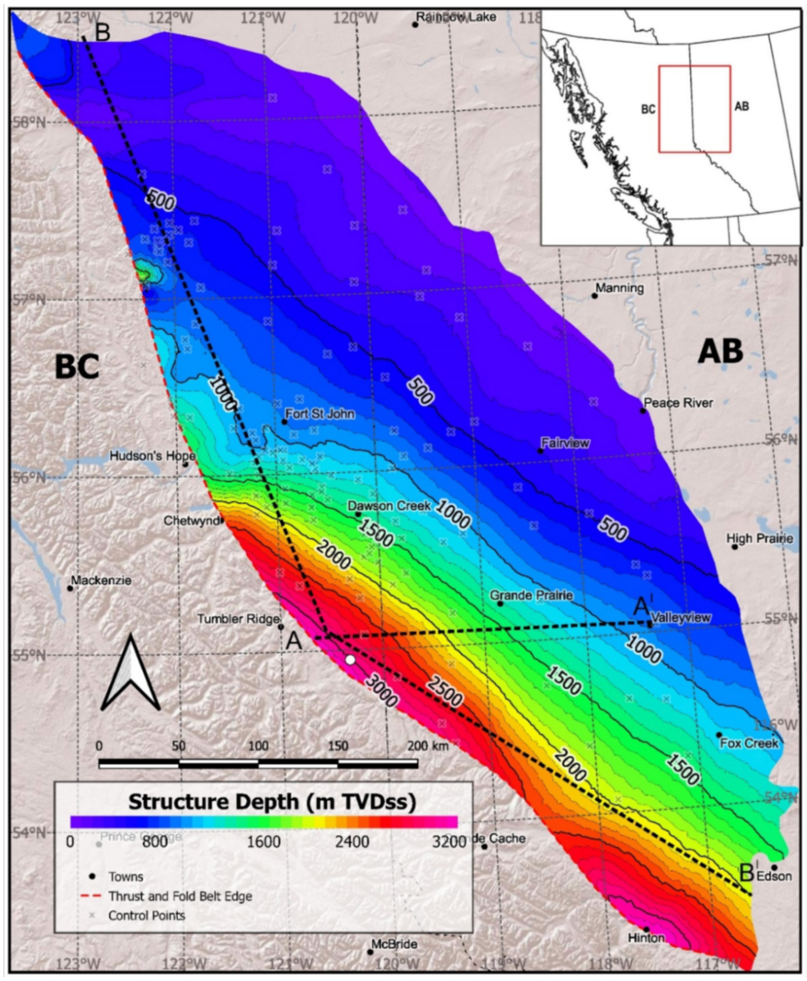

Figure 6.3: Structural Variation of the Montney Formation Across British Columbia and Alberta. The structure map depicts a gradual deepening of the Montney Formation towards the southwest (reprinted with permission from Chalmers et al. (2022)).

solely be directed towards interpreting the data.

6.4 Methodology

The steps of the interpretation of the seismic data depends on the objective of the work. Our objective is to understand the geologocal sructure in the area and find a correlation between microseismic data to understand the fracture propogation after the hydraulic fracture treatment.

The study began by importing seismic data in .segy format into Seisware, a geophysical modeling software. Following this, well data was imported as well. At this

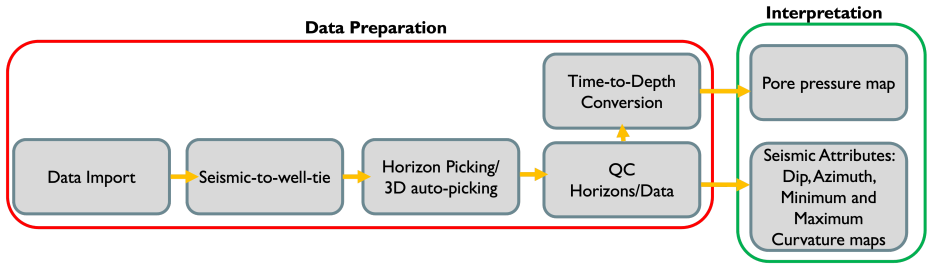

Figure 6.4: Seismic interpretation workflow: Data preparation involves linking well information with seismic-to-well tie, time to depth conversion, QC, and horizon picking. Interpretation focuses on understanding seismic attributes such as Dip, Azimuth, Maximum and Minimum Curvature, and Pore Pressure Mapping.

juncture, we adhered to the standard workflow for seismic data analysis, as illustrated in Figure 6.4. Initially, we conducted seismic-to-well tie, proceeded with horizon picking, quality control (QC) of the data, and time-to-depth conversion. Subsequently, we transitioned to the interpretation phase, during which we generated seismic attributes such as dip, azimuth, curvature, and pore pressure maps from time map and depth map.

6.4.1 Data Preparation

Seismic-to-well-tie

Establishing a well tie to seismic data is a pivotal step in characterizing reservoirs. This process involves aligning seismic reflection data with well log data to precisely identify key horizons within seismic reflections.

Figure 6.5 illustrates the schematic of the well-tying process. Initially, the acoustic impedance log is digitized, utilizing measurements from density and sonic logs (P-wave velocities). Subsequently, the acoustic impedance log aids in calculating the reflection coefficient at a perpendicular angle. In the final stage, the series of reflection coefficient is generated by convolving the wavelet with the reflection coefficient, and then correlated with the original seismic reflection data. This process significantly enhances the reliability of seismic data, particularly when there are discrepancies between lithological information and well logs (Tylor-Jones & Azevedo, 2023; White

& Simm, 2003). Wavelets play a crucial role in seismic-to-well ties, enabling the generation of synthetic seismic traces from well-log data for comparison with processed seismic traces near the well.

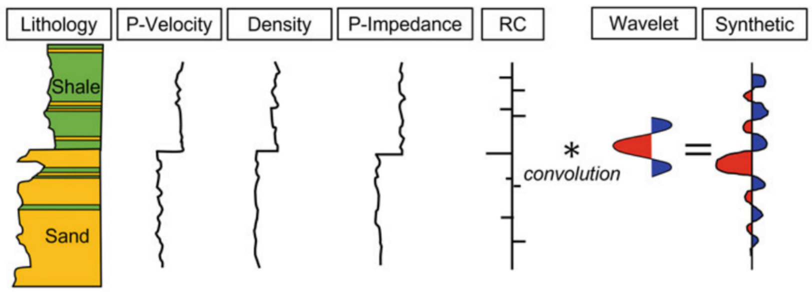

Figure 6.5: Illustration depicting the methodology of well-tying, wherein velocity and density logs are utilized to generate reflections, enabling the production of synthetic seismic data (reprinted from Tylor-Jones and Azevedo (2023) with permission from Springer Nature BV).

Our approach to the seismic-to-well tie is qualitative, relying on visual comparisons between synthetics and seismic data, assuming familiarity with the wavelet under analysis. This process will be conducted for the three wells, which are later crucial for the well top identifications to aid to pick horizon and time-to-depth conversion. While various partially and fully automated well-tie algorithms exist, it is widely recognized that human intervention is indispensable for an accurate well tie (Herrera & van der Baan, 2014; Nivlet et al., 2020). Ensuring precise wavelet estimation is paramount for a robust well tie.

The accurate estimation of the wavelet in our data will rely on software performance. We plan to analyze the correct wavelet from the seismic data using inline and crossline data. As the data was acquired with dynamite, our main assumption is the wavelet to be 0 phased. For the wavelet itself, we will use a Ricker wavelet with a frequency of around 30 Hz.

Horizon Picking

In this stage, seismic traces were meticulously examined and selected to construct a seismic model, enabling the delineation of subsurface features such as the depth to reflectors and the locations of faults. Seismic horizons are typically interpreted by identifying peaks, troughs, or zero crossings along consistent seismic waveforms. Manual picking is a common approach to horizon interpretation, albeit time-consuming and heavily reliant on the experience of interpreters (Wu et al., 2022).

Automated pickers, while they may appear to only detect peaks, troughs, and zero crossings on neighboring traces, actually use internal rules like correlation coefficient, dip, and coherence. These rules help them pick through moderately good data with complex waveforms. However, these automated systems are affected by the signal-to-noise (S/N) ratio of the seismic data:

1. A high S/N ratio means the reflections in the data are smooth and continuous, making autotracking reliable.

2. Low S/N ratio data lacks smoothness or consistency in the reflections, making it hard for autotracking to pick reliable horizons.

In our approach, we will utilize an auto-picker to select peaks or troughs based on the formation reflection. However, in areas where autopicking proves inadequate or unreliable, we employ manual picking to ensure accurate identification of seismic features. We will sequentially pick data points covering both inline and crossline directions. Subsequently, we will employ a 3-D autopicker to further refine the picks for other inlines and crosslines. This method streamlines the picking process and saves time.

Following each pick, we will conduct quality control (QC) of the data. However, it's important to note that the provided data may not be of uniform high quality; hence, we will strive to identify the seismic reflection that best represents the structural geology of the Montney formation. Hence, supplementary techniques like thickness calculations (isochron analysis) can be employed to assess the suitability of the updated horizon for accurately characterizing the geological features of the Monterey Formation.

Time to depth Conversion

Time-to-depth conversion is a critical process in seismic data analysis, where each data point in the time domain is assigned a corresponding depth coordinate. This conversion is essential for accurate seismic interpretation and geomodeling. Sonic logs, among other well logs, play a key role in this conversion by providing data to transition wells from the depth to time domain.

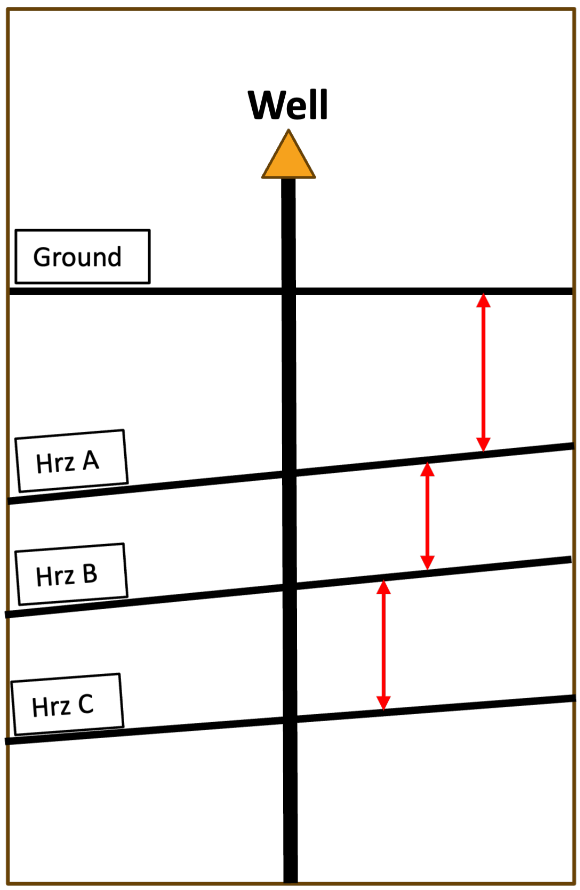

Figure 6.6: Visualization of interval velocities computed from ground level (for onshore seismic) to the primary horizon Hrz A, followed by calculations for layer A between Hrz A and Hrz B, and layer B between Hrz B and Hrz C. Sonic data reveals vertical velocity variations within each layer (drawn in accordance to GMDK (2015)).

Interval velocities, which represent the average velocity between two horizons, and average velocities, indicating the mean velocity between the ground and a specific horizon, are utilized in this conversion process (GMDK, 2015; Quintero & Tejada, 2020). In our analysis, we focus on interval velocities, which are computed along each well. This computation involves determining the velocity variations vertically within a geological unit, integrating these variations to compute interval velocities.

To compute interval velocities, we rely on well tops, the depth of which is known, and the two-way time (TWT) derived from the time-converted wells. The interval velocity is calculated as the ratio between the change in depth and the change in TWT. In cases where the interval velocity remains relatively constant across wells, an average constant interval velocity may be assigned to the entire unit. Conversely, when there are sufficient wells and variations in interval velocity between them, interpolation techniques are applied to generate an interval velocity map. This map assigns interval velocity values to every point of the seismic cube (GMDK, 2015). The concept of interval velocity has been illustrated in figure 6.6.

In our analysis, we will leverage data from three wells along with their corresponding three well tops to conduct time-to-depth conversion. The three well tops we used are Halfway, Doing, and Montney D4, as these well tops were common to all three wells. The inclusion of three wells and their associated well tops enhances the accuracy of the velocity model. By comparing velocities at these points, we can generate a more precise velocity model, enabling us to capture the geology of the subsurface more effectively.

6.4.2 Interpretation

Following the digitalization of seismic horizons and the completion of time-to-depth conversion, our next task involves interpreting the seismic data and generating seismic attributes. This segment of the workflow aims to elucidate the primary concepts underlying seismic attributes and integrate them with microseismic data.

Attributes serve both qualitative and quantitative purposes in interpretation. For instance, qualitatively, maps of dip magnitude, dip azimuth, or residual structure can be utilized to discern detailed fault trace patterns on a horizon (Chopra & Marfurt, 2008). Quantitatively, attributes may be employed to correlate with reservoir properties measured in boreholes.

In our analysis, we will incorporate a range of seismic attributes including dip, azimuth, minimum and maximum curvature, as well as a pore pressure map derived from the depth map. Following attribute interpretation, our focus will shift towards correlating microseismic data with these attributes. This correlation will provide valuable insights into the propagation of fractures, enhancing our understanding of subsurface dynamics.

Dip and Azimuth Map

Time-structure and amplitude-extraction maps, dip and azimuth maps of interpreted seismic reflectors are crucial for analyzing 3D seismic data. These maps provide information on the inclination and direction of seismic reflectors, similar to how strike and dip reveal the orientation of sedimentary layers. Dip magnitude (θ) measures the angle between the steepest direction of a plane and a horizontal plane, ranging from 0 to 90 degrees, while dip azimuth (Φ) indicates the direction (relative to north) in which the plane is dipping, with values from 0 to 360 degrees. These attributes are not only valuable for identifying broad structural features but also for detecting faults with minimal displacement (Chopra & Marfurt, 2007; Koson et al., 2013).

The procedure for computing dip and azimuth is generally uncomplicated (Figure 6.7). These metrics, denoting the extent and orientation of dip, are derived from the time gradient vector at each location along the interpreted horizon, considering both inlines and crosslines. Typically, dip and azimuth values are depicted on distinct maps. It's crucial to plot these maps separately because faults, which impact the mapped horizon, may not always be equally discernible.

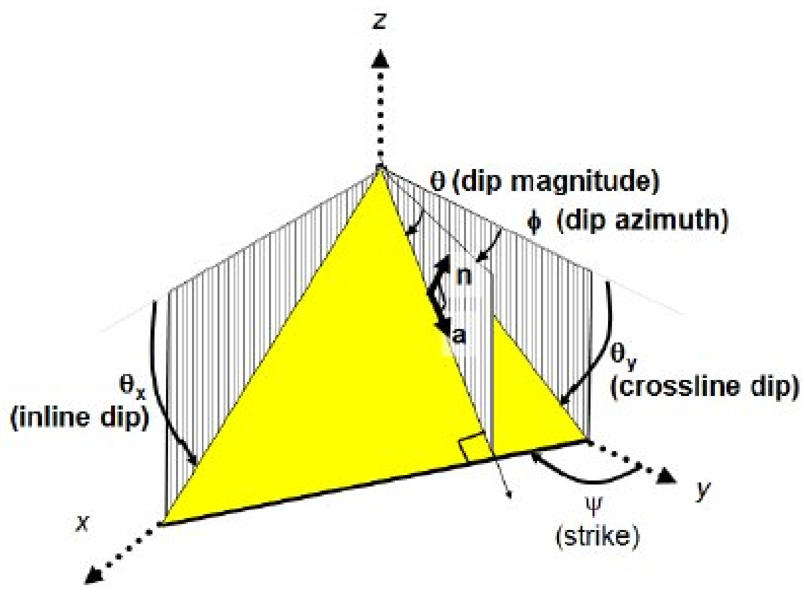

Figure 6.7: Diagram illustrating the terminology used for dip magnitude and azimuth. The vectors **n** and **a** represent unit vectors perpendicular to the plane and indicating the dip along the reflector, respectively. $\boldsymbol{\theta}\mathbf{x}$ and $\boldsymbol{\theta}\mathbf{y}$ denote the apparent dips along the inline and crossline, respectively. $\boldsymbol{\theta}$ denotes the dip magnitude, while $\boldsymbol{\theta}$ represents the dip azimuth (reproduced from Rijks and Jauffred (1991) with permission from Society of Exploration Geophysicists (SEG)).

For example, in the context of a fractured zone, Figure 6.8 illustrates the Nun River field in the Niger Delta, derived from dip magnitude and dip azimuth volumes, respectively. While large faults are easily visible in amplitude volumes due to significant reflector displacement, subtle faults with minor reflector displacement are highlighted using dip magnitude and azimuth, as demonstrated by Rijks and Jauffred (1991). Further exploration of additional examples within the same chapter is necessary for a thorough understanding of dip and curvature interpretation.

Furthermore, in the subsurface, rock formations are typically laid down in layers. The movement of fluids within and between these layers is primarily influenced by the permeability of the rocks. For instance, shale commonly exhibits significantly lower permeability vertically compared to horizontally, especially when shale beds are flat-lying (Liu et al., 2018). Consequently, fluid finds it challenging to flow vertically through shale beds but can more easily migrate horizontally. This implies that water

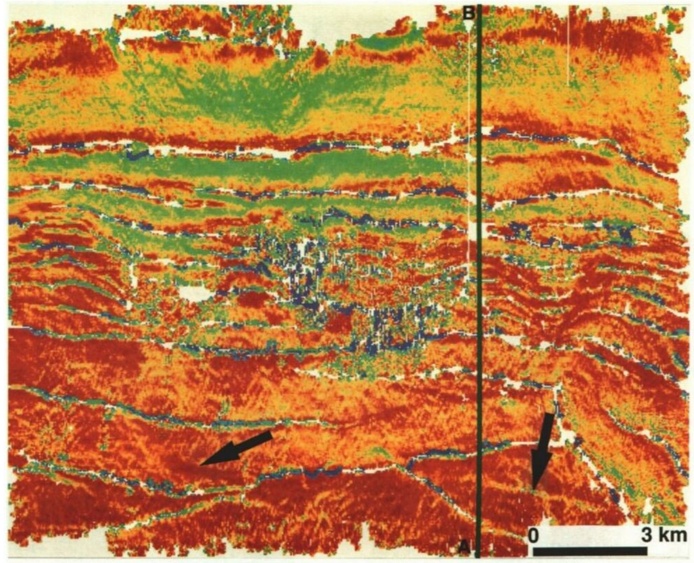

(a) Dip magnitude depicted on a time map. Regions of greater dip are indicated by green colors, while areas of shallower dip are depicted in red,

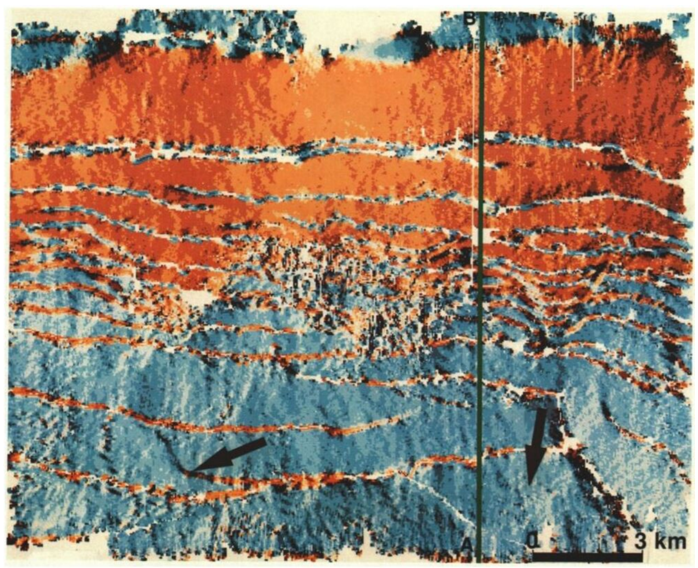

(b) Dip azimuth and shaded relief overlaid on the same time map. Blue and orange colors indicate opposite dip direction.

Figure 6.8: Dip magnitude and Dip azimuth map depicted on a time map. Black arrows denote lineations where subtle changes in dip occur (reproduced from Rijks and Jauffred (1991) with permission from Society of Exploration Geophysicists (SEG)).

would preferentially flow along the horizontal bedding planes in shale, where natural flow pathways exist, rather than attempting vertical movement, where flow pathways are scarce. Therefore, it becomes crucial to comprehend the dip angle in our area, even if no natural faults or fractures have been identified. We will utilize azimuth and dip maps in conjunction with microseismic data to achieve a more comprehensive understanding of subsurface dynamics.

Minimum and maximum curvature Map

Curvature measures how much a curve or surface bends. In sedimentary structures, which start out mostly flat when they first form, they change shape over time due to external forces. Along the direction where the most pressure is applied, they might bend more easily and develop cracks, which can be where fractures gather (Chopra & Marfurt, 2007; Gauthier et al., 2017; Suo et al., 2012). Minimum and maximum curvatures is adept at identifying faults with drag and those with minimal displacement, which may be challenging to detect using other attributes like coherence. Unlike coherence, which pinpoints the exact fault location, curvature more commonly delineates folds, flexures, and faults by highlighting areas of maximum and minimum anomalies (Mai et al., 2009).

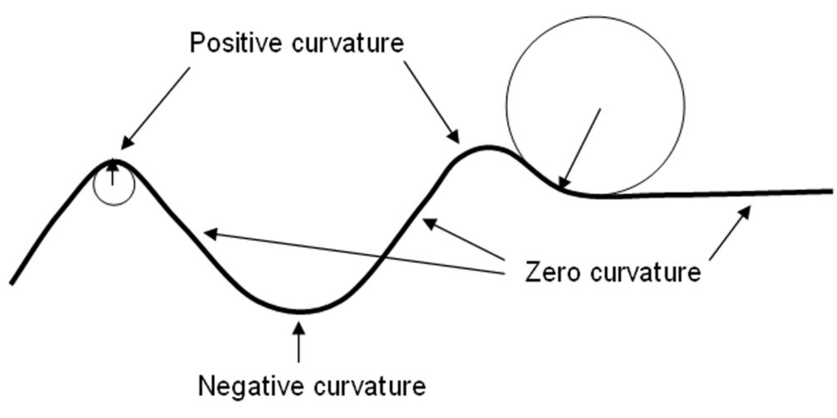

Figure 6.9: 2D curvature profile along a line. Anticlinal features exhibit positive curvature, synclinal features show negative curvature, and planar features, whether horizontal or dipping, demonstrate zero curvature (reproduced from Chopra and Marfurt (2007) with permission from Society of Exploration Geophysicists (SEG)).

In two dimensions, curvature is defined as the radius of a circle tangential to a curve (Figure 6.9). Positive curvature indicates anticlines, negative curvature denotes synclines, and linear portions of a curve exhibit zero curvature, such as areas with constant dip. Locally, a 2D line can be approximated by a parabolic curve, where the curvature coefficient, k, is inversely proportional to the radius of curvature (Chopra & Marfurt, 2007; Silva et al., 2012).

In three dimensions, curvature is determined by fitting two circles tangential to a surface, residing in orthogonal planes. The centers of these circles lie along an axis perpendicular to a tangent plane to the surface. The first circle, adjusted to have the minimum radius possible, defines the maximum curvature (k_{max}). The second circle, perpendicular to the first, has a radius equal to or greater than the maximum curvature and defines the minimum curvature (k_{min}) for a quadratic surface. These curvature measurements provide a straightforward means of assessing reflector shape, independent of bulk rotations and translations (Chopra & Marfurt, 2007, 2008).

In our analysis, we will employ a horizon-based method. To mitigate the influence of artifacts, we aim to identify a reflector that accurately represents the geology of the Montney Formation while maintaining consistency across the areas of interest. Additionally, we will explore the potential correlation between curvature maps and microseismic data to further analyze the subsurface characteristics.

Pore Pressure Map

Pore pressure significantly impacts reservoir stimulation, especially in unconventional reservoirs, where it regulates crack initiation and propagation. Fluids flow from a high pressure toward a lower pressure in a system (Kutz, 2011). Therefore, hydraulic fracture fluid is prone to move in the direction where the pore pressure is lower.

If there are variations in pore pressure around the tip of the fracture, the fracture tends to propagate towards regions of higher pore pressure (Ma et al., 2023). In a recent study by Ma et al. (2023), it was found that the initial pore pressure increase the effective stress. It was found that the initial pore pressure may not only exert an effective stress on the formation but also result in a fracturing mechanism with high breakdown pressure. Subsequently, Prabhakaran et al. (2017) conducted a statistical analysis of 421 fracturing data in 13 wells to demonstrate that effective stress in the reservoir significantly impacts fracture network characteristics. They concluded that higher effective stress results in wider, shorter, and more radial fractures.

Therefore, it is crucial in our study to define pore pressure and establish its correlation with fracture propagation. Fortunately, Han and van der Baan (2024) has computed the pore pressure gradient for our study area using DFIT data and extrapolating pressure versus time plots. Based on his calculations, the pore pressure gradient is 12.2 kPa (Table 6.1). The detailed explanation of the table is given in chapter 2. By multiplying this value with the depth map from seismic data, we can generate a pore pressure map for the area. This map will allow us to identify changes in pore pressure, aiding our understanding of fracture propagation. Hence, integrating this map with microseismic data constitutes a crucial step in comprehending fluid behavior. Increased pore pressure can elevate the breakdown pressure, potentially leading to shorter fractures. In cases where the pore pressure gradient is higher on one side of the well, it may result in uni-directional hydraulic fracture propagation.

6.5 Results and Discussion

This study began by importing the seismic data into the geophysical modeling software Seisware. Then, we followed the steps outlined in Figure 6.4. First, we matched the seismic data with well data, picked horizons, and checked the data quality. Next, we converted time to depth. In the interpretation stage, we created seismic attributes like dip, azimuth, and curvature, as well as a map of pore pressure.

Table 6.1: Comparative Analysis of In-Situ Stress Calculations: Insights from Han and van der Baan (2024), Shen et al. (2018) and Enlighten Geoscience (2021)

	Study by Han and van der Baan (2024)	Study by Enlighten Geoscience (2021) in KSMMA region	Study by Shen et al. (2018) in Fox Creek region
p_p(kPa/m)	$10.5 - 13.0$	$11.5 - 13.4$	16
σ_h(kPa/m)	$16.6 - 18.0$	$16.0 - 19.0$	17–21
σ_H(kPa/m)	$21.1 - 22.7$	$27.5 - 32.5$	33 ± 2
σ_v(kPa/m)	$24.5 - 25.5$	$25.1 - 25.3$	23–26
σ_H direction (deg)	$30 - 40$	$30 - 50$	$30 - 50$
In-situ stress regime	Normal fault	Strike-slip fault	Strike-slip fault

6.5.1 Data Preparation: Integrating Well Data with Seismic Data and Horizon Picking

Seismic-to-well tie

The well-to-seismic tie serves as a crucial method for correlating seismic reflection data with well log data to identify picking horizons in seismic profiles. In this study, we utilized the SeisWare program for our analysis.

The seismic-to-well-tie process commences with synthetic generation. To establish the well-seismic tie, density and sonic logs are employed to formulate an acoustic impedance log. This log delineates variations in acoustic impedance among rock layers, contributing to the reflection coefficient. Following this, we extracted a wavelet from the stacked seismic traces. The reflection coefficient was automatically convoluted with the extracted wavelet to produce synthetic seismograms by SeisWare. The results of the synthetic generation, along with the input data, are illustrated for three wells in Figure 6.10. In this figure, the first and second columns present the sonic and density logs, respectively, providing a comprehensive overview of the well log data.

The third column displays the generated seismograms with extracted wavelet (red). One can see that the generated synthetic data for Well 3 and Well 4 exhibits similarity, a characteristic attributed to their close proximity in terms of location. Once

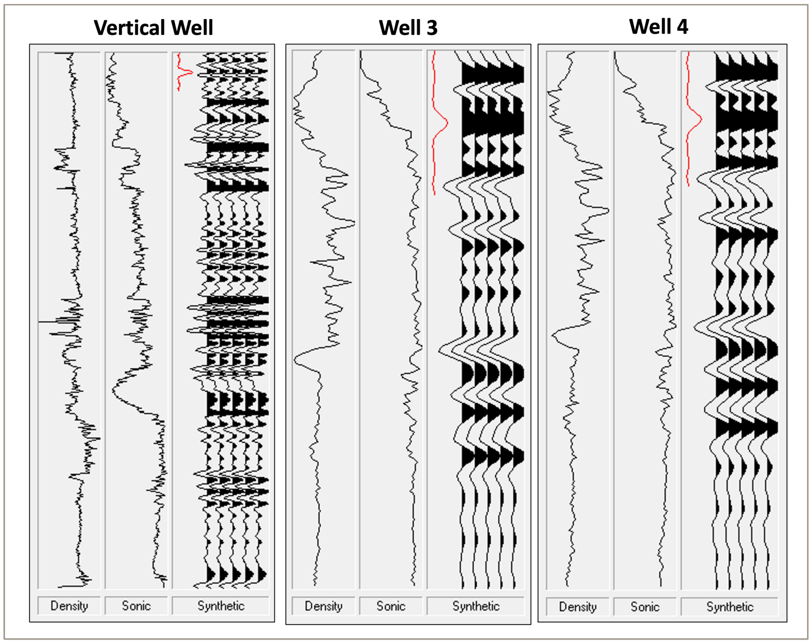

Figure 6.10: The synthetic seismogram data for three wells is provided. For each well, the first column represents density values, the second column represents sonic values, and the third column presents the synthetic results. The red line indicates the wavelet extracted from the inline and crossline data near the well, generated by the Seisware software.

the synthetic data has been generated, we proceed to match the well with the wells (Well 3, Well 4, and the vertical well). The results of the seismic-to-well tie procedure are depicted in Figure 6.11. All wells are represented in black, and the annotated generated seismograms are plotted beside the wells. The synthetic's quality relies on the well log's quality, the amplitudes of side lobes from extracted wavelets, and the success or failure in extracting a representative wavelet from noisy data.

Let's begin by examining the vertical well. This well is deeper, reaching the Belloy formation, which creates a strong reflection at 1230 ms in the seismic reflection data. We used this horizon to establish the well tie for the vertical well, applying a bulk shift of -28 ms. We intentionally avoided using stretch and squeeze to prevent modifications to the response. After aligning with the deepest feature, we checked the correlation between other reflections. It is evident that the shallower section exhibits mismatches, linked to near-surface effects.

Next, we addressed the two horizontal wells, Well 3 and Well 4. The results are presented on the left side of Figure 6.11. Since there were no strong reflections below the well due to its shorter length, our focus was on aligning the seismogram by applying a similar bulk shift of approximately -35 ms. Overall, a satisfactory match was achieved.

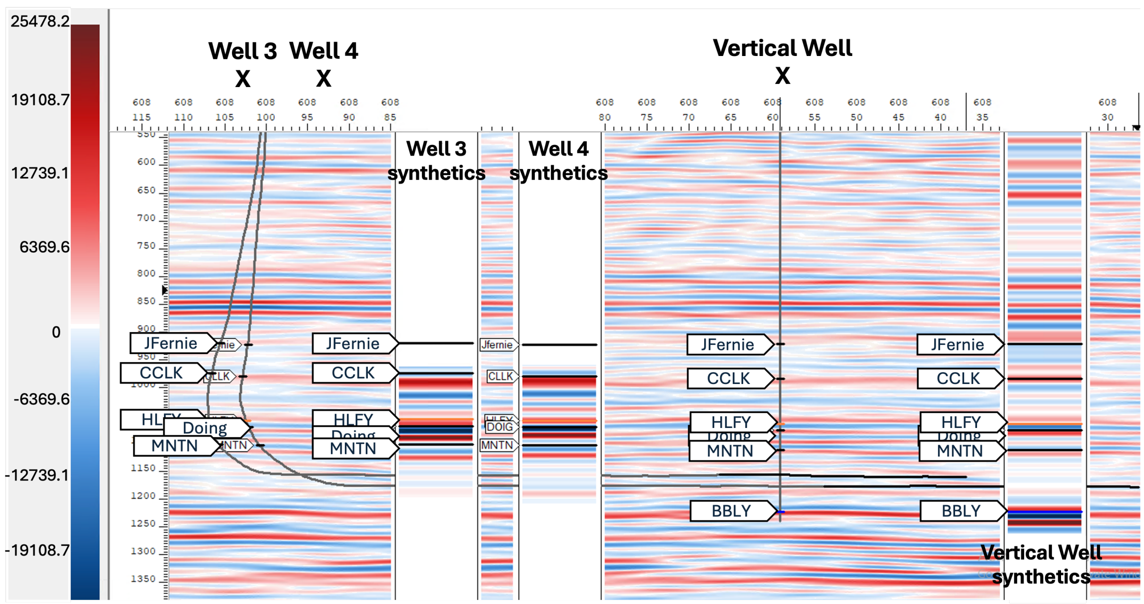

Figure 6.11: Synthetic seismograms for three wells (two horizontal and one vertical) plotted alongside the respective well logs. The good match between the wells and seismic has been made.

Horizon picking/tracing

The synthetic data generated for the three wells played a crucial role in identifying the well tops. Given our primary focus on the horizontal well, our attention was specifically directed towards the horizon picking procedure for the Middle Montney members D1, D2, D3, D4, and Belloy. As mentioned in the previous chapter, we had only identified the top depth of the Middle Montney (MNTN) members for the vertical well. Leveraging the correlation among the wells after the seismic-to-well tie procedure, we successfully pinpointed horizons D1, D2, D3, D4 and Belloy for the horizontal wells. The corresponding start location of the horizons have been annotated on the right corner of the figure. The decision on which amplitude response to use for the horizon picking (trough or peak) were crucial aspects of the process. It is noteworthy that for MNTN D4 we utilized peak, while for the remaining horizons, troughs were employed.

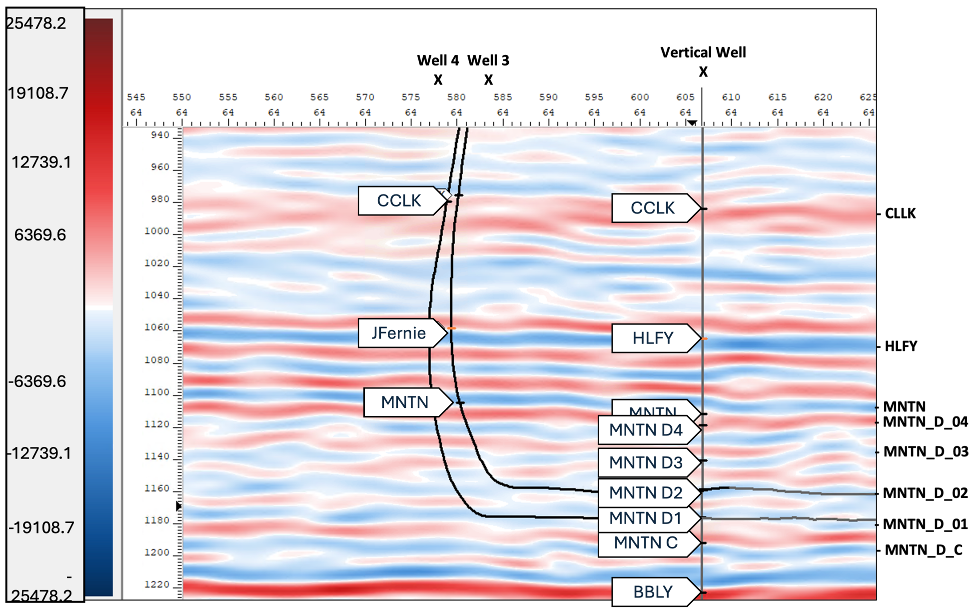

Figure 6.12: Seismic reflection overlaid with well tops to illustrate the alignment consistency among three wells. Middle Montney (MNTN) members were only provided for the vertical well.

After identification of well tops, we have moved to the picking horizons. The picking process involved a thorough analysis of discontinuities, with selections made at 10 inline and 20 crossline increments. The picking process was uncomplicated, facilitated by the relatively flat nature of the seismic reflection data, which lacked any faults.

The results are depicted in Figures 6.13a, 6.13b, 6.14a and, 6.14b, where the time maps of MNTN D1, D3, D4, and Belloy horizons (with scales) are displayed.The time map derived from horizon picking will provide the basis for generating the Seismic attribute map, enabling structural interpretation of the area. Since the program handles attribute calculations autonomously, our focus will primarily be on interpreting the resulting data.

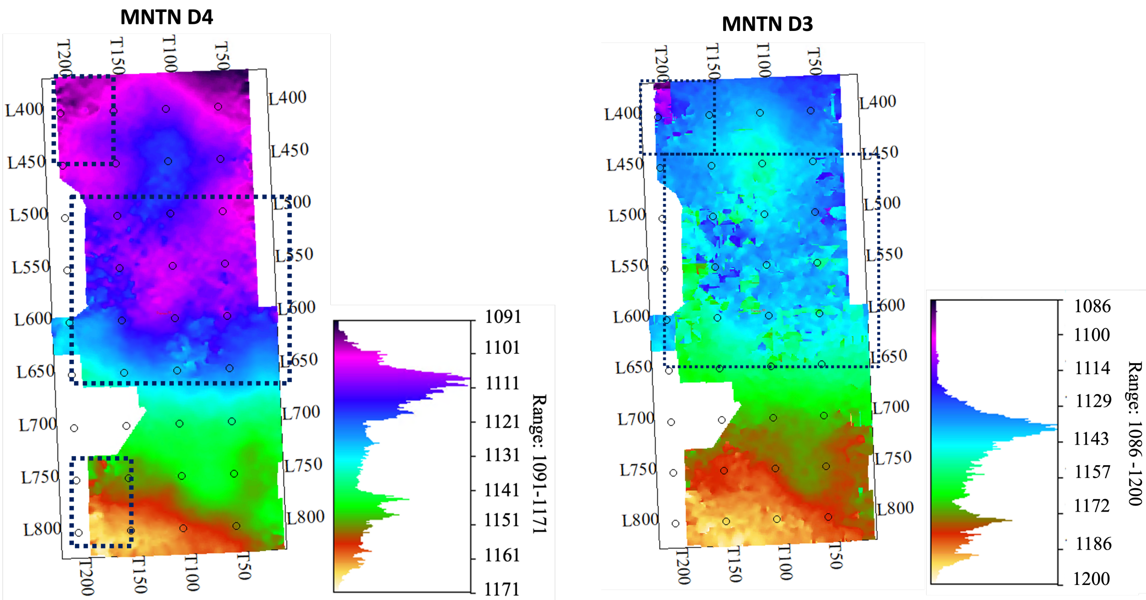

(a) MNTN D4: Time Map with color scale. (b) MNTN D4:: Time Map with color scale.

Figure 6.13: Time map after horizon picking: (a) MNTN D4 ; (b) MNTN D3. The black brackets represents the zones with acquisition artefacts.

Quality Control

We conducted horizon picking for MNTN D1, D3, D4, and Belloy and the results are illustrated in Figures 6.13a, 6.13b, 6.14a and, 6.14b. It is evident that D4, D3 and D1 exhibit non-smooth characteristics, attributed to data quality issues and discontinuities in some horizons (outlined by dark dashed rectangles). Consequently, we refrained from horizon picking for D2, which is situated between D3 and D1 and faced similar challenges.

Examining these complications closely, as depicted in Figure 6.15, the annotations represent the picked horizons MNTN D3 (black) and MNTN D1 (dark red). The first figure focuses on the complications primarily associated with the D3 horizon in the marked area on the basemap. The top figure corresponds to xline, while the bottom

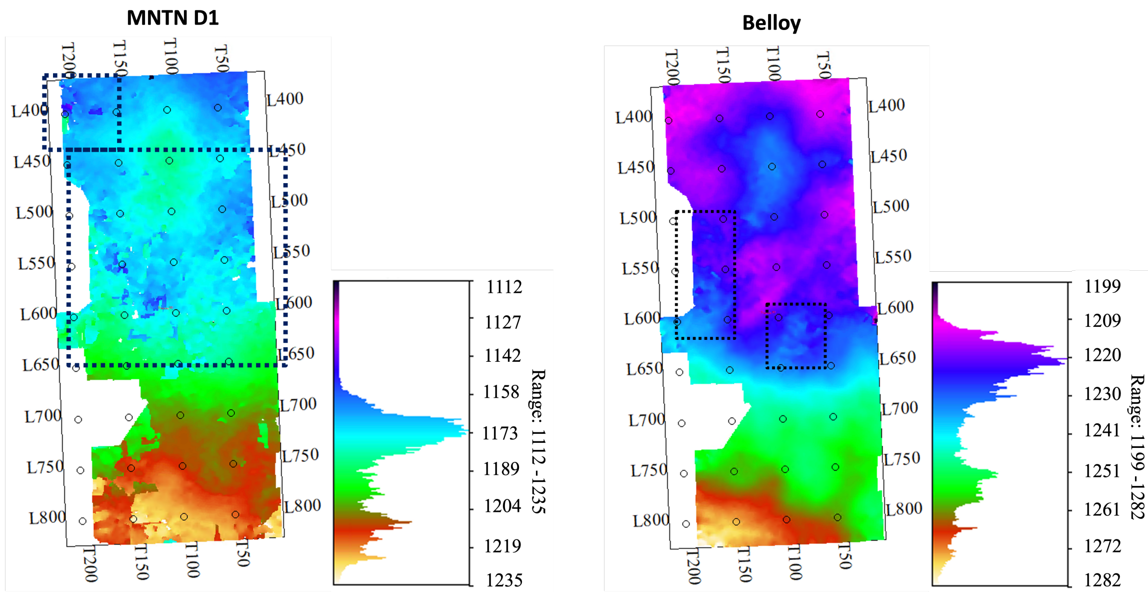

(a) MNTN D1: Time Map with color scale. (b) Belloy: Time Map with color scale.

Figure 6.14: Time map after horizon picking: (a) MNTN D1; (b) Belloy. Black brackets represent zones with acquisition artifacts. Belloy, which exhibits minimal artifacts, portrays the geology of the Montney accurately.

one corresponds to inline. It is evident from both the inline and crossline figures that there are interrupted horizons, consistently observed from the top to the bottom of the figure. This consistency suggests that the data may produce artifacts due to quality issues. Moreover, it is observable that the D3 horizon forms a trough and, in the indicated section, fades between two peaks. This complexity made the picking process challenging, and the autopick function in the software failed to detect these features in different sections, resulting in artefacts. This feature has been identified due to data quality issues, as evident in the inline figure with artefacts and faded sections.

Furthermore, the thickness between MNTN D4 and Belloy remains constant, as illustrated in Figure 6.16, where we have indicated the inline location on the isochron map between MNTN D4 and Belloy. The thickness remains constant, with the annotated north portion showing a thickness of 113 ms, while in the south, it is 110 ms, representing a consistent thickness. In the same figure 6.16, we have plotted the

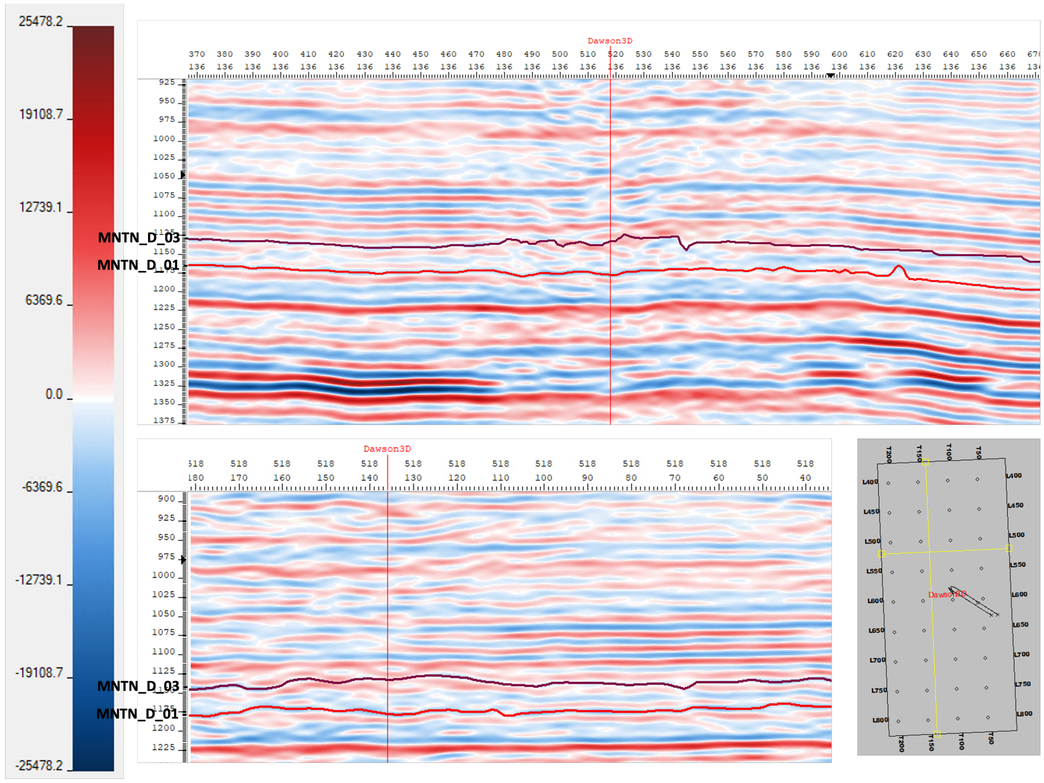

Figure 6.15: Quality Control (QC) assessment of the horizon picking. The base map indicates the location of the inline and crossline data for Montney D4 and Montney D3, highlighting areas with artifacts. The red line denotes the corresponding inline and crossline locations on seismic section. Regions along the red line exhibit low-quality data, posing challenges for picking. Notably, discerning troughs is difficult due to their proximity to converging peaks.

isochron time map of MNTN D4 and Belloy, showing a difference of 113 ms primarily. However, artifacts are still visible, mainly due to the Montney D4 formation. Hence, to delve deeper into interpretations, we've employed Belloy, which vividly portrays the geological high and lows.

Time-to-Depth Conversion

The process of time-to-depth conversion proved to be straightforward. Initially, we selected three horizons (Halfway, Doig and Montney D4), each with its top depth derived from available data, to establish the interval velocity model. This method ensured accuracy in presenting the interval velocity model. Employing a model consisting of three layers, our conversion technique utilized an average velocity down to

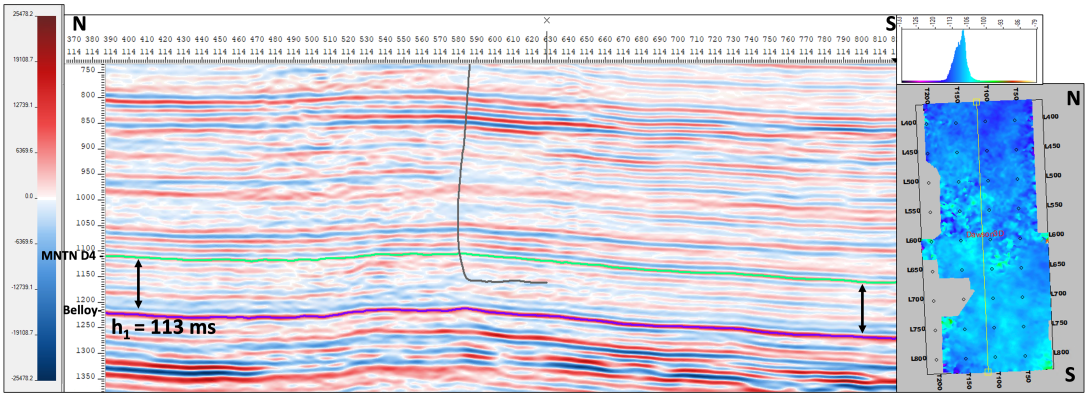

Figure 6.16: Isochron map displaying inline locations. The map illustrates a consistent thickness between the Belloy and Montney D4 horizons. This phenomenon is depicted on a seismic section where, from north to south, the thickness between these horizons remains approximately constant; in the north, it measures 113 ms, while in the south, it is 110 ms.

the first layer, followed by interval velocities for subsequent layers. We shown the results in table 6.2, where we represent the velocities from 3 wells for Halfway, Doig, and Montney D4.

Table 6.2: 1D velocities for 3 layers in 3 wells.

Well	Halfway		Doig		Montney D4	
	Velocity	Depth	Velocity	Depth	Velocity	Depth
Well 1	3447.5	1840.0	5947.5	1870.0	5036.3	1960.7
Well 3	3445.4	1820.0	6155.6	1855.5	4549.2	1941.3
Vertical well	3444.3	1820.0	6247.8	1856.7	4647.1	1943.7

The generated 3 layers model was applied to generate the time-depth conversion results, as illustrated in Figure 6.17. The left panel displays the time map of Belloy, while the right panel showcases the depth map of Belloy. It is evident that there are artifacts present post-conversion. However, these artifacts primarily overlap with regions where either no data is available or regions deemed outside of our area of interest. This observation is particularly pertinent as we intend to utilize this map for pore pressure calculations.

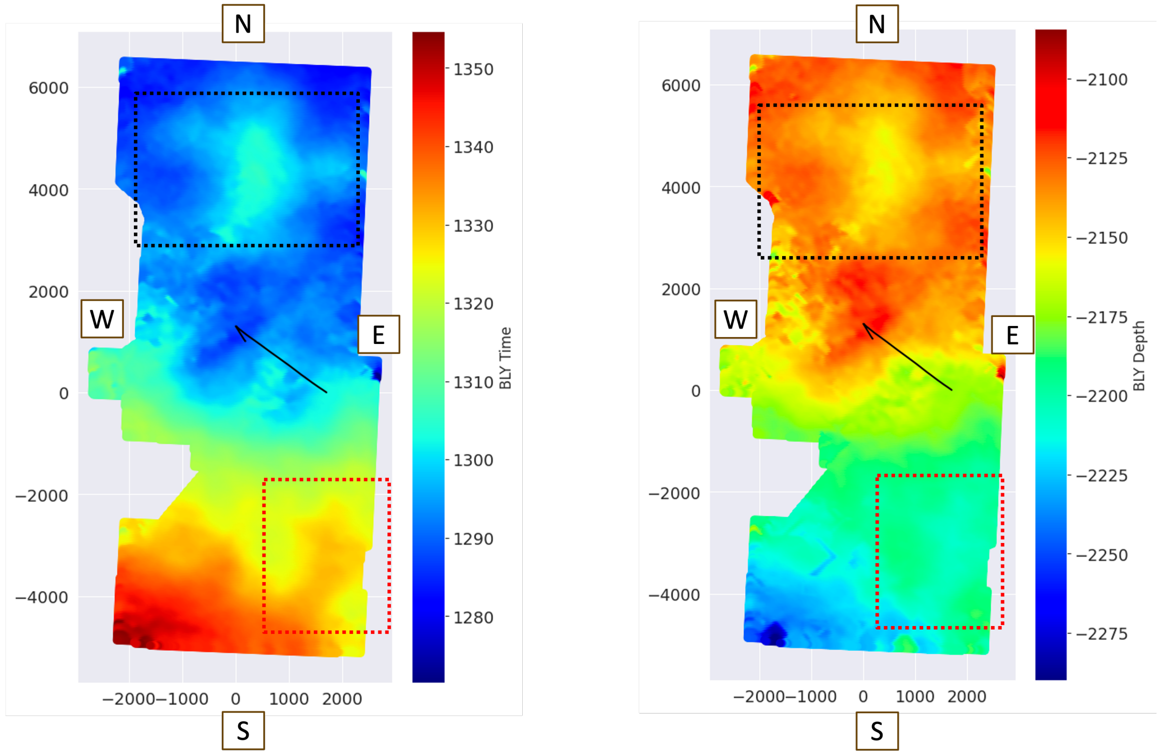

(a) Annotated time map of the Belloy horizon.

(b) Annotated depth map of the Belloy horizon.

Figure 6.17: Annotated maps of the Belloy horizon: (a) Time map; (b) Depth map. The black line denotes the well. The depth decreasing from Northeast to Southwest. The black bracket indicates the presence of a structural low. The red bracket represents the potential channel location.

6.5.2 Seismic Interpretation: Generation of Seismic Attributes and Pore Pressure Map with Interpretation

Time Map and Depth Map

Figure 6.17a and 6.17b display time-structure and depth maps for the Belloy formations interpreted from a 3D seismic volume acquired in Alberta, Canada. Both figures exhibit similar patterns, indicating successful time and depth conversions. The color bars in the figures represent time and depth, respectively, while the black line denotes the location of the well of interest. Annotations are utilized to depict geological directions, including North, South, West, and East.

Due to the similarity observed in both figures, we will interpret them concurrently.

Both datasets exhibit artifacts resulting from picking, especially on the edges. One can see the geological low in the north of the figure, forming a distinctive circular shape (black dashed rectangle). The red dashed line represents the potential channel. A clear northeast to southwest dipping trend is observable, with evident transition zones indicating higher dipping, particularly noticeable in the middle and southern regions of the figure where the colors transition from red to light green, and from light green to blue in the depth map, respectively. Variations in depth are evident along the length of the well, with the southwest (SW) section displaying more pronounced changes compared to the northwest (NW) section.

To estimate the changes in depth around the well, we selected points from the heel of the well. The depth shifted by 20 meters towards the southwest and by 11 meters towards the northeast over a distance of 1200 meters from the heel. The southwest and northeast dipping angles are 0.93 and 0.52, respectively. The change in depth from the heel of the well to the toe (2133 meters) is 51 meters, resulting in a dipping angle of approximately 1.5 degrees, which closely aligns with the dip calculation based on wellbore logs.

We anticipate that even minor variations in depth may exert a significant influence on the propagation of microseismic events. This is because deeper sections correspond to higher pore pressure. Such increases may influence the movement of fracture fluid, as fluids tend to flow towards zones with lower pressure.

Dip Map and Azimuth Map

We have used time map of Belloy to calculate the horizon based dip and azimuth map. The results are presented in figure 6.18. The black line represents the location of the well.

Interpreting the dipping map, as depicted in Figure 6.18a, reveals that the maximum dip value is approximately 10 degrees, with the majority of the area exhibiting dips around 1 degrees. The area represents consistent dipping. However, to simplify and describe the area, we have divided the seismic area roughly into 3 zones: Zone 1, Zone 2, and Zone 3. Zone 1 and Zone 3. Zone 1 is the area where a structural low was present, while Zone 3 is where we interpreted the channels. Zone 2 shows relatively high dipping values. One can observe that this dipping is mostly affected by data quality, which is discussed in the QC section and presented within square brackets. Furthermore, the dipping along the wellbore is varying, overlapping with the results in Chapter 5. Such inconsistency in dipping angles can significantly affect hydraulic fracture propagation.

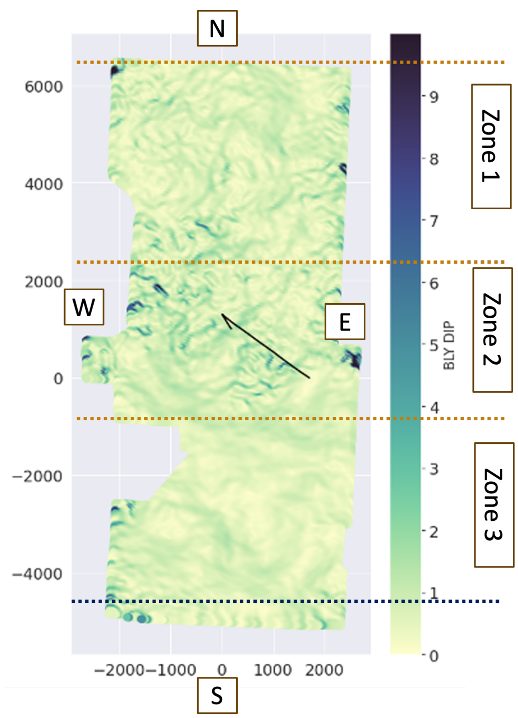

(a) Belloy horizon dip attribute map. Regional dip is small. Zone 2 displays higher dipping attributed to data quality compared to Zone 1 and 3.

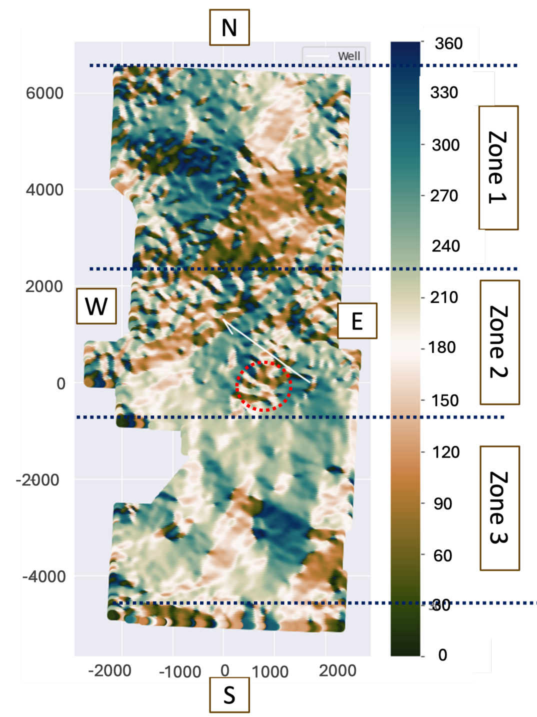

(b) Belloy horizon azimuth attribute map. Regional dip direction: Southwest. Local dips vary in Zones 1 and 2, while aligning with regional dip in Zone 3.

Figure 6.18: Horizon-based attribute maps of the Belloy horizon. (a) Dip attribute; (b) Dip azimuth attribute map. The well trajectory is depicted by the black line. The study area has been divided into zones to simplify the interpretations.

The azimuth map in Figure 6.18b illustrates directional trends relative to North (0 degrees), with orange indicating northeast and green representing southwestward orientations. The regional dip in the area predominantly follows a southwest direction. In Zone 3, the dipping azimuth aligns with the regional dip except in areas where channels are observed, indicating significant changes. Zones 1 and 2 exhibit varying azimuth directions, likely due to geological characteristics such as structural lows in Zone 1, while in Zone 2, we attribute it to the transition from higher to lower depths.

Around the wellbore, complex structural complexities are evident, with local dip azimuth differing from the regional dip in certain zones, creating intricate patterns. On the northeast side of the well, dipping aligns with the regional dip, while on the southwest side, the dip is reversed. We interpret that circled zone is the artefact related. Overall, asymmetry suggests potential differential fluid flow conditions, with the southwest side possibly encountering higher pore pressure due to deeper, more compacted rock layers, while the northeast side may offer relatively easier fluid passage.

Pore Pressure Map

We've generated a pore pressure map utilizing a straightforward methodology, leveraging a pore pressure gradient of 12.2 KPa as per Han and van der Baan (2024). This gradient was applied to our depth map to produce the pore pressure distribution across the area. Our aim is to observe how pore pressure varies due to changes in azimuthal dipping within the study area, with subsequent analysis intended to explore potential correlations with microseismic (MS) data.

The pore pressure map is depicted in Figure 6.19, with the well delineated by the black line. Notably, pressure levels within the interval exhibit considerable variation. Progressing from north to south, there's a discernible increase in pressure, indicating greater resistance to fluid flow in the northwest quadrant relative to the well. Furthermore, upon closer inspection, fluctuations in pore pressure around the wellbore are evident. Specifically, a significant pressure shift of approximately 400 kPa is observed at the midpoint of the well, transitioning from the southwest (SW) to the northeast

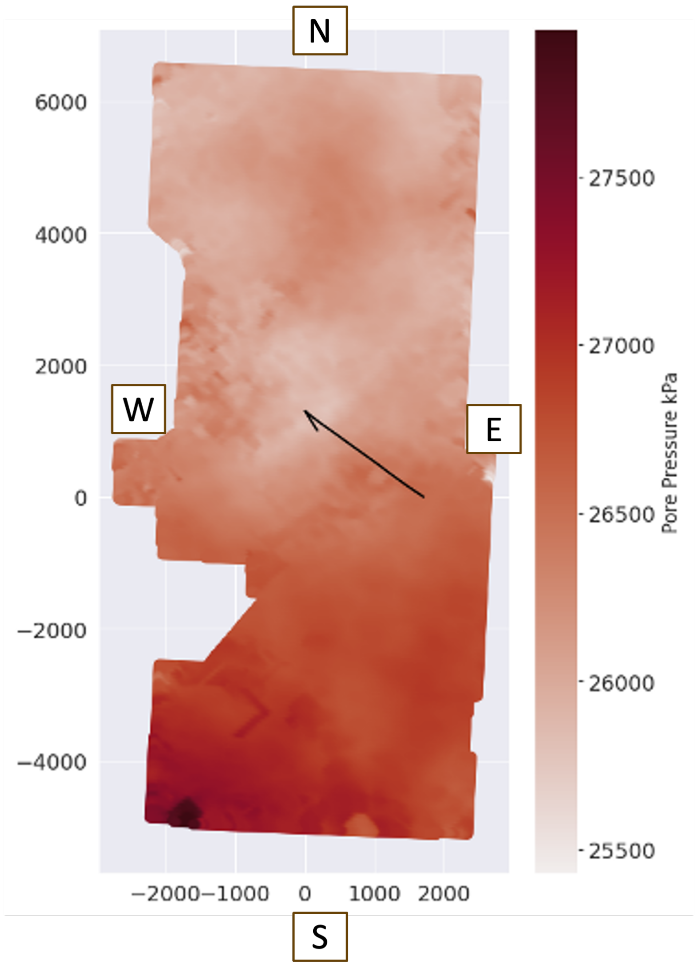

Figure 6.19: The pore pressure map generated from the depth map of the Belloy horizon by multiplying the depth with the pore pressure gradient of 12.2 kPa from Han and van der Baan (2024). The pore pressure increases towards the southwest direction due to the dipping. Variations in pore pressure are observed around the well.

(NE) side. This change could potentially pose challenges to hydraulic treatments in this region.

Maximum and Minimum Curvature Map

The analysis of both minimum and maximum curvature maps is pivotal for discerning faults and fractures within the area of interest. These maps portray the variations in curvature across the study area, offering insights into its structural deformations that potentially lead to cracks. Particularly, regions displaying elevated curvature values often signify zones of heightened bending, indicative of faulting or folding.

Figure 6.20 illustrates the maximum and minimum curvature maps, showcasing the subtle disparities between these two maps. There are spatial differences in the curvature across the area, representing the deformation which may correspond to the fractures. Therefore, we will carry out the interpretation for both of them together.

Zone 3 has the least curvature variations, while Zone 1 represents relatively medium curvature variations. Among them, Zone 2 experiences the most variations. This could be because in this zone there are artifacts (circles) that have affected the results. The well is situated in Zone 2 where around it, a high number of fractures can be identified. Based on the previous chapter 5, we have identified 56 fractures. Along the well, there are two dominant preferential strikes of the curvatures, one being perpendicular to the wellbore, while another being parallel to the well direction. The wellbore perpendicular curvatures align with the principal azimuth direction and the preferred fracture propagation direction (transverse to the wellbore).

6.5.3 Seismic Interpretation: Microseismic Events and Seismic Attributes

The integration of MS data with seismic attributes is crucial for comprehending the geological impact on seismic data. Our initial focus is on integrating MS data with the azimuth attribute. Given the complexity of this integration, representing all 38 stages in plots is impractical. Therefore, we've opted to plot the locations of each stage and indicate those propagating in the Southwest direction with black arrows based on MS cloud analysis (Figure 6.1). The results are illustrated in Figure 6.21, where we observe that hydraulic fractures tend to move toward the Northeast direction because this direction corresponds to the up-dip direction.

Furthermore, we have endeavored to correlate the propagation of microseismic events with changes in pore pressure within the region. Figure 6.22 on left shows where we have plotted the well trajectory with hydraulic treatment stages (black

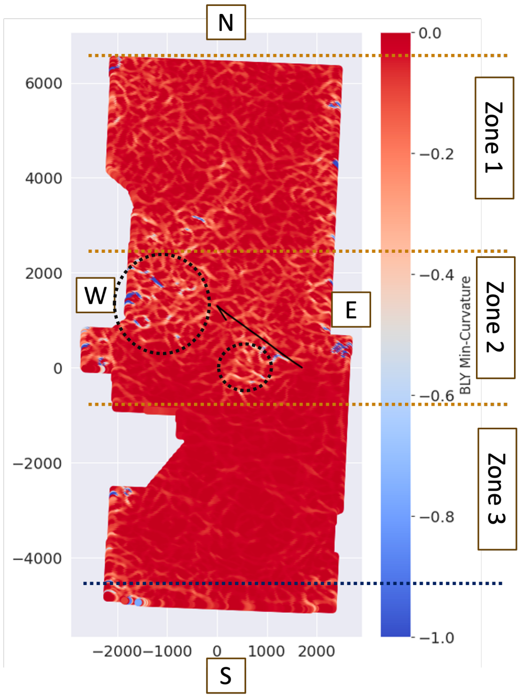

(a) Horizon-based minimum curvature map for the Belloy formation. Lighter red/white areas indicate smaller curvatures, representing structural lows.

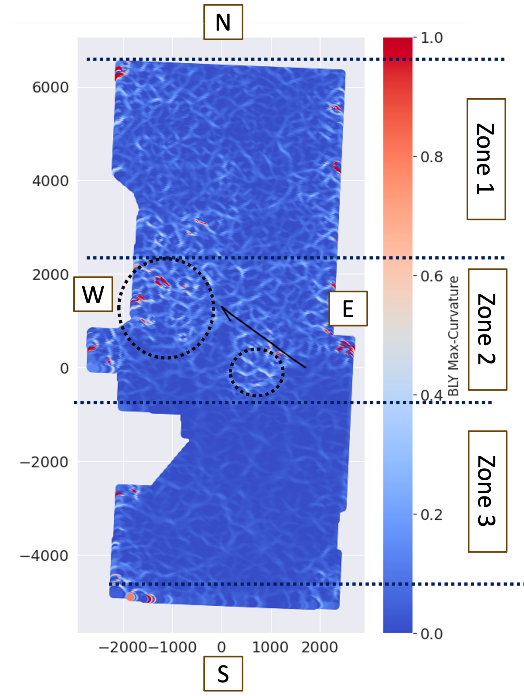

(b) Horizon-based maximum curvature map for the Belloy formation. Lighter red/white areas indicate high curvatures, representing structural highs.

Figure 6.20: Horizon-based curvature maps for the Belloy formation: (a) Minimum curvature map and (b) Maximum curvature map. The study area has been divided into three zones: Zone 1, medium curvature; Zone 2, high curvature; and Zone 3, low curvature zones. The well is situated in a high curvature zone, exhibiting two striking curvature directions: parallel and perpendicular to the wellbore. The circles represents the artefacts.

dots), and arrows indicate the stages toward which MS moves in the SW direction. The circle represents the location where artifacts exist due to horizon picking, causing low pore pressure (bright color). The pore pressure is increasing toward the SW direction. As we know, fluid tends to move toward the direction where less pressure is observed. Additionally, higher initial pore pressure corresponds to a higher formation breakdown pressure. This phenomena is much obvious around the circled zone that elevated pressure forced all the events move toward NE region (right figure). Toward the heel of the well, it is obvious that pressure is relatively uniformly distributed.

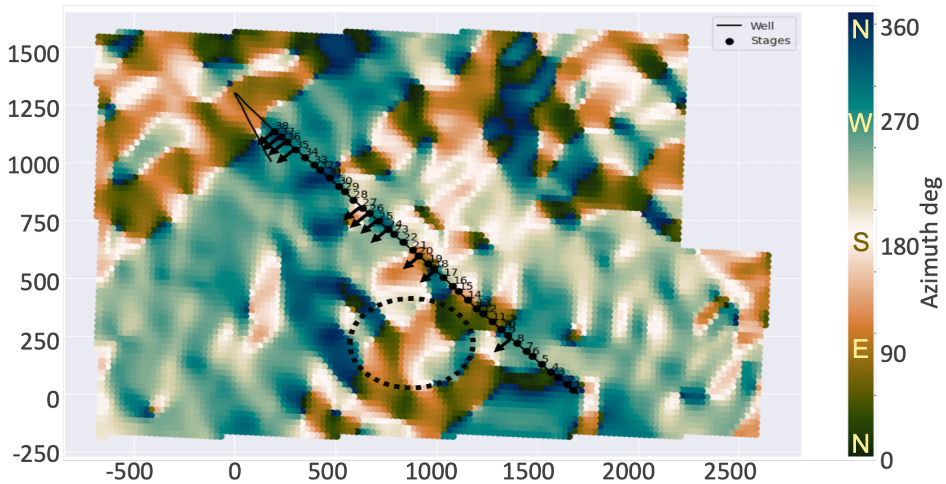

Figure 6.21: The dip azimuth attribute map of the Belloy horizon (Figure 6.18b) zooms in on the well area. The black line marks the well trajectory, and dots show the depth of hydraulic fracture treatment ports. Black arrows indicate stages where microseismic events mainly moved southwestward. The circle highlights an artifact. Initial observations suggest microseismic events trend toward the northeast, up-dip direction.

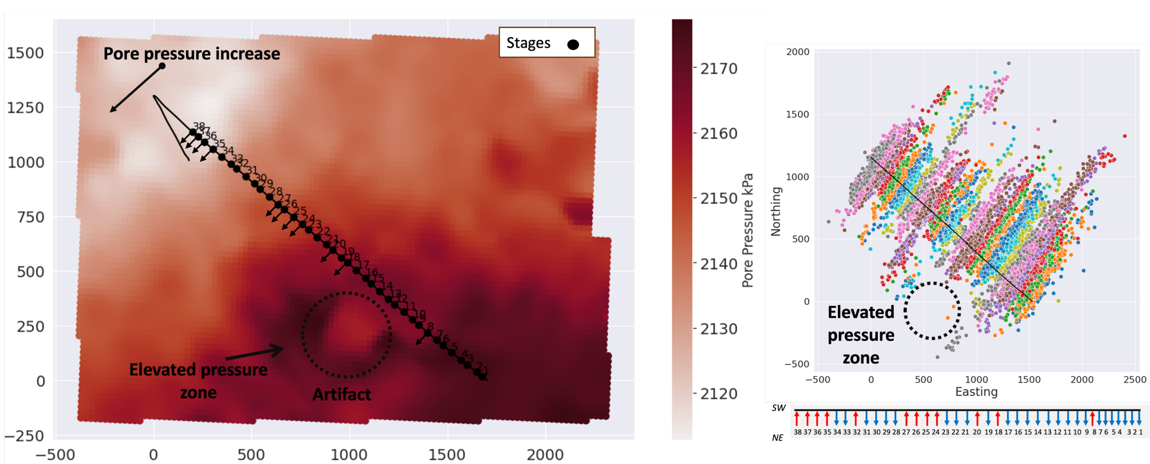

Figure 6.22: The left figure shows pore pressure map focuses on the Belloy horizon (Figure 6.19), centered on the well. The black line depicts the well trajectory, while dots denote the depth of hydraulic fracture treatment ports. Black arrows highlight stages where microseismic events predominantly moved southwestward. The circle denotes data quality issues. Initial observations suggest microseismic events tend to move NE when pressure is high in the SW. Right figure shows planar view of microseismic clouds. The circled zone represents the elaveted pressure zone that forces events to move toward NE direction.

6.6 Conclusions

Understanding geophysical data, particularly reflection seismic data, is essential for understanding the effect of geology on microseismic event propagation. Our objective is to comprehensively understand the geology in the area, which will serve as a means to understand fracture propagation dynamics by integrating structural and pore pressure analyses.

Initially, we generated seismic maps such as time, Azimuth, Dip, Maximum, and Minimum curvature, as well as a pore pressure map, once we successfully performed seismic-to-well-tie, horizon picking, and time-depth conversion. Generally, the dipping of the area is small, and the regional azimuth direction is SW. For the simplicity of interpretation and defining geological features, we have divided the zone into 3, with our area of interest, where the well is located, being zone 2. Zone 2 has data quality issues. Overall, this area corresponds to a relatively high dip angle, and the local azimuth varies from the regional dip. Integration with MS reveals that most of the events move toward the NE direction because it is the updip direction. Pore pressure analysis also revealed that pore pressure increases toward the SW direction, which is the reason why most of the events move toward the NE direction. The minimum and maximum curvature exhibit two strike directions, one of them being perpendicular to the wellbore, which aligns with the microseismic event propagation direction. The Dip map shows that the general dip in the area is small, with the regional dip directed toward the SW direction, but the local dip changes over the area.

The overall results reveal that the unidirectional propagation of the hydraulic fractures is due to the pore pressure distribution, which is related to dip and dip azimuth.

Chapter 7

Stress Analysis

7.1 Summary

Understanding horizontal stresses is pivotal in multi-stage fracturing operations to comprehend fracture propagation dynamics. As stages progress, the minimum horizontal stress escalates, reshaping stress anisotropy and causing phenomena such as stress interference or stress shadow. These alterations significantly influence hydraulic fracture propagation, as demonstrated by Ortega Perez and van der Baan (2024)), who correlated microseismic cloud patterns with factors like stress shadows. Additionally, our cloud analysis revealed stages (5, 10, 35, and 30) exhibiting arching towards subsequent stages, coinciding with a decrease in fracture length (Figure 7.2, 7.3). This phenomenon prompts further investigation to ascertain if the shift in cloud behavior is associated with horizontal stress flips.

In this chapter, we employ Instantaneous Shut-in Pressure (ISIP) analysis to capture mechanical stress interference effects. Each hydraulic fracturing stage amplifies stress perpendicular to the fracture propagation axis, resulting in increased ISIP values. Utilizing the Stress Escalation Model (SEM) by Roussel (2017) allows us to quantify horizontal stress anisotropy and fracture height dimensions. Mechanical interference not only modulates stress magnitude but also orientation, potentially influencing fractures to move towards or away from the existing fractures (Roussel, 2017). By calculating fracture heights through ISIP analysis and corroborating them with microseismic observations, we determine fracture dimensions and spacing. Application of our method to field datasets yields estimations closely aligning with observations, validating the robustness of our approach.

This chapter delves into ISIP analysis across four wells, with a focused examination of Well 3. Our findings suggest no discernible stress reorientation across any of the wells. However, our analysis indicates a stress interference from previous stages might be the cause of variation in fracture length and propagation. Comparing fracture height results derived from microseismic data with those from ISIP analysis validates the efficacy of our method.

7.2 Introduction

There are four wells in the area that have undergone multistage hydraulic treatment. For our analysis, we will use these four wells to analyze the mechanical stress interference. The locations of the wells have been illustrated in Figure 7.1. One can see that Well 1 and Well 3 have been drilled into two different horizons. The distance (True Vertical Depth (TVD)) between the horizontal sections of the wells is approximately 100 meters.

Figures 7.2 and 7.3 present a detailed depiction of microseismic activity, grouped into sets of five stages each. Notably, in stages 5, 10, 35, and 30, the observed planar view indicates a tendency towards arching towards the subsequent stage. This phenomenon suggests a potential link to stress reorientation during hydraulic fracturing. Consequently, it is imperative to employ the Stress Escalation Method (SEM) to investigate whether this arching behavior stems from horizontal stress flips, thus elucidating the underlying mechanics driving the observed microseismic activity.

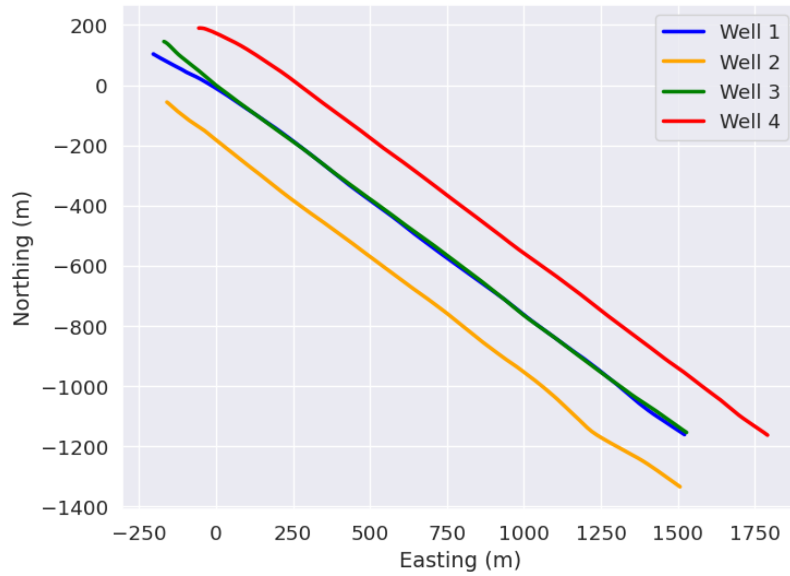

(a) Geometry of Wells: Lateral view

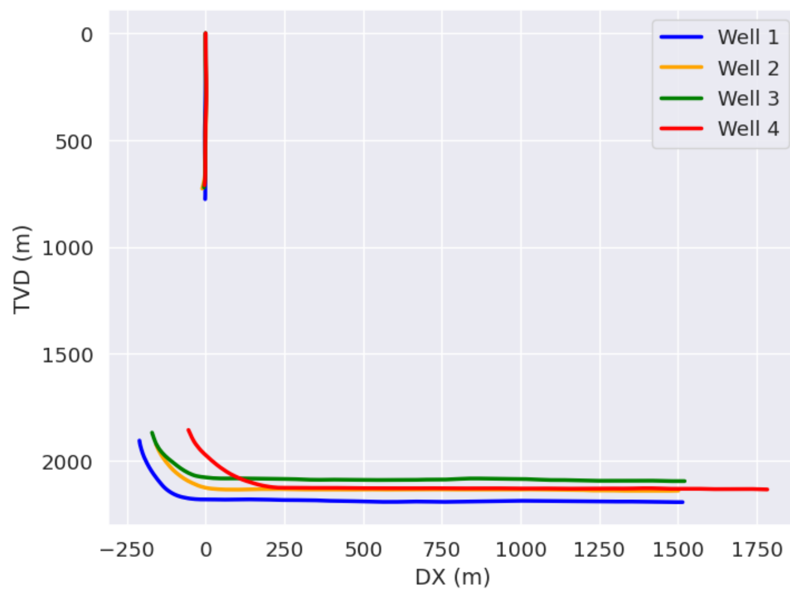

(b) Geometry of Wells: Upper view

Figure 7.1: The wells are visually differentiated by color, with their numbering following the sequence of hydraulic fracture treatments. The landing height difference between Well 1 and Well 3 is 100 m.

7.3 Theory

Better ways of understanding hydraulic fractures help us see how well wells are completed by looking at the fracture network. Deciding how far apart to put hydraulic

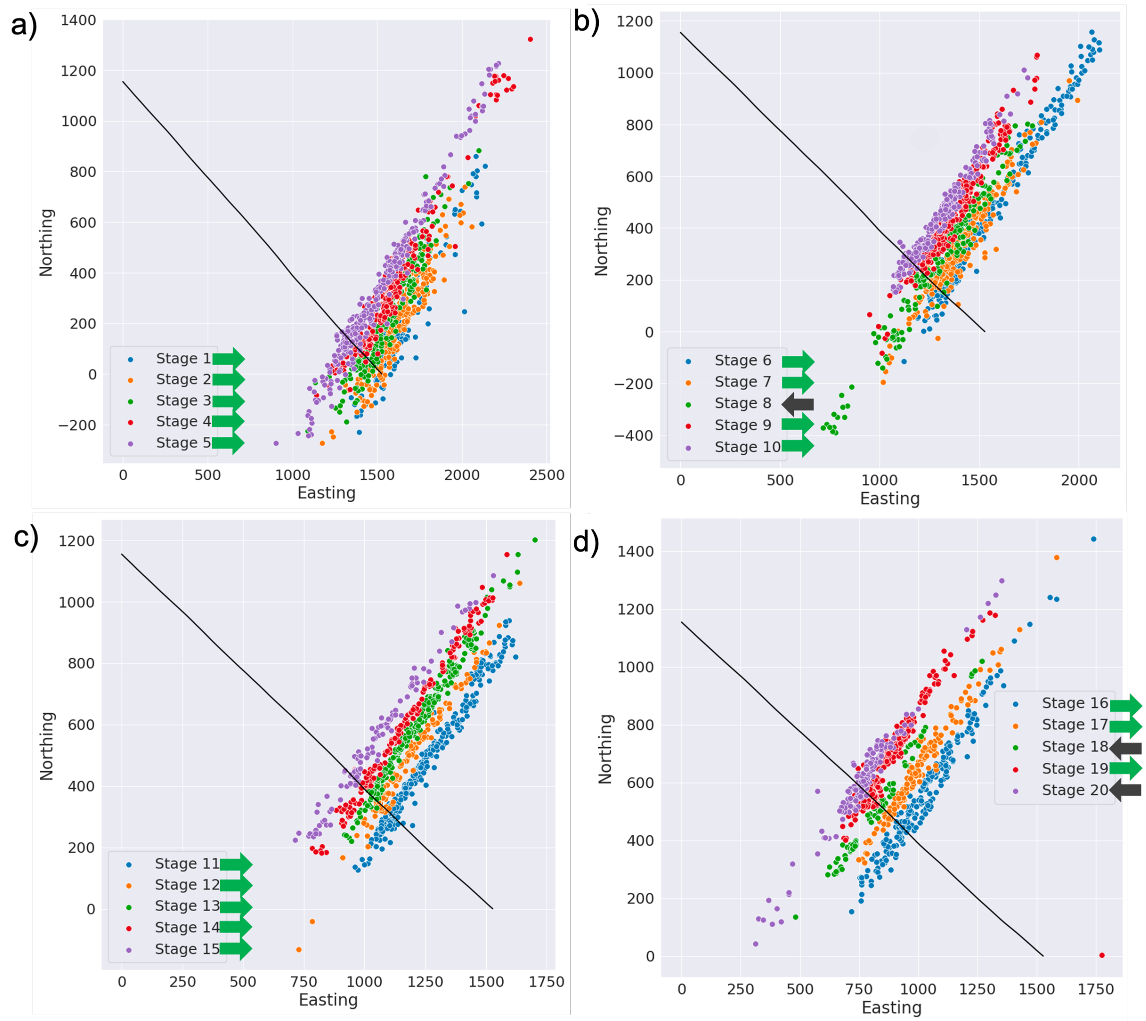

Figure 7.2: Planar view of the microseismic clouds for: (a) Stages 1-5; (b) Stages 6-10; (c) Stages 11-15; (d) Stages 15-20. The arrows represent the direction of propagation, green is Northeast while gray is southwest

fracturing stages is important for making horizontal wells work better in unconventional reservoirs. Even though many in the industry believe using more stages and placing them closer together is the way to go, real-world experience shows that this doesn't always make production better (Roussel, 2017; Yu & Sepehrnoori, 2013). In fact, tighter spacing can add incrementally less hydrocarbon production per stage because closely spaced stages interfere with one another, causing systematic interference phenomena collectively referred to as the "stress shadow." Fisher et al. (2004) demonstrated that creating a hydraulic fracture generates a zone of altered local stresses

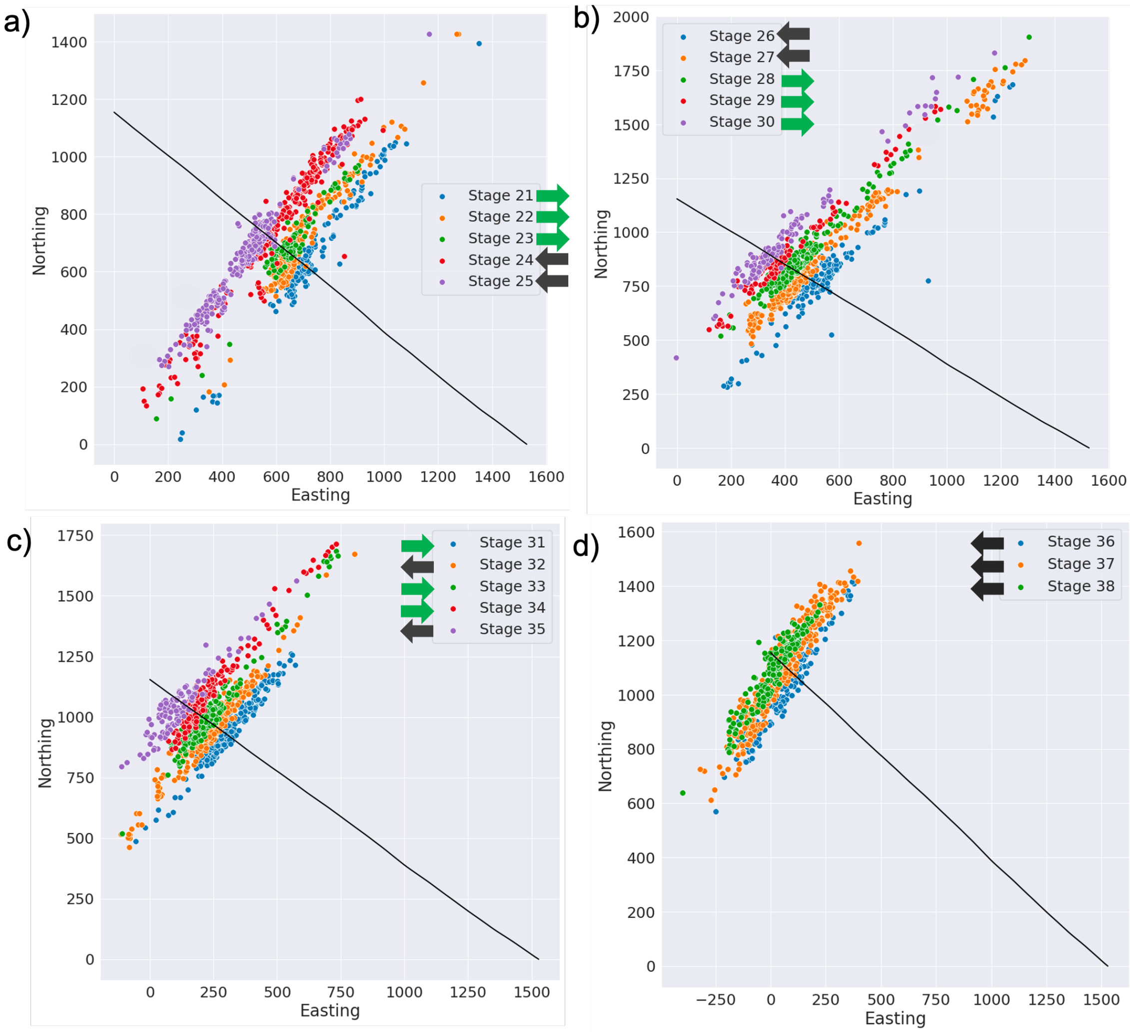

Figure 7.3: Planar view of the microseismic clouds for: (a) Stages 21-25; (b) Stages 26-30; (c) Stages 31-35; (d) Stages 35-38. The arrows represent the direction of propagation, green is Northeast while gray is southwest

that may impact the orientation of subsequent fractures due to the stress shadow.

7.3.1 Horizontal Stress Anisotropy

Roussel (2017) offered a method to discern whether a stress plateau results from overcoming in-situ horizontal stress anisotropy, causing stress reorientation or occurs normally. The stress plateau represents the total stress interference induced at the end of the hydraulic fracture treatment. To grasp mechanical stress reorientation better, we can analyze the distribution of maximum horizontal stress around a dilated fracture. Figure 7.4 was created using the method outlined by Roussel (2017). The figure depicts two scenarios: When a fracture extends, it triggers stress around it, influenced by the stress load, which reflects the net pressure from preceding stages. If the stress load is smaller than the net pressure in the subsequent stage, the net pressure is high enough to propagate the fracture transversely (perpendicular) to the wellbore (Case 1). This phenomenon is also presented in Table 7.1, where the horizontal stress anisotropy is more than the total stress interference ($\sigma_{plateau}$), representing the plateau to be "normal". If the stress load is higher than the net pressure in the subsequent stage, induced stresses are high enough that the stress interference between two fractures affects the fracture propagation, forcing the fractures to propagate longitudinally (Case 2). This phenomenon is also presented in Table 7.1, where the horizontal stress anisotropy is less than the total stress interference ($\sigma_{plateau}$), and fractures move toward the next stage representing the plateau to be "Stress reorientation". Table 7.1 also represents the 3rd case where the horizontal stress anisotropy is slightly higher than the total stress interference; in such cases, "limited orientation" occurs.

As the in-situ stress anisotropy decreases, the deviation of the horizontal stress anisotropy direction from its initial orientation increases during multi-stage fracturing Roussel (2017) and Roussel et al. (2021). When the space between stages or the horizontal stress difference decreases, fractures are more likely to change direction from transverse. This tendency towards reorientation increases, as noted by Roussel (2017).

7.3.2 Instantaneous Shut-in Pressure (ISIP)

In multistage fracturing, the ISIP characterizes the pressure necessary to propagate fractures in the formation. ISIP is correlated to the net fracture pressure (p_{net}) inside the fracture, the closure stress (σ_{hmin}), and the accumulated stress $\Delta\sigma_{shadow}$ (Moradi, 2021).

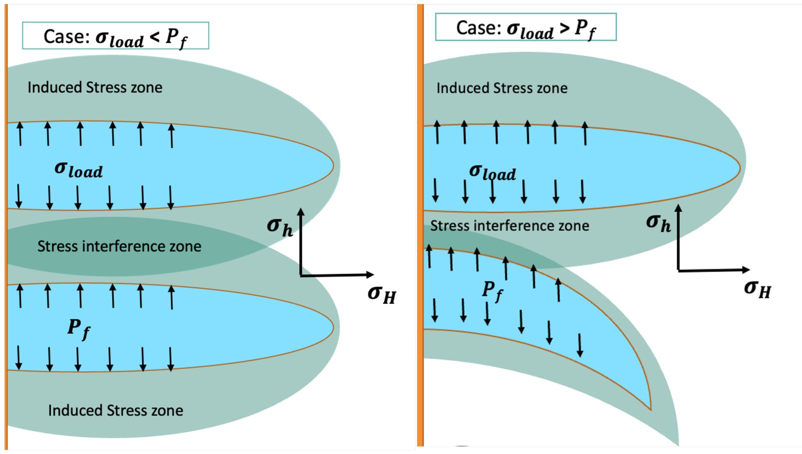

Figure 7.4: Illustration of the physics of the SEM method: The left figure represents the plateau stage where stress load (σ_{load}) is smaller than the net pressure (P_{net}), leading to transversal fracture propagation. The right figure illustrates stress reorientation, where stress load (σ_{load}) exceeds the net pressure (P_{net}), resulting in longitudinally propagating fractures.

Table 7.1: Phenomenon responsible for stress plateau (Modified from Roussel (2017).

Case	Phenomena	Plateau
$\sigma_{\text{load}} > \text{ISIP}(1) - \sigma_{\text{hmin}}$	$\sigma_{\text{hmax}} - \sigma_{\text{hmin}} \sim \Delta\sigma_{\text{plateau}}$	Reorientation
$\sigma_{\text{load}} \approx 0.5(\text{ISIP}(1) - \sigma_{\text{hmin}})$	$\sigma_{\text{hmax}} - \sigma_{\text{hmin}} \geq \Delta\sigma_{\text{plateau}}$	Limited Reorientation
$\sigma_{\text{load}} < 0.5(\text{ISIP}(1) - \sigma_{\text{hmin}})$	$\sigma_{\text{hmax}} - \sigma_{\text{hmin}} > \Delta\sigma_{\text{plateau}}$	Normal

$$\text{ISIP}_{(\text{n})} = \text{p}_{\text{net}} + \sigma_{\text{hmin}} + \Delta\sigma_{\text{shadow}}\,(\text{n}-1), \tag{7.1}$$

as the hydraulic treatment stage increases, a higher pressure is expected to be exerted for each subsequent stage to initiate new fractures. Additionally, with successive fractures occurring, the stress reversal area widens Soliman et al. (2008). Following the initial stages, the closing stress escalates rapidly, as evident in stress escalation curves (Roussel, 2017).

Assuming $\Delta\sigma_{\text{shadow}}$ is equal to zero (no stress interference effect in the first stage within the well), (p_{net}) can be derived using the ISIP of the first stage as

$$\text{ISIP}(1) = (p_{net})_{@\text{ shut-in}} + \sigma_{\text{hmin}} \,. \tag{7.2}$$

7.3.3 Stress Escalation Model (SEM)

The propagation of induced fractures disrupts stress and strain in their vicinity, which is essential for understanding fracture characteristics, particularly fracture height. There's a relationship between the increase in stress away from a fracture and its half-height, h_f, indicating its geometry. Analytical equations for stress disturbance due to a pressurized crack were derived by Sneddon (1946), considering two extreme cases: semi-infinite fractures ($L_f >> 2h_f$) and penny-shaped fractures ($L_f = 2h_f$), where L_f represents half the fracture length. The stress interference decay for these geometries is illustrated in Figure 1, perpendicular to the fracture face and through its midpoint.

Later, Roussel (2017) proposed an analytical model for the cumulative stress interference from multiple fracturing stages. This model involves two parameters: the stress correction factor, $\mathit{\Phi}_s$ (stress decay factor), and the stress load σ_{load} (recently named as residual stress, σ_r, in a study by Roussel et al. (2021)). The stress load signifies the remaining pressure in hydraulic fractures at the beginning of the next stage, often observed to be less than half of the net fracturing pressure during shut-in in numerous field cases (Roussel, 2017; Roussel et al., 2021).

If the fracture length is much larger than its height (semi-infinite), and the completion design and mechanical properties are uniform along the lateral, Roussel (2017) describe the increase in ISIP from stress shadowing for each stage using Equations 7.3 and 7.4:

$$\Delta\sigma_{\text{shadow}}\,(n) = \frac{\Phi_s \sigma_{load}}{1 - \Phi_s}\left(1 - \Phi_s^{n-1}\right) \tag{7.3}$$

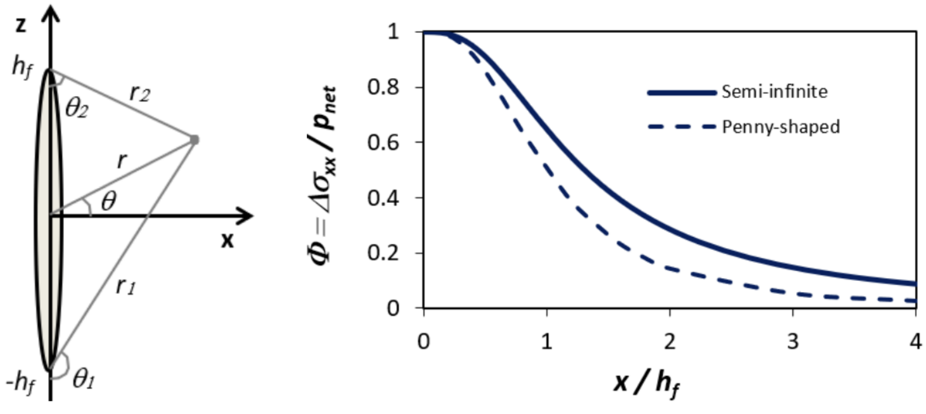

Figure 7.5: Comparison of analytical solutions for the stresses normal (y=z=0) to a semi-infinite and penny-shaped fracture. h_f represents the fracture halft length, x represents the fracture length, Φ represents the stress correction factor, $\Delta\sigma_{xx}$ represents the minimum horizontal stress, P_{net} represents the net pressure (reproduced from Roussel (2017) with permission from Society of Petroleum Engineers (SPE)).

$$\Phi_s = \frac{1}{N_p}\sum_{i=1}^{N_p} 1 - \left(\frac{i \times s_f}{2h_f}\right)^3 \left[1 + \left(\frac{i \times s_f}{2h_f}\right)^2\right]^{-3/2} \tag{7.4}$$

Here, Equation 7.3 calculates the change in shadow stress for each stage, where Φ_s represents the stress decay factor in semi-infinite fracture, σ_{load} is the residual stress, and n denotes the stage number. Equation 7.4 defines Φ_s, which depends on the number of clusters per stage and the spacing between them. The simulation results for load-normalized shadow stress for different spacing-to-height ratio with a single perforation cluster value has been illustrated in figure 7.6.

To express the total number of stress interference, Roussel (2017) shown the expression as the stress plateau which is derived by calculating the limit of Equation 7.3 as stage numbers goes toward infinity:

$$\Delta\sigma_{\text{plateau}} = \lim_{\text{n}\to\infty} \Delta\sigma_{\text{shadow}}(n) = \lim_{\text{n}\to\infty}\left(\frac{\Phi_s\sigma_{load}}{1-\Phi_s}\left(1-\Phi_s^{n-1}\right)\right) = \frac{\Phi_s\sigma_{load}}{1-\Phi_s} \tag{7.5}$$

Equation 7.5 can be applied to estimate the collective stress interference resulting from a horizontal stimulation after completing a multistage hydraulic fracturing pro-

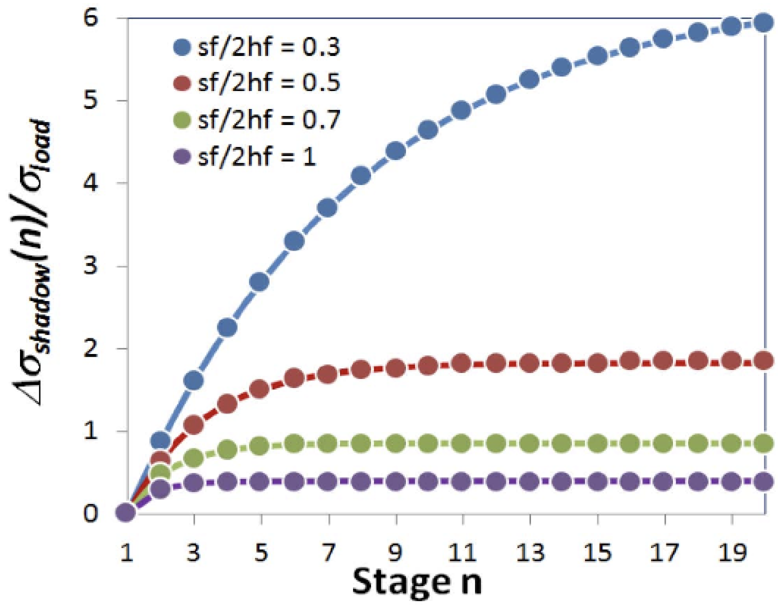

Figure 7.6: Load-normalized magnitude of stress interference versus the number of fracture stages for different $s_f/2h_f$ ratios for a single perforation cluster (reproduced from Roussel (2017) with permission from Society of Petroleum Engineers (SPE)).

cess. This estimation holds for different combinations of cluster numbers and spacing values, considering typical values for the stress load and hydraulic fracture height, as outlined by Roussel (2017).

Escalation equation and type-curves

Later, Roussel (2017) introduced Equation (7.6) by leveraging the method of depicting the response of a first-order, linear time-invariant (LTI) system to a step input. The introduced formula represents the escalation of stress shadow and reaching a plateau.

$$\Delta\sigma_{\text{shadow}}\left(n\right) = \Delta\sigma_{\text{plateau}}\left(1 - e^{\frac{1-n}{\text{escalation}}}\right). \tag{7.6}$$

Through iterative processes of constructing the multi-stage stress interference model using equation 7.3 and 7.4 for various stages and aligning it with the stress escalation equation (equation 7.6) across multiple combinations of perforation clusters per stage, Roussel (2017) established a correlation. This correlation elucidates how the spacing-to-height ratio relates to two critical parameters: the induced stress plateau

($\Delta\sigma_{\text{plateau}}$) and the escalation number (Escalation), as evidenced in figure 7.7 (Roussel, 2017; Roussel et al., 2021). A significant finding from Roussel (2017) is that a singular ratio of stage spacing to height corresponds precisely to a particular value of either the escalation number or the stress plateau.

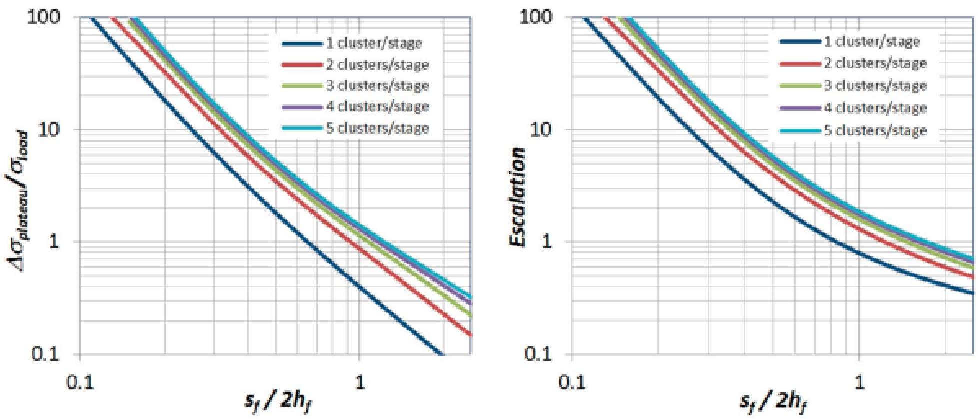

Figure 7.7: Type-curves of (a) the load-normalized stress plateau and (b) the escalation number for different numbers of perforation clusters (reproduced from Roussel (2017) with permission from Society of Petroleum Engineers (SPE)).

The interference ratio is the slope of the stress escalation curve when the normalized by the load at the beginning (Figure 7.8). It signifies the direct relationship between stress plateau and spacing-to-height ratio. This interference ratio is calculated directly from the plot of stress interference as it corresponds to the slope of the curve at the origin (Equation 7.7) (Roussel, 2017). If the slope is steep at the beginning, it means more fracture stages are causing stress interference. The maximum limit is when the slope reaches a value of 1 (Roussel, 2017).

$$\frac{d}{dn}\left(\frac{\Delta\sigma_{\text{shadow}}\,(n)}{\sigma_{\text{load}}}\right)_{n=1} = \frac{\Delta\sigma_{\text{plateau}}}{\sigma_{\text{load}}}\frac{d}{dn}\left(1-e^{\frac{1-n}{\text{Escalation}}}\right)_{n=1} = \frac{\Delta\sigma_{\text{plateau}}}{\sigma_{\text{load}}\ *\ \text{Escalation}}, \tag{7.7}$$

Just like the escalation number and the load-normalized stress plateau, Roussel (2017) also created type-curves for the interference ratio, which correspond to the spacing-to-height ratio.

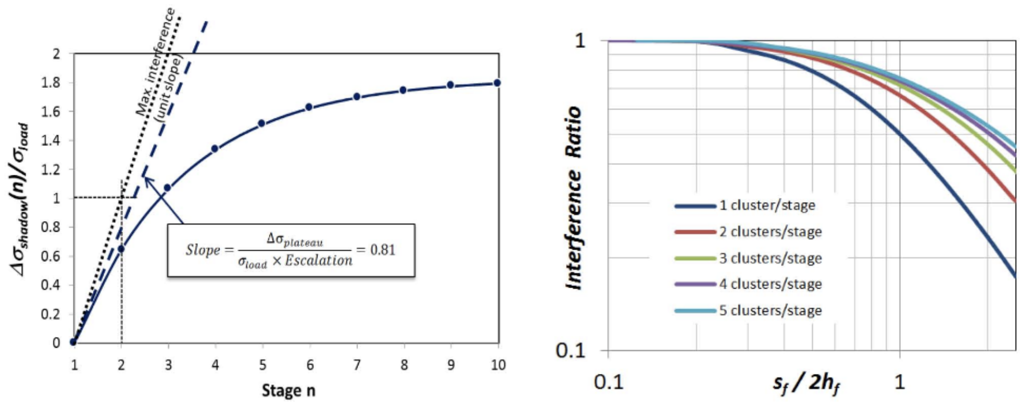

Figure 7.8: (a) Graphical representation of the Interference Ratio; (b) Type-curve of Interference ration or different numbers of perforation clusters (reproduced from Roussel (2017) with permission from Society of Petroleum Engineers (SPE)).

Another crucial step in ISIP analysis is the calculation of the fracture height. When the stress plateau is normally occurring, the net pressure is enough to propagate the fracture transversely to the wellbore. Therefore, Roussel (2017) suggests using Equation 7.8 to calculate the fracture height from the relation between escalation and spacing-to-height-ratio:

$$2h_f = s_f * N_p * \left(\frac{\text{escalation}}{1.928}\right)^{-1.36}, \tag{7.8}$$

where $\mathrm{N_p}$ is the number of perforation clusters. The perforation clusters affect stress interference. The more perforation clusters there are, the more fractures propagate, increasing stress interference.

7.4 Methodology

7.4.1 Data

One of the important parameters for ISIP analysis is closure pressure (minimum horizontal stress), which has been calculated by Han and van der Baan (2024). The results of his analysis have been shown in Table 7.2 and detailed in Chapter 2. Based on his calculation, the minimum horizontal stress gradient is 16.6 − 18.0 kPa. For our analysis, we have used the maximum value of the determined values. As the maximum True Vertical Depth (TVD) is approximately 2100 m, the closure stress for the area is determined to be 37,800 kPa.

Table 7.2: In-Situ Stress Calculations: Insights from Han and van der Baan (2024).

	Values
σ_h(kPa/m)	$16.6 - 18.0$
σ_H(kPa/m)	$21.1 - 22.7$
σ_v(kPa/m)	$24.5 - 25.5$

Another important input parameter for ISIP analysis is the number of clusters and stage spacing in each well. Each stage exhibits a different number of perforation clusters and varying stage spacing. While there is slight variability in the number of perforation clusters and stage spacing within stages of a single well, we have opted to utilize the average values for both parameters. This decision is crucial for the ISIP analysis. To provide a visual representation of the average values for the number of perforation clusters and stage spacing across wells, we have presented them in Table 7.3.

Table 7.3: Input Parameters Table for SEM Methodology

Well Number	Average perf. Cluster	Average Spacing	Number of stages
Well 1	3	52.7	39
Well 2	3	52.7	37
Well 3	3	52.7	38
Well 4	3	52.7	17

7.4.2 ISIP value acquisition

The term "Instantaneous Shut-In Pressure" (ISIP), also known as end-of-stage pressure, can be a bit misleading. Previous researchers, like McLennan and Roegiers (1982), have pointed out that shut-in pressures don't stabilize immediately after shut-in. Before shut-in, there are often sudden drops in pump rate, which can cause pressure oscillations in the wellbore, known as water hammer. These oscillations can make evaluating ISIP more complicated. This phenomenon is illustrated in Figure 7.9. Various studies have looked into selecting ISIP data. Study by Roussel et al. (2021) explored ISIP evaluation using different methods such as signal processing, quadratic fit, linear fit, and manual pick. Figure 7.9 demonstrates one of these methods (quadratic fit) for evaluating ISIP. The red dashed line represents the quadratic fit to the pressure decay. The intersection point of the quadratic fit with the pressure at shut-in (black dashed line) represents the ISIP. In our approach, we'll use the manual method, similar to the quadratic fit method where we imagine a line passing through the pressure decay zone. The intersection of the imaginary line at shut-in will provide the ISIP value.

Additionally, we'll use bottomhole pressure, which also shows similar oscillations. Bottomhole pressure is preferred because it already accounts for the fluid column pressure.

7.4.3 SEM method methodology

Step 1: We acquire ISIP data as denoted in previous paragraph. ISIP denotes the pressure required to propagate the fractures and correlates to the net pressure inside the fracture, rock closure pressure, and stress shadow (equation 7.1). For the first stage, there is no mechanical interference caused by the previous stage (equation 7.2). Therefore, we normalize ISIP data by subtracting the first stage from all ISIP data.

$$\Delta\sigma_{\text{shadow}}(n) = ISIP(n) - ISIP(1). \tag{7.9}$$

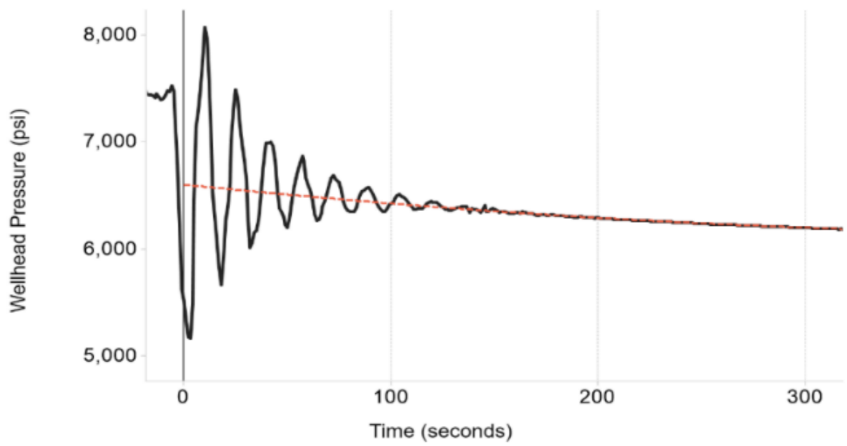

Figure 7.9: Analyzing wellhead pressure fluctuations during shut-in with ISIP determination through quadratic fit (red line), a method pioneered by Roussel et al. (2021) for enhanced evaluation (reproduced from Roussel et al. (2021) with permission from Society of Petroleum Engineers (SPE)).

This adjustment is essential since subtracting the first stage ISIP from all ISIP values reveals the stress shadow from the preceding stages.

Step 2: After obtaining the stress shadow profile for the well, we employ the Levenberg-Marquardt algorithm to fit the escalation equation (Equation 7.6). This fitting process enables the determination of the stress plateau, denoted as σ_{load}, along with the escalation value.

Step 3: In this step we use curves derived by Roussel and Sharma (2011), which we will show later how they can be estimated using the excel sheets. We employ the escalation value in the escalation type-curves developed by Roussel (2017) (refer to Figure 7.7) to determine the spacing-to-height ratio. Once the spacing-to-height ratio is determined, we utilize that value to ascertain the interference ratio using interference ratio type-curves depicted in Figure 7.8. Once the matching has been done we have acquired the necessarily values for further analysis. We use the stress interference ratio, stress plateau and escalation value in equation 7.7 to calculate the stress load. The fracture height is calculated using the equation 7.8.

Step 4: Proceeding to the next stage involves computing the net pressure, denoted as P_{net}, utilizing Equation 7.2. Each well is assigned a singular net pressure value through this calculation.

The workflow summary is presented in Table 7.4. Upon acquiring all required values including stress load, net pressure, and derived fracture height, we interpret the fracture propagation mechanism based on the theory outlined in Table 7.1.

Table 7.4: Refined Step-by-Step Workflow for SEM Analysis adapted from Roussel (2017)

Step 1: Normalize the ISIP data to represent stress shadow

- Subtract ISIP(1) from all stages to present stress shadow. (equation 7.9)

Step 2: Acquire Escalation and Stress Plateau values ($\Delta\sigma_{\text{plateau}}$)

- Fit equation 7.6 to data with least-square method to obtain escalation and stress plateau ($\Delta\sigma_{\text{plateau}}$).

Step 3: Obtain fracture height (h_f) and stress load (σ_{load})

- Use escalation value in figure 7.7 to find spacing to-height ratio ($s_f/2h_f$)
- Use spacing to-height ratio ($s_f/2h_f$) in figure 7.8 to obtain stress interference ratio
- Use equation 7.7 to calculate stress load (σ_{load})
- Use equation 7.8 to calculate the fracture height

Step 4: Find value of net pressure $(p_{\text{net}})_{\text{@shut-in}}$

- Employ equation 7.2 to find net pressure $(p_{\text{net}})_{\text{@shut-in}}$ using ISIP(1) and σ_{hmin}

Table 7.5: Correlation equations for Stress Escalation type-curves. The variable y represents escalation, while x denotes the spacing-to-height ratio, $s_f/2h_f$.

Perforation cluster/Stage	Correlation equation
1	$y = 0.9982x^2 - 1.2635x - 0.106$
2	$y = 0.871x^2 - 1.3907x + 0.1081$
3	$y = 0.1491^3 + 0.8288x^2 – 1.276x + 0.1959$
4	$y = -0.1461x^3 + 0.8636x^2 – 1.3581x + 0.2309$
5	$y = -0.1571x^3 + 0.8763x^2 – 1.3599x + 0.264$

7.4.4 Curve matching technique

The theoretical foundation of ISIP analysis is straightforward, yet the intricacies involved in computing the stress load (σ_{load}) and fracture height are complex, necessitating the derivation of type-curves as elaborated by Roussel (2017). Consequently, we opted for a straightforward approach rather than time-consuming extrapolation. To align each individual curve, namely the Escalation type (Figure 7.7) and interference-type-curve (Figure 7.8), we employed logarithmic correlation, resulting in equations that can be readily implemented in an Excel spreadsheet for efficient computations, akin to the method proposed by Roussel (2020). Notably, a single logarithmic function sufficed to accurately match each entire curve. Refer to Tables 7.6 and 7.5 for a comprehensive listing of the equations corresponding to each type-curve, constructed under the assumption of semi-infinite hydraulic fractures.

7.5 Results and Discussion

7.5.1 Determining ISIP

The process of determining the Instantaneous Shut-In Pressure (ISIP) and the initial rate of pressure decline relied on the pressure measurements. For our analysis, we simply used the bottomhole pressure at shut-in time. Figure 7.10 represents the

Table 7.6: Correlation equations for Stress interference type-curves. the variable y represents stress interference ratio, while x denotes the spacing-to-height ratio, $s_f/2h_f$.

Perforation cluster/Stage	Correlation equation
1	$y = 0.2258x^4 - 0.0833x^3 - 0.7351x^2 - 0.8978x - 0.3003$
2	$y = 0.0358x^4 - 0.2074x^3 - 0.6427x^2 - 0.58x - 0.1758$
3	$y = -0.0585x^4 - 0.2472x^3 - 0.5002x^2 - 0.4528x - 0.1432$
4	$y = -0.0171x^4 - 0.1505x^3 - 0.4101x^2 - 0.4055x - 0.1306$
5	$y = 0.0181x^4 - 0.0985x^3 - 0.383x^2 - 0.3853x - 0.1199$

pumping pressure at the shut-in interval. One can observe that the pressure at shut-in is not stable; it fluctuates. Rather than employing sophisticated methods, we adopted a manual approach to select the ISIP for each stage. As illustrated in Figure 7.10, we have used a imaginary line that represents the pressure fluctuation. The ISIP value has been determined by intersecting this imaginary line with the pressure drop (indicated by the black point) at shut-in, as demonstrated for a single stage in Figure 7.10. This procedure has been consistently followed for all stages across all four wells and illustrated in figure 7.11.

Observing the ISIP data reveals significant variations across stages. Particularly intriguing is the phenomenon wherein, for wells comprising more than 20 stages, ISIP values tend to decrease below those recorded at the initial stage. Examining well 2, for instance, the initial ISIP value stands at 45,700 kPa, yet by stage 20, it declines to 45,200 kPa. Similar trends are observed for well 1 and well 3. As previously discussed in theory, ISIP values typically increase due to stress shadowing from preceding stages. These fluctuations may be attributed to changes in lithology or pore pressure, which could influence the physical properties of the formation, including fracture propagation pressure (P_{net}).

A notable phenomenon is observed in the initial stage of Well 3, where the ISIP

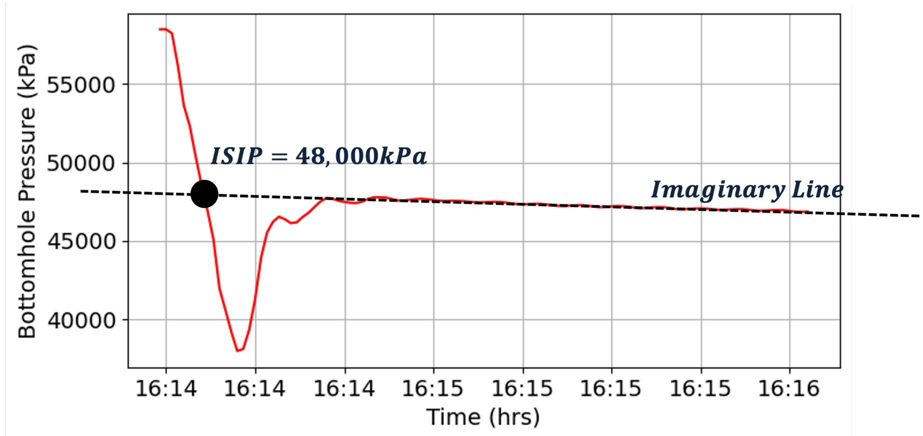

Figure 7.10: Visualization of Bottomhole Pressure Zoomed at Shut-In Time: capturing bottomhole pressure fluctuations. An imaginary line is used to trace pressure drop points, and the corresponding crosspoint with bottomhole pressure at shut-in is considered as the ISIP value. Consistent methodology is applied across all stages in four wells.

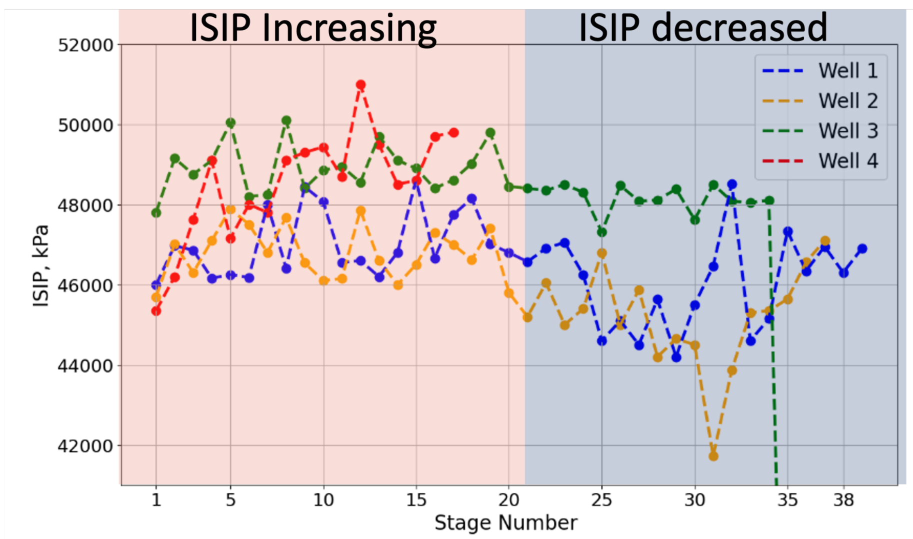

Figure 7.11: Illustration of ISIP data for all stages in four wells. Beyond stage 20, wells 1, 2, and 3 exhibit a decrease in ISIP below the initial value, as depicted by the red and blue zones in the figure. Notably, well 3 (green line) displays an initial ISIP value higher than any other, attributed to hydraulic fracturing in well 1, which penetrates a different formation in the same area. Additionally, Well 3 demonstrates a notable decrease in ISIP values across the last three stages, indicating a significant alteration in formation properties.

value at first stage is notably higher compared to other wells within the area. This occurrence is attributed to the hydraulic fracturing of Well 1, which shares the same location as Well 3 but with differing landing heights (Figure 7.1). We interpret this disparity as indicative of stress shadowing induced by the hydraulic fracture treatment, resulting in an elevation of the ISIP value for the first stage of Well 3. Consequently, we rectified this discrepancy by adjusting the ISIP value for the initial stage using the average ISIP values obtained from the first stages of three other wells. Such correction is crucial, neglecting this adjustment may compromise the accuracy of subsequent calculations and interpretations. For further analysis, we focused on the corrected data of Well 3, specifically the first 20 stages, as illustrated in Figure 7.12.

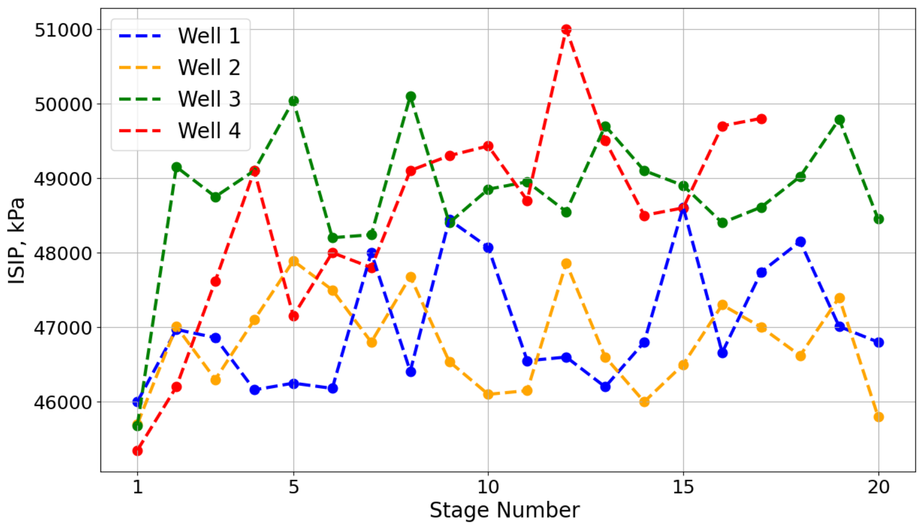

Figure 7.12: Illustration of the first 20 stages for four wells. The ISIP at the first stage for each well has been correlated to other wells to ensure more accurate results. The higher ISIP at the first stage is resultant of hydraulic fracturing processes prior to well 3 in wells 1 and 2, leading to an increase in p_{net}.

7.5.2 ISIP Analysis

In the initial stage of hydraulic fracturing, no stress shadow is observed from preceding stages within the well. However, as subsequent stages progress, the ISIP values are influenced by preceding stages, leading to an increase from the initial stage ISIP value. Consequently, to accurately represent the data solely in terms of stress shadowing, it is necessary to subtract the first stage ISIP value from all subsequent stages in a well. We have done this procedure for all 4 wells. Moving forward, we applied the stress escalation equation (Equation 7.6) to the dataset, allowing us to derive the escalation number and stress plateau ($\sigma_{plateau}$). Figure 7.13 illustrates the fitted graph displaying the stress shadow data over the stages. The outcomes of this fitting procedure are detailed in Table 7.7.

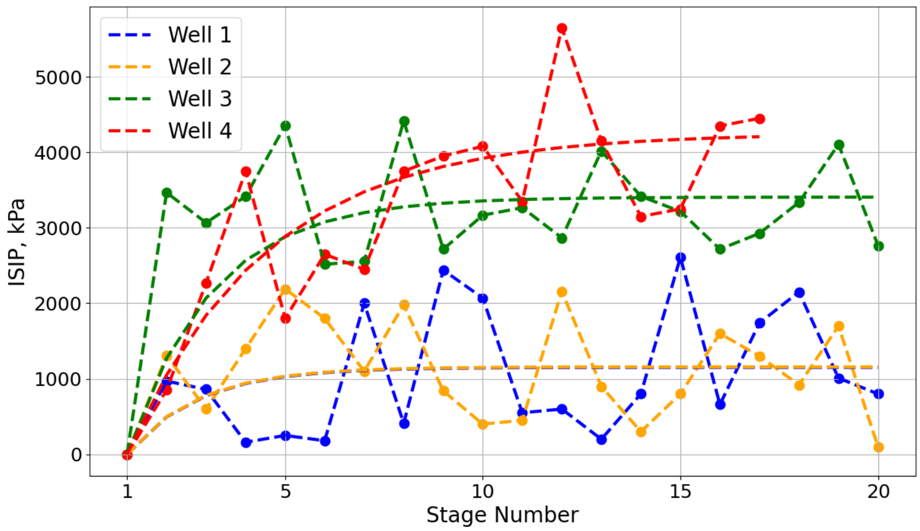

Figure 7.13: Illustration of the escalation model (equation 7.6) fitting graph for calculating the stress plateau ($\sigma_{plateau}$) and escalation for four wells using 20 stages. Prior to fitting, ISIP at the first stage was subtracted from all ISIP values across the stages to account for stress interference (stress shadow), as the first stage is not subject to any stress interference.

Upon examining the stress plateau values ($\sigma_{plateau}$) and escalation as detailed in Table 7.7, a notable pattern becomes evident: Wells 1 and 2 exhibit similar plateau levels, while Wells 3 and 4 demonstrate notably higher values. These discrepancies cannot be attributed to differences in completion design, as the average fracture spacing remains consistent at 52.7 m across all wells. Notably, the distance between Well 4 and its nearest neighbor is 150 m. Furthermore, Well 3 shares the same location as Well 1 but with differing landing heights. The observed higher stress plateaus in Wells 3 and 4 may be attributed to several factors. Firstly, proximity to previous wells may suggest that the hydraulic fracture treatments in these prior wells have influenced the stress conditions. Alternatively, lithological variations could also

Table 7.7: Table depicting stress plateau (σ_{plateau}) and escalation results based on the fit in Figure 7.13.

Well	Stress Plateau (kPa)	Escalation
Well 1	1351	4.3
Well 2	1157	1.78
Well 3	3399	2.1
Well 4	4248	3.5

contribute to the observed differences. Further analysis is warranted to ascertain the primary factors contributing to the elevated stress plateau values in Wells 3 and 4.

Following this, we leverage the type-curves developed by Roussel (2017) to align the escalation value and ascertain the spacing-to-height ratio. To do this, we have used matching technique using Excel. The matching technique has been shown in the methodology. The results of matching has been shown in Figure 7.14. The small dots on top of the curves represent our matching technique. In the same Figure 7.14, we have shown automated matching process for Well 4. The identified escalation value for Well 4 is 3.5; the corresponding spacing-to-height ratio, $S_f/2h_f$, is 0.53. Using defined spacing-to-height value from the escalation curve, we matched it in Interference ratio type-curves; the interference ratio is 0.87. Later we have used Equations 7.7 and 7.8 to calculate stress load and fracture height as below:

$$\sigma_{\text{load}} = \frac{\Delta\sigma_{\text{plateu}}}{\text{Interference ratio } * \text{ Escalation}} = \frac{4,248}{0.87 * 3.5} \approx 1,395kPa, \tag{7.10}$$

$$2h_f = s_f * N_p * \left(\frac{\text{escalation}}{1.928}\right)^{-1.36} = 2 * 52.7 * 3 * (\frac{3.5}{1.928})^{-1.36} \approx 163.5m. \tag{7.11}$$

The fracture height, $2H_f$, and stress load, σ_{load}, are calculated, with their values being 163.5 m and 1,395 kPa, respectively. Later we have calculated the net pressure, P_{net} using the relation of ISIP shown in equation 7.12 as shown below:

$$p_{\text{net}} = (ISIP(1)) - \sigma_{\text{hmin}} = 45,350 - 37,800 = 7,550kPa. \quad (7.12)$$

The calculated value for the Net pressure is 7,550 kPa. The same procedure has been applied to all wells, and the results are presented in Table 7.8. Notably, the stress load values for well 1 and well 2 are similar, at 868 kPa and 869 kPa respectively, and are lower compared to the other wells. However, the stress load values for well 3 and well 4 are notably higher, at 2040 kPa and 1400 kPa respectively. Additionally, the Net pressure, P_{net} values, calculated by subtracting the first ISIP from the minimum horizontal stress, are depicted in the figure. For wells 1 and 2, the value is 8200 kPa, while for wells 3 and 4, it is 7800 kPa and 7700 kPa respectively. In all cases, the stress load is considerably smaller than the Pnet pressure, indicating that the stress shadow is insufficient to overcome the stress anisotropy necessary to alter the horizontal stresses (stress regime).

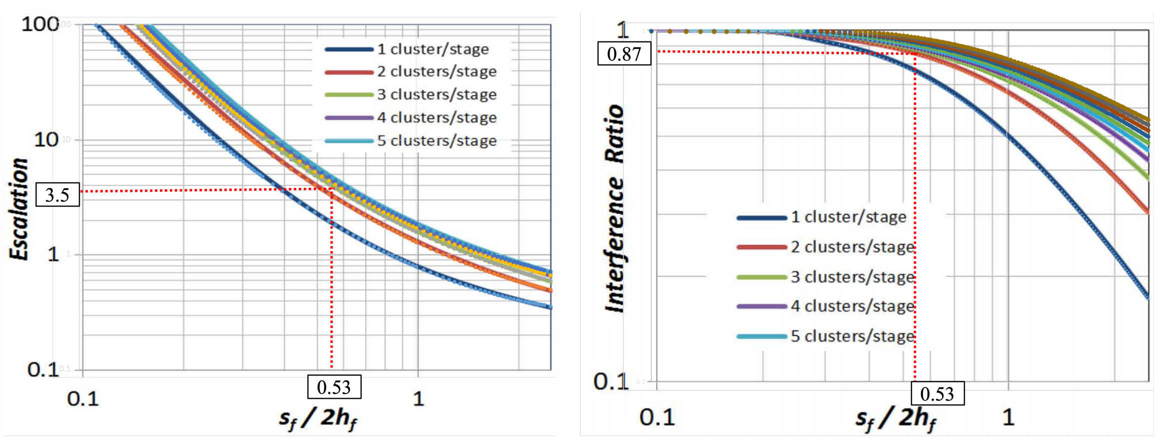

Figure 7.14: An illustration showcasing our utilization of type-curves depicting (a) the escalation and (b) the stress interference ratio for well 4. The red dashed line signifies the matched values for Escalation, spacing-to-height ratio, $\frac{s_f}{2h_f}$, and interference ratio.

Our analysis highlights the presence of the stress shadow phenomenon, which likely influenced fracture propagation. The unidirectional propagation of the fractures creates stress interference or stress shadow, which inhibits further propagation and redirects fractures in the opposite direction. Particularly noteworthy is well 3, where

Table 7.8: Table Displaying Results Following Workflow for Stress Load, Fracture Height, and P_{net} Pressure Calculations.

Well	Stress Load (kPa)	Fracture height (m)	P_{net} pressure (kPa)
Well 1	868	149 ± 20	8200
Well 2	869	149 ± 20	8200
Well 3	2040	169 ± 20	7800
Well 4	1395	163.5 ± 20	7550

fracture propagation predominantly occurs on one side. The significant stress load of 2040 kPa may impede propagation towards the northeast side, potentially prompting fractures to propagate towards the southwest. This phenomenon, initially proposed by Ortega Perez (2022), finds support in our observations of stress load, suggesting the possible existence of such phenomena due to the high value of stress load.

7.5.3 Validation of the results with MS derived fracture heights

Given that the plateau phenomenon is a typical occurrence, the calculated fracture height (as shown in Table 7.8) can be considered reliable and suitable for comparison with MS-derived fracture heights to validate the results. To facilitate this comparison, we present the Microseismic-derived fracture height (average) for all four wells alongside the ISIP-derived height in Table 7.9. It's worth noting that the uncertainties in ISIP data are associated with the number of perforation clusters. To quantify these uncertainties, we varied the number of perforation clusters when we employed the type-curves and observed changes in the calculated heights. The results indicated a variation of approximately 20 meters, thus we incorporated uncertainties as ± 20 meters.

Indeed, the close alignment between the results of MS-derived and ISIP-derived fracture heights is as anticipated. With the plateau phenomenon being a typical occurrence, there is no reorientation of stress that might truncate the height of fractures.

Table 7.9: Comparison Table of Fracture Heights Derived from MS and ISIP Data.

Well	Average MS derived height (m)	ISIP derived height
Well 1	157.83	149 ± 20
Well 2	142.48	149 ± 20
Well 3	162.8	169 ± 20
Well 4	175.5	163.5 ± 20

This implies that the calculated stress load is valid, and it can be utilized in conjunction with pore pressure results to comprehensively understand fracture propagation dynamics.

7.6 Conclusion

Based on the results obtained from our ISIP analysis across the four wells, several key findings emerge, shedding light on the complex dynamics of fracture propagation and stress interference in hydraulic fracturing operations.

Firstly, our examination of ISIP data revealed significant variations across stages, with intriguing patterns emerging, particularly for wells with more than 20 stages. The ISIP values decrease towards the initial stage, suggesting potential changes in formation layers and properties impacting fracture propagation pressures (P_{net}) such as pore pressure variations.

The SEM method revealed that none of the wells generated enough stress to alter the horizontal stresses. Therefore, the arching observed in the microseismic clouds is likely not due to a stress flip in the horizontal stresses but could be related to natural fractures in the area. Additionally, we noted a high calculated stress load of 2040 kPa for well 3, which may have contributed to increased stress during the propagation of fractures in the NE direction, potentially influencing fracture propagation in the opposite direction.

As no reorientation in horizontal stresses occurred, the fracture height calculation was deemed reliable, demonstrating a strong correlation between fracture heights derived from microseismic (MS) data and those from instantaneous shut-in pressure (ISIP).

Chapter 8

Integration Chapter

8.1 Summary

The microseismicity presents an intriguing pattern, displaying considerable variability across treatment stages. Many events predominantly propagate in a northeast direction, while the length of the microseismic clouds fluctuates throughout the stages. Despite these observable phenomena, the underlying cause of this unusual behavior remains elusive. Consequently, our objective in this chapter is to analyze and integrate multidisciplinary data to investigate and better understand the hydraulic fracture propagation in the Montney Formation. The research is initiated by understanding the effect of treatment parameters using a simple geomechanical model, the Perkins-Kern-Nordgren model. Secondly, we used microseismic data to understand the cloud propagations, the impact of distance between treatment well and monitoring well with magnitude-distance plots, R-T plots to understand the event propagation over time, and a model-based approach to understand the change in the fracturing regime. Later, we used the microseismic cloud analysis result in conjunction with the PKN model to understand the correlation and analyze the effect of treatment parameters. Then, we investigated geological phenomena on both small and large scales. To investigate geological phenomena on a small scale, we looked at the features around the wellbore using basic well logs and FMI logs. Using these, we analyzed the lithology/bedding changes, azimuth, and dip of natural fractures. We also used microseismic data in conjunction to understand the potential effect of the microseismic events. To understand geology on a larger scale, we used seismic reflection data where we interpreted seismic attributes such as dip, azimuth, maximum and minimum curvature. With such attributes, we understood potential geological phenomena which we later used in conjunction with microseismic data to understand the effect of geology in fracture propagation. Later, we also wanted to understand the effect of stress shadow on the propagation of the microseismic data. The stress shadow affected fracture propagation and forced fractures to propagate towards the southwest direction. We tried to use all the data in conjunction with microseismic data to understand the phenomena. However, we never correlated different analysis results. I will integrate the findings from each chapter to validate the observations and possible cases. In this chapter, we mainly show the observations from different chapters with potential answers to the objective of the study.

8.2 Introduction

I examined 38 stages within Horizontal Well 3 located in a Montney reservoir in southwestern Alberta. Figure 8.1 depicts microseismic activity across all stages, color-coded for clarity. It's noticeable that the microseismic clouds vary in size and shape from stage to stage, with some displaying elongated fracture lengths while others appear shorter. Fracture propagation directions are indicated by blue and red arrows, denoting northeast and southwest directions, respectively. The changes in fracture length across stages are also evident in the cloud height and NE and SW cloud lengths depicted in Figures 8.2 and 8.2. Additionally, arrows provided in Figure 8.1 highlight the predominant propagation towards the North-East. However, the cause of this phenomenon remains unknown.

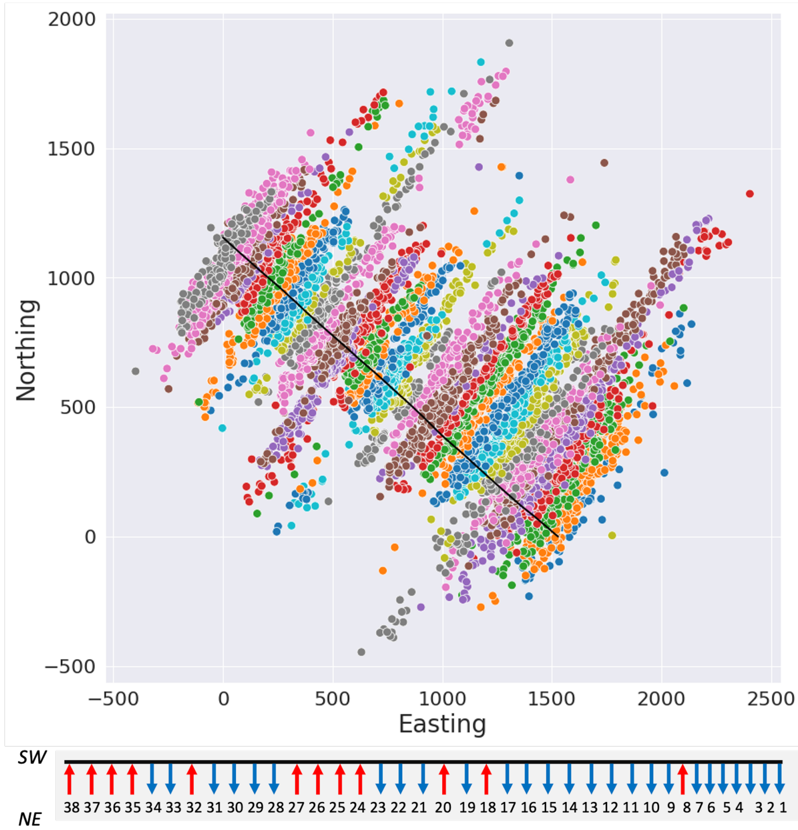

Figure 8.1: Overview of Microseismic Clouds: Arrows depict propagation trends. Blue denotes northeast movement, red indicates SW. Predominantly, propagation is northeastward. Up to stage 17, most events move toward the northeast direction, but after stage 17, the event direction changes, exhibiting a cyclic pattern where stages with predominantly northeast movement are followed by stages moving in the opposite direction.

8.2.1 Observations

Treatment Parameters

I computed Perkins-Kern-Nordgren model fracture-half length for each 38 stages in Well 3. This analysis uses treatment parameters such as stage duration, injection rate, and Plane strain modulus and fracture height from each stage. This analysis was previously made by Ortega Perez and van der Baan (2024) where she used constant fracture height and constant Plane strain modulus. the reason we wanted to employ these parameters because we wanted to understand the treatment parameters only. Analysis reveled that the results almost identical with Ortega Perez and van der Baan

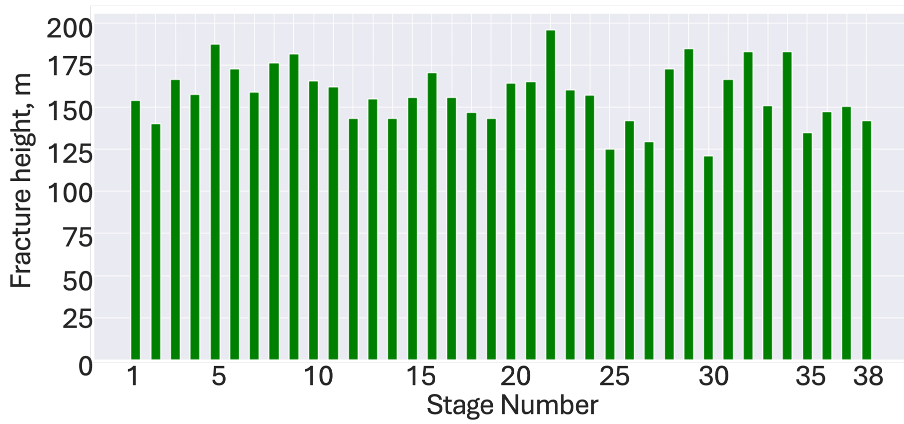

Figure 8.2: Graph depicting the measured height (after magnitude threshold and reclassification) for all microseismic clouds, representing the fracture height for every stage. The cloud height over the stages exhibits a cyclic pattern of increase and decrease. The fracture height fluctuates across stages. The average height is 162.8 meters.

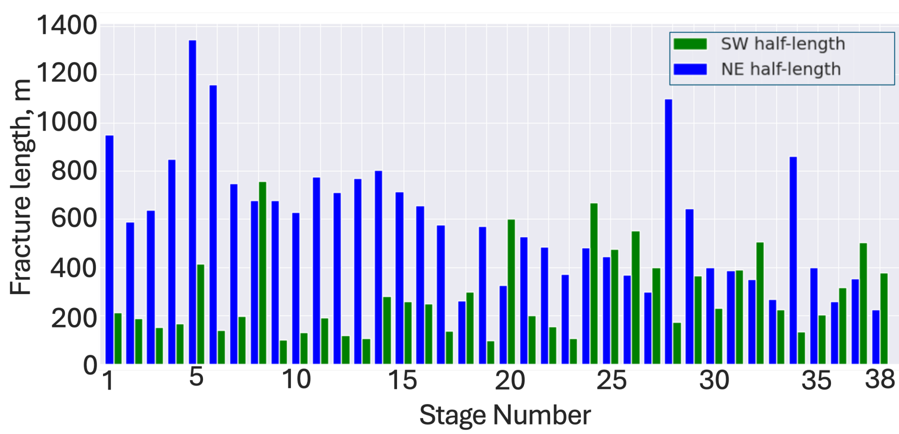

Figure 8.3: Graph illustrating the measured length of microseismic clouds, indicating fracture length for each stage. Blue denotes the northeast wing of the fracture, while green represents the southwest wing. The initial 17 stages exhibit longer fracture lengths in the northeast direction. However, in subsequent stages, the fracture lengths become similar between the southwest and northeast wings, both relatively shorter than those of the northeast wing in the first 17 stages.

(2024) results except in some stages the Plane strain modulus has affected. In figure 8.4, I present the MS fracture half length in NE and SW with PKN half-length.

Our analysis reveals significant disparities in fracture lengths, particularly noticeable in the SW and NE wings compared to the PKN model. These differences highlight the oversights of the PKN model, such as neglecting critical parameters like leak-off, as anticipated by Ortega et al. (2022).

In the NE wing, both initial and later stages show relatively smaller discrepancies, especially during stages 1 to 15, where both the NE wing results and the PKN model indicate longer fracture half-lengths. However, during intermediate stages (15 to 25), disparities intensify due to complications in completions and prolonged treatment periods.

Conversely, the southwest side exhibits a lack of similarities, with an increase in fracture length on the NE side contrasting with a decrease on the southwest side. This disparity highlights the complex and variable nature of fracture propagation within the well.

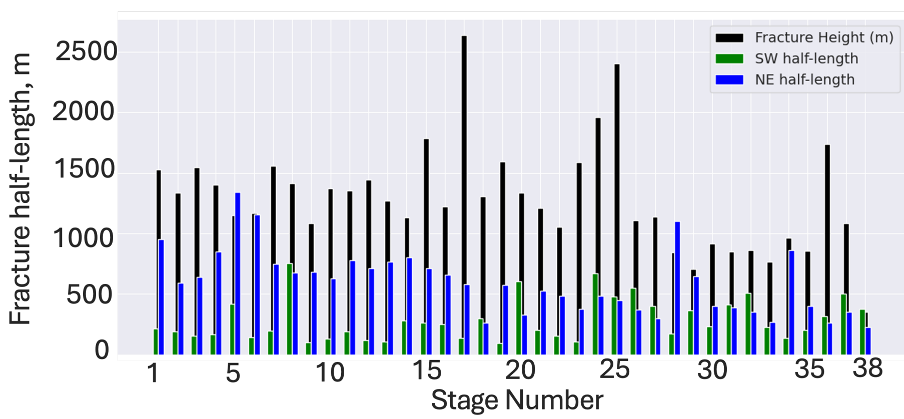

Figure 8.4: PKN fracture half-lengths at injection completion (black) and microseismic cloud lengths for Northeast (blue) and Southwest (red) shown side by side.Significant discrepancies between PKN and MS results are apparent, especially for the middle stages (17-26). The initial and later stages show correlation with NE half fracture length

Microseismic analysis

During microseismic analysis, we identified three main patterns: ”Normal,” ”Reactivation,” and ”Halted-growth,” with each stage showing different combinations of fracturing regimes (Figures 8.5 and 8.6). The arrows represent the trend in hydraulic fracturing (HF) treatment propagation.

On the northeast side, "Reactivation" and "Normal" patterns dominate, indicating fluid passage through pre-existing fractures, with occasional instances of halted growth. Conversely, the southwest side exhibits dominance of "Halted-growth" and "Normal" patterns, with sporadic "Reactivation" instances correlating with southwest propagation.

Figure 8.6 delineates hydraulic treatment regimes for all stages, showing varied regimes between the well's sides. The northeast side predominantly displays the Perkins-Kern-Nordgren (PKN) regime, transitioning to longer lengths later, while the southwest side typically starts with a different regime such as KGD. Consistent patterns or regimes were challenging to identify in southwest propagation.

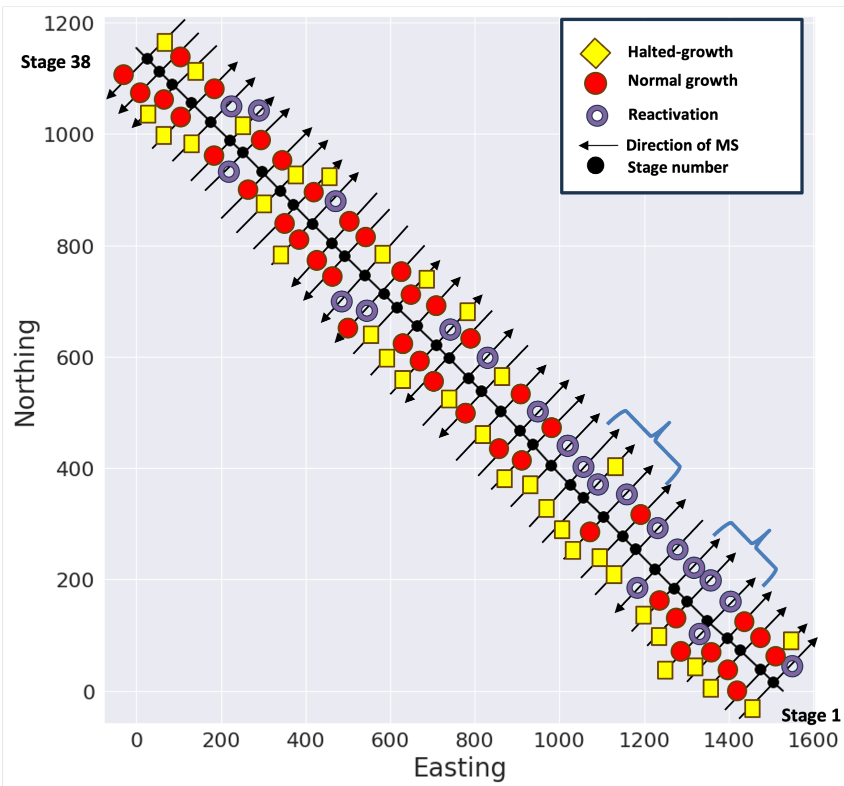

Figure 8.5: Overview of microseismic (MS) observations across stages, depicting propagation patterns in radial-time (r-t) plots: "Normal" (red circle), "Reactivation" (purple circular ring), and "Halted-growth" (yellow rhombus). Black arrows indicate HF treatment propagation trend. The bracket highlights stages where we suspect the reactivation of the same pre-existing fractures. Most of the reactivation happens toward the toe of the well explaining the longer fracture length up to stage 17.

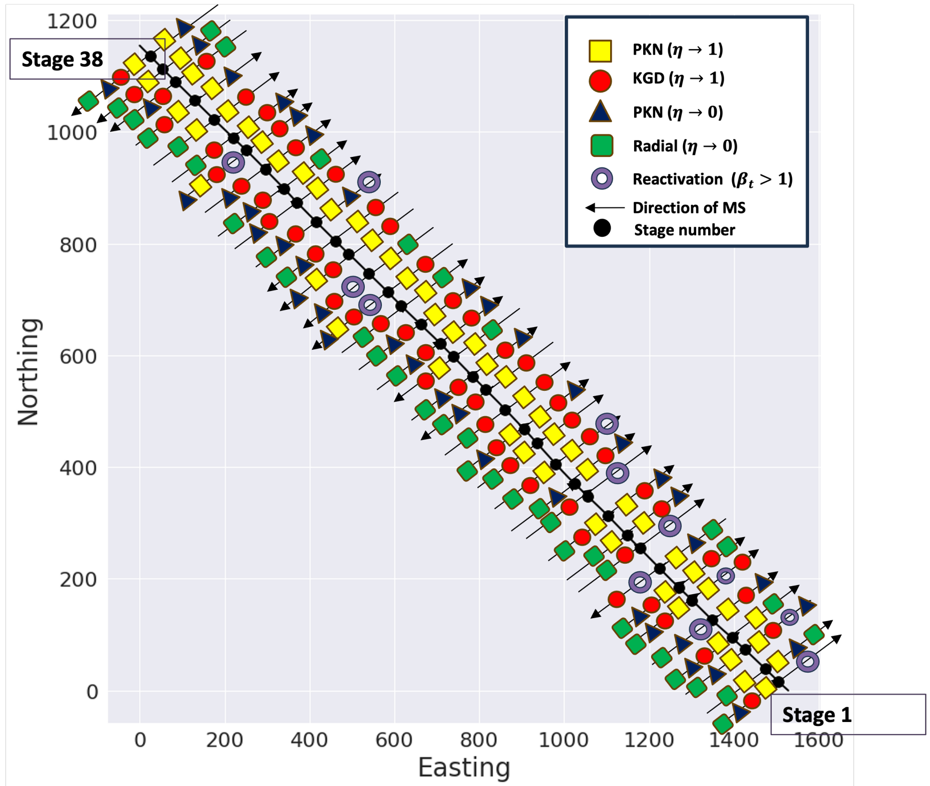

Figure 8.6: Overview of hydraulic fracture (HF) treatment regimes: "Reactivation" (β_t shown as purple circular rings), PKN ($\eta \to 1$) represented by yellow squares or red circles, and Radial flow denoted by green squares or blue triangles. Black arrows indicate HF treatment propagation trend. The blue brackets indicate the stages during which the "Reactivation" of pre-existing fractures occurred for the same fracture. The NE side is mostly characterized by the PKN and KGD regimes, while the SW side is mostly characterized by the KGD and Radial regimes.

Natural fracture analysis

The correlation between natural fractures and FMI logs revealed that the reactivation pattern is because of the conductive fractures in the area. The figure represents the result from chapter 5. Figure 8.7 presents a plan view of the well, showing various types of fractures from FMI logs: Discontinuous Resistive fractures (blue), Resistive Fractures (orange), Conductive fractures (green), and Discontinuous Conductive fractures (red). The black dots represent hydraulic stages from stage 1 to 38.

Observations indicate that reactivation mainly occurs towards the toe of the well, where Discontinuous Conductive fractures prevail, while Discontinuous Resistive fractures are more common towards the heel. Stages exhibiting "reactivation" patterns are mostly localized, with minimal overlap with Discontinuous Resistive fractures. This analysis suggests that "Reactivation" primarily aligns with Conductive, Discontinuous Conductive, and Resistive fractures, with Discontinuous Resistive fractures having minimal impact on hydraulic fracture propagation. In some stages, reactivations happen due to pre-existing fractures while in some cases, the reactivation happens due to previously reactivated fractures (the brackets).

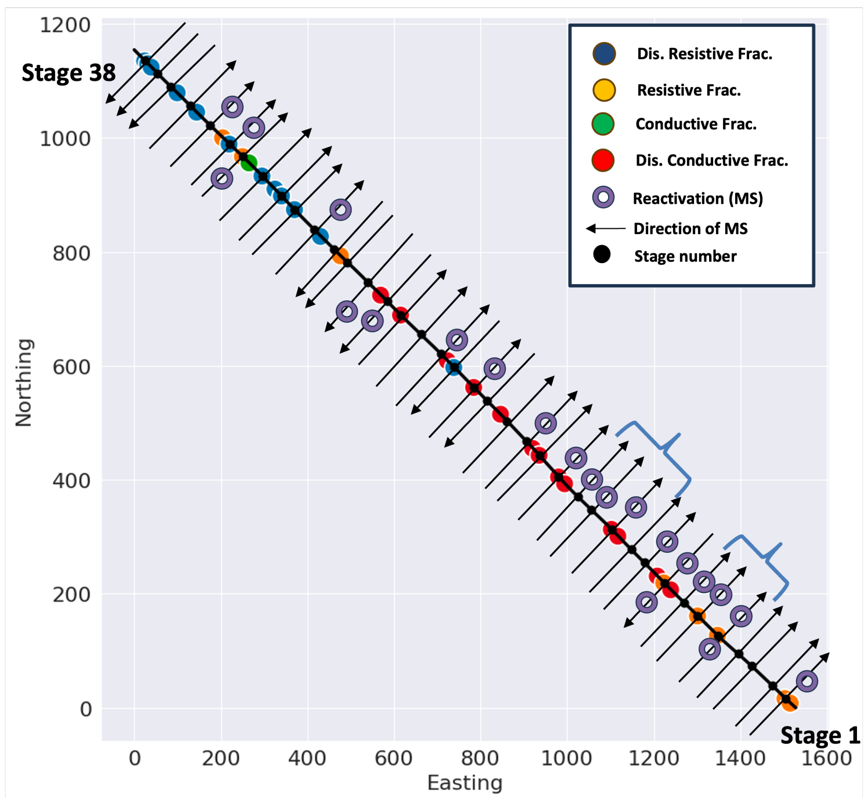

Figure 8.7: Planar view of the well: Black dots indicate treatment stages, with arrows showing propagation direction. Stages displaying a "Reactivation" pattern are marked with purple rings. Natural fractures are depicted as follows: Dis. Conductive (red), Dis. Resistive (blue), Resistive (yellow), Conductive (green). Most conductive fractures appear toward the toe of the well. Reactivation patterns overlap with conductive fractures. Some reactivation patterns do not overlap with any fractures because they occur due to the activation of prefiously reactivated fractures (indicated with brackets).

Well logs

In Figure 8.8, the upper tracks illustrate observed bedding changes derived from FMI data. Red dots mark the bullseye pattern, while the zones represent distinct landing formations: Montney D2 marked in red and D3 in blue. Conversely, the lower track in Figure 8.8 presents findings from fundamental well logs, with low gamma ray regions depicted in yellow and low gamma ray regions in grey. Each figure features black dots corresponding to locations of hydraulic fracture treatments.

Based on the basic well logs, there appears to be a variation in the mineralogy of the formation from the middle of the well towards the toe compared to the heel of the well. The change in gamma ray is attributed to either the presence of K-feldspar or clay. The dashed lines represent where we have observed resistivity horns. To correlate the results with FMI, we have shown the FMI-derived results using the simple approach discussed in Chapter 5. FMI and basic well log results show a change in the landing horizon (dashed red rectangle) where dashed lines align with the FMI-derived zones. A minor inconsistency is observed at the heel, where FMI logs suggest that the well has not changed the horizon, while resistivity readings suggest a change in bedding. We have mentioned that this inconsistency could be the result of resistive fractures toward the heel of the well that affected resistivity readings, or irregularities in the bedding.

ISIP analysis

We conducted data analysis on four wells situated within the same vicinity. In the initial phase of our methodology, we began by acquiring the ISIP (Initial Shut-In Pressure) data for each stage across all four wells. The resulting ISIP extractions for all stages across the four wells are illustrated in Figure 8.9. Observing the ISIP data, it becomes apparent that it varies significantly across stages. Notably, an intriguing phenomenon emerges for wells with more than 20 stages, the ISIP results tend to decrease nearing or being lower than the ISIP data recorded at the initial stage. This

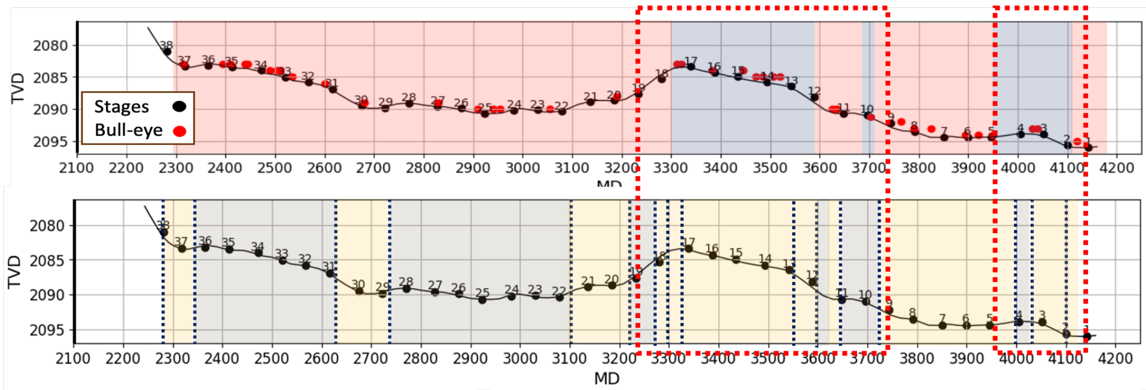

Figure 8.8: Integration of wellbore data and Formation Micro-Imager log. The red bracketed zones represent where the well has moved out of the horizon, as indicated by the FMI analysis and the observed resistivity changes in these zones.

Table 8.1: Table Displaying Results Following Workflow for Stress Load, Stress Plateau , and P_{net} Pressure Calculations.

Well	Stress Load (kPa)	Stress Plateau (kPa)	P_{net} pressure
Well 1	868	1351	8200
Well 2	869	1157	8200
Well 3	2040	3399	7800
Well 4	1400	4248	7700

variation can be attributed to either pore pressure variations or changes in lithology.

The comprehensive results of the ISIP analysis are depicted in Table 8.1. This table outlines stress load, net pressure, and stress plateau values. Notably, the well under consideration exhibits a stress load of approximately 2040 kPa, signifying a notably high value. However, while this value surpasses the net pressure, it falls short of inducing a flip in horizontal stresses. Nevertheless, it remains sufficient to trigger mechanical stress interference, thereby augmenting stress levels and impeding the free movement of fractures. Additionally, the stress plateau is recorded at 3399 kPa, similarly indicating a substantial magnitude.

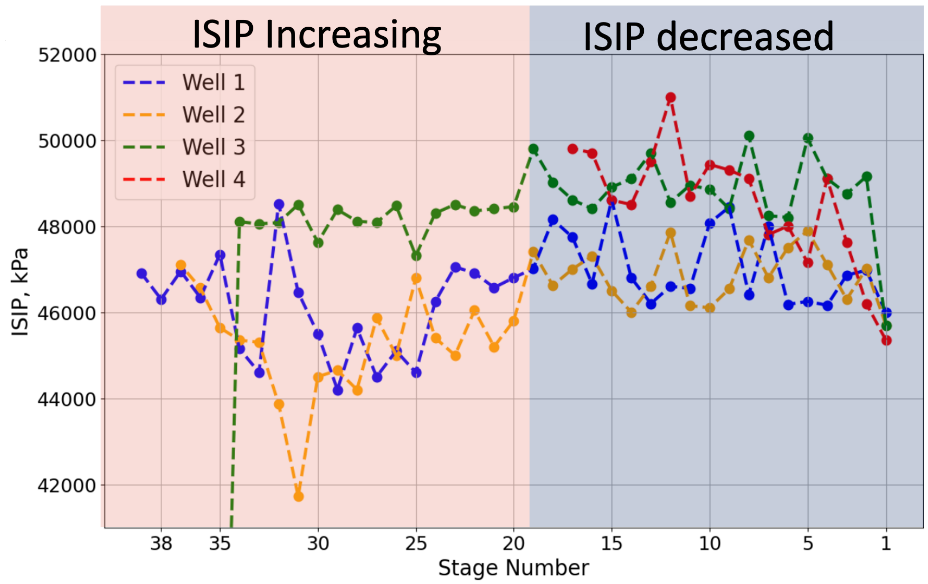

Figure 8.9: Illustration of ISIP data for all stages in four wells. Beyond stage 20, wells 1, 2, and 3 exhibit a decrease in ISIP below the initial value, as depicted by the red and blue zones in the figure. These discrepancies may be associated with the elevated pore pressure zone toward the toe of the well or changes in landing height or lithology.

Microseismic analysis: Distance bias

The primary objective in investigating the distance bias in event detection is to ascertain whether the spacing between the observation well and the monitoring well has introduced a bias, resulting in the predominant detection of microseismic events on the east side of the well. The results of the magnitude threshold analysis are depicted in Figure 8.10b. It is evident that there is a substantial reduction in the number of events after the filtering process compared to the original data presented in Figure 8.10a. However, there is no discernible alteration in the pattern of event cloud propagation. The decrease in event count primarily occurs around the fractures, indicating that the filtering process did not eliminate events on one side of the well. This observation suggests that the distance between the treatment well and the observation well does not influence the unidirectional microseismic event propagation.

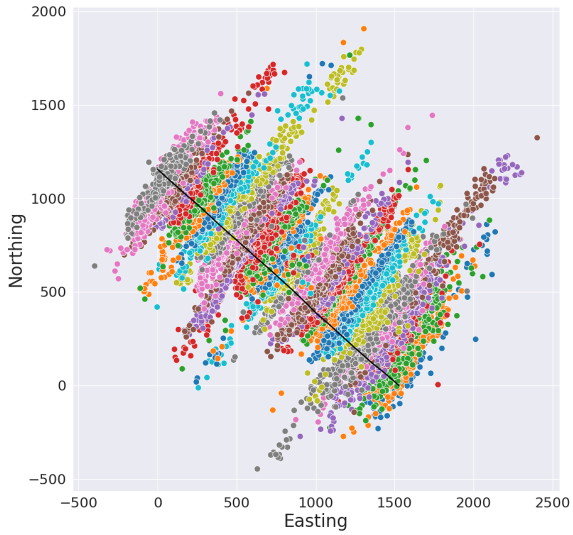

(a) Original microseismic clouds,

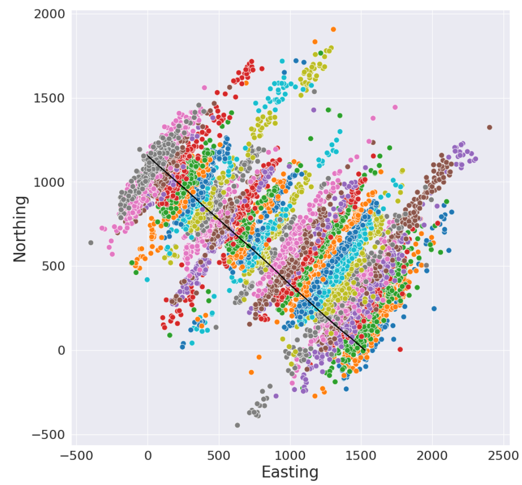

(b) Microseismic event pattern with -3.2 magnitude filter,

Figure 8.10: Planar views of microseismic cloud distributions: (a) Original data, (b) After applying magnitude cut-off. The main change after the magnitude threshold filter is the thickness of each stage's clouds. There is no effect on the unidirectional propagation of the clouds; it remains the same.

Seismic reflection: Dip and pore pressure map

Figures 8.11 and 8.12 present two pivotal outcomes derived from the seismic reflection analysis. In Figure 8.11, the dipping results are illustrated, delineating the trend in hydraulic fracture treatment stages. The black dots represent the treatment stages, while arrows indicate the propagation direction. The regional dip is in the southwest direction. It is very normal that the propagation of events is in the northeast direction, which is the updip direction. This is because this zone is shallower and facilitates easier fluid movement through this zone, potentially exhibiting smaller pressures.

Moreever, Figure 8.12 showcases the pore pressure map, unveiling a non-uniform distribution of pore pressure around the well. Such heterogeneity profoundly impacts fracturing pressure, with high initial pore pressure augmenting the breakdown pressure. Notably, there is a discernible increase in pressure from the northeast (NE) towards the southwest (SW) direction, which is anticipated to influence the unidirectional propagation of fractures. This phenomenon is much more obvious around the circled zone in the left figure, where high pressure is observed. The right figure in the circled zone shows an elevated pressure zone that forces MS events to move toward the NE direction. Toward the heel of the well, it is obvious that pressure is relatively uniformly distributed.

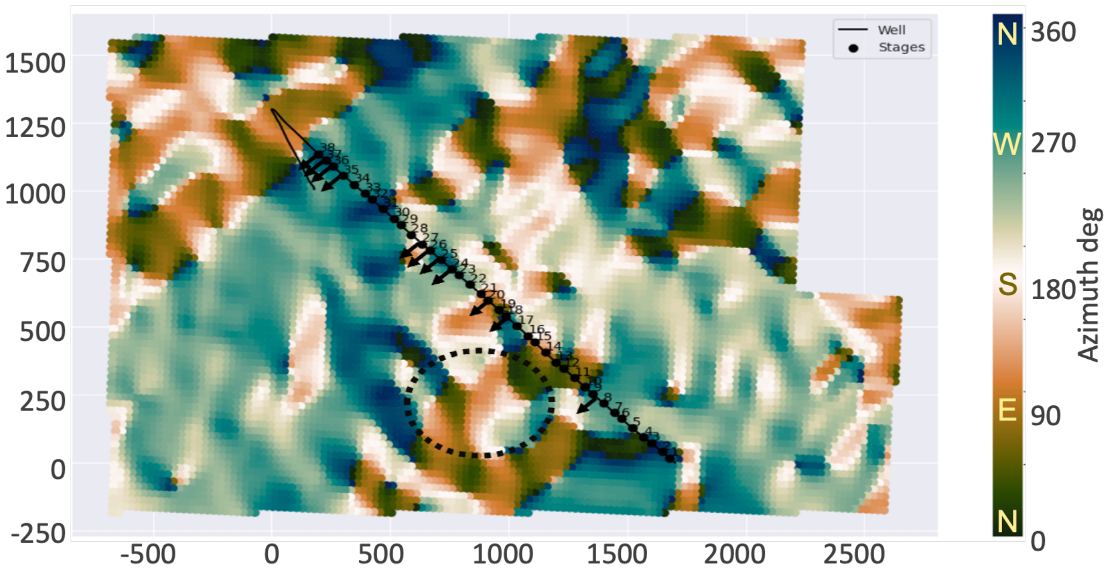

Figure 8.11: The horizon-based dip azimuth attribute map of the Belloy horizon, focusing on the area around the well. The black line depicts the well trajectory, while dots denote the depth of hydraulic fracture treatment ports. Black arrows highlight stages where microseismic events predominantly moved southwestward. The circle denotes data quality issues. Initial observations suggest microseismic events tend to move up-dip direction.

8.3 Variability of microseismic clouds across stages

The treatment analysis indicates that the PKN has overestimated the fracture half-length. Ortega Perez and van der Baan (2024) has stated that some of these discrepancies, especially in the middle stages, are due to the competition issues. However, these discrepancies we observed overall in the stages are normal because the PKN model has idealized the fracture propagation. The results based on the model-based approach show that fractures are propagating in different regimes. The stages show different regimes at different periods of hydraulic fracturing, which explains why the

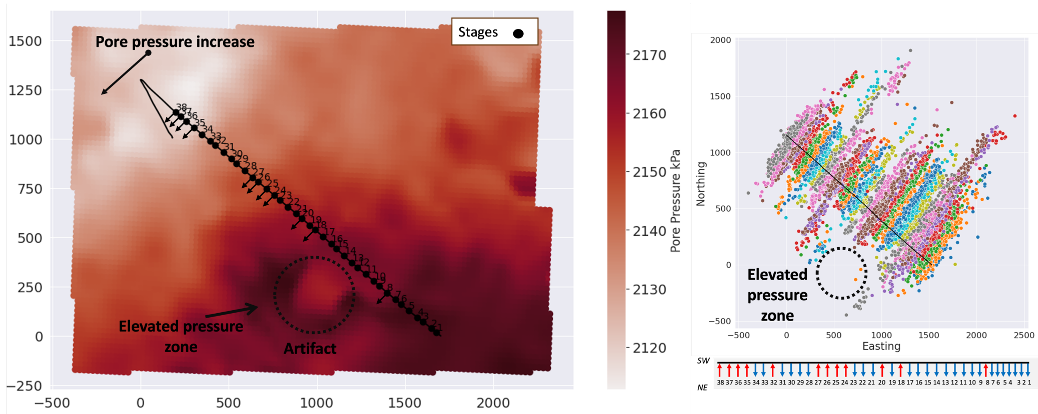

Figure 8.12: The left figure shows pore pressure map focuses on the Belloy horizon (Figure 6.19), centered on the well. The black line depicts the well trajectory, while dots denote the depth of hydraulic fracture treatment ports. Black arrows highlight stages where microseismic events predominantly moved southwestward. The circle denotes data quality issues. Initial observations suggest microseismic events tend to move northeastward when pressure is high in the southwest. Right figure shows planar view of microseismic clouds. the circled zone represents the elevated pressure zone that forces events to move toward NE direction.

PKN model has failed to estimate the fracture length correctly.

On the other hand, the overview of the results shows that the treatment parameters have affected the data, causing long fractures in the early stages and relatively shorter fractures in the late stages, representing that treatment parameters and treatment duration have affected the data. On the other hand, microseismic results show that early stages up to stage 17 show reactivation patterns (Figure 8.5). This is also shown by the FMI results up to stage 19, where discontinuous conductive (open) fractures are around the wellbore (Figure 8.7). Such phenomena only exist for a few stages toward the heel of the well. The existing natural fractures and observed "reactivation" patterns cause longer fractures as well.

The well displays a noticeable shift in mineral composition, with gamma ray values decreasing towards the bottom (toe) of the well and increasing towards the top (heel). It's worth considering that this variation could potentially be attributed to the presence of K-feldspar, suggesting that the change in microseismic behavior might not solely be due to lithological differences.

On another note, there's a discernible change in Instantaneous Shut-In Pressure (ISIP) across the stages, particularly notable is the decrease in ISIP values after stage 20. These observations suggest variations in formation properties along the wellbore. This aligns with the findings from well log analysis, indicating that lithological changes might indeed be a contributing factor. However, it's also important to note that towards the bottom of the well, there's an increase in pore pressure. This rise in pore pressure could potentially influence the observed increase in ISIP.

In summary, this holistic analysis suggests that the treatment parameters have influenced the length of the fracture cloud. While longer treatment durations may have initially impacted longer fractures, geological factors such as preexisting fractures and changes in pore pressure have significantly influenced fracture propagation.

8.4 Uni-directional propagation

The analysis based on event magnitudes indicates that the distance between the treatment and monitoring wells hasn't influenced the uni-directional cloud propagation. This is because, after the magnitude distance analysis, there was no significant decrease in event size in the SW direction.

On the other hand, seismic reflection data shows that the regional dip is in the SW direction. Local dip varies around the well, mainly attributed to changes in dip direction due to quality issues. Therefore, we say that the direction of the dip has not influenced the fractures' propagation. However, the fractures propagate updip direction. This is because the pressure toward the updip direction is less. The initial pore pressure having lower values causes lower breakdown pressure. Some parts of the formation have elevated pore pressure zones that force the fractures toward the opposite direction. Therefore, we conclude that the non-uniform pressure distribution appears to be the primary driver of fracture propagation, forcing the fractures to propagate toward the NE direction.

8.5 Stress shadow affect

The ISIP data indicates a drop below the initial ISIP value observed after stage 19, suggesting a change in the formation characteristics affecting the ISIP data. Specifically, the earlier zone (blue) exhibits a high ISIP value compared to the later side, indicating a shift in formation properties. Such observations are crucial for understanding the behavior of the formation. Moreover, these findings align with the results of well logs, where we have seen change in the lithology. Additionally, we observed that the well trajectory deviated from the initially drilled formation layer, which can also impact ISIP results.

In Figure 8.1, it is evident that up to stage 17, fractures predominantly propagate in one direction, but after stage 17, there's a change where fractures sometimes propagate towards the NE and other times towards the SW. According to the findings of Ortega Perez and van der Baan (2024), stress shadows may influence fracture propagation. As per her suggestion, when fractures predominantly move towards one side, they induce stress on that side. Subsequently, when stress reaches a high level, fractures change direction and propagate towards the opposite, less stressed direction (SW). This phenomenon is observed here as the stress load value is high.

It's noted that the stress load values in the initial stages do not significantly impact fracture propagation. We posit that this is because the well has moved out of the trajectory, nullifying the exerted stress. Alternatively, the zone where we have observed high pore pressure has forced the fractures to propagate in the NE direction. However, after stage 17, when the well remains in the same zone and no elevated pore pressure zone exists, stress load from previous stages affects propagation, indicating that stress load forces fractures to propagate in the opposite direction.

8.6 Defined Scenario for the Well 3

To generalize our observations, we have created a figure summarizing the interpretation and integration of different zones. Figure 8.13 represents the planar view of the well. To illustrate that pore pressure is increasing toward the southwest, I have colored both sides of the well in different colors: the higher pressure side with light red, while the lower pressure zone is in blue. We have also defined the high pore pressure zone (darker red). To account for the landing height change, we have included different colors such as blue and orange. The semicircle around the fracture represents the increase in stress around them, and once they increase enough to create sufficient pressure, it forces subsequent fractures to propagate toward the opposite direction. The absence of such behavior up to stage 17 is because there are high-pressure zones that force the fractures toward the northeast, and also at this section, the well has moved out of the horizon where the effect of stress shadow has been nullified. We have also included the stages where a "reactivation" pattern was observed, represented by a cloud shape.

8.7 Conclusion

The analysis of multidisciplinary data reveals that fracture propagation is predominantly influenced by geological phenomena such as natural fractures, formation properties, landing height of the well, and changes in pore pressure. While the treatment parameters do have an impact on the cloud pattern, they are not the primary cause. Natural fractures, for instance, influence fractures to extend towards the toe of the well, where conductive fractures are observed. This phenomenon is further supported by microseismic analysis, which indicates the reactivation of the same fractures in certain stages. Additionally, the change in lithology also affected fracture propagation, with fractures being longer in sandstone-rich formations.

The unidirectional propagation of fractures can be attributed to the dipping to-

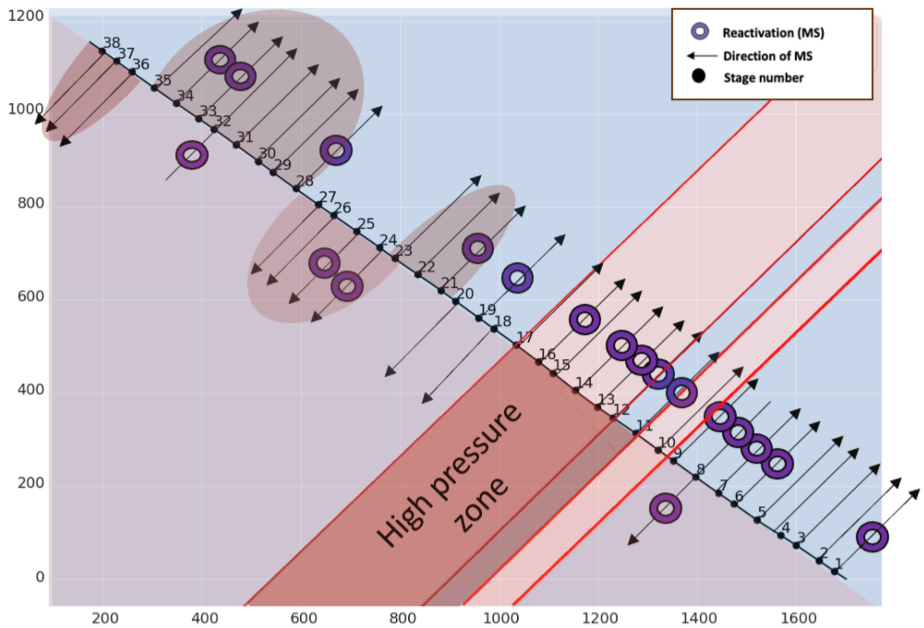

Figure 8.13: Planar view illustrating pore pressure distribution and fracture behavior within the well. Higher pressure zones depicted in light red, contrasting with lower pressure areas in blue. The darker red denotes the high pore pressure zone. Landing height changes represented by varied colors such as blue and orange. Fractures inducing stress concentration depicted by a semicircle, influencing subsequent fracture propagation. The absence of such behavior until stage 17 attributed to high-pressure zones directing fractures northeastward, and the nullification of stress shadow effect beyond the horizon. "Reactivation" patterns marked by cloud shapes.

wards the southwest (SW) direction, corresponding to areas of high pore pressure. Consequently, fractures tend to migrate towards zones where less pressure is exerted. However, as the pressure exerted by fracture propagation increases, fractures are compelled to move in the opposite direction. This behavior is less evident in the initial stages, primarily due to the well moving out of the horizon.

Chapter 9

Conclusions and suggested directions for future research

9.1 Conclusions

Hydraulic fracturing is a complex method used to extract hydrocarbons from unconventional reservoirs by stimulating the well in multiple stages. This process involves injecting fluid and proppants into the formation at high pressures, which creates fractures in the rock, allowing trapped hydrocarbons to flow more freely. During our observations, we noticed distinct propagation patterns in each stage, primarily moving northeast. Additionally, we observed variations in fracture properties and changes in the direction of fracture propagation. These behaviors were previously unclear, so this thesis integrates engineering parameters, reflection seismic data, well data (such as well logs and well tops), and downhole microseismic data to investigate the anomalous behavior of microseismicity.

Firslty, we tried to analyze the treatment parameters. We use engineering data to explore the impact of treatment parameters on hydraulic fracture treatments. Microseismicity exhibits a notable pattern with variability across treatment stages, including predominant northeast propagation and fluctuating microseismic cloud lengths. Our objective was to investigate the influence of treatment parameters using the Perkins-Kern-Nordgren (PKN) model, building upon its previous application by Ortega Perez and van der Baan (2024). We refined the approach by assigning distinct values to the Plane strain modulus, E' and fracture height, h for each stage, aiming to mitigate geomechanical property influences on the model. Additionally, we incorporated stage duration derived from microseismic data propagation time. The findings suggest that changes in treatment parameters alone may not fully account for observed anomalies in propagation behavior.

Secondly, we aimed to elucidate the mechanisms driving such behavior through comprehensive microseismic propagation analysis. We investigated distance vs. magnitude plots to assess if directional propagation correlates with treatment and monitoring well distances. Cloud analysis and r-t plots further refine our understanding of propagation dynamics, incorporating equations to model radial distance growth over time. Integration of microseismic and Perkins-Kern-Nordgren (PKN) methods clarifies treatment parameter influences. Findings suggest that distance between wells alone doesn't explain directional cloud behavior, with dynamic changes in fracture characteristics observed. Various propagation regimes are identified, emphasizing the complexity of fracture dynamics. Discrepancies between microseismic and PKN results highlight the need for continued analysis. This study contributes to a deeper understanding of hydraulic fracturing mechanics, though further research is warranted for complete comprehension of fracture propagation phenomena.

Thirdly, we used well logs understand the small-scale geological features near the wellbore, such as natural fractures and bedding plane changes. Understanding these effects is crucial for optimizing fracturing strategies and enhancing reservoir performance. Here, we focus on analyzing the influence of these features within the Montney Formation. Our methodology includes examining basic well logs and Formation Microimager (FMI) logs to detect variations in formation properties and identify natural fractures and bedding plane alterations. Our findings provided insights into how these features impact fracture propagation, confirming their presence and correlating them with observed variations in fracture propagation and microseismic data. This analysis underscored the significance of considering small-scale geological features in hydraulic fracturing operations for effective reservoir management.

Additionally, we utilized seismic reflection data to comprehend the structural geology and pore pressure variation in the area. For structural geology analysis, we generated seismic attributes including dip, azimuth, maximum curvature, and minimum curvature. Our analysis revealed a southwest regional dip, with most fractures propagating in the updip direction. Furthermore, we employed a pore pressure map to identify elevated pore pressure zones, which compelled most events to move toward the low-pressure zone, predominantly in the northeast direction. This analysis helped us understand how structural geology and pore pressure have influenced fracture propagation.

Furthermore, we employed ISIP (Instantaneous Shut-In Pressure) analysis to capture mechanical stress interference, observing how each fracturing stage adjusts stress perpendicular to the propagation axis and influences ISIP values. By utilizing the Stress Escalation Model, we quantified stress anisotropy and fracture height. Through a detailed examination of four wells, particularly Well 3, we found no significant stress reorientation. Therefore, we concluded that the arching behavior in the microseismic clouds is not related to stress reorientation. Additionally, calculated stress loads indicate high values, meaning that when most fractures propagate in one direction, the stress load may force subsequent stages to propagate in the opposite direction. This understanding helps explain the cyclic change in propagation direction of the microseismic clouds observed after stage 17 in the data.

Finally, the synthesis of findings from surface seismic, microseismic, borehole, and engineering data culminate an understanding of hydraulic operational dynamics. The integration of different findings indicate that the microseismic data was mostly influenced by the geology. Through this integration, we have achieved the following objectives:

1. Treatment parameters have an impact on the cloud pattern, but they are not the primary cause of fracture propagation.

2. MS results indicates that there are different propagation patterns, and different fracture propagation regimes that microseismic clouds exhibits and they are mostly propagating in NE direction.

3. Fracture propagation is predominantly influenced by geological phenomena such as natural fractures, formation properties, and changes in pore pressure. Natural fractures influence fractures to extend towards the toe of the well, where conductive fractures are observed, supported by microseismic analysis indicating reactivation of the same fractures. Unidirectional propagation of fractures is attributed to dipping towards the southwest (SW) direction, corresponding to areas of high pore pressure; fractures migrate towards zones of lower pressure, but as propagation pressure increases, fractures may move in the opposite direction.

4. The stress shadow has indeed affected the propagation of the fractures. It increased the stresses and forced fractures to move in the opposite direction. In earlier stages, the stress shadow does not cause as much impact as before. This could be due to either the well moving out of the trajectories or the presence of a high-pressure zone that the stress load cannot overcome.

In conclusion, this thesis elucidates the root causes of abnormal microseismic behavior in Montney treatments. The geological factors such as natural fractures, variations in pore pressure, and regional dipping, alongside the landing height of the well and the stress shadow effect, influence the propagation of microseismic events. These factors create unidirectional propagation and variations in directional trends within the hydraulically fractured fractures.

9.2 Suggested directions for future research

1. When we conducted the seismic analysis, we utilized horizon-based seismic attributes, which are affected by the presence of artifacts related to data quality. Therefore, for future research, we recommend using volume-based seismic attributes to ensure that seismic artifacts do not cause misinterpretations.

2. The calculation of pore pressure in this work utilized a simple approach; adopting more sophisticated methods could enhance understanding of pore pressure dynamics. Further research is warranted to investigate residual stress changes, which were not explored in this study. This will enhance the understanding of one directional propagation.

3. To better understand stress perturbations around fractures, future studies could analyze stress dynamics for each stage individually, as the current approach analyzed all 20 stages collectively.The stress perturbation analysis across the 38 stages may give better understanding of fracture propagation.

4. Future research endeavors could involve conducting flow-geomechanics simulations to explore and validate observed phenomena from this study. Specifically, investigating scenarios where hydraulic fractures propagate asymmetrically, halting on one side while continuing on the other, could provide valuable insights into fracture behavior under varying geological conditions. To do so, one can integrate the stress field, stress shadow, and geological factors such as natural fractures and geological structure, as well as pore pressure variation.

Bibliography

Adachi, J., & Detournay, E. (2002). Self-similar solution of a plane-strain fracture driven by a powerlaw fluid. *International Journal for Numerical and Analytical Methods in Geomechanics*, *26*(6), 579–604.

Bahrami, N., Pena, D., & Lusted, I. (2016). Well test, rate transient analysis and reservoir simulation for characterizing multi-fractured unconventional oil and gas reservoirs. *Journal of Petroleum Exploration and Production Technology*, *6*(4), 675–689.

Barthwal, H., & van der Baan, M. (2019). Role of fracture opening in triggering microseismicity observed during hydraulic fracturing. *Geophysics*, *84*(3), KS105–KS118.

Bearinger, B. D. (2022). Complete hydraulic fracture modeling of the full Montney. *Geoconvention, 2022*. https://geoconvention.com/wp-content/uploads/abstracts/2022/73316-complete-hydraulic-fracture-modeling-of-the-full-m.pdf

Becerra, D., Clarkson, C. R., Ghanizadeh, A., Pires de Lima, R., Tabasinejad, F., Zhang, Z., Trivedi, A., & Shor, R. (2021). Evaluation of reservoir quality and forecasted production variability along a multi-fractured horizontal well. part 1: Reservoir characterization. *Energies*, *14*(19), 6154.

Becker, M. W., Coleman, T. I., & Ciervo, C. (2020). Distributed acoustic sensing as a distributed hydraulic sensor in fractured bedrock. *Water Resources Research*, *56*(9), e2020WR028140.

Bell, J., Price, P., & McLellan, P. (1990). In-situ stress in the western Canada Sedimentary Basin. *Bulletin of Canadian Petroleum Geology*, *38*(1), 157–157.

Belyadi, H., Fathi, E., & Belyadi, F. (2019). *Hydraulic fracturing in unconventional reservoirs: Theories, operations, and economic analysis*. Gulf Professional Publishing.

Bunger, A., Detournay, E., & Garagash, D. I. (2005). Toughness-dominated hydraulic fracture with leak-off. *International journal of fracture*, *134*, 175–190.

CER. (2023). *Increased horizontal drilling in western Canada*. Retrieved 2024, from https://www.cer-rec.gc.ca/en/data-analysis/energy-markets/market-snapshots/2015/market-snapshot-increased-horizontal-drilling-in-western-Canada.html

Chalmers, G. R., Lacerda Silva, P., Bustin, A. A., Sanlorenzo, A., & Bustin, R. M. (2022). Geology and geochemistry of the hydrocarbon compositional changes in the Triassic Montney formation, western Canada. *Energies*, *15*(22), 8677.

Chevrot, V., Hernandez, S., & Harris, N. (2020). Example of fluid migration and distribution modelling in unconventional reservoirs from the Montney formation, northeastern British Columbia (nts 093p, 094a). https://ba-cdn.sfo3.digitaloceanspaces.com/Clients/Geoscience/pdf/SummaryofActivities2020/EW/Sch_Chevrot_EWSOA2020.pdf

Chopra, S., & Marfurt, K. J. (2007). *Seismic attributes for prospect identification and reservoir characterization*. Society of Exploration Geophysicists.

Chopra, S., & Marfurt, K. J. (2008). Emerging and future trends in seismic attributes. *The Leading Edge*, *27*(3), 298–318.

Cipolla, C., Maxwell, S., Mack, M., & Downie, R. (2011). A practical guide to interpreting microseismic measurements. *SPE Unconventional Resources Conference/Gas Technology Symposium*, SPE–144067.

Dang, T. (2008). Application of photogrammetry for measuring dip and dip direction and creating 3d model for slope and face of underground works. *Proceedings of the International Conference on Advances in Mining and Tunneling Conference, Hanoi, Vietnam*, 19–23.

Davey, H. (2012). *Geomechanical characterization of the Montney shale northwest Alberta and northeast British Columbia, Canada*. Colorado School of Mines.

Davies, G. R., Moslow, T. F., & Sherwin, M. D. (1997). The lower Triassic Montney formation, west-central Alberta. *Bulletin of Canadian Petroleum Geology*, *45*(4), 474–505.

Detournay, E. (2004). Propagation regimes of fluid-driven fractures in impermeable rocks. *International Journal of Geomechanics*, *4*(1), 35–45.

Djabelkhir, N. (2020). Simulation of notch driven hydraulic fracture in open hole completion.

Dontsov, E., & Suarez-Rivera, R. (2020). Propagation of multiple hydraulic fractures in different regimes. *International Journal of Rock Mechanics and Mining Sciences*, *128*, 104270.

Economides, M., & Nolte, K. (2000). *Reservoir stimulation* (3rd).

Egbobawaye, E. I. (2013). *Tight gas reservoir characterization in Montney formation, northeastern British Columbia, western Canada*. University of Alberta (Canada).

Ellis, D. (2003). Formation porosity estimation from density logs. *Petrophysics-The SPWLA Journal of Formation Evaluation and Reservoir Description*, *44*(05).

Ellis, D., Case, C., & Chiaramonte, J. (2003). Tutorial-porosity from neutron logs i-measurement. *Petrophysics-The SPWLA Journal of Formation Evaluation and Reservoir Description*, *44*(06).

Enlighten Geoscience, L. (2021). Pressure, stress and fault slip risk mapping in the Kiskatinaw seismic monitoring and mitigation area, British Columbia. *BC Oil and Gas Research and Innovation Society (ER-Seismic-2020–01)*.

Fan, L., Thompson, J. W., & Robinson, J. R. (2010). Understanding gas production mechanism and effectiveness of well stimulation in the haynesville shale through reservoir simulation. *Canadian unconventional resources and international petroleum conference*.

Faraj, B., Williams, H., Addison, G., McKinstry, B., Donaleshen, R., Sloan, G., Lee, J., Anderson, T., Leal, R., Anderson, C., et al. (2002). Shale potential of selected Upper Cretaceous, Jurassic, Triassic and Devonian shale formations, in the WCSB of western Canada: Implications for shale gas production. *A Report for Gas Technology Institute (GTI), Des Plains, Illinois, USA*.

Fisher, M., Heinze, J., Harris, C., Davidson, B., Wright, C., & Dunn, K. (2004). Optimizing horizontal completion techniques in the barnett shale using microseismic fracture mapping. *SPE Annual Technical Conference and Exhibition, 90051-MS*.

Gauthier, S., Puech, W., Bénière, R., & Subsol, G. (2017). Digitized 3D mesh segmentation based on curvature analysis. *Electronic Imaging*, *6*(3DIPM-005), 33–38.

Geertsma, J., & De Klerk, F. (1969). A rapid method of predicting width and extent of hydraulically induced fractures. *Journal of petroleum technology*, *21*(12), 1571–1581.

Ghosh, S. (2022). A review of basic well log interpretation techniques in highly deviated wells. *Journal of Petroleum Exploration and Production Technology*, *12*(7), 1889–1906.

Ghosh, S., Hooker, J. N., Bontempi, C. P., & Slatt, R. M. (2018). High-resolution stratigraphic characterization of natural fracture attributes in the Woodford shale, Arbuckle wilderness and us-77d outcrops, Murray county, Oklahoma. *Interpretation*, *6*(1), SC29–SC41.

Gilchrist, W. (2008). Compensated neutron log response issues-a tutorial. *SPWLA Annual Logging Symposium*, SPWLA–2008.

GMDK, G. K. (2015). *5.2 time-to-depth conversion*. Retrieved 2024, from https://gmdk.ca/intro-geomodeling/chapter-5-geophysicists-and-geomodeling/5-3-seismic-interpretation-and-stratigraphic-modeling

Gong, B., Manuel, E., Liu, Y., Forand, D., Malizia, T., Tohidi, V., & Saldana, A. (2021). Interpretation of LWD acoustic borehole image logs: Case studies from North American shale plays. *SPWLA Annual Logging Symposium*, D031S027R003.

Grace, M., & Newberry, B. (1998). *Geological applications of dipmeter and borehole electrical images*. Schlumberger Oilfield Services.

Halliburton. (2005). *Array compensated true resistivity tool field operational manual*. Retrieved 2024, from https://pdfcoffee.com/qdownload/acrt-i-fom-d00204472-pdf-free.html

Han, H., & van der Baan, M. (2024). Constraint strategies for estimating in-situ stress from borehole measurements. *Geomechanics for Energy and the Environment*, *37*, 100518.

Hanks, T. C., & Kanamori, H. (1979). A moment magnitude scale. *Journal of Geophysical Research: Solid Earth*, *84*(B5), 2348–2350.

Herrera, R. H., & van der Baan, M. (2014). A semiautomatic method to tie well logs to seismic data. *Geophysics*, *79*(3), V47–V54.

Hossain, M., Rahman, M., & Rahman, S. (2000). Hydraulic fracture initiation and propagation: Roles of wellbore trajectory, perforation and stress regimes. *Journal of petroleum science and engineering*, *27*(3-4), 129–149.

Howard, G. C., & Fast, C. (1957). Optimum fluid characteristics for fracture extension. *Drilling and production practice*.

Jin, G., & Roy, B. (2017). Hydraulic-fracture geometry characterization using low-frequency das signal. *The Leading Edge*, *36*(12), 975–980.

Kendall, D. R. (2001). *Sedimentology and stratigraphy of the lower triassic Montney formation, peace river basin, subsurface of northwestern Alberta*. MS thesis.

Kimmitt, K. P. (2011). Developing a stage tool for cemented back monobore completions with open hole multi-stage systems in the Montney. *International Petroleum Technology Conference*, IPTC–15267.

King, G. E. (2010). Thirty years of gas shale fracturing: What have we learned? *SPE Annual Technical Conference and Exhibition?*, SPE–133456.

Koson, S., Chenrai, P., & Choowong, M. (2013). Seismic attributes and their applications in seismic geomorphology. *Bulletin of Earth Sciences of Thailand*, *6*(1), 1–9.

Krause, F., Wiseman, A., Williscroft, K., Solano, N., Morris, N., Meyer, R., & Marr, R. (2011). The montney formation: Mineralogy, what shall it be? *Canadian Society of Petroleum Geologists, Canadian Society of Exploration Geophysicists, Canadian Well Log Society, Joint Annual Convention*.

Kuppe, F. C., Nevokshonoff, G., Haysom, S., et al. (2012). Liquids rich unconventional Montney reservoir: The geology and the forecast. *SPE Canadian unconventional resources conference*.

Kutz, M. (2011). *Applied plastics engineering handbook: Processing and materials*. William Andrew.

Li, L., Tan, J., Schwarz, B., Staněk, F., Poiata, N., Shi, P., Diekmann, L., Eisner, L., & Gajewski, D. (2020). Recent advances and challenges of waveform-based seismic location methods at multiple scales. *Reviews of Geophysics*, *58*(1), e2019RG000667.

Liu, Z., Gao, B., Hu, Z., Du, W., Nie, H., & Jiang, T. (2018). Pore characteristics and formation mechanism of high-maturity organic-rich shale in Lower Cambrian Jiumenchong formation, southern guizhou. *Petroleum Research*, *3*(1), 57–65.

Lofts, J., Bedford, J., Boulton, H., Van Doorn, J., & Jeffreys, P. (1997). Feature recognition and the interpretation of images acquired from horizontal wellbores. *Geological Society, London, Special Publications*, *122*(1), 345–365.

Lofts, J., & Bourke, L. (1999). The recognition of artefacts from acoustic and resistivity borehole imaging devices. *Geological Society, London, Special Publications*, *159*(1), 59–76.

Luthi, S. M., & Souhaite, P. (1990). Fracture apertures from electrical borehole scans. *Geophysics*, *55*(7), 821–833.

Ma, D., Wu, Y., Yin, J., Lu, J., Hu, D., & Zhou, H. (2023). Effect of initial pore pressure on the hydraulic fracturing of tight sandstone: An experimental study. *Geomechanics and Geophysics for Geo-Energy and Geo-Resources*, *9*(1), 15.

Mai, H., Marfurt, K. J., & Tan, M. T. (2009). Multi-attributes display and rose diagrams for interpretation of seismic fracture lineaments, example from cuu long basin, vietnam.

Maxwell, S. (2014). *Microseismic imaging of hydraulic fracturing: Improved engineering of unconventional shale reservoirs*. Society of Exploration Geophysicists.

McDaniel, B. (2010). Horizontal wells with multi-stage fracs provide better economics for many lower permeability reservoirs. *SPE Asia Pacific Oil and Gas Conference and Exhibition*, SPE–133427.

McLennan, J., & Roegiers, J.-C. (1982). How instantaneous are instantaneous shut-in pressures? *SPE Annual Technical Conference and Exhibition?*, SPE–11064.

Moradi, P. M. (2021). Sera: An isip analysis approach to estimate fracture height and correlate stress escalation and relaxation in multifrac horizontal wells. *Results in Engineering*, *11*, 100241.

Mossop, G., & Shetsen, I. (1994). Introduction to the geological atlas of the western Canada sedimentary basin. *Geological Atlas of the Western Canada Sedimentary Basin, edited by: Mossop, GD and Shetsen, I., Canadian Society of Petroleum Geologists and Alberta Research Council, Alberta*, 1–11.

Nelson, G., & Rghei, A. (2008). Explosive growth, protected areas and conservation abu dhabi, united arab emirates (uae).

Nguyen, H. T., Lee, J. H., & Elraies, K. A. (2020). A review of PKN-type modeling of hydraulic fractures. *Journal of Petroleum Science and Engineering*, *195*, 107607.

Nivlet, P., Smith, R., & AlBinHassan, N. (2020). Automated well-to-seismic tie using deep neural networks. In *SEG technical program expanded abstracts 2020* (pp. 2156–2160). Society of Exploration Geophysicists.

Nordgren, R. (1972). Propagation of a vertical hydraulic fracture. *Society of petroleum engineers journal*, *12*(04), 306–314.

Nustes Andrade, J., & van der Baan, M. (2021). Real-time analysis and forecasting of the microseismic cloud size: Physics-based models versus machine learning. *Geophysics*, *86*(6), KS175–KS186.

Orchard, M., & Zonneveld, J.-P. (2009). The Lower Triassic Sulphur Mountain formation in the Wapiti Lake area: Lithostratigraphy, conodont biostratigraphy, and a new biozonation for the lower olenekian (smithian). *Canadian Journal of Earth Sciences*, *46*(10), 757–790.

Ortega Perez, A. K. (2022). Hydraulic fracture monitoring: Integrated analysis of das, pumping information, microseismicity and PKN modelling.

Ortega Perez, A. K., & van der Baan, M. (2024). Interpretation of low-frequency distributed acoustic sensing data based on geomechanical models. *Geophysics*, *89*(2), M47–M59.

Perkins, T., & Kern, L. (1961). Widths of hydraulic fractures. *Journal of petroleum technology*, *13*(09), 937–949.

Popp, M. (2015). Completion and stimulation optimization of montney wells in the Karr field. *PhD diss., University of Calgary.*

Porter, J., Price, R., & McCrossan, R. (1982). The western Canada sedimentary basin. *Philosophical Transactions of the Royal Society of London. Series A, Mathematical and Physical Sciences*, *305*(1489), 169–192.

Prabhakaran, R., De Pater, H., & Shaoul, J. (2017). Pore pressure effects on fracture net pressure and hydraulic fracture containment: Insights from an empirical and simulation approach. *Journal of Petroleum Science and Engineering*, *157*, 724–736.

Prenoslo, D., Furlong, C. M., Gingras, M. K., Playter, T., & Zonneveld, J.-P. (2018). The sedimentology, stratigraphy and reservoir characteristics of the Montney D1 and D2 horizons in the Greater Pouce Coupe area. *Bulletin of Canadian Petroleum Geology*, *66*(1), 338–358.

Proverbs, I., Bann, K., Fratton, C., Frostad, C., & Juska, A. (2018). Facies architecture and sequence stratigraphy of the Lower Triassic Montney formation, NE British Columbia: Fundamental controls on the distribution of 'sweet spots' in a world-class unconventional reservoir. *Bulletin of Canadian Petroleum Geology*, *66*(1), 237–258.

Quintero, J., & Tejada, M. (2020). Time to depth conversion: Velocity modelling in the Llanos basin, onshore Colombia. *Journal of South American Earth Sciences*, *100*, 102557.

Rajput, S., & Thakur, N. K. (2016). Chapter 10 - the road ahead and other thoughts. In S. Rajput & N. K. Thakur (Eds.), *Geological controls for gas hydrate formations and unconventionals* (pp. 327–357). Elsevier. https://doi.org/https://doi.org/10.1016/B978-0-12-802020-3.00010-2

Richter, P., Parker, T., Woerpel, C., Wu, Y., Rufino, R., & Farhadiroushan, M. (2019). Hydraulic fracture monitoring and optimization in unconventional completions using a high-resolution engineered fibre-optic distributed acoustic sensor. *First Break*, *37*(4), 63–68.

Rider, M. H., & Martin, K. (2014). *The geological interpretation of well logs* (3rd). Rider-French Consulting Limited, Scotland, 2011.

Rijks, E., & Jauffred, J. (1991). Attribute extraction: An important application in any detailed 3-d interpretation study. *The Leading Edge*, *10*(9), 11–19.

Rodvelt, G. (2020). Enhanced hydro-fracturing. In *Coal Bed Methane* (pp. 219–254). Elsevier.

Roussel, N. (2017). Analyzing isip stage-by-stage escalation to determine fracture height and horizontal-stress anisotropy. *SPE Hydraulic Fracturing Technology Conference and Exhibition, 184865-MS*.

Roussel, N. (2020, August). Methods for shut-in pressure escalation analysis [US Patent 10,753,181].

Roussel, N., & Sharma, M. M. (2011). Optimizing fracture spacing and sequencing in horizontal-well fracturing. *SPE Production & Operations*, *26*(02), 173–184, SPE-127986–PA.

Roussel, N., Swan, H., Snyder, J., Nguyen, D., Cramer, D., & Ouk, A. (2021). Evaluation and insights from instantaneous shut-in pressures. *Unconventional Resources Technology Conference, 26–28 July 2021*, 2545–2563.

Rozhko, A. Y. (2010). Role of seepage forces on seismicity triggering. *Journal of Geophysical Research: Solid Earth*, *115*(B11).

Safinya, K., Le Lan, P., Villegas, M., & Cheung, P. (1991). Improved formation imaging with extended microelectrical arrays. *SPE Annual Technical Conference and Exhibition?*, SPE–22726.

Salah, M., Orr, D., Meguid, A. A., Crane, B., & Squires, S. (2016). Multistage horizontal hydraulic fracture optimization through an integrated design and workflow in Apollonia tight chalk, Egypt from the laboratory to the field. *Abu Dhabi international petroleum exhibition and conference*, D021S025R006.

Schmitt, D. R., Currie, C. A., & Zhang, L. (2012). Crustal stress determination from boreholes and rock cores: Fundamental principles. *Tectonophysics*, *580*, 1–26.

Segall, P., & Lu, S. (2015). Injection-induced seismicity: Poroelastic and earthquake nucleation effects. *Journal of Geophysical Research: Solid Earth*, *120*(7), 5082–5103.

Shapiro, S., Dinske, C., & Rothert, E. (2006). Hydraulic-fracturing controlled dynamics of microseismic clouds. *Geophysical Research Letters*, *33*(14).

Shapiro, S., & Dinske, C. (2009). Scaling of seismicity induced by nonlinear fluid-rock interaction. *Journal of Geophysical Research: Solid Earth*, *114*(B9).

Shapiro, S., Huenges, E., & Borm, G. (1997). Estimating the crust permeability from fluid-injection-induced seismic emission at the ktb site. *Geophysical Journal International*, *131*(2), F15–F18.

Shen, L., Schmitt, D., & Haug, K. (2018). Measurements of the states of in situ stress for the duvernay formation near fox creek, west-central Alberta. *Alberta Energy Regulator/Alberta Geological Survey, AER/AGS Report*, *97*, 29.

Shovkun, I., & Espinoza, D. N. (2019). Propagation of toughness-dominated fluid-driven fractures in reactive porous media. *International Journal of Rock Mechanics and Mining Sciences*, *118*, 42–51.

Silva, P. M., Martins, L., & Gattass, M. (2012). Horizon indicator attributes and applications. In *SEG technical program expanded abstracts 2012* (pp. 1–6). Society of Exploration Geophysicists.

Singer, J. (1992). An example of log interpretation in horizontal wells. *The Log Analyst*, *33*(02).

Slim, M. I. (2007). Borehole-image log interpretation and 3d facies modeling in the Mesaverde group, Greater Natural Buttes field, Uinta basin, Utah. *2000-2009-Mines Theses & Dissertations*.

Smithson, T. (2015). Measuring porosity downhole. https://www.slb.com/resource-library/oilfield-review/defining-series/defining-porosity#:~:text=and%20neutron%20porosity.-,Porosity%20Measurements,unit%20volume%E2%80%94the%20electron%20density

Sneddon, I. N. (1946). The distribution of stress in the neighbourhood of a crack in an elastic solid. *Proceedings of the Royal Society of London. Series A. Mathematical and Physical Sciences*, *187*(1009), 229–260.

Soliman, M. Y., East, L., & Adams, D. (2008). Geomechanics aspects of multiple fracturing of horizontal and vertical wells. *SPE Drilling & Completion*, *23*(03), 217–228.

Suo, C., Peng, S., Chang, S., Duan, R., & Wang, G. (2012). A new calculating method of the curvature to predicting the reservoir fractures. *Procedia Environmental Sciences*, *12*, 576–582.

Tylor-Jones, T., & Azevedo, L. (2023). *A practical guide to seismic reservoir characterization*. Springer Nature.

Ugueto, G., Todea, F., Daredia, T., Wojtaszek, M., Huckabee, P. T., Reynolds, A., Laing, C., & Chavarria, J. A. (2019). Can you feel the strain? das strain fronts for fracture geometry in the BC Montney, Groundbirch. *SPE Annual Technical Conference and Exhibition*.

Valko, P., Economides, M., & Leoben, M. U. (1993). Fracture height containment with continuum damage mechanics. *SPE Annual Technical Conference and Exhibition?*, SPE–26598.

Van Der Baan, M., Eaton, D., & Dusseault, M. (2013). Microseismic monitoring developments in hydraulic fracture stimulation. *ISRM international conference for effective and sustainable hydraulic fracturing*, ISRM–ICHF.

Vishkai, M., & Gates, I. (2019). On multistage hydraulic fracturing in tight gas reservoirs: Montney formation, Alberta, Canada. *Journal of Petroleum Science and Engineering*, *174*, 1127–1141.

Wang, H., Li, M., & Shang, X. (2016). Current developments on micro-seismic data processing.

Wang, Y., & Miskimins, J. L. (2010). Experimental investigations of hydraulic fracture growth complexity in slickwater fracturing treatments. *Tight gas completions conference*.

Warpinski, N. (2009). Microseismic monitoring: Inside and out. *Journal of Petroleum Technology*, *61*(11), 80–85.

Weatherford. (2015). *Compact™ formation evaluation oil-base mud microimager*. Retrieved 2024, from https://www.weatherford.com/documents/brochure/products-and-services/formation-evaluation/compact-oil-base-mud-microimager/

White, R., & Simm, R. (2003). Tutorial: Good practice in well ties. *First break*, *21*(10).

Wilson, A. (2021). Structural geology and sedimentology of west erregulla-5 from borehole image logs.

Wright, S. J. (2006). *Numerical optimization* (2nd). https://www.math.uci.edu/~qnie/Publications/NumericalOptimization.pdf

Wu, H., Li, Z., & Liu, N. (2022). Variable seismic waveforms representation: Weak-supervised learning based seismic horizon picking. *Journal of Petroleum Science and Engineering*, *214*, 110412.

Yousefzadeh, A., Li, Q., Virues, C., & Aguilera, R. (2018). An interpretation of microseismic spatial anomalies, b-values, and magnitude analyses to identify activated fracture networks in horn river basin. *SPE Production & Operations*, *33*(04), 679–696.

Yu, W., & Sepehrnoori, K. (2013). Simulation of proppant distribution effect on well performance in shale gas reservoirs.

Zhou, Q. (2008). Log interpretation in high-deviation wells through user-friendly tool-response processing. *SPWLA Annual Logging Symposium*, SPWLA–2008.

Zonneveld, J.-P., & Moslow, T. F. (2018a). Palaeogeographic evolution of the montney in the western Canada sedimentary basin.

Zonneveld, J.-P., & Moslow, T. F. (2018b). Palaeogeographic setting, lithostratigraphy, and sedimentary framework of the Lower Triassic Montney formation of western Alberta and northeastern British Columbia. *Bulletin of Canadian Petroleum Geology*, *66*(1), 93–127.

Zou, C. (2013). *Unconventional petroleum geology*. Elsevier. https://doi.org/10.1016/B978-0-12-397162-3.00003-7